

CHARACTERISATION OF FAILURE IN COMPOSITE MATERIALS  
WITH ACOUSTIC EMISSION AND CORRELATION WITH  
MICROMECHANICS

by

Fatih Ertuğrul Öz

B.S., Manufacturing Engineering, Istanbul Technical University, 2008

M.S., Mechanical Engineering, Boğaziçi University, 2012

Submitted to the Institute for Graduate Studies in  
Science and Engineering in partial fulfillment  
of the requirements for the degree of  
Doctor of Philosophy

Graduate Program in Mechanical Engineering

Boğaziçi University

2018

## ACKNOWLEDGEMENTS

It is not possible to write my feelings about Prof. Nuri Ersoy only in one page. I had a long academic journey with him. He has been more than a supervisor to me. His guidance on my thesis with his great intuition about composite materials helped me to stay motivated and never lose my hope during my PhD study. Working with Prof. Stepan Vladimirovich Lomov has been another fortune for me since my research visit to KU Leuven. His intuition about composite materials has influenced me on this research field. His deep understanding about composite materials and his guidance accelerated the progress of this thesis and expanded the content of this thesis. I appreciate the patience and guidance of these two outstanding supervisors who cautiously followed my study.

I would like to acknowledge Prof. Fazıl Önder Sönmez and Assoc. Prof. Nilüfer Özyurt Zihnioğlu for their suggestions during progress of my study. I would like to express my gratitude Prof. Bülent Ekici and Prof. Melih Papila for becoming my PhD jury members. I feel really lucky since my supervisors and jury members are very strong academics in the field of composite materials and that makes me feel like I can compete with entire world.

I would like to thank my colleagues from our research group. Especially Onur Yüksel, Kenan Çınar and Sina Ahmadvash. I would not be able to complete manufacturing and test my specimens without them. We did not only helped each other's study but also to the important companies involved with composite materials in Turkey. Then I would like to thank Yakup Okan Alpay, Anıl Uzal, Farzad Bina, Mehmet Can Engül, Mert Kılınçel and Sina Narimani. I will never forget their support. I would also like to thank Katleen Valoons, Delphine Depuyt, Man Zhu and Mahoor Mehdikhani for helping me during my research in KU Leuven.

I devote this thesis to my beloved family. This thesis would not have been possible without their love and encouragement. They are the most special part of my life.

Finally I would like to acknowledge the support of the Boğaziçi University Research Fund, Istanbul Development Agency (ISTKA), and TUBITAK BİDEB 2214-A under project codes 10020/15A06D3, ISTKA/BIL/2012/58 and 1059B141600673 respectively.

## **ABSTRACT**

# **CHARACTERISATION OF FAILURE IN COMPOSITE MATERIALS WITH ACOUSTIC EMISSION AND CORRELATION WITH MICROMECHANICS**

Polymer composites fail through complex damage mechanisms. It is not easy to determine stress levels for onset of various damage mechanisms with a single uniaxial tension test, since their stress-strain responses do not provide a clear yield point or stiffness degradation during loading. Acoustic Emission (AE) is an important technique used to detect damage in composite materials. An AE signal is an ultrasonic wave resulting from the sudden release of the strain energy when damage initiates and contains information about the damage mode. General conclusions in literature for the correlation of damage modes with corresponding AE characteristics are relied on interpretations rather than direct observation of damage modes. In this thesis, damage progression in Carbon Fibre Reinforced Plastic composites are investigated using AE technique. Optical instruments are used to obtain reliable correlations with damage modes and the AE events. First unidirectional laminates are tested. Artificial defects in the form of slits are incorporated at certain plies during manufacturing to stimulate damage in desired sequence. Tension tests are stopped at certain stress levels before the ultimate strength and specimen edges are investigated with optical microscope to identify damage modes and correlate with AE characteristics. Then results are compared with predictions of a progressive damage model implemented using Finite Element Micromechanical Model and a very good consistency is achieved. In the second part, Digital Image Correlation (DIC) and in-situ edge observation are applied simultaneously during the tension tests of different quasi-isotropic laminates. They provide robust evidences for damage mode correlations. The k-means++ clustering algorithm is used to group similar AE events. It is seen that damage progression and their AE characteristics change with lay-up sequence. The results obtained in this thesis put the reliability of AE based damage mode classifications, widely adopted in literature, in question and a new classification scheme is proposed.

## ÖZET

### **KOMPOZİT MALZEMELERDE HASARIN AKUSTİK EMİSYON İLE BELİRLENMESİ VE MİKROMEKANİK İLE İLİŞKİLENDİRİLMESİ**

Polimerik kompozit malzemeler karmaşık hasarlanma mekanizmaları sonucunda kırılırlar. Bu hasarlanma meknizmalarının tetiklendiği seviyeleri tek bir çekme testi ile belirlemek kolay değildir. Çünkü, bu malzemelerin gerilme-gerinme davranışları net bir akma noktası veya rijitlik bozulması göstermemektedir. Akustik Emisyon (AE) tekniği, kompozit malzemelerde hasar tayini için kullanılan önemli bir yöntemdir. Bir AE sinyali, hasar olduğunda şekil değiştirme enerjisinin ani biçimde salınması sonucu oluşan bir ultrasonik dalgadır ve hasar hakkında bilgiler içermektedir. Literatürde, hasar tipleri ve AE karakteristikleri arasındaki ilişkiler ile ilgili genel sonuçların çoğu direkt gözlemlere değil, yoruma dayanmaktadır. Bu tez çalışmasında, Karbon Elyaf Takviyeli Plastik kompozitlerde meydana gelen hasarlanmalar AE yöntemi kullanılarak incelenmektedir. AE sinyalleri ve hasar tipleri arasında güvenilir bir ilişki kurulabilmesi için optik gözlem yöntemleri kullanılmıştır. İlk olarak tek yönlü dizilime sahip numuneler test edilmiştir. Bu numuneler üretilirken belli bir katmana kesikler açılarak sunni kusurlar oluşturulmuş ve hasarlanma sırasının istenen biçimde ilerlemesi sağlanmıştır. Bu numunelerin çekme testleri, dayanımlarından daha düşük gerilme seviyelerinde durdurulup, numuneler optik mikroskoplarla incelenerek hasar tipleri belirlenmiş ve AE sinyalleri ile eşleştirilmiştir. Bu sonuçlar, Sonlu Elemanlar Mikromekanik Yöntemi ile gerçekleştirilen bir ilerlemeli hasar analizi modeli öngörülerini ile karşılaştırılmıştır ve ikisi arasında iyi bir tutarlılık elde edilmiştir. Çalışmanın ikinci bölümünde, izotropik-benzeri numunelerin çekme testleri sırasında Sayısal Görüntü Korelasyonu (DGK) yöntemi ve numune kenarının yerinde gözlemi yöntemleri kullanılmıştır. Bu yöntemler, hasar tiplerinin eşleştirilmesi için kuvvetli deliller sağlamaktadır. Benzer özelliklere sahip sinyallerin gruplandırılması için k-means++ kümeleme algoritması kullanılmıştır. Hasar tiplerinin ilerlemesi ile bunların AE özelliklerinin, dizilimler değişikçe farklılaştığı görülmüştür. Bu tez çalışmasının sonuçları, literatürde yaygın olarak kabul gören AE yöntemine dayalı hasar sınıflandırmasının güvenilirliğini sorgulanır hale getirmekte ve yeni bir sınıflandırma önermektedir.

## TABLE OF CONTENTS

ACKNOWLEDGEMENTS .....	iii
ABSTRACT.....	iv
ÖZET .....	v
TABLE OF CONTENTS.....	vi
LIST OF FIGURES .....	ix
LIST OF TABLES .....	xvii
LIST OF SYMBOLS .....	xviii
LIST OF ACRONYMS/ABBREVIATIONS .....	xix
1. INTRODUCTION.....	1
1.1. Motivation.....	1
1.2. Literature Review.....	10
1.2.1. Evaluation of AE Results with Respect to Single Parameter .....	11
1.2.2. Evaluation of AE Results with Respect to Cluster Algorithms.....	28
1.2.3. Summary of Literature .....	42
1.3. Objective .....	45
2. EXPERIMENTAL METHODS .....	47
2.1. Material and Manufacturing .....	47
2.2. Specimen Preparation .....	49
2.2.1. Smooth Tension Specimens .....	50
2.2.2. Open-Hole Tension Specimens .....	51
2.2.3. Slit Specimens .....	52
2.2.4. Grinding and Polishing.....	53
2.3. Tension Tests .....	56
2.4. Acoustic Emission .....	59

2.4.1.	MISTRAS AE System.....	60
2.4.2.	VALLEN AE System.....	61
2.4.3.	The k-means++ Clustering Algorithm. ....	63
2.4.4.	Digital Image Correlation.....	65
2.4.5.	Edge Microscopy.....	65
3.	RESULTS AND DISCUSSION .....	67
3.1.	Mechanical Test Results of Unidirectional $[0]_5$ Laminates .....	67
3.2.	Damage Mode Identification in Unidirectional $[0]_5$ Laminates .....	70
3.2.1.	Long-Slit Specimens .....	70
3.2.2.	Short-Slit Specimens .....	78
3.2.3.	Smooth Specimens .....	82
3.2.4.	Kaiser and Felicity Effects .....	86
3.2.5.	Comparison with Finite Element Micromechanical Model .....	87
3.3.	Damage Mode Identification in Smooth Quasi-Isotropic Laminates .....	90
3.3.1.	$[-45_2/0_2/+45_2/90_2]_s$ Laminates .....	92
3.3.2.	$[90_2/-45_2/0_2/+45_2]_s$ Laminates .....	101
3.3.3.	$[0_2/+45_2/90_2/-45_2]_s$ Laminates .....	104
3.3.4.	$[+45_2/90_2/-45_2/0_2]_s$ Laminates .....	109
3.3.5.	Summary of the Damage Sequence in Smooth QI Laminates .....	114
3.4.	Damage Mode Identification in Open-Hole Quasi-Isotropic Laminates.....	117
3.4.1.	$[-45_2/0_2/+45_2/90_2]_s$ OHT Laminates .....	119
3.4.2.	$[90_2/-45_2/0_2/+45_2]_s$ OHT Laminates .....	124
3.4.3.	$[0_2/+45_2/90_2/-45_2]_s$ OHT Laminates .....	129
3.4.4.	$[+45_2/90_2/-45_2/0_2]_s$ OHT Laminates .....	134
3.4.5.	Summary of the Damage Sequence in OHT QI Laminates .....	142
4.	CONCLUSION .....	145

5.	FUTURE WORK .....	148
6.	REFERENCES .....	150

## LIST OF FIGURES

Figure 1.1.	Schematic representation of molecular structures of polymers. [1] .....	2
Figure 1.2.	Comparison of materials with respect to strength vs. density [2] .....	3
Figure 1.3.	Classification of composite types [1] .....	4
Figure 1.4.	Comparison of fibre types [3].....	4
Figure 1.5.	(a) Percentage of materials used in Boeing B787 [4] (b) The trend for usage of carbon fibre in airplanes for the last 40 years [5]. .....	4
Figure 1.6.	Schematic of damage modes in composite materials .....	5
Figure 1.7.	Schematic views of damage detection with AE system .....	7
Figure 1.8.	Comparison of results with previous studies. [10] .....	12
Figure 1.9.	Selected AE results from uniaxial tension tests (a) with respect to clusters (b) peak frequency classification [26]. .....	18
Figure 1.10.	Evolution of surface temperature and AE counts throughout cycles [27] .....	19
Figure 1.11.	(a) Relationship of AE and IRT (b) Relationship of DIC and IRT [28]. .....	20
Figure 1.12.	Comparison of cumulative AE energy with (a) Energy density increase (b) Stiffness degradation [28]. .....	21
Figure 1.13.	Stress-strain response of a 3DNCOW GFRP composite with cumulative AE energy curve [33]. .....	22

Figure 1.14.	Damage mode progression in 3DNCOW CFRP composites [34, 35]...	23
Figure 1.15.	Progression of peak frequency values with applied stress and correlation with transverse cracks in 90° plies during tension tests of; (a) [90/0] <sub>6s</sub> , (b) [0/90] <sub>6s</sub> (b) laminates [36].	24
Figure 1.16.	Frequency centroid vs. source/sensor distance in different sensors [37].	25
Figure 1.17.	Energy and amplitude ranges of damage modes in hybrid composite [38]	26
Figure 1.18.	Correlation of damage modes with AE results for a carbon/S-glass composite [38].	26
Figure 1.19.	AE Clusters with waveforms of individual signals [50].	31
Figure 1.20.	Progression of damage modes in XP laminates [50].	31
Figure 1.21.	Flowchart of pattern recognition approach with voting and cluster validity indices [52].	33
Figure 1.22.	(a) Suitable clusters (b) unsuitable cluster representations [52].	34
Figure 1.23.	(a) Total variability of data by PCA (b) PCA representation of Fuzzy C-means clusters in 2D projection [56].	35
Figure 1.24.	Flowchart of clustering algorithm [57].	36
Figure 1.25.	(a) Optimal cluster numbers (b) Presentation of cluster groups for three different laminate types [57].	37
Figure 1.26.	Progression of AE clusters through the tests for three different laminates [57].	37

Figure 1.27.	Comparison of actual cracks with AE detection [58].....	38
Figure 1.28.	Transverse crack at inner yarns, b. Cluster groups and correlation of CL1 with transverse cracks [70].....	41
Figure 1.29.	Workflow of Andrew <i>et al.</i> study [71].....	42
Figure 1.30.	Outline of the thesis.....	46
Figure 2.1.	Autoclave at Boğaziçi University Composites Laboratory .....	48
Figure 2.2.	Manufacturer's recommended cure cycle for AS4/8552 [72].....	49
Figure 2.3.	Layout for preparation of QI specimens.....	50
Figure 2.4.	Drilling composite test specimens.....	52
Figure 2.5.	Schematic view and micrograph of (a) long-slit (b) short-slit .....	53
Figure 2.6.	Grinding the specimens in Boğaziçi University.....	54
Figure 2.7.	(a) Metallic box used to fix specimens constantly (b) Grinding machine in KU Leuven.....	55
Figure 2.8.	UD [0] <sub>5</sub> specimen configurations. ....	57
Figure 2.9.	Test setup used in Boğaziçi University. ....	57
Figure 2.10.	Specimen configurations of QI laminates. ....	58
Figure 2.11.	Test setup used in KU Leuven.....	59
Figure 2.12.	Vallen AE system .....	62
Figure 2.13.	Localization of AE activity [84].....	63

Figure 2.14.	(a) Speckle pattern (b) $\varepsilon_1$ strain map calculation in AoI.....	66
Figure 2.15.	Typical edge image from $[-45_2/0_2/+45_2/90_2]_s$ with certain damage modes.....	66
Figure 3.1.	(a) Upward concave non-linear stress-strain curve (b) Stress-strain curves and stiffening elastic moduli developments in interrupted tests of smooth $[0]_5$ laminates.....	69
Figure 3.2.	Stress-strain curves and stiffening elastic moduli developments in interrupted tests of thin-slit $[0]_5$ laminates. ....	70
Figure 3.3.	Stress-strain curve and cumulative AE energy up to final failure for a long-slit specimen. Interruption levels are indicated.....	71
Figure 3.4.	(a). Micro damage modes in long-slit specimen at the end of test (b). Macro damage mode on long-slit specimen at final failure. ....	72
Figure 3.5.	Stress-strain curve vs. different AE parameters for an uninterrupted test of a long-slit specimen. ....	73
Figure 3.6.	Interrupted test results for two different long slit specimens. ....	74
Figure 3.7.	Damage progression within long-slit Specimen #1.....	77
Figure 3.8.	Stress-strain curve and cumulative AE energy up to final failure for a short-slit specimen. Interruption levels are indicated.....	78
Figure 3.9.	Interrupted test results for a short-slit specimen.....	80
Figure 3.10.	Damage progression in short-slit specimen.....	81
Figure 3.11.	Macro damage mode on short-slit specimen at final failure. ....	82

Figure 3.12.	Stress-strain curve and cumulative AE energy up to final failure for a smooth $[0]_5$ specimen. Interruption levels are indicated. ....	82
Figure 3.13.	Interrupted test results for two different non-slit $[0]_5$ specimens. ....	84
Figure 3.14.	(a) Edge micrograph of damage after 1900 MPa (b) Damage modes observed after 2000 MPa, (c) Fibre breaks at the end of last test. ....	85
Figure 3.15.	Comparison of test results with micrographs of short-slit specimens ...	87
Figure 3.16.	Comparison of $[0]_5$ test results with FEMM. ....	89
Figure 3.17.	(a) Residual stress distribution at the end of cure cycle, (b) Damage progression during tension loading .....	89
Figure 3.18.	A summary of the stress-strain curves and AE registration for the tested laminates. Markers and lines of different colours correspond to different individual tests. ....	91
Figure 3.19.	Cluster groups for of $[-45_2/0_2/+45_2/90_2]_s$ laminate. ....	93
Figure 3.20.	Accumulation of AE clusters throughout a test in $[-45_2/0_2/+45_2/90_2]_s$ laminate: (a) full gage length; (b) edge observation region only; (1) events amplitude; (2) events weighted frequency; (3) events location. ....	96
Figure 3.21.	Damage progression in $[-45_2/0_2/+45_2/90_2]_s$ . ....	97
Figure 3.22.	Distance of clusters to AE sensor on $[-45_2/0_2/+45_2/90_2]_s$ laminate. ....	100
Figure 3.23.	Accumulation of AE clusters throughout the test in $[90_2/-45_2/0_2/+45_2]_s$ laminate: (a) full gage length; (b) edge observation region only; (1) events amplitude; (2) events location. ....	102
Figure 3.24.	Damage progression in $[90_2/-45_2/0_2/+45_2]_s$ . ....	103

Figure 3.25.	(a) Comparison of CL1 with optical detection (b) Surface cracks through the specimen gauge length at the end of the test and its comparison with AE detections throughout all the test in $[90_2/-45_2/0_2/+45_2]_s$ . ....	104
Figure 3.26.	(a) Distribution of AE clusters in a representative test (b) Summary of cluster boundaries from five tests for $[0_2/+45_2/90_2/-45_2]_s$ . ....	105
Figure 3.27.	Accumulation of AE clusters throughout a test in $[0_2/+45_2/90_2/-45_2]_s$ laminate: (a) full gage length; (b) edge observation region only; (1) events amplitude; (2) events weighted frequency; (3) events location. ....	107
Figure 3.28.	Damage progression in $[0_2/+45_2/90_2/-45_2]_s$ . ....	108
Figure 3.29.	Comparison of transverse cracks in $90^\circ$ plies a. with CL1, b. with CL4. ....	109
Figure 3.30.	(a) Distribution of AE clusters in a representative test (b) Summary of cluster boundaries from five tests of $[+45_2/90_2/-45_2/0_2]_s$ . ....	110
Figure 3.31.	Accumulation of AE clusters throughout a test in $[+45_2/90_2/-45_2/0_2]_s$ laminate: (a) full gage length; (b) edge observation region only; (1) events amplitude; (2) events location. ....	112
Figure 3.32.	Damage progression in $[+45_2/90_2/-45_2/0_2]_s$ . ....	113
Figure 3.33.	A summary of the stress-strain curves and AE registration for the tested OHT specimens. Markers and lines of different colours correspond to different individual tests. ....	118
Figure 3.34.	(a) Distribution of AE clusters in a representative test, (b) Summary of cluster boundaries from five tests for $[-45_2/0_2/+45_2/90_2]_s$ . ....	120

Figure 3.35. Accumulation of AE clusters throughout a test in  $[-45_2/0_2/+45_2/90_2]_s$  laminate: (a) full gage length; (b) edge observation region only; (1) events amplitude; (2) events weighted frequency; (3) events location. .... 122

Figure 3.36. Damage progression in  $[-45_2/0_2/+45_2/90_2]_s$  laminate. .... 123

Figure 3.37. (a) Distribution of AE clusters in a representative test (b) Summary of cluster boundaries from five tests for  $[90_2/-45_2/0_2/+45_2]_s$ ,..... 124

Figure 3.38. Accumulation of AE clusters throughout a test in  $[90_2/-45_2/0_2/+45_2]_s$  laminate: (a) full gage length; (b) edge observation region only; (1) events amplitude; (2) events weighted frequency; (3) events location 127

Figure 3.39. Damage progression in  $[90_2/-45_2/0_2/+45_2]_s$  laminate. .... 128

Figure 3.40. (a) Distribution of AE clusters in a representative test (b) Summary of cluster boundaries from five tests for  $[0_2/+45_2/90_2/-45_2]_s$ ,..... 129

Figure 3.41. Accumulation of AE clusters throughout a test in for  $[0_2/+45_2/90_2/-45_2]_s$  laminate: (a) full gage length; (b) edge observation region only; (1) events amplitude; (2) events weighted frequency; (3) location. .... 132

Figure 3.42. Damage progression in  $[0_2/+45_2/90_2/-45_2]_s$  laminate. .... 133

Figure 3.43. Location of high amplitude events. .... 134

Figure 3.44. Summary of cluster groups for  $[+45_2/90_2/-45_2/0_2]_s$  (a) Clusters from a representative test (b) Cluster boundaries, averaged from five test results..... 135

Figure 3.45.	Accumulation of AE clusters throughout a test in for $[+45_2/90_2/-45_2/0_2]_s$ laminate: (a) full gage length; (b) edge observation region only; (1) events amplitude; (2) events weighted frequency; (3) events location. ....	138
Figure 3.46.	Damage progression in $[+45_2/90_2/-45_2/0_2]_s$ laminate. ....	139
Figure 3.47.	X-Ray micro CT images of $[+45_2/90_2/-45_2/0_2]_s$ laminates at the end of; (a) 60% of ultimate strength, (b) 80% of ultimate strength [94]....	141
Figure 3.48.	Final failure modes in (a) $[+45_4/90_4/-45_4/0_4]_s$ laminates [78] (b) $[+45_2/90_2/-45_2/0_2]_s$ in this thesis. ....	142

## LIST OF TABLES

Table 1.1.	List of NDT techniques [6].....	6
Table 1.2.	Definition of AE parameters. ....	8
Table 1.3.	Test types and investigated damage modes [10]. ....	12
Table 1.4.	Test laminates and distinguished damage modes [21]. ....	15
Table 1.5.	Comparison of damage modes in terms of peak frequency values. ....	18
Table 1.6.	Amplitude and frequency ranges, attributed to damage modes in literature. ....	44
Table 2.1.	Physical and mechanical properties of AS4/8552 [72–74]. ....	47
Table 2.2.	QI laminates.....	58
Table 3.1.	Mechanical Test Results for 5-ply UD specimens. ....	67
Table 3.2.	Summary of cluster groups of AE results for $[-45_2/0_2/+45_2/90_2]_s$ laminate. ....	92
Table 3.3.	Damage sequence and their AE characteristics in smooth QI laminates. ....	116
Table 3.4.	Damage sequence and their AE characteristics in each OHT laminates. ....	144
Table 5.1.	Test specimens and their lay-up and geometrical properties. ....	149

## LIST OF SYMBOLS

$E_1$	Longitudinal Elastic Modulus
$E_2$	Transverse Elastic Modulus
$G_{12}$	In-Plane Shear Modulus
$G_{23}$	Out-of-Plane Shear Modulus
$L_G$	Gauge Length
$w$	Specimen Width
$t$	Specimen Thickness
$\rho_f$	Fibre density
$\rho_r$	Resin density
$\rho_c$	Laminate density
$\sigma_u^T$	Ultimate Tensile Strength
$\varepsilon_u^T$	Ultimate Tensile Strain
$\sigma_1^T$	Longitudinal Tensile Strength
$\sigma_2^T$	Transverse Tensile Strength
$\sigma_1^C$	Longitudinal Compression Strength
$\tau_{12}^S$	In-Plane Shear Strength
$\nu_{12}$	In-Plane Poisson's Ratio
$\nu_{23}$	Out-of Plane Poisson's Ratio

## LIST OF ACRONYMS/ABBREVIATIONS

3DNCOW	3 Dimensional Non-Crimp Orthogonal Woven
A	Amplitude
ABFH	Broad Amplitude-High Frequency
AE	Acoustic Emission
AHFL	High Amplitude-Low Frequency
ALFL	Low Amplitude-Low Frequency
AoI	Area of Interest
CCD	Charge-Coupled Device
CFRP	Carbon Fibre Reinforced Polymer
CL1	Cluster Group 1
CL2	Cluster Group 2
CL3	Cluster Group 3
CL4	Cluster Group 4
CMG	Composite Materials Group
CNN	Competitive Neural Network
D	Duration
DCB	Double Cantilever Beam
DIC	Digital Image Correlation
E	Acoustic Emission Energy
ENF	End-Notch Flexure
FEM	Finite Element Modelling
FEMM	Finite Element Micromechanical Model
FFT	Fast Fourier Transformation
FRQ-C	Frequency Centroid
GFRP	Glass Fibre Reinforced Polymer
HDPE	High Density Polypropylene
KU Leuven	Katholieke Universiteit Leuven
log E	Logarithmic Value of Acoustic Emission Energy

MMB	Mixed-Mode Bending
NDT	Non-Destructive Testing
OH	Open-Hole
OHT	Open-Hole Tension
PCA	Principal Component Analysis
P-FRQ	Peak Frequency
PP	Polypropylene
QI	Quasi-Isotropic
R	Rise Time
RA	Rise Amplitude
RVE	Representative Volume Element
SEM	Scanning Electron Microscope
SOM	Self Organizing Map
ST-FFT	Short Time Fast Fourier Transformation
UD	Unidirectional
WF	Weighted Frequency
XP	Cross Ply

# 1. INTRODUCTION

## 1.1. Motivation

Saving energy or reducing its consumption is the main aim of mankind in today's world. Even though it is related with different areas of engineering, materials science is the most important discipline that affects this aim. Innovations in this field provide opportunities to produce lighter and stronger structures that can provide less energy consumption. One of the most popular materials for this purpose are "Composite Materials" which, instead of having single constituents, have at least two different constituents which are gathered together to combine specific favourable characteristics of each constituent. While one constituent (reinforcement) provides strength and stiffness for the overall material system, the other constituent (matrix) is used to keep the reinforcement together.

There are several types of composite materials. They can be classified with respect to their constituents' type. Only polymer composites are described in this thesis. Polymer composites are named according to the polymer matrix type used. Primarily, they can be divided into two groups; thermoplastic and thermosetting polymer composites.

The main difference between the aforementioned polymer matrix types is their processing characteristics. Thermoplastic polymers are recyclable; they soften when heated and harden when cooled and that is continuously repeatable. On the other hand, thermosetting polymers become permanently hardened when they are formed. This processing ability is due to their molecular structure. While thermoplastic polymers consist of long, linear or branched molecular chains thermosetting polymers consist of strong network polymers. Raising temperature can diminish the secondary bonding forces between the atoms in thermoplastic polymers. However, the covalent crosslinks between adjacent molecular chains in thermosetting polymers cannot be degraded [1]. Difference between the molecular structures can be seen in Figure 1.1.

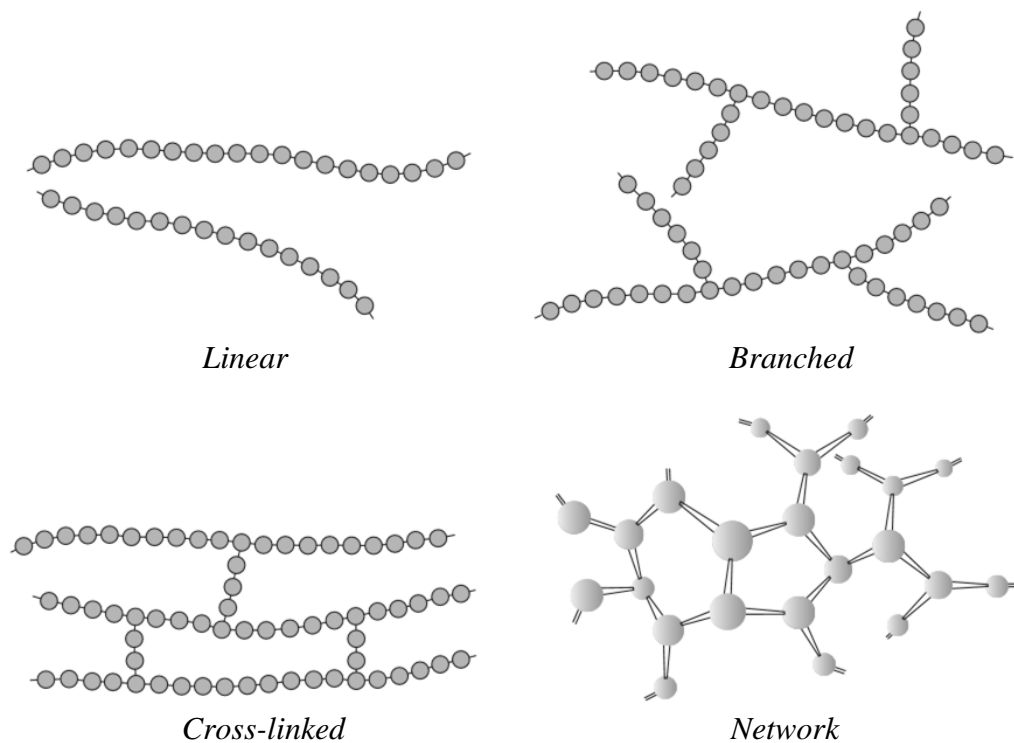


Figure 1.1. Schematic representation of molecular structures of polymers. [1]

Polymer composites are highly preferred materials due to their low density-to-high strength ratio. Figure 1.2 shows a comparison of different material types with respect to strength vs. density. It can be seen that polymers and composites have comparable strength with metals and ceramics but have lower density. High strength and low density are the key characteristics to reduce energy consumption for transportation. Thermoplastic polymers are generally used in automobiles and interior products of other vehicles while thermosetting composites are mostly used in marine and aerospace industry. Also, as mentioned before, recyclability is a very favourable property of thermoplastic polymers for automotive industry where there the regulations for recyclability is tighter as compared with marine and aerospace industries. These are the primary reasons for such diversity for their area of use.

Aside from the polymer matrix type, composites can be divided into sub-groups with respect to the type of reinforcement. Figure 1.3 shows these classes. The type of composite investigated in this thesis is shown within red rectangles in Figure 1.3 namely continuous fibre reinforced composites. Different types of continuous (aligned) fibre reinforcements are used within thermosetting polymer composites as shown in Figure 1.4. Carbon fibres have the higher strength than aramid and glass fibres. Because of this, Carbon Fibre Reinforced

Plastics (CFRP) are used in aerospace industry, while Glass Fibre Reinforced Thermosetting Polymer (GFRP) composites are mainly preferred in marine industry. Continuous carbon fibre reinforced thermosetting polymer composites are type of composites that are investigated primarily in this thesis.

Due to their higher strength, the demand to CFRP composites is increasing in the aerospace industry day by day. The trend for the use of carbon fibres throughout last 40 years and usage of CFRP composites in Boeing B787 plane can be seen in Figure 1.5. At least 50% of the whole airplane consist of composites and almost all of them are CFRP composites as shown in Figure 1.5.(a). Weight of carbon fibre in an airplane has increased 30 tones in the last 40 years as shown in Figure 1.6.(b). It is a very distinguished and advanced industry where very careful attention should be paid from the design stage to the end product. In fact, more careful attention should be paid during service since a small fault or damage can cause a catastrophic failure. This makes damage detection a very crucial and necessary subject in the field of composite materials.

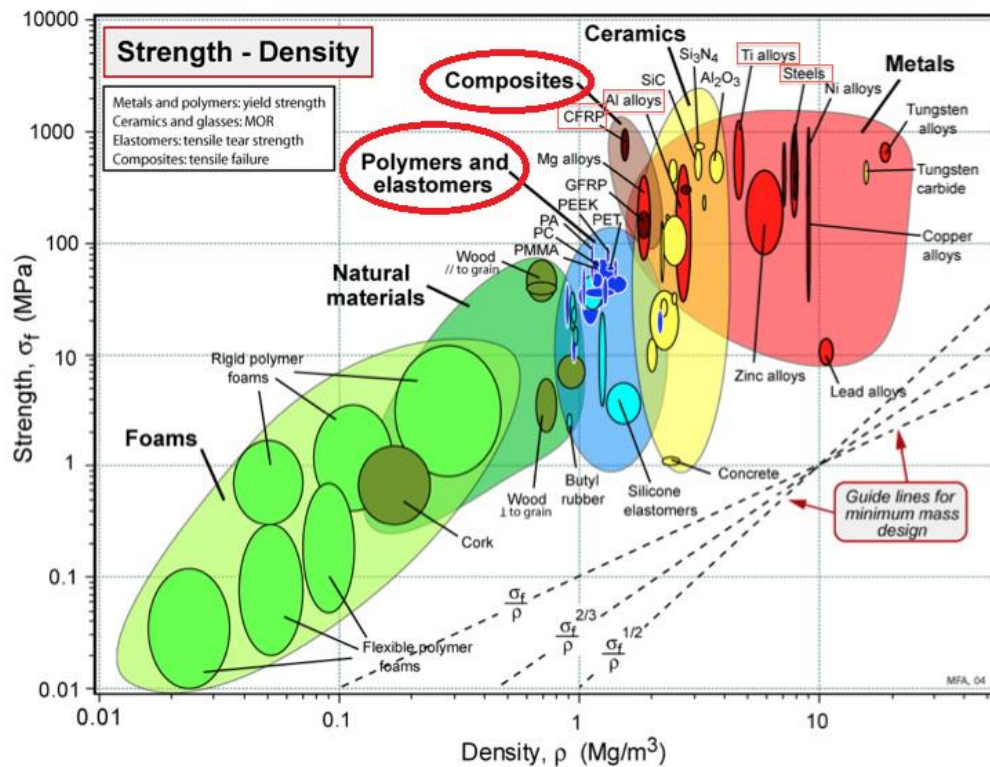


Figure 1.2. Comparison of materials with respect to strength vs. density [2]

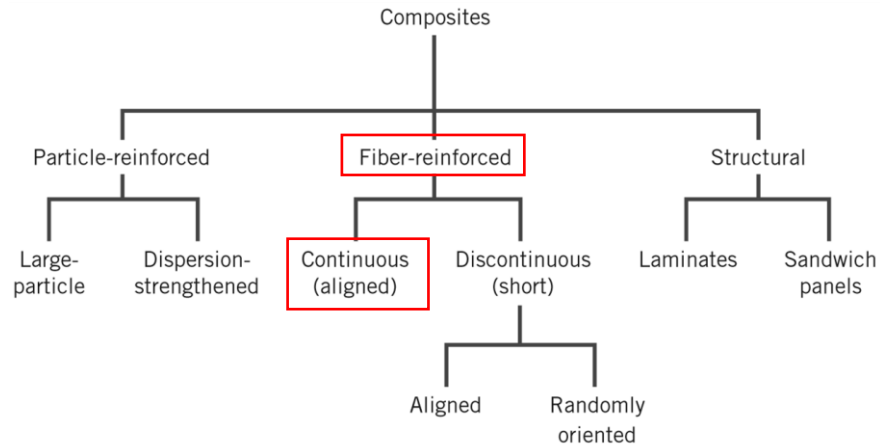


Figure 1.3. Classification of composite types [1]

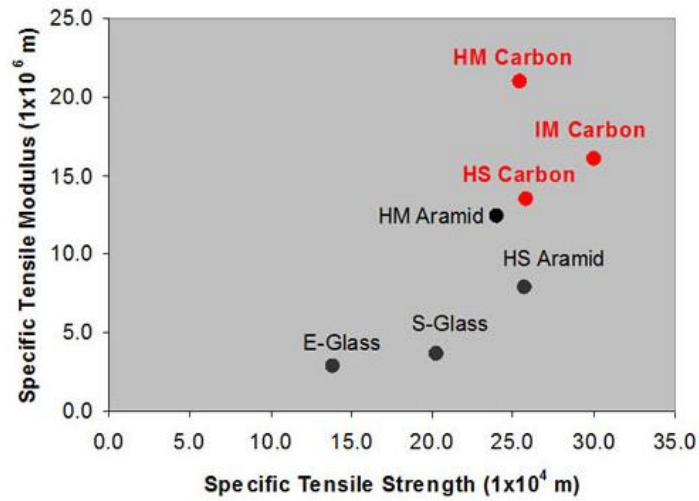


Figure 1.4. Comparison of fibre types [3]

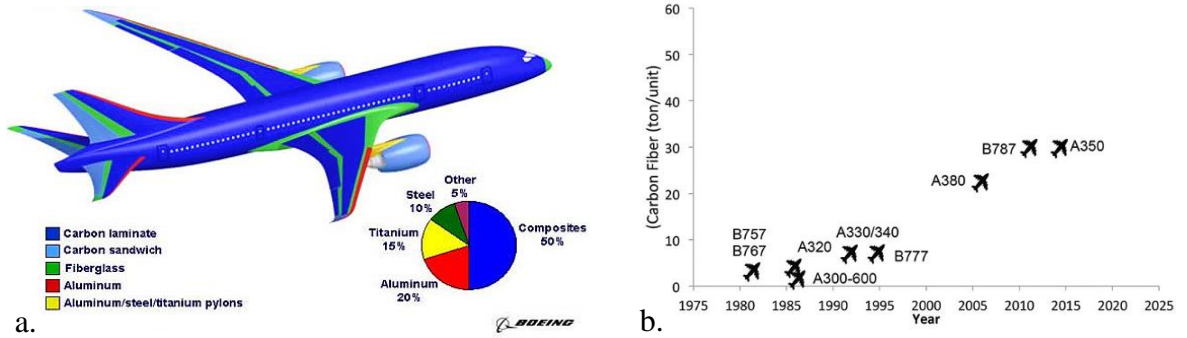


Figure 1.5. (a) Percentage of materials used in Boeing B787 [4] (b) The trend for usage of carbon fibre in airplanes for the last 40 years [5].

Damage in composite materials consists of complex physical mechanisms. Not only understanding these mechanisms but also detecting the damage is a very important task to be fulfilled. There are different damage modes present in composite materials varying from micro to macro scales. Generally, micro damage modes initiate in composite materials which causes macro and more catastrophic damage modes. Figure 1.6 shows a schematic of damage modes in a composite material. Damage modes coloured red represent transverse matrix cracks, damage modes coloured represent delaminations between plies, and finally fibre damage modes are pointed in green ovals in Figure 1.6. Damage initiation occurs in the form of micro damage modes, so it is very difficult to notice them with naked eye. In fact, there is not obvious yield point or slope change in tension stress-strain curves of composite materials as in metallic materials. So, additional techniques are required to detect damage levels in composite materials.

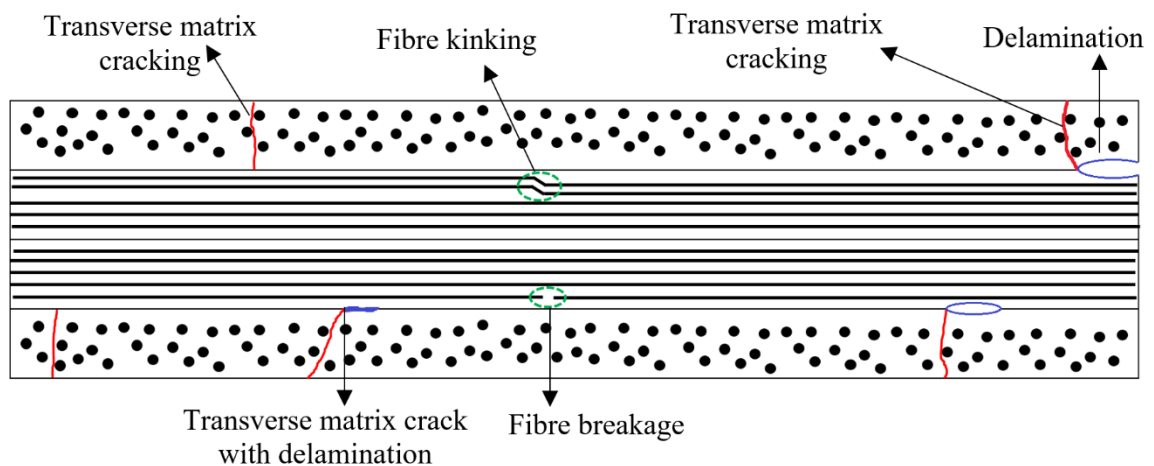


Figure 1.6. Schematic of damage modes in composite materials

It is highly important to detect damage without destroying the structure. This can be done successfully by using Non-Destructive Techniques (NDT). In a simple way, it can be said that NDT is used to inspect and detect the irregularities in structures which are not visible by naked eye. There are numerous NDT techniques. Table 1.1 summarizes a list of them. Visual inspection is limited to detection of macroscopic defects. Dye penetrant technique requires application of a liquid into the structure which reduces the integrity of structure. Magnetic particle technique can be applied to ferromagnetic materials only. Microscopy can be applied to very small regions. Radiography and ultrasonic techniques

require to transmit a signal to the structure. Electromagnetic testing can be applied to electrically conductive materials only. Moreover, these techniques cannot be applied during service. They are actually post-mortem applications which does not allow tracking damage initiation and propagation during service. Last two techniques in Table 1.1 are online inspection techniques that can be applied during service. In addition to this, a transmission of a signal is not required with these two techniques. Instead of sending a signal to detect a damage, damage itself causes a signal which is captured with a thermal camera in thermography or detected with sensors in Acoustic Emission (AE) technique. However, very high resolution is required to detect micro damage modes with a thermal camera during infrared testing. Also, it is not easy to detect a damage or an irregularity at inner sections of the structure with thermography. On the other hand, AE technique can be used to inspect the entire structure by placing AE transducers or sensors on different regions of the structure easily.

Table 1.1. List of NDT techniques [6]

1.	Visual Inspection
2.	Dye Penetrant
3.	Magnetic Particle
4.	Microscopy
5.	Radiographic
6.	Ultrasonic
7.	Electromagnetic (Eddy Current)
8.	Thermography (Infrared)
9.	Acoustic Emission

AE is a highly preferred online NDT method applied simultaneously during service or mechanical tests of composite materials. It allows “hearing” and identifying damage. An AE signal is an ultrasonic wave resulting from the sudden release of the strain energy when damage occurs. When critical stress values are exceeded in a material, it fails locally (on microscale) and the strain energy stored is suddenly released where mechanical stress waves are induced. These waves can be detected with suitable sensors. The mechanical information

picked up from the material is then converted into an electrical signal. Each of these signals contain information in time and frequency domain that are originated from a micromechanical event. A representative diagram of damage detection with AE system is shown in Figure 1.7. Definitions of AE parameters shown in Figure 1.7 are briefly given in Table 1.2. First six AE parameters can be directly extracted from an AE signal while the last two, namely Rise Amplitude, RA and Weighted Frequency, WF are calculated by using some features as shown in Equations 1 and 2 respectively.

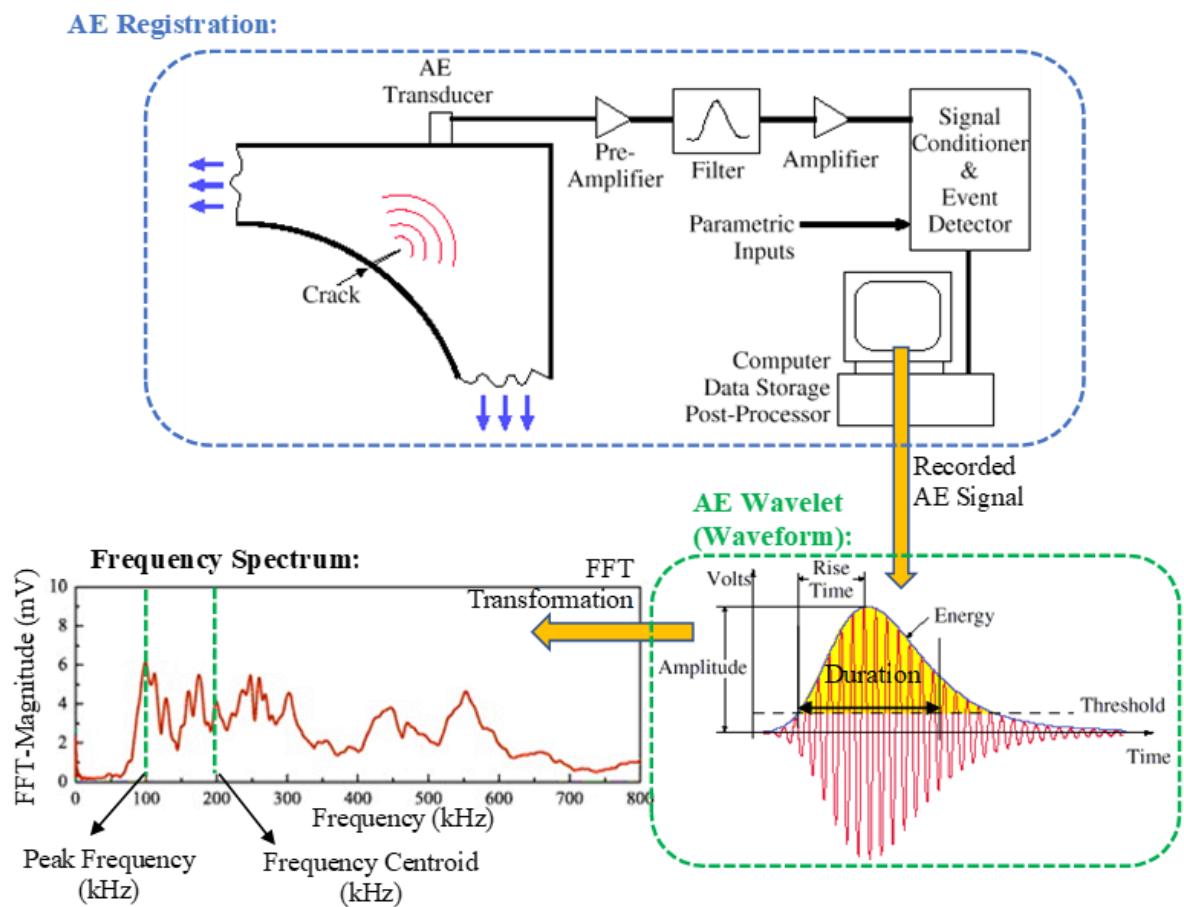


Figure 1.7. Schematic views of damage detection with AE system

Table 1.2. Definition of AE parameters

AE Parameter	Definition	Unit
Amplitude (A)	Greatest voltage in a waveform	dB
Rise time (R)	Time interval between the first threshold crossing and the signal peak	$\mu$ s
Duration (D)	Time difference between the first and last threshold crossings	$\mu$ s
Energy (E)	Measure of the area under the envelope of the rectified linear voltage time signal from the transducer	aJ
Peak Frequency (P-FRQ)	Frequency value corresponds to maximum FFT magnitude	kHz
Frequency Centroid (FRQ-C)	Weighted frequency average	kHz
Weighted Frequency (WF)	Geometric mean of peak frequency and frequency centroid. (Equation 1)	kHz
Rise Amplitude (RA)	Shows reciprocal of gradient in AE signal waveform. (Equation 2)	-

$$RA = R/A \quad (1)$$

$$WF = \sqrt{(P - FRQ) \cdot (FRQ - C)} \quad (2)$$

where R is the rise time of a signal, A is the amplitude, P-FRQ is the maximum or peak frequency and FRQ-C is the frequency centroid of gravity value of a signal.

Although AE technique is the most easily applied NDT technique in Table 1.1, it has some drawbacks. The most important drawback is the difficulty of interpreting the recorded AE signals to correlate them to damage modes. Even though this technique has been applied to composite materials for this aim for the last fifty years, characteristics of recorded AE

signals corresponding to a particular damage mode have not reached standardized conclusions yet. In order to correlate the damage modes with corresponding AE signals, visual observation techniques can be used to inspect the damage and correlate with AE signals. Optical microscopy technique can be applied to very small regions. However, it can be used to inspect damage after tests for small regions on the edge of the specimens. Additionally, Digital Image Correlation (DIC) can be successfully used as an NDT technique. It is a full-field deformation measurement technique that calculates displacements by comparing the deformed digital images with undeformed, reference digital images of the sample surface [7]. Sample surfaces, used with DIC calculations, should have inherent patterns. This is not valid for composite materials, since they have smooth surfaces. So, speckle patterns should be attained on specimen surfaces carefully. Two contrast colours should be applied. While one forms the layer, the other colour should form the speckle patterns for DIC calculations. However, DIC is limited to track in-situ surface deformations but it can be applied simultaneously with AE registration during mechanical tests.

General conclusions in literature for the correlation of damage modes with corresponding AE characteristics are relied on interpretations rather than direct observation of damage modes. Moreover, these correlations are accepted universally. Effect of different lay-up sequences on AE characteristics of same damage modes is not stated in literature. Thus, it is highly crucial to obtain reliable correlations between damage modes and AE characteristics with strong evidences in different laminate types. This is the objective of this thesis. AE technique is the primary tool for damage detection in this thesis and additional tools such as microscopy and DIC measurements are used to detect and provide robust correlations between damage modes and their corresponding AE signals. Specimens with various lay-up sequences, including a central hole or not, are investigated in this thesis within a large experimental test programme. Important studies in literature about damage detection in composite materials with AE technique are summarized in the next section. Afterwards, the objective of this thesis is explained in detail which briefly states that provides reliable and robust conclusions to the literature by fulfilling the incomplete and required tasks up to now.

## 1.2. Literature Review

This section is focused on summarizing the studies in which AE technique is primarily used for damage detection in fibre reinforced polymer composite materials. By the end of September 2017, there were 2232 articles that can be found by Scopus database search using keywords “acoustic emission” and “composite” [8]. These studies include ceramic matrix, metal matrix and polymer matrix composites. When the results are filtered for “polymer composites”, 910 articles can be found [8]. First use of AE technique in polymer composite materials for damage detection dates back to 1970s. Although the application of this technique dates back to fifty years ago, it is still a very hot topic. Highest number of papers were published in 2015 with 74 studies, followed by 68 studies in 2014 and 67 studies in 2016. 62 papers have been published this year until the end of September 2017 [8]. Early studies consider AE technique for damage initiation and damage mode identification with respect to amplitude. It was accepted as a robust technique for determination of damage threshold levels for the next 20 years after 1970. 1990s was the era when home type personal computers started to become popular and easily accessible. With faster computational speed this technological development enabled Fast Fourier Transformation (FFT) calculations to be carried out easily which provided to use peak frequency and frequency centroid parameters for damage mode classifications in composite materials. Especially peak frequency has been assumed to be a selective AE parameter for damage mode classification. Damage mode classifications with respect to single AE parameters were highly used until late 2000s. In fact, it is still used due to its low post-processing requirements. Then, multi-parametrical statistical algorithms were started to be used for clustering recorded AE signals in 2000s. At the same time, post-mortem observations have been used to correlate AE signals with damage modes until now. In order to provide stronger proofs for damage mode correlation with corresponding AE signals, in-situ observations have gained importance since 2015. Today, in-situ visual observation techniques show that use of AE alone for damage mode identification is being proven to be insufficient. Progress of the studies using AE technique for damage detection is described in this section.

In literature, correlation of AE signals with corresponding damage modes are still done with two different techniques. First one is classification of AE signals with respect to single AE parameter and correlating them with damage modes. Second one is using

statistical clustering algorithms to group similar AE signals and correlating them with damage modes. Because of these two methods, studies in literature are given in two different subsections. Finally, all of the cited studies are summarized in a third last subsection with respect to the materials tested and ranges of certain AE parameters.

### **1.2.1. Evaluation of AE Results with Respect to Single Parameter**

One of the most important study using single AE parameter evaluation for damage mode correlation was done in 1994 by Barre *et al.* [9]. Damage mechanisms in short glass fibre reinforced polypropylene was tested with AE registration under tensile, fatigue and crack propagation tests. Four different materials, containing fibres with different lengths, were tested to examine the effect of fibre length to material strength. Scanning Electron Microscopy (SEM) at the end of tests were quantified with AE results and provided identification of damage modes with respect to amplitude values of recorded signals. It was concluded that low amplitude signals refer to matrix cracks while high amplitude signals represent fibre damage modes. This study showed the great potential for damage mode investigation in composite materials when results of online AE registration technique were supported with SEM observations after failure. Conclusions of this study (correlations between low amplitude-matrix cracks and high amplitude-fibre breaks) have been accepted as general classification of damage modes with respect to amplitude values. Because of this widely adopted convention, this study is the most cited article in literature [8].

Second most cited study was prepared by De Groot *et al.* [10] to determine a relationship between the peak frequency contents and failure modes, obtained from simultaneous AE monitoring during tension tests of CFRP composites. For this purpose, different unidirectional (UD) laminates were tested to distinguish damage modes, since one mode is assumed to be dominant within each lay-up. Table 1.3 presents the investigated damage modes in each test. AE interpretations from each test were believed to be validated by comparing damage modes and peak frequency values from another test, such as; comparing peak frequency values of matrix cracking in pure resin with 90° tests. Results of this study were presented together with previous studies in Figure 1.8. This study has been one of the most influential studies for the use of AE technique for damage mode identification in composite materials.

Table 1.3. Test types and investigated damage modes [10]

Test Type	Investigated Damage Modes
Pure resin tension test	- Matrix cracking
90° tension test	- Matrix cracking - Debonding (minor)
Lap Shear	- Matrix cracking - Debonding
Double Cantilever Beam (DCB)	- Matrix cracking - Debonding - Fibre pull-out (minor) - Fibre failure (minor)
0° tension test	- Fibre fracture - Fibre pull-out
10° tension test	- Debonding - Fibre pull-out
Uncured prepreg tension test	- Fibre fracture

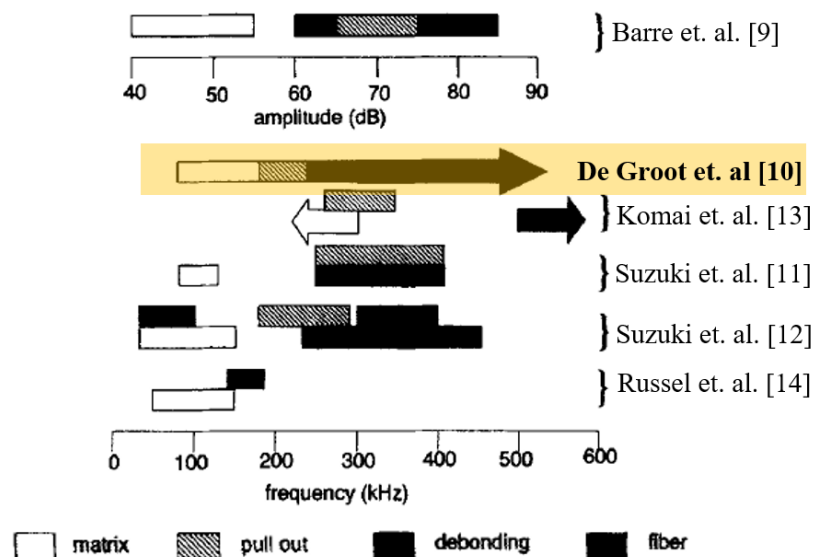


Figure 1.8. Comparison of results with previous studies. [10]

Ceysson *et al.* [15] used electrical resistance measurements for damage mode identification in CFRP composites and compared those to AE results. Accumulation of electrical resistance measurements throughout the tests were seen to consist of three different stages. Edge micrographs were taken at these stages and compared with measurements. It was seen that electrical resistance measurements allowed in-situ damage detection for correlation of AE signals with induced damage modes with respect to amplitude values.

Kim *et al.* [16] applied online AE registration technique during cyclic tension tests of plain woven CFRP composite specimens containing double edge notches. Damage occurrence at notch-tips was monitored by video extensometer during the tests. Besides, fibre failures at late cycles were interpreted with respect to the change in secant modulus. More importantly, cyclic loadings with simultaneous AE registrations showed the importance of two phenomena. Kaiser and Felicity effects. It was seen that few or no AE signals were recorded up to the maximum load level of previous cycles which is named as Kaiser effect in composite materials [17]. At late cycles, much more AE signals were recorded before reaching the maximum load level of previous cycle due to Felicity effect. It is the ratio of load at significant AE activity onset in the current cycle to the maximum load reached in previous cycle [17]. A very sharp decrease was observed at Felicity ratio in this study. This was interpreted to be due to fibre breaks induced at late cycles.

Kotsikos *et al.* [18] used AE technique to characterize damage progression in cross-ply (XP) GFRP polyester composites under pure bending fatigue loading. Laminates were exposed to sea water for long-term to investigate the effect of corrosion to fatigue life. It was the first study involved with AE technique to investigate the effect of corrosion in composites. It was found that damage progression in unexposed specimens were due to matrix cracking only whereas matrix cracking, debonding and delamination was seen to take place in the specimens exposed to sea water. Amplitude characteristics of these damage modes were low amplitude, low amplitude with high duration and intermediate amplitude with low duration respectively. It was mentioned that fibre breaks would possibly have high amplitude characteristics, but this argument was not proven.

Bohse *et al.* [19] studied the AE characteristics of micro damage modes in High Density Polyethylene reinforced polypropylene (HDPE/PP), single fibre reinforced glass, carbon reinforced and glass fibre reinforced polycarbonate composites and unidirectional

(UD) multi glass fibre reinforced polypropylene. AE characteristics of each damage mode within different composites containing different fibre types were distinguished and identified. A correlation between AE energy and fracture energy release rate was obtained.

Quispituba *et al.* [20] used AE technique to develop a stiffness degradation model to represent damage progression in sandwich composites under static and fatigue loading. Sandwich structures are generally designed to sustain loads under bending. This was the first study that addressed the mechanical performance and damage progression of sandwich structures under tension loading. Material in consideration was cross-ply (XP) CFRP composite plates with kraft paper filled urethane honeycomb core where honeycomb and CFRP composite plates were bonded with resin of composite plates. Four specimen types were tested where three of them were variations of dogbone; smooth dogbone, dogbone with central hole, dogbone with edge notches and smooth rectangular specimens. Correlation between AE signals and damage modes were done with respect to the evaluation of amplitude and energy parameters. Low amplitude and energy signals were believed to represent core damage and highest amplitude and energy signals were interpreted to represent fibre damage modes. Matrix cracks were believed to cause high amplitude signals whose values were close to fibre breaks. Results of this study showed that when urethane core was filled between CFRP plates damage was initiated with core failure which was followed by interfacial damage and later on fibre breaks. Addition of a core with a lower stiffness and strength between fibre reinforced laminates could result in different damage mode progression. This can also be interpreted for composite types. For example, AE results in GFRP composites should not be relied on to interpret the results of CFRP composites, since each of them has different material characteristics which can cause considerable difference in characteristics of registered AE signals.

Ramirez-Jimenez *et al.* [21] believed that, the output of their study gives a clear identification of various failure modes present in composite materials. It would lead to knowledge of the microscopic and macroscopic damage state of composite materials. Real time AE registration was performed during tension tests of thermoplastic GFRP-PP specimens with different lay-up sequences ( $[90]_8$ ,  $[0]_8$ ,  $[+45/-45]_s$ ,  $[0/90]_s$ ). In addition to them, center-holed  $[0]_8$ ,  $[+45/-45]_s$  specimens were also tested to investigate the effect of center-hole to AE characteristics. Specific specimen types were tested to distinguish damage modes clearly as shown in Table 1.4. The hypothesis was that each micro mechanical event

would have distinctive waveform like a fingerprint. AE results were interpreted with respect to peak frequency values of AE signals. Silent behaviour of PP was taken into account during classification. Because, no AE signals were recorded during tension tests of neat PP except final fracture. So, it was assumed that no matrix cracking occurs during tests. Since no matrix cracking was expected, it was relatively easy to classify frequency groups for corresponding damage modes. Low frequency groups were believed to represent debonding while high frequency signals were believed to be registered due to fibre breaks. Interpretations of AE results were validated with SEM observations at the end of the tests. Only post-mortem observations were used in this study but this does not really guarantee the consistency and reliability for correlation of AE results with damage modes.

Table 1.4. Test laminates and distinguished damage modes [21]

Test Type	Detected Damage Modes
[90] <sub>8</sub>	Fibre/matrix debonding
[0] <sub>8</sub>	- Fibre breaks
[0] <sub>8</sub> (with center-hole)	- Fibre pull-out - Fibre/matrix slippage
[+45/-45] <sub>s</sub>	- Interlaminar shear
[0/90] <sub>s</sub>	- Distinguish damage occurrence in 90° and 0° plies

Literature involving using AE technique for damage detection in composite materials mostly covers smooth, or unnotched specimens under tension tests. Very few studies cover open-hole tension (OHT) tests. Quispituba *et al.* [20] considered one sandwich dogbone specimen with a central hole and Ramirez-Jimenez *et al.* [21] covered two OHT tests just to see the effect of notch to peak frequency distribution of AE signals recorded during loading but the main aim was not the investigation of OHT samples. Third study in this field was done by Loutas *et al.* [22]. In this study, they examined the performance of frequency-based methodologies for AE data evaluation for damage progression in UD [0]<sub>3</sub> GFRP-polyester composites. Three major frequency bands were observed during the tests and energy levels of AE signals, were related to the evolution of damage modes in material and those are similar to authors' previous study [21].

Jong *et al.* [23] investigated the propagation of transverse matrix cracking in XP CFRP composites under tension tests with AE registration. Identification of transverse matrix cracking was interpreted with respect to waveform characteristics. Waveforms and wave attenuation characteristics of different laminate types were compared. Then damage modes were classified with respect to the peak frequency values of the AE signals. Moreover, hybrid laminates were taken into consideration in which transverse cracking was identified in conjunction with AE results and predictions of Finite Element Modelling (FEM).

Bussiba *et al.* [24] tested three different composite systems under tension and bending. Materials used in this study were; metal fibre reinforced glare, graphite reinforced epoxy and carbon/carbon composites. Effect of temperature to damage progression was also investigated. Damage progression was tracked by using number of counts and energy parameters of AE signals. In addition to this, FFT and Short Time FFT (ST-FFT) analysis were performed for damage mode classifications. Classifications of AE results were supported with optical microscopy and SEM observations of specimens at different load levels. Good agreements between AE results and damage modes were presented in this study. In addition to this, similarities between the predictions of a micro-mechanical model and AE results in this study provided an important methodology for damage detection and quantification in composite materials.

Bourchak *et al.* [25] used AE energy as fatigue parameter for quasi-isotropic (QI) CFRP composites. Smooth and open-hole specimens were tested under quasi-static tension and tension-tension fatigue tests. Low amplitude AE signals were believed to represent matrix cracks whereas high amplitude signals indicate delaminations and fibre breaks similar to Barre *et al.* [9]. Damage progression during OHT tests was as follows; first matrix cracks in 90° plies were observed to occur, which was verified with microscopy observations. Then it led to ply delaminations between 90° and 45° plies, and catastrophic failure occurred eventually with sudden failure in 0° plies. However, damage sequence was different in laminates where 90° plies were not present. Damage sequences in both laminate types were consistent with interpreted AE characteristics. Besides, AE energy was seen to be a strong parameter to determine damage threshold levels. After inspecting the damage modes present in laminates, fatigue tests were performed. Different cyclic load forms were applied according to the ultimate strength of laminates. In the end, it was seen that AE technique can effectively determine damage threshold levels, identify the location of the damage modes

successfully, allow cyclic fatigue testing at representative stress levels to failure stresses and provide a useful damage parameter and failure criteria in the form of AE energy as the basis of a cumulative damage fatigue life prediction model.

Gutkin *et al.* [26] examined CFRP composites under various mechanical tests. The objective of this study was to identify AE characteristics of damage modes within simple laminates, as in [10, 19, 21], then classify the damage modes in more complex laminates with respect to pre-determined AE characteristics. Different laminate configurations were tested under different tests such as; uniaxial and compact tension tests, compact compression, DCB and End-Notch Flexure (ENF) tests. Peak frequency was chosen to be used for classification of AE signals. In addition to this, pattern recognition analysis was applied and AE signals were clustered with k-means algorithm. Details of this algorithm is given in the next subsection. Examples of test results with respect to clustering algorithm are shown in Figure 1.9.(a). Only fibre breaks and matrix cracks with debonding were expected in  $[0^\circ]_8$  tests, and only matrix cracks with fibre/matrix debonding were expected in  $[90^\circ]_{16}$ . However, results in Figure 1.9.(a) show that, there are four cluster groups found in  $[0^\circ]_8$  and three cluster groups for  $[90^\circ]_{16}$ . Explanations of these clusters are given in the next subsection 1.2.2. At the same time peak frequency classification is shown in Figure 1.9.(b). Each coloured bands represent a different damage mode in Figure 1.9.(b). It is seen that number of frequency bands in Figure 1.9.(b) representing the damage modes are different from cluster groups in Figure 1.9.(a). Totally different AE characteristics were obtained for  $[90^\circ/0^\circ]_{8s}$  in which peak frequency groups were not consistent with what was observed in  $[0^\circ]_8$  and  $[90^\circ]_{16}$  for expected damage modes. But still, authors compared the results for peak frequency classification with [10, 21]. A comparison of damage mode correlations in terms of peak frequency values are given in Table 1.5. There are inconsistencies for the AE characteristics of damage modes in these three studies [10, 21, 26] since there were no in-situ observations. But still they have been highly referred studies for classification of AE signals with respect to peak frequency in composite materials.

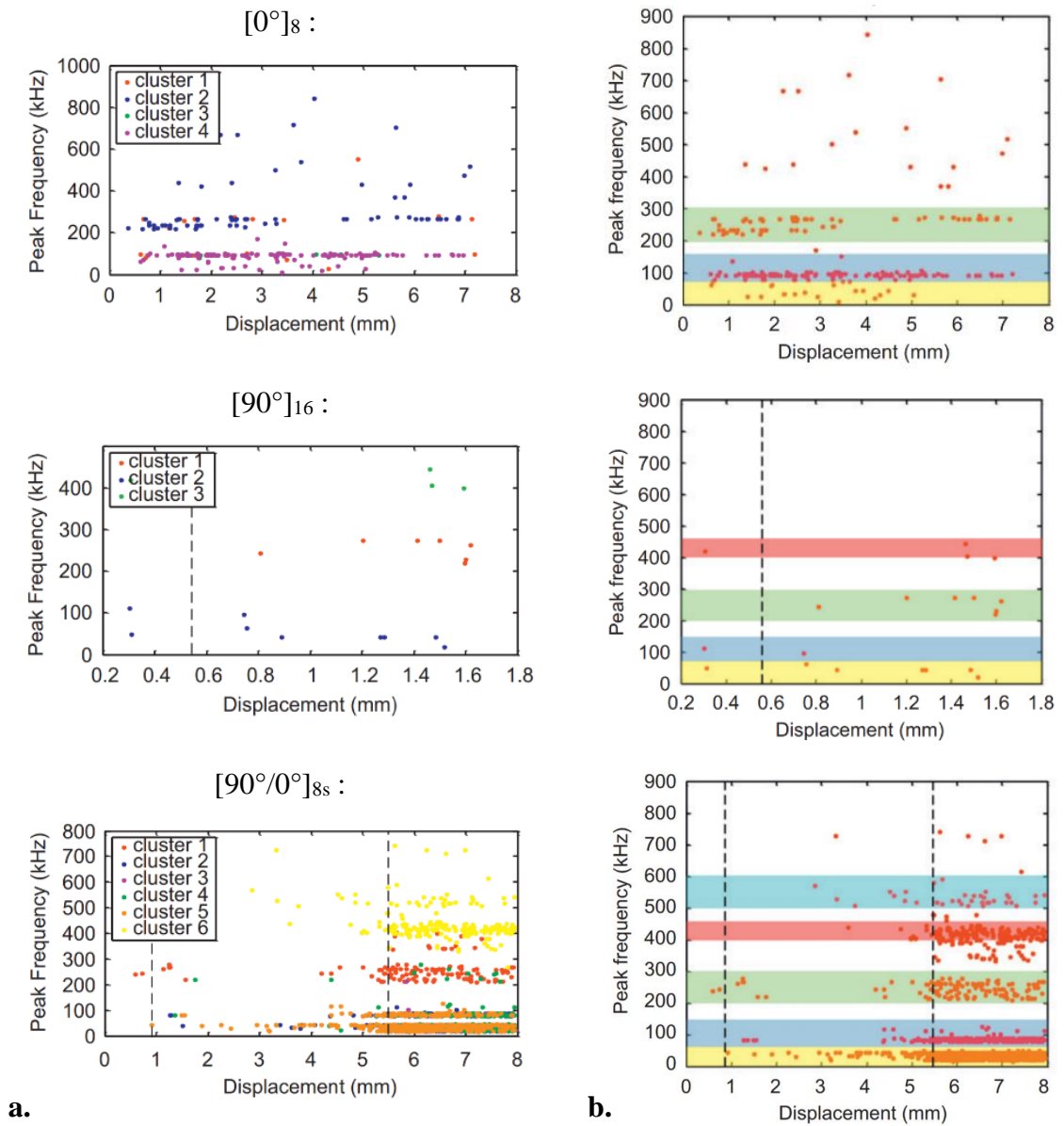


Figure 1.9. Selected AE results from uniaxial tension tests (a) with respect to clusters (b) peak frequency classification [26].

Table 1.5. Comparison of damage modes in terms of peak frequency values

Ref.	Matrix cracking	Debonding	Delamination	Fibre pull-out	Fibres Breakage	
[10]	50-180	220-300	225-300	180-220	>300	kHz
[21]	90-110	-		200-300	>420	
[26]	<50	200-300	50-150	500-600	400-500	

Naderi *et al.* [27] used AE and infrared thermography (IRT) methods for damage detection during cyclic bending tests of GFRP composites. Dissipated thermal energy and damage evolution during bending fatigue were calculated according to the temperature drop rate by stopping the fatigue test at various number of cycles. AE was also utilized to corroborate the thermography results in characterizing the degradation progression. The results of these two non-intrusive techniques showed similar evolutionary response revealing the existence of degradation stages as shown in Figure 1.10.

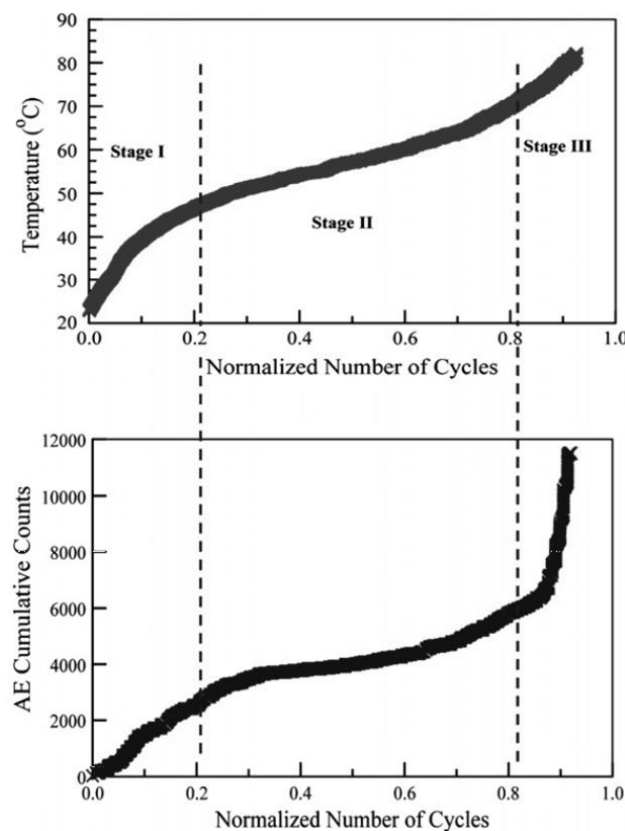


Figure 1.10. Evolution of surface temperature and AE counts throughout cycles [27]

Cuadra *et al.* [28] performed hybrid NDT testing for damage detection during tensile and fatigue tests of GFRP composites by applying AE registration with DIC and IRT. Full-field strain measurement with DIC and thermal mapping with IRT enable to detect hot spots during loading which provide a correlation with AE activity. Figure 1.11. shows relationship between NDT techniques. At point 2 in Figure 1.11.(a), there is a sudden drop in stress due to the damage initiation, detected in DIC image in Figure 1.11.(b) at 1.88 % strain. At the

same time, distinct increases can be seen in both AE and IRT activities in which AE demonstrating a large increase in both their event density and amplitude. AE signals were classified with respect to rise time and peak frequency parameters. Low peak frequency signals were believed to represent matrix cracking according to previous interpretations in literature. In addition to this, early registered AE signals had low peak frequency values and that was consistent with early damage mode expectation for matrix cracking. High peak frequency signals were believed to represent fibre/matrix debonding and fibre breakage according to the interpretations of previous studies. In the same study [28], multi-instrumental NDT approach provided to quantify the hysteric fatigue behaviour by measuring stiffness degradation, energy dissipation and average strain as a function of cyclic loading. Moreover, AE energy was seen to be a useful parameter to indicate the damage thresholds levels during fatigue life as shown in Figure 1.12. This study provided important evidences for damage mode correlation with AE registration. Even though results in Figure 1.11. and Figure 1.12 are useful for clear damage detection, it is not sufficient for damage mode identification. Since two optical techniques were limited to the surface of the laminates.

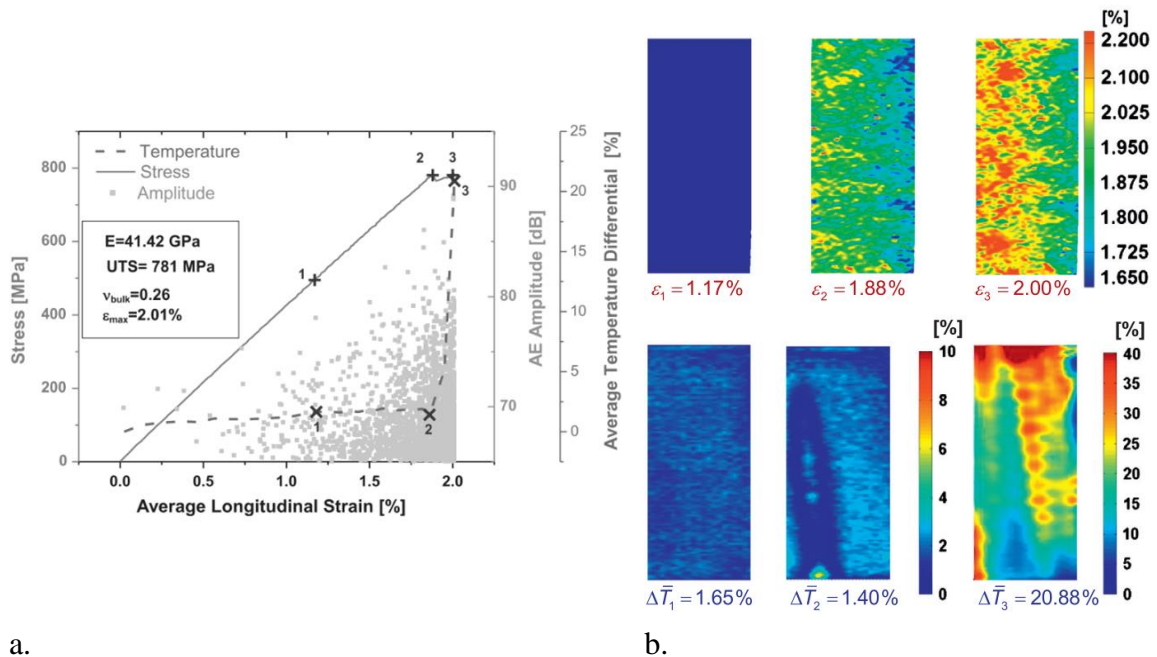


Figure 1.11. (a) Relationship of AE and IRT (b) Relationship of DIC and IRT [28].

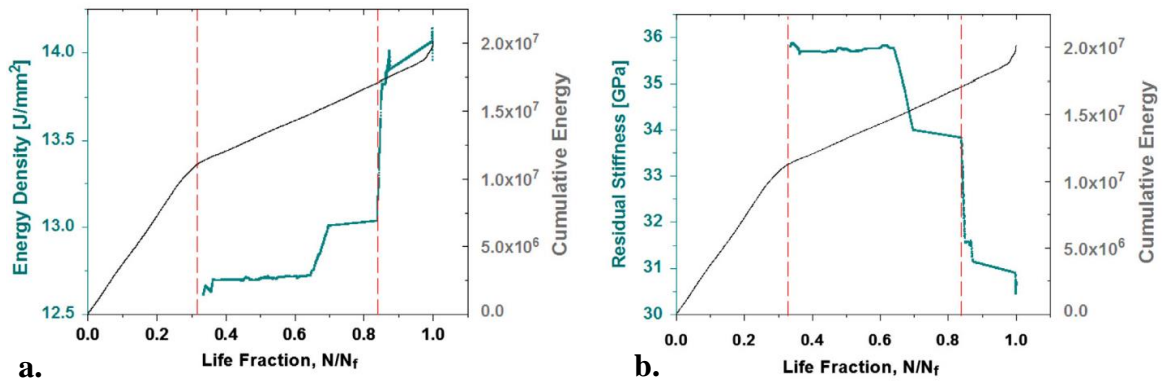


Figure 1.12. Comparison of cumulative AE energy with (a) Energy density increase (b) Stiffness degradation [28].

Liu *et al.* [29] used AE technique for damage mode identification during OHT tests. The effect of two different hole sizes in three different XP and QI CFRP laminates was investigated with AE technique. Energy, counts and amplitude were used for damage mode classification. Microscopy investigations after failure were done which enabled to make basic correlation between damage modes and AE characteristics. Interpretations of micro damage mode propagation during testing was done with respect to the SEM observations after failure which means that correlations are not from direct in-situ observations.

The most influential studies involving AE technique for damage detection has been performed by Composite Materials Groups (CMG) in Materials Engineering Department of Katholieke Universiteit Leuven (University of Leuven: KU Leuven) for the last 15 years under the supervision of Prof. Stepan Lomov. Initially they used cumulative AE energy curves to determine the important damage threshold levels during tension tests of textile composites [30–34]. An example of damage threshold detection is shown in Figure 1.13 for a 3D non-crimp fabric orthogonal woven (3DNCOW, as named by the authors) GFRP composite [33]. Arrows in Figure 1.13 indicate the damage threshold levels determined from jumps in cumulative AE energy curves where  $\varepsilon_{min}$  represents the threshold for initiation of low energy signals which is negligible for damage initiation. First damage threshold strain level is  $\varepsilon_1$  in Figure 1.13 since it corresponds to considerable change in the slope of cumulative AE energy curve. Then second damage threshold level is shown with  $\varepsilon_2$  which corresponds to cause a substantial change in the cumulative AE energy curve [30–34].

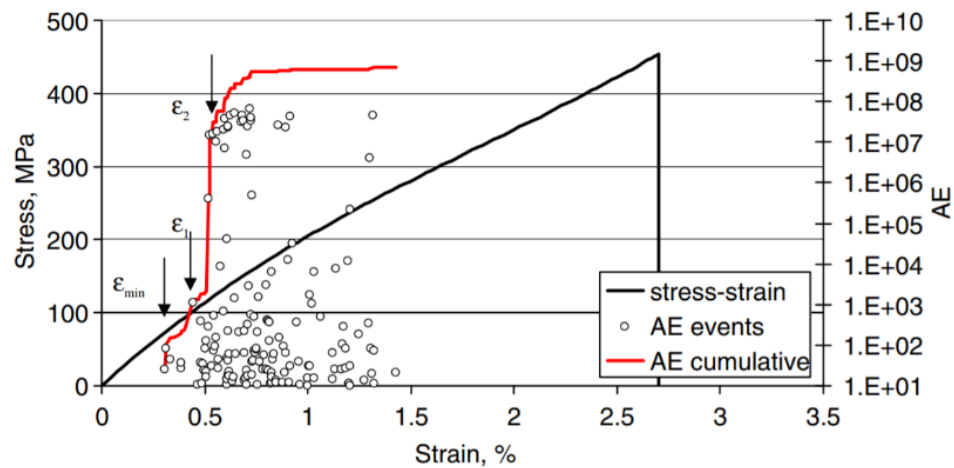


Figure 1.13. Stress-strain response of a 3DNCOW GFRP composite with cumulative AE energy curve [33].

First study of CMG of KU Leuven consisting use of AE for damage mode identification in composite materials was applied to 3DNCOW CFRP composites under tension loading in 2014 [35]. Lomov *et al.* [35] used the frequency classes for damage modes determined by Gutkin *et al.* [26]. Specimens tested in [26] were made from UD CFRP prepregs, which was a totally different material system than the one used in this study [35]. Tests were stopped at certain levels and different cross-sections of the tested specimens were investigated with post-mortem optical-microscopy. These observations showed the inconsistency between the pre-determined frequency groups for damage modes in [26] and the damage modes in this study [35] due to the fact that the different material system and the lay-up sequence. It was concluded that the frequency groups, determined by Gutkin *et al.* in [26], shown in Table 1.5 were robust groups for damage mode classification in CFRP composites and they should be correlated with present damage modes in 3DNCOW composites, shown in Figure 1.14, but not the damage modes in Table 1.5. This study proved that pre-determined frequency groups for damage modes in a composite system cannot be applied to a different composite system, since it can cause misinterpretations for the correlation of damage modes with AE results. Also, it showed the insufficiency of using single AE parameters for damage mode correlations. Prof. Lomov, believed the necessity of statistical algorithms for evaluation of AE results instead of single parameter classification and developed a clustering algorithm for this purpose. Details of further studies consisting clustering algorithms are given in next section.

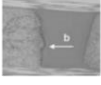
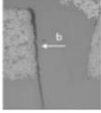
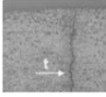
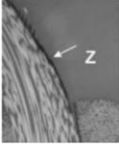
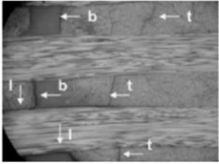
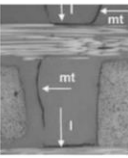
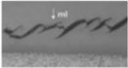
Applied strain	Damage characterization	transverse on yarn boundary (b)	transverse inside yarns (t)	boundaries of Z-yarns (Z)	transverse in matrix pockets (mt)	longitudinal in matrix pockets (ml)
0.005	Sporadic cracks on boundaries of the yarns		n/a	n/a	n/a	n/a
0.01	Well-developed system of transversal cracks and cracks on boundaries of the yarns; sporadic transversal matrix cracks					n/a
0.016 (failure)	Massive transversal cracks; local debondings on the boundaries of the yarns and matrix cracks parallel to the sample surface					

Figure 1.14. Damage mode progression in 3DNCOW CFRP composites [34, 35].

Misinterpretations encountered by Lomov *et al.* [35] are highly possible. As mentioned before, general assumption for damage mode classification was as follow; matrix cracks and fibre breakage were believed to correspond to low and high peak frequency values respectively as shown in Table 1.5. However, Baker *et al.* [36] and Maillet *et al.* [37] showed that this assumption cannot be true since the stacking sequence had considerable effect on AE characteristics of the same damage mode in different XP and QI stacking sequences made from CFRP materials. The only damage mode was transverse cracks in 90° plies during tension tests of  $[0/90]_{6s}$  and  $[90/0]_{6s}$  laminates. However, it was seen that high peak frequency signals were recorded for  $[0/90]_{6s}$  whereas only low frequency events were recorded initially for  $[90/0]_{6s}$  as shown in Figure 1.15. It was also seen that multiple frequency groups were activated due to transverse cracks in 90° plies. Each frequency groups did not represent different damage modes but they were seen to be in good agreement with transverse cracks of 90° plies in different plies as seen in Figure 1.15. This work showed that the through thickness distance of the damage, in other words, the through thickness position of the 90° plies, highly affects the AE characteristics of same damage mode. Besides, high frequency signals were seen to not only represent fibre breaks which is a very crucial finding for classification of damage modes.

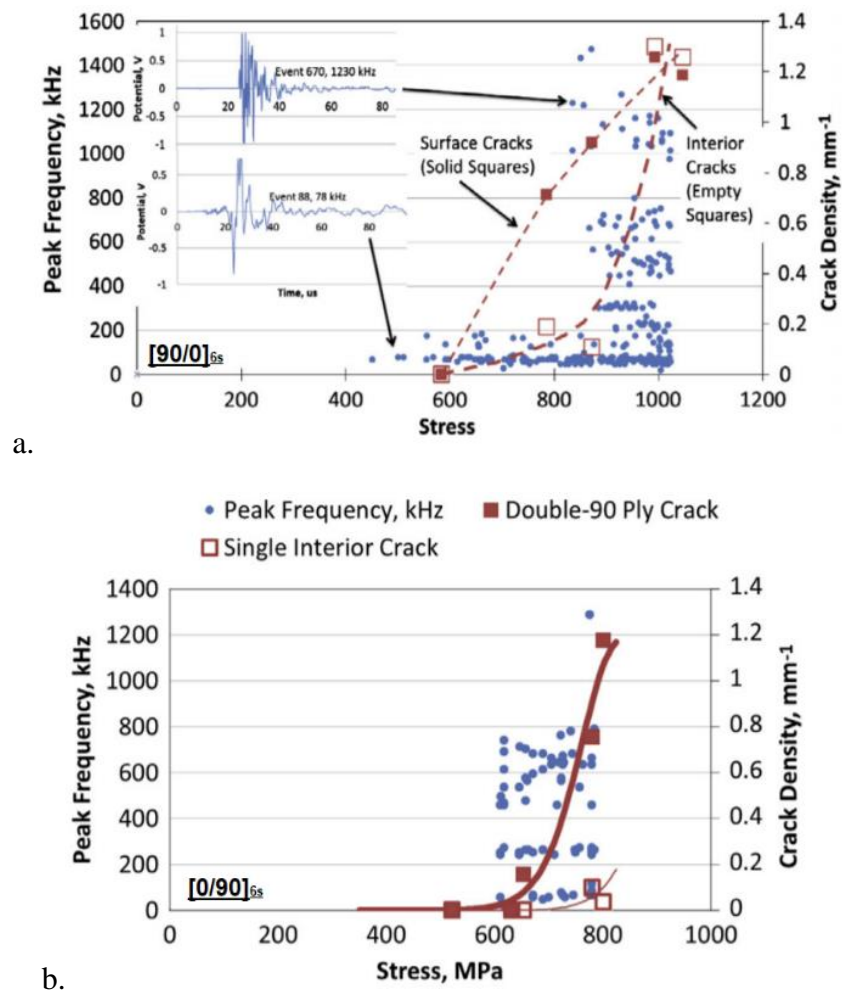


Figure 1.15. Progression of peak frequency values with applied stress and correlation with transverse cracks in  $90^\circ$  plies during tension tests of; (a)  $[90/0]_{6s}$ , (b)  $[0/90]_{6s}$  (b) laminates [36].

Furthermore, Maillet *et al.* [37] showed the effect of attenuation to AE characteristics of recorded signals due to induced damage by using the AE results of the tests done by Baker *et al.* [36]. It was seen that waveforms of a signal in time and frequency domain were different in sensors at different distances to the damage source. It meant that same damage mode could correspond to distinct characteristics at each sensors due to attenuation. Figure 1.16 presents the change in frequency centroid values of registered signals with respect to distance between sensors and damage source. The characterization of effects of frequency-dependent energy attenuation on the values of frequency contents showed that source-sensor distance and material thickness were the two most limiting factors for damage mode identification of transverse matrix cracks in  $90^\circ$  plies. Baker *et al.* and Maillet *et al.* [36, 37]

showed that classification with respect to single AE parameters cannot be reliable for damage mode identification in composite materials. Because, characteristics of registered AE signals could be affected with the stacking sequence and distance of damage source to AE sensor. Besides, multiple frequency groups could be activated due to a single damage mode. This may cause misinterpretations for AE results. Application of in-situ optical techniques with AE was suggested with Baker and Maillet *et al.* for efficient damage mode identification [36, 37].

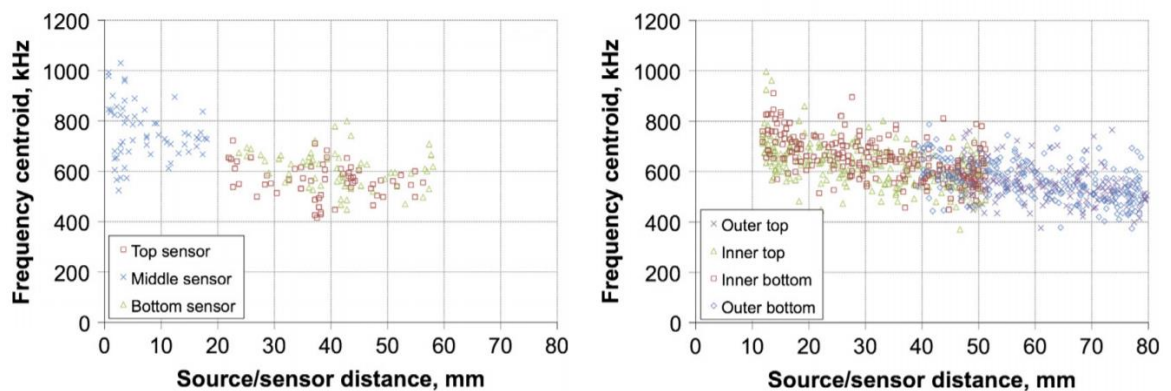


Figure 1.16. Frequency centroid vs. source/sensor distance in different sensors [37].

Fotouhi *et al.* [38] used AE technique to determine the AE characteristics of damage modes in thin ply UD carbon/glass fibre reinforced hybrid composites. Due to the transparency of the hybrid laminates, ply fragmentation and delaminations could be detected with naked eye during tests and correlated with AE results. This provided a link between AE results and ply-fragmentation with delamination damage modes in hybrid composites. Damage mode classification with respect to energy and amplitude parameters is shown with the characteristics of noise signals in Figure 1.17. This is very important but it was not mentioned in previous studies. Noise signals can cause wrong interpretations, so they should be distinguished. In addition to this, small amplitude ranges of noise and damage modes overlapped in Figure 1.17 but using energy and amplitude parameters together enabled to distinguish signals more clearly. Otherwise, classification with respect to amplitude only would cause insufficient results. Damage mode propagation and correlation with AE results are presented in Figure 1.18. Availability of in-situ damage mode detection with naked eye

provided a strong correlation with AE results. AE characteristics of damage modes are determined accurately. Thus, in-situ damage tracking is very important for robust mapping of AE characteristics to damage modes.

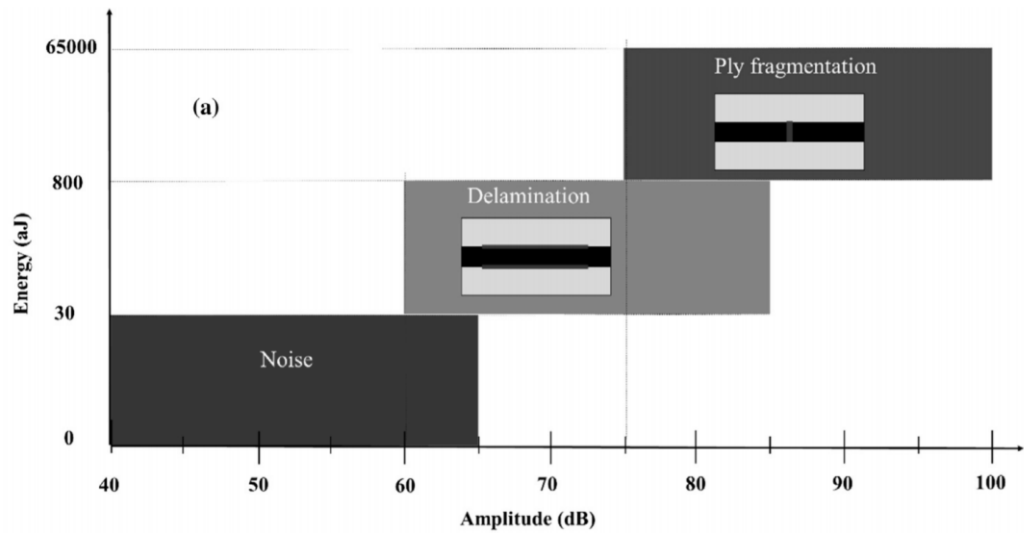


Figure 1.17. Energy and amplitude ranges of damage modes in hybrid composite [38]

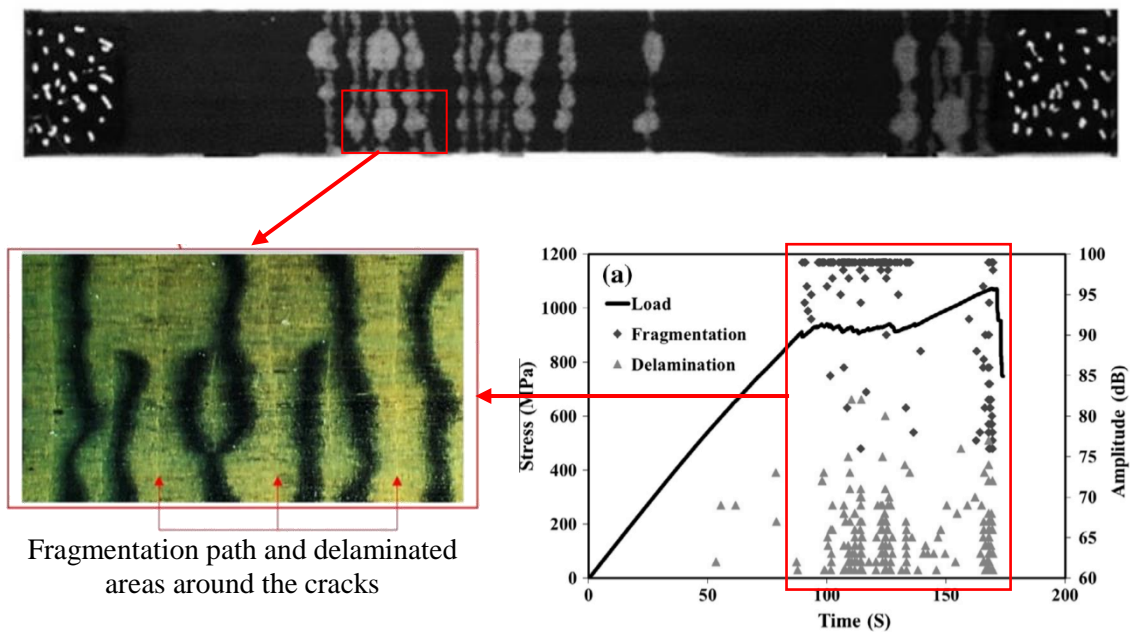


Figure 1.18. Correlation of damage modes with AE results for a carbon/S-glass composite [38].

Even though single AE parameter for damage mode correlation is not sufficient for the abovementioned reasons, it is still applied in recent studies. Mohammadi *et al.* [39] quantified AE results for damage modes of UD GFRP laminates under OHT tests. Single constituents such as fibre bundles and neat resin samples were tested to determine peak frequency characteristics of fibre break and matrix crack damage modes. While fibre breaks and matrix cracks corresponded to highest and lowest peak frequency groups, frequency band between them was assumed to represent fibre/matrix debonding. Wavelet Packet Transform (WPT) and Fuzzy C-Means (FCM) clustering approaches were applied to classify damage mechanisms in the specimen during OHT tests of GFRP tests. These results were verified by comparing with, FE analysis predictions. At the end, SEM observations after failure was used to support the results. Overall FE and test results showed similarity. It was found that the difference for damage mode quantification were 15 % and 42 % between WPT-AE and FCM-AE respectively. In this study, accumulation of recorded AE signals during the tests were not presented. As previous studies, this study is also lack of in-situ damage tracking. So correlation of damage modes with respect to single AE parameter and supporting results with SEM observations at the end only could cause misinterpretations.

Most of the studies summarized up to this point focused primarily on the use of AE technique during tension tests. Few of them used this technique during fracture tests [10, 19, 24, 26]. They performed Mode-I fracture tests (Double Cantilever Beam: DCB tests) to determine the AE characteristics of delamination. Actually, it is the most important damage mode that generally causes considerable degradation in material stiffness. In order to detect delamination initiation, its propagation and its effect on mechanical performance, AE technique was used during various fracture tests consisting; DCB, End Notch Flexure (ENF) for Mode-II and mixed-mode bending (MMB) tests for smooth and sandwich composite plates. Bakhtiary Davijani *et al.* [40] used AE technique during DCB tests of woven GFRP composites to investigate the initiation and propagation of delamination by Sentry function that combines the AE energy and strain energy of the material. It is the logarithmic value of the ratio of strain energy to AE energy. Sentry function has degrading characteristic inherently through loading. It was seen that combination of AE energy with strain energy could provide prominent information for initiation and progression of delamination during DCB tests. Najafabadi and Fotouhi used AE technique during various fracture tests [41–46]; DCB for Mode-I, End Notch Flexure (ENF) for Mode-II and mixed-mode bending (MMB)

tests for smooth and sandwich composite plates [41–46]. Sentry function was utilized to detect considerable damage threshold levels during these tests. Even though the AE characteristics of delamination under different fracture tests was determined primarily, AE characteristics of different damage modes, matrix cracking, fibre breaks, fibre/matrix debonding were also determined in terms of amplitude and peak frequency values by testing single constituents [43, 44]. Similar AE signals registered during fracture tests were then classified by relying on these results. More importantly it was seen that AE energy parameter can be used effectively to calculate the mode-I, mode-II and mixed-mode fracture toughness values as an alternative method to classical determination methods [41]. Damage mode classification in these studies are questionable but the efficiency of using AE technique for calculation of fracture toughness values is a very important progression in this field.

### **1.2.2. Evaluation of AE Results with Respect to Cluster Algorithms**

Results of the studies presented in previous subsection provided important insight for the progress in use of AE for damage detection in composite materials from 1990s until today. However, insufficiency of single parameter evaluation for damage mode identification has been revealed through 2000s. Even though damage modes are classified with respect to certain amplitude and peak frequency ranges, signals with different frequency ranges can be registered due to a single damage mode as proved by Baker and Maillet *et al.* and shown in Figure 1.15 [36, 37]. Another drawback was seen in [26]; even though matrix cracking was occurring in low strain levels during tension tests of  $[0]_8$  laminate, different frequency groups were activated and shown with distinct colours in Figure 1.9. Each colour in Figure 1.9 were said to represent different damage modes [26]. This kind of overlapping can occur due to lay-up sequence, signal attenuation, very closely occurring damage sources, noise signals and calibration quality of AE equipment. Because of such reasons, evaluation of multi-parameter techniques were required to quantify AE signals. Pattern recognition is one of the most important multi-parameter technique used for evaluation of AE results. Pattern recognition techniques rely on the classification of several parameters into clusters that form similar patterns, in other words having similar characteristics. They can be divided into two groups. First one is supervised case in which the damage modes should be known

since the algorithm associates input signals to a given class or cluster established from training examples. Secondly, unsupervised pattern recognition techniques do not require presented training set. They have a complete methodology that consist of procedures for descriptor selection, cluster analysis and its validity to group signals with similar characteristics [47].

First study concerning pattern recognition techniques for damage mode classification with evidences assigning damage modes to signal clusters was done by Huguet *et al.* [47] where formation of Kohonen's self-organizing map for AE data was developed. It is an unsupervised neural network algorithm, developed by Mao and Jain [48]. Readers should refer to cited references for the details of Kohonen's self-organizing map and its neural network algorithm [47, 48]. Tensile stresses with simultaneous AE registration were applied to glass fibre reinforced polyester composites to produce specific damage modes and identify their AE characteristics with Kohonen algorithm. First pure resin was tested to detect the AE characteristics of matrix cracking and then [45]<sub>12</sub> and [90]<sub>12</sub> samples were tested to determine fibre/matrix decohesion. It was seen that these two damage modes had different amplitude, duration and energy values but instead of single parameter classification six parameters were evaluated together to cluster AE signals with Kohonen's map. It was seen that this method provided good results for the abovementioned damage modes. This study has been one of the most innovative studies related with using AE technique for damage mode identification in polymer composites due to the new pattern recognition approach used for AE results. Because of this, it is the third highest cited study for this research area filtered with keywords "acoustic emission" and "composite" [8].

Godin *et al.* [49] tested the classification capabilities of supervised and unsupervised pattern recognition methods. A methodology based on the use of k-means clustering "learning data set" and Kohonen's neural network classifier. First of all, pure polyester, [45]<sub>12</sub> and [90]<sub>12</sub> samples were tested in this study to determine AE characteristics of matrix cracking and fibre/matrix decohesion as in authors' previous study [47]. Secondly, k-means clustering algorithm was applied to separate AE signals into two classes. Classes were validated with experimental results of the first step. Validated results of previous step provided training data set for the third step, in which supervised pattern recognition was used to classify AE results with respect to Kohonen's neural network method. An unknown signal type was classified into nearest neighbour with respect to Eucladian distance. Then results

of these three steps showed a good correlation with the results with respect to Kohonen's map in authors' previous study [47]. After verification with previous study, training data set was developed with fibre breaks from single fibre fragmentation tests. AE characteristics of fibre breaks were determined and it was seen that distinguishing AE characteristics of fibre breaks from fibre/matrix decohesion was very difficult. It was proven that, methodology tested in this study could be applied to GFRP composites with more complex laminations.

After the effectiveness of Kohonen's Map method were demonstrated with AE signals registered from UD laminates [47, 49], Godin *et al.* applied the methodology which combines k-means and Kohonen's map methodology in [49] for XP GFRP epoxy composite laminates to monitor the damage sequence [50]. In this study, Davies-Bouldin index was used to choose number of clusters. It is an index that shows the measure of the validity of the number of clusters with k-means algorithm. Low Davies-Bouldin index means better clusters. Results in this study showed consistency with authors' previous results. Delamination damage mode in angle ply laminates was added as an additional class successfully. Three cluster groups of AE signals with respect to amplitude and rise time is shown in Figure 1.19 where the waveforms of individual signals from three clusters are plotted. It is highly important to note that, cluster groups in Figure 1.19 overlap each other. It was mentioned in this study that obtaining clusters without overlapping was not possible. So that was one important problem for clustering. It is seen that signals from each cluster have distinct signal waveforms in Figure 1.20. The A-type and B-type waveforms represent matrix cracking and fibre/matrix debonding respectively. They were identified in authors' first study [47], whereas D-type waveform was identified for delamination in this study [50]. In addition to them another waveform, C-type, was identified in previous study [49] due to fibre breaks but not shown in Figure 1.20. Progression of damage modes through the tension tests of each XP laminates can be seen in Figure 1.20.

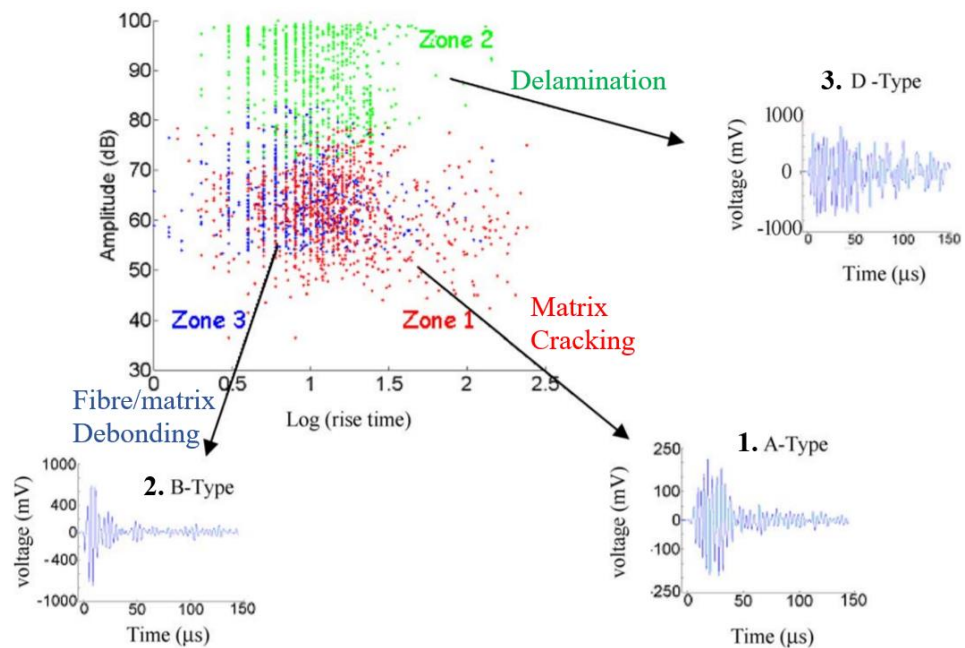


Figure 1.19. AE Clusters with waveforms of individual signals [50].

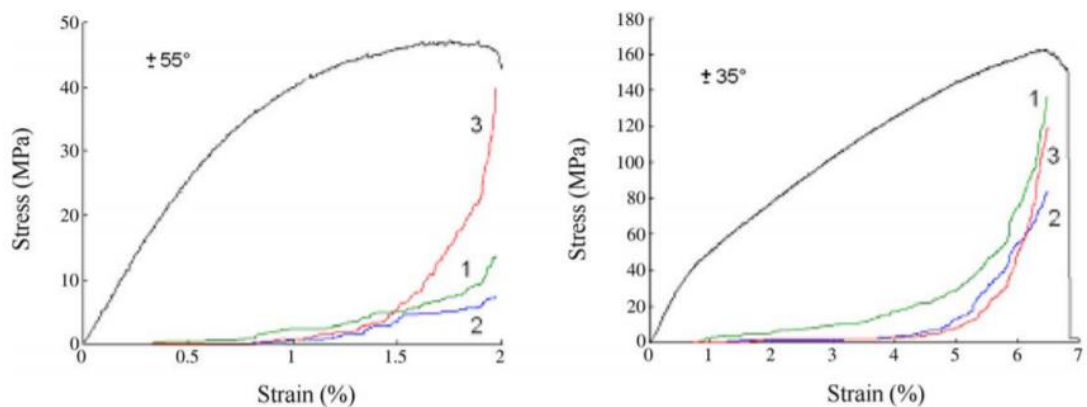


Figure 1.20. Progression of damage modes in XP laminates [50].

These three studies provided a considerable insight for the application of clustering algorithms to AE results in literature. It was seen that Kohonen's map and k-means clustering algorithms were highly effective for classification of damage modes [47, 49, 50]. Furthermore, Godin *et al.* [51] applied AE registration during tension tests of aged and unaged glass fibre reinforced polyester composites. Effect of hydrolytic aging to damage progression was examined by evaluating the AE results with the proposed methodology. It was verified in this study that this methodology could be applied to any composites for damage mode identification.

Gutkin *et al.* used clustering algorithms for damage mode classification as mentioned previously [26]. Peak frequency classifications, described in previous section, were compared with three different unsupervised pattern recognition techniques; k-means, Self Organising Map (SOM) combined with k-means and Competitive Neural Network (CNN). It was found that SOM combined with k-means algorithm was found to be the most effective analysis method. It is similar to what was done by Godin *et al.* [49, 50]. Silhouette coefficient was used to choose the number of clusters in SOM combined k-means clustering algorithm. Silhouette coefficient is a value indicates the measure for the similarity of an object to its own cluster. High Silhouette coefficient means more dense and well-separated clusters as opposed to Davies-Bouldin index. Different cluster numbers were obtained for various laminates due to the different damage modes present in each laminate type. Unexpected clusters were obtained for simple laminate types, which were used to identify AE characteristics of certain damage modes. For example, only fibre breaking and fibre/matrix debonding were expected in  $[0]_8$  or matrix cracking and fibre/matrix debonding in  $[90]_{16}$  laminates respectively. However, four clusters were found for  $[0]_8$  and three for  $[90]_{16}$  laminates as seen in Figure 1.9. Even though it is a very important study that compares three unsupervised pattern recognition methods with peak frequency classification, there are some problems encountered for the most effective clustering algorithm.

A semi-automated pattern recognition approach was developed by Sause *et al.* [52]. It was based on k-means algorithm. Optimal number of clusters were evaluated by considering different evaluation indices at the same time. Davies-Bouldin, Tou indices, Rousseeuw's silhouette validation method and Hubert's Gamma statistics were evaluated at the same time automatically and doing a sort of averaging when the optimal number of clusters is not the same for all cases. Then the automatically determined optimal number of clusters were validated with a voting scheme. The flowchart of the pattern recognition approach and the evaluation of cluster numbers are presented in Figure 1.21. This approach was examined for AE results registered during four-point-bending tests of XP CFRP composites made from UD preregs. A new parameter was introduced by Sause *et al.* in this study [52]. It is weighted peak frequency which provides an improvement for the representative characteristics of frequency associated with an AE signal combining the discriminative efficiency of the peak frequency with the information on the average frequency content of the signal expressed by the frequency centroid. Its value is geometric

mean of peak frequency and frequency centroid as shown in Equation 2. Three clusters were obtained from four tests and four clusters were obtained for only two tests. Representation of clusters for two different results are shown in Figure 1.22. with respect to partial power vs. weighted peak frequency diagram. While Figure 1.22.(a) represents a suitable cluster whereas Figure 1.22.(b) represents an unsuitable cluster as the one in Figure 1.19. Unsuitable cluster representation in Figure 1.22.(b) was due to noise signals which caused a fourth cluster and overlapping of clusters. So, this study clearly proved the negative effect of noise signals for the analysis of AE results. In the end, the pattern recognition approach proposed in this study was seen to provide suitable clusters. The characteristics of signals in each clusters were seen to be consistent with proposed AE characteristics determined from single constituents' tests [19, 21] and finite element simulations [53].

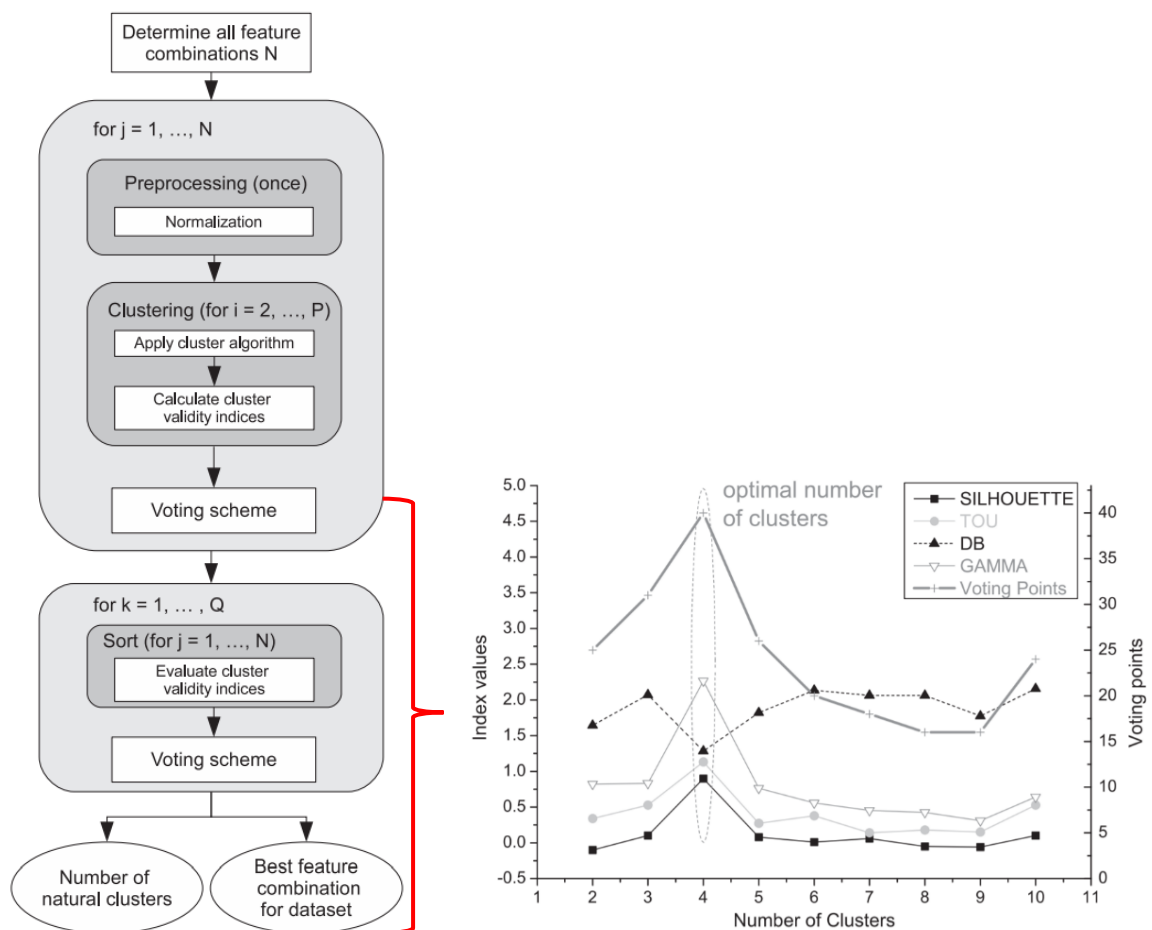


Figure 1.21. Flowchart of pattern recognition approach with voting and cluster validity indices [52].

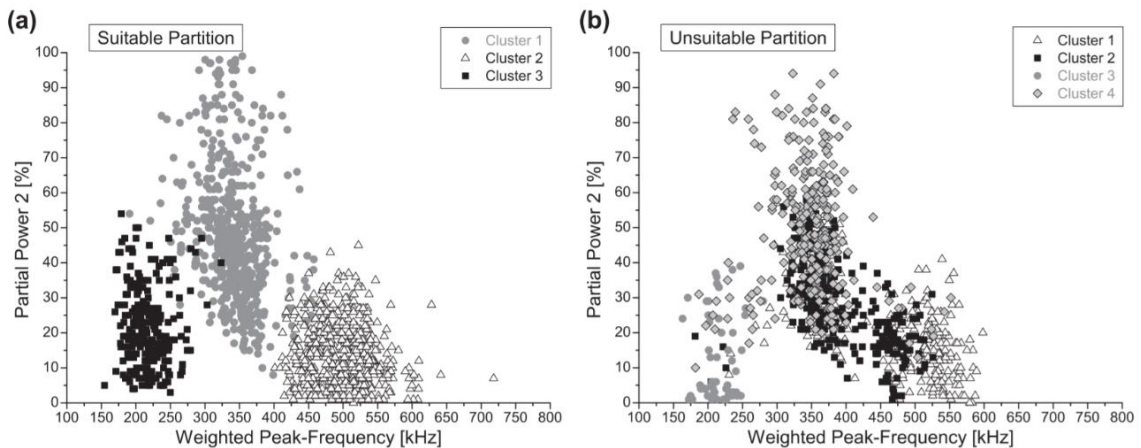


Figure 1.22. (a) Suitable clusters (b) unsuitable cluster representations [52].

The pattern recognition method developed in [52] was used to quantify damage modes in mode-I loading of GFRP and CFRP composites made from UD preregs by Sause *et al* [54]. SEM observations were applied after tests to investigate fracture surface and correlate AE cluster groups with corresponding damage modes. Signal waveforms from each cluster that represent different damage modes were compared with FE signal simulations and a good agreement was obtained between simulations and real waveforms. So, Sause *et al.* [54] verified their pattern recognition technique for correlation of AE signals with damage modes under DCB loading for different composite materials.

Kempf *et al.* [55] examined the performance of Sause *et al.*'s pattern recognition technique [52] to investigate the different interactions and damage progression of glass and carbon fibre in combination with epoxy and polyurethane matrices under tension and fatigue loading. AE clusters obtained for matrix cracking, debonding and fibre failure were very similar to clusters obtained in [52]. It was seen that the combination of static tension or dynamic fatigue tests of composite materials with online acoustic emission provided a strong tool to understand the basic structure–property-relationships and microscopic damage growth mechanisms that partially detected from the transparent matrices during the tests.

Oskouei *et al.* [56] identified damage modes in GFRP-polyester composites, made from woven fabrics and preregs, under DCB testing by applying an unsupervised pattern recognition approach. Fuzzy C-means clustering algorithm was combined with Principal Component Analysis (PCA) to classify recorded AE signals. Application of PCA is very

important to reduce the dimension of the data. Figure 1.23.(a) shows that first two principal components represent the 90 % of the total variability in the signal space. It means that 90 % of variance of the six dimensional (6D) data (six different AE parameters used in this study; amplitude, duration, rise time, counts, energy and peak frequency [56]) can be presented in 2D space. 2D projection of AE signals formed in three different classes are shown in Figure 1.23.(b) without overlapping and that proves the success of the clustering algorithm. It proves the ability of PCA to reduce the dimensions and computational time of the overall analysis. Three different clusters were obtained in this study which represent matrix cracking, fibre matrix debonding and fibre failure. It was found that peak frequency characteristics of signals from each cluster groups were consistent with the trend proposed in literature. However no optical investigation was performed as evidences in this study. So, correlations between AE signals and damage modes were relied on interpretations.

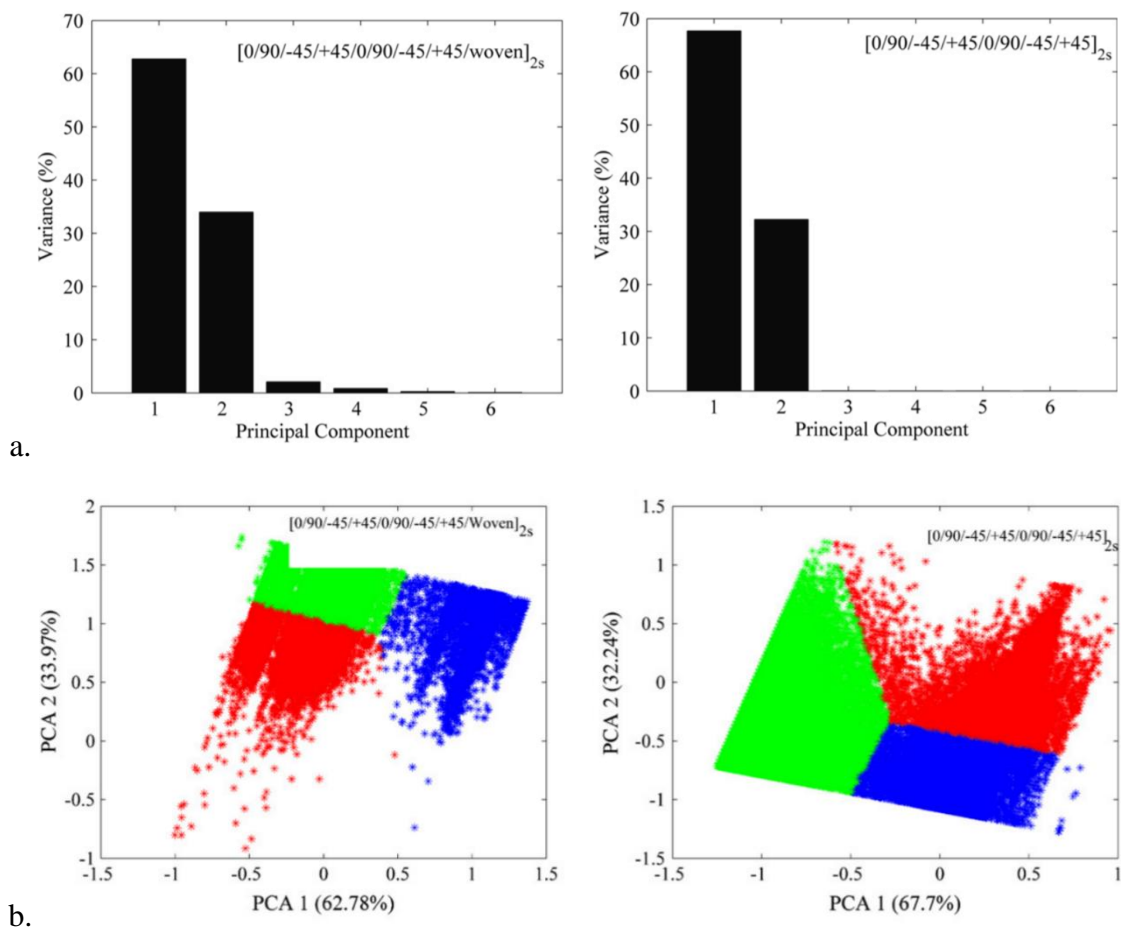


Figure 1.23. (a) Total variability of data by PCA (b) PCA representation of Fuzzy C-means clusters in 2D projection [56].

Lomov *et al.* experienced the insufficiency of classification with respect to peak frequency contents obtained from different materials [35]. They required the necessity of multi-parameter statistical algorithms for evaluation of AE results together instead of single parameter. Li *et al.* [57] developed k-means++ clustering algorithm and applied it for the tension test results of 2D plain weave and 3DNCOW GFRP epoxy composites from previous studies [32, 33]. Flowchart of the clustering algorithm is shown in Figure 1.24. Details of this algorithm is explained in Section 2.4.3, since this algorithm is used for clustering of AE results in this thesis. Optimal cluster numbers were found to be four with respect to the combination of high Silhouette Coefficient (SC) and low Davies-Bouldin (DB) indices [57]. Optimal cluster number and representation of clusters with respect to amplitude vs. peak frequency diagram for three different specimen types are shown in Figure 1.25. It was seen that cluster groups do not overlap on each other which proves the success of the clustering algorithm. It was hypothesized that CL1, CL2, CL3 and CL4 were believed to represent matrix cracking, fibre/matrix debonding and delamination damage modes due to the similarity of waveforms with A-type, B-type and D-type signals given in Figure 1.19. In addition to this, CL4 was believed to represent fibre breaks since it has highest peak frequency values. Progression of AE clusters occurred in expected sequence. First CL1 and CL2 started and CL3 and CL4 signals were seen to occur later as shown in Figure 1.26. It is another reason for the hypothesis of authors but the verification of correlations was left as a future work.

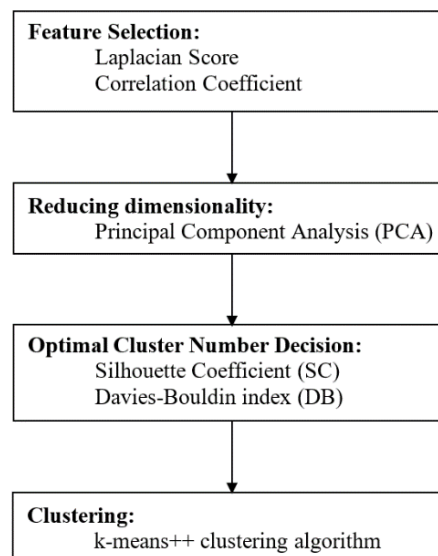


Figure 1.24. Flowchart of clustering algorithm [57].

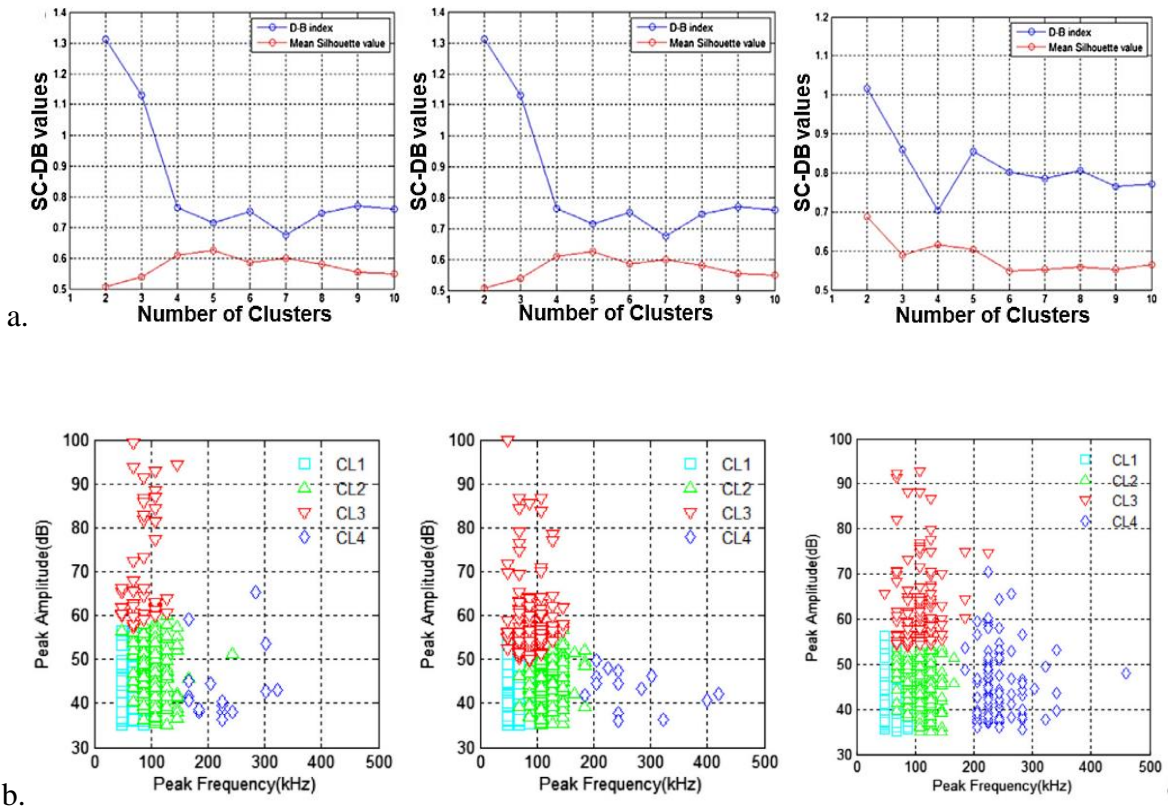


Figure 1.25. (a) Optimal cluster numbers (b) Presentation of cluster groups for three different laminate types [57].

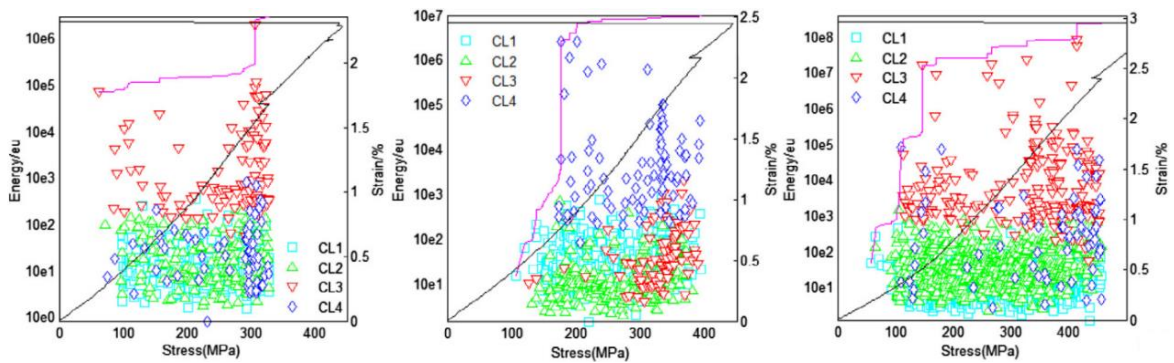


Figure 1.26. Progression of AE clusters through the tests for three different laminates [57].

Furthermore, Li *et al.* [58] applied optical observation with AE registration during tension tests of 2D plain weave GFRP epoxy composites. Transparency of the laminates provided cracks to be visible in backlit photos captured during tensile tests. Matrix cracks in the yarns and localized delaminations were detected with this optical technique. Then, they were correlated with AE clusters obtained with the clustering algorithm, developed in authors' previous study [57]. Thus, cluster groups determined in this study were correlated with actual cracks. Three cluster groups were classified with respect to amplitude and frequency centroid values. Low amplitude-low frequency (ALFL), broad amplitude-high frequency (ABFH) and high amplitude-low frequency clusters (AHFL) were obtained which were correlated with transverse cracks, fibre failure and delamination respectively by comparing with actual cracks during loading. A comparison for progression of AE clusters with optical detection of actual cracks can be seen in Figure 1.27. Correlation of transverse cracks and delaminations with ALFL and AHFL clusters, respectively, were seen to be highly consistent and reliable. However, ABFH signals were believed to represent fibre breaks with respect to the early works in this area. There were no evidences presented for correlations and it was relied on interpretations. Even though the reliability of this correlation is doubtful, this was the first study that provided strong evidences for correlation of different damage modes with AE signals by applying in-situ optical damage tracking. Besides it enabled to verify the authors' proposed cluster algorithm [57] with strong evidences.

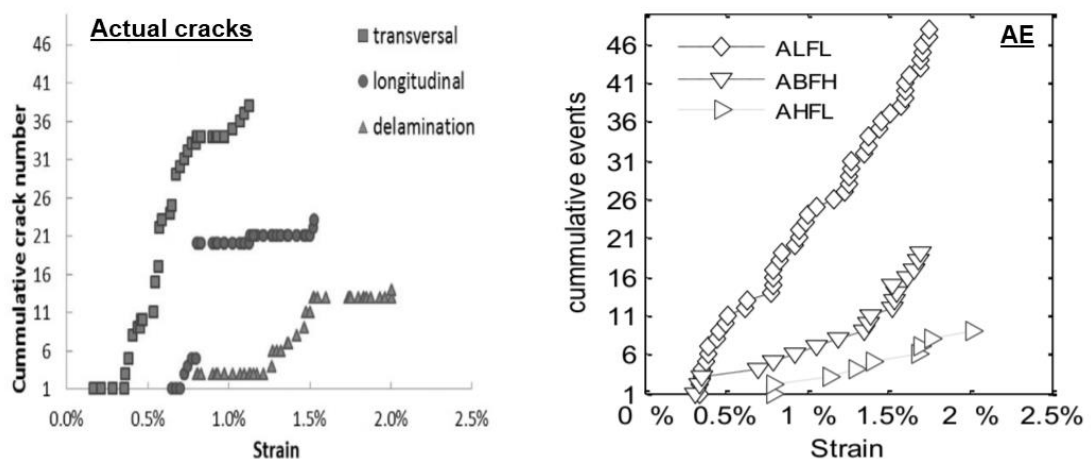


Figure 1.27. Comparison of actual cracks with AE detection [58].

Authors of these studies [57, 58] progressed their study by testing the efficiency of the k-means++ clustering algorithm with 2D twill and 3DNCOW CFRP epoxy composites [59]. In this study, the test results from [34] were evaluated with the proposed clustering algorithm. Characteristics of cluster groups for CFRP composites showed similarity with GFRP composites with small differences. Lower frequency bound of the high frequency cluster, which was believed to represent fibre breaks, was higher than GFRP composite. It was believed to be due to the higher stiffness of the carbon fibre. Correlation between high frequency AE events with fibre breaks was relied on Weibull statistical estimation and it showed earlier start of individual fibre breaks than AE cluster for woven fabric yarns. Two reasons were proposed for such discrepancy. Firstly, it was believed that isolated fibre breaks could not create a noticeable AE event and high frequency signals were not recorded during early strain levels. Secondly, Weibull estimates high number of breaks than reality. Eventually, correlation between high frequency clusters and fibre breaks was not proven. Besides the correspondence of high frequency clusters is still not clear.

In-situ damage tracking is relatively easy when the laminates are transparent, as in Li *et al.*'s study [58]. It is not easy for non-transparent materials, as CFRP composites. Digital Image Correlation (DIC) could be a good option for damage detection on material surface [31, 60–68]. It can provide a direct correlation of surface cracks with AE recordings. Sawan *et al.* [69] used DIC technique with AE registration during tension tests of open-hole (OH) CFRP laminates and bending tests of smooth CFRP laminates. In this study, clustering quality indicators, such as; Silhouette coefficient, Davies-Bouldin index, Dunn's indices were not used to choose optimum cluster numbers. Drawback of these indication method was shown by comparing the determined number of clusters with any other number. Gaussian distribution with a trial-error like technique was used for grouping instead. Distinct AE groups were correlated with damage modes obtained with DIC. This is another study that judges the reliable correlation of an AE group with a single damage mode. Damage mode correlation was assessed as follow; if a damage source causes different AE events, then both damage and AE events accumulation would start at the same time. On the other hand, if several damage modes would cause similar AE characteristics then the AE activity rate was expected to change considerably when corresponding damage modes initiate. Two AE groups were found for OH [0]<sub>6</sub> laminate. Accumulation of low amplitude AE group was consistent with propagation of longitudinal splitting, tangential to the hole. Second AE group

with high amplitude characteristics were interpreted to be fibre-related damage modes. Two reasons were asserted for the later. First was the assumption in literature for correspondence of high amplitude characteristics of this group. The second reason was the onset strain level. Initiation strain level of this second AE group agreed well with the degradation of elastic modulus from load-displacement curve. Thus, it was believed to be fibre-related damage mode. A different lamination was tested to investigate the effect of out-of-plane motion with DIC and correlate it with AE groups.  $[0/90/-45/+45/0/90/-45/+45/0/90]_s$  laminate, with additional four  $0^\circ$  plies on top plies in the middle section, was tested. Initiation and propagation of shear failure was detected with 3D DIC technique and that was seen to be consistent with the accumulation of high amplitude AE group. On the other hand, low amplitude AE group was started very early and it was believed to correspond matrix cracks at inner plies. This study showed the importance of DIC for providing optical evidences of damage modes and their correlation with AE groups. However, only one group was correlated with a damage mode with evidences. The second groups in each test were interpreted to matrix cracks or fibre breaks with respect to the assumptions in literature.

DIC is not sufficient to track micro cracks at inner plies. Carvelli *et al.* [70] applied DIC to detect surface cracks and full-field strain measurement with AE registration during tension tests of XP woven CFRP thermoplastic composite. However, no surface cracks were detected on material surface. In addition to this, in-situ edge observation was done by a high-speed Charge-Coupled Device (CCD) camera with a high magnification lens to follow micro damage propagation at inner plies and correlate them with AE clusters. Clustering algorithm, developed by Li *et al.* [57] was also used in this study. Correlation of transverse cracks at inner yarns with low amplitude and low frequency clusters (CL1) are shown in Figure 1.28. Only transverse cracks at inner yarns (shown within red circles in Figure 1.28.(a)) were correlated with a cluster group. Correspondence of other clusters was not determined but still this study proved the effective performance of k-means++ clustering algorithm for transverse cracks at inner plies of woven CFRP thermoplastic composites. Also, it is an important study that presented how to track micro damage modes at inner plies in non-transparent CFRP composites.

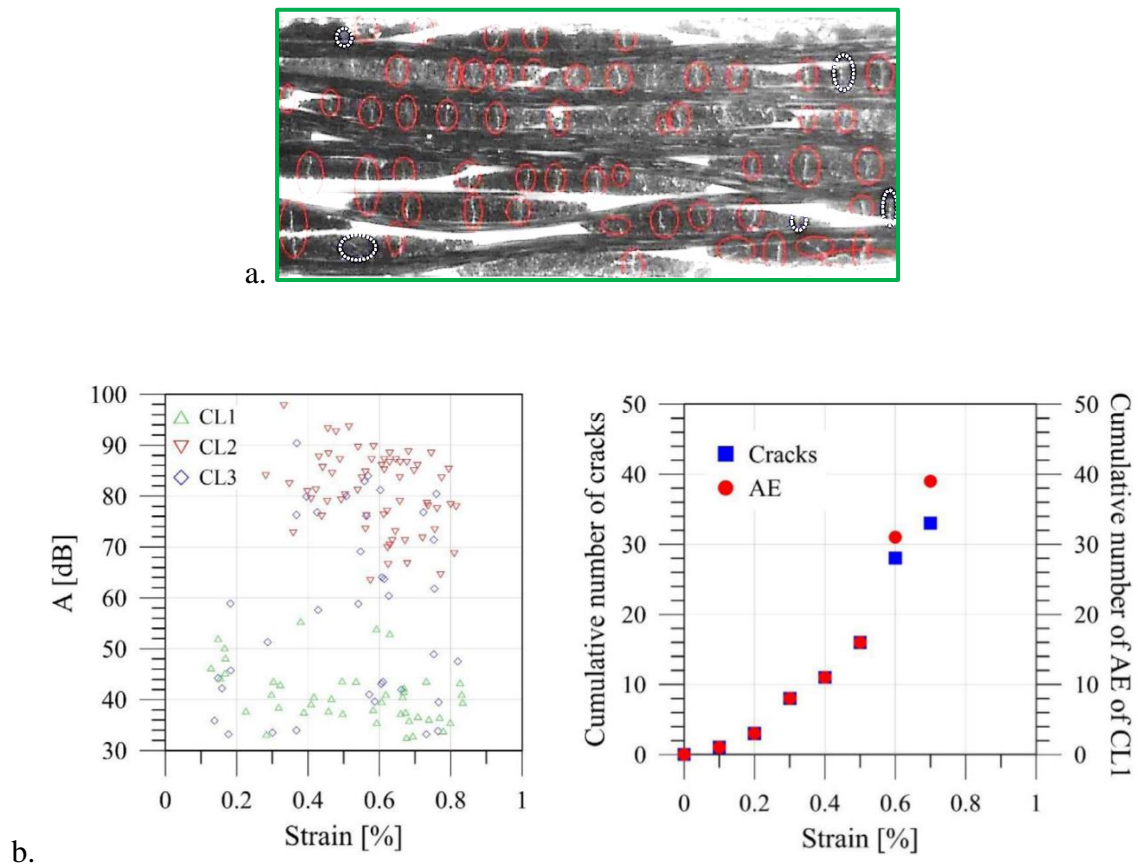


Figure 1.28. Transverse crack at inner yarns, b. Cluster groups and correlation of CL1 with transverse cracks [70].

Andrew *et al.* [71] used the same algorithm, developed by Li *et al.* [57] for the analysis of AE signals registered during compression tests of smooth and repaired GFRP composites. In addition to AE, DIC was utilized to do a qualitative and quantitative assessment of damage progression. The flow chart of the study can be seen in Figure 1.29. Different composites were tested under compressive loading. These materials are listed in Figure 1.29. AE and DIC damage profiles differed in each specimen type. However, AE results showed that optimal cluster numbers were found to be three with respect to Silhouette Coefficient and Davies-Bouldin Index for each specimen types. Clusters were classified with respect to their amplitude values, based on the results in literature, AE clusters were related to matrix or resin cracking, fibre/matrix debonding and fibre micro buckling from low to high amplitude clusters respectively. Discontinuities in the full-field DIC strain maps due to the damage modes enabled to make correlation with AE results.

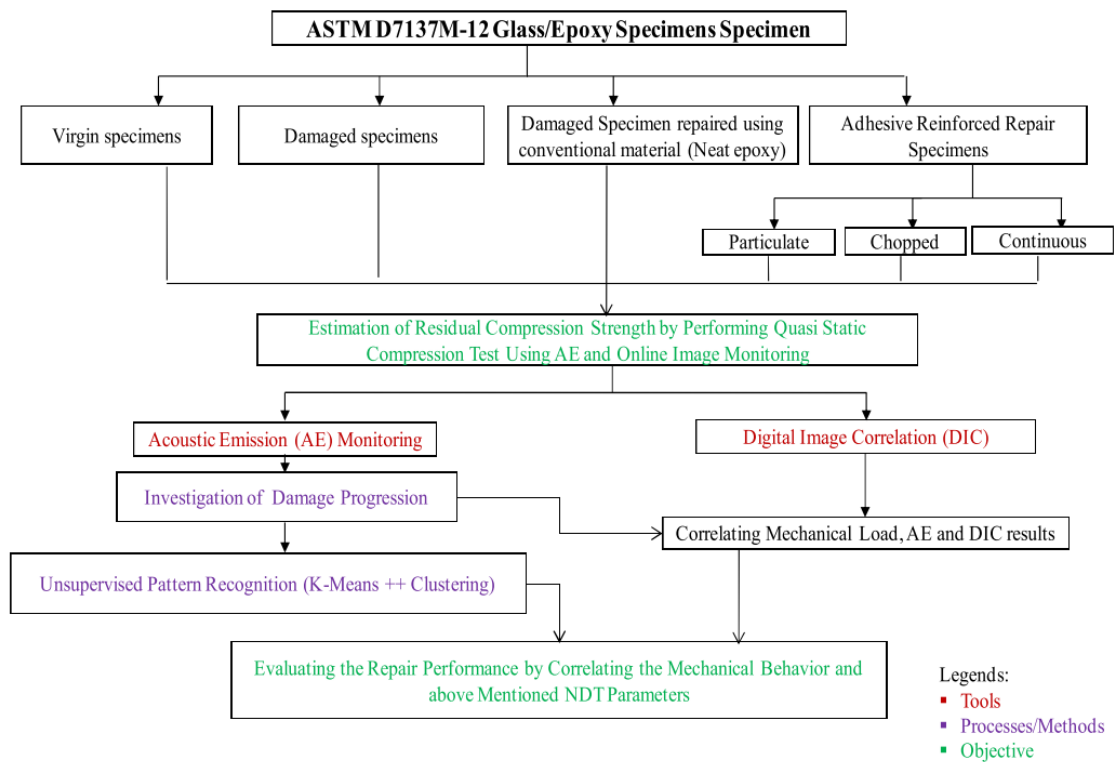


Figure 1.29. Workflow of Andrew *et al.* study [71].

### 1.2.3. Summary of Literature

Damage mode classification with respect to single AE parameters have been used in literature until today due to its simple post-processing requirements [9, 10, 15, 16, 18–29, 35, 38–46]. It was seen that a single damage mode could cause registration of different AE frequency ranges. Because of this, evaluation of multi-parameters with pattern recognition techniques have been used to cluster AE signals with similar characteristics as a second classification technique [26, 47, 49, 50, 52, 54–59, 69–71]. These studies include different composite laminates; GFRP [9, 18, 21, 22, 24, 27, 28, 39, 40, 47, 49, 50, 54–58, 71], CFRP [10, 15, 20, 23, 25, 26, 29, 35, 52, 54, 55, 59, 69, 70] and hybrid composites [38].

Generally, AE was used during uniaxial quasi-static tests. Mostly smooth specimens were tested under tension tests [9, 10, 15, 19–21, 24–26, 28, 35, 47, 49, 50, 55, 57–59, 70]. Few studies investigated OHT tests [20–22, 25, 29, 39, 69]. Considerable number of studies

involved with using AE technique to investigate the characteristics of delaminations under different fracture modes [10, 19, 24, 26, 40–46, 54, 56]. AE was used during flexural tests only in three studies [27, 52, 69]. Damage modes under compression test was investigated only in one study [71]. Furthermore, AE technique was applied to determine damage threshold levels and damage mode identification during cyclic tests in few studies [9, 16, 18, 20, 25, 27, 28, 55].

Damage modes were classified with respect to amplitude and peak frequency ranges mostly. Correlation of lowest amplitude/peak frequency and highest amplitude/peak frequency groups with matrix cracking and fibre failure respectively has been assumed as a fundamental classification in literature. Fibre/matrix debonding and delamination were believed to be represented between the ranges of these groups. Some authors tested single constituent (fibre or matrix) to identify AE characteristics of specific damage modes only [10, 19, 21, 39, 43, 44, 47, 49]. This is not a reliable method since wave propagation properties of materials change when they are composed with other constituents. Some others compared AE interpretations with analytical or FE models [23, 39, 52, 59]. Table 1.6 shows a summary of the amplitude and peak frequency ranges attributed to different damage modes in literature. There is no standardized ranges for delamination and debonding and even for all damage modes in Table 1.6. It is not surprising since characteristics of AE signals vary due to several reasons; materials of constituents, laminate type and its dimensions, AE sensors, threshold levels and attenuation. This was barely mentioned in literature.

AE correspondence of fibre breaks were not proven but it was believed that high frequency signals were registered due to this damage mode. Some authors used post-mortem observations and tried to verify this assertion [9, 18, 21, 29, 35, 39, 41, 43–45, 49, 54]. Unfortunately, this method did not really prove the relationship of amplitude/frequency signals with fibre breaks. Baker *et al.* [36] and Maillet *et al.* [37] provided invaluable findings to damage classification. It was seen that high frequency signals did not really correspond to fibre breaks and could be registered due to transverse cracks. Besides, AE signals with different amplitude/frequency values could be activated at the same time due to a single damage mode. These studies proved that application of AE technique alone is not sufficient for damage mode identification. In-situ observations should be applied for robust correlation of damage modes with AE characteristics.

Table 1.6. Amplitude and frequency ranges, attributed to damage modes in literature.

Reference	Matrix cracking	Debonding	Delamination	Fibre pull-out	Fibres Breakage
	Amplitude, dB				
[9]	40-55	60-65	60-65	65-85	85-95
[15]	45-55	-	55-65	65-85	-
[16]	40-60	60-80	80-100	-	80-100
[18]	40-55	55-75	55-75	-	80-100
[25]	60-77		77-90	>90	
[29]	40-60	50-70	60-80	80-100	80-100
[43]	75-85	-	60-80		85-105
[50]*	40-80	50-80	70-100	70-100	70-100
[57]*	35-55	55-100	35-80	-	35-80
[58]*	<55	-	>55		35-100
[59]*	≤70				30-90
	Peak Frequency, kHz				
[10]	50-180	220-300	225-300	180-220	>300
[21]	90-110	-		200-300	>420
[23]	200-600	200-350	100-500	700-1100	>1500
[24]	≈140	≈300		-	≈405
[26]	<50	200-300	50-150	500-600	400-500
[28]	<300				≥300
[39]	80-250	250-375	-	-	375-480
[43]	170-250	-	100-130		350-450
[44]	140-250	250-350			350-450
[57]*	50-80	50-150	150-500	-	150-500
[58]*	<180	-	>180		>180
[59]*	<300				≥300
*: Determined with clustering algorithm					

### 1.3. Objective

There are numerous studies can be found in literature which aimed to find a relation between damage modes and the AE correspondence as presented in previous section. Unfortunately, only few of these studies provided optical evidences of damage modes for the corresponding AE characteristics. This is limited to the transverse matrix cracks in 90° plies only [36, 58, 70]. Most of the correlations relied on interpretations without any optical proof. In order to obtain robust and reliable damage mode identification with AE technique, it is highly important to provide optical proofs and correlate them with true AE characteristics. Moreover, the effect of different lay-up sequences on AE characteristics of same damage modes is not stated in literature. It should be investigated since the lay-up orientation can affect the wave propagation properties and hence, AE characteristics of same damage modes might be different in different laminates.

The objective of this study is to obtain direct and reliable correlations between damage modes and the corresponding AE characteristics in CFRP laminates. Various types of laminates are taken into consideration to investigate the effect of different geometrical and lay-up properties on damage progression and their AE characteristics in each type. For this purpose, specimens with various lay-up sequences, including a central hole or not, are investigated in this thesis. Two different experimental programmes are performed in this thesis as outlined in Figure 1.30. Both of them include in-situ damage observation during the tension tests to provide direct correlations between damage modes and AE characteristics. First part of the thesis consists the tension tests of UD [0]<sub>5</sub> laminates, conducted in Mechanical Engineering Department at Boğaziçi University. In this work, artificial defects in the form of slits are incorporated at certain plies during manufacturing to stimulate damage in desired sequence. Tension tests are stopped at stress levels before ultimate strength and specimen edges are investigated with optical microscope to identify damage modes and then they are correlated with certain characteristics of AE signals registered up to that stress level. Results of these tests are compared with predictions calculated by a Finite Element Micromechanical (FEMM) model. It enables to verify the FEMM model. According to the author's knowledge, it is the first study that provides a direct correlation of damage modes in UD [0]<sub>n</sub> laminates that is used to verify the predictions of a FEMM model. Second part of the experimental work is completed in Materials Engineering

Department of University of Leuven (KU Leuven). AE signals registered during tension tests of smooth and open-hole QI laminates are evaluated with the k-means++ clustering algorithm to group similar signals. Multi-instrumental optical techniques, DIC for surface damage, in-situ edge microscopy for micro damage modes at inner plies, are used to provide reliable damage mode correlations with AE results. It is the first study that provides direct correlations between different damage modes and AE clusters in UD and QI laminates.

This thesis clearly demonstrates the necessity of using in-situ observation techniques simultaneously with AE registration during mechanical tests for damage mode correlations in composite materials. The results obtained in this thesis put the reliability of AE based damage mode classifications, widely adopted in literature, in question and a new classification scheme is proposed.

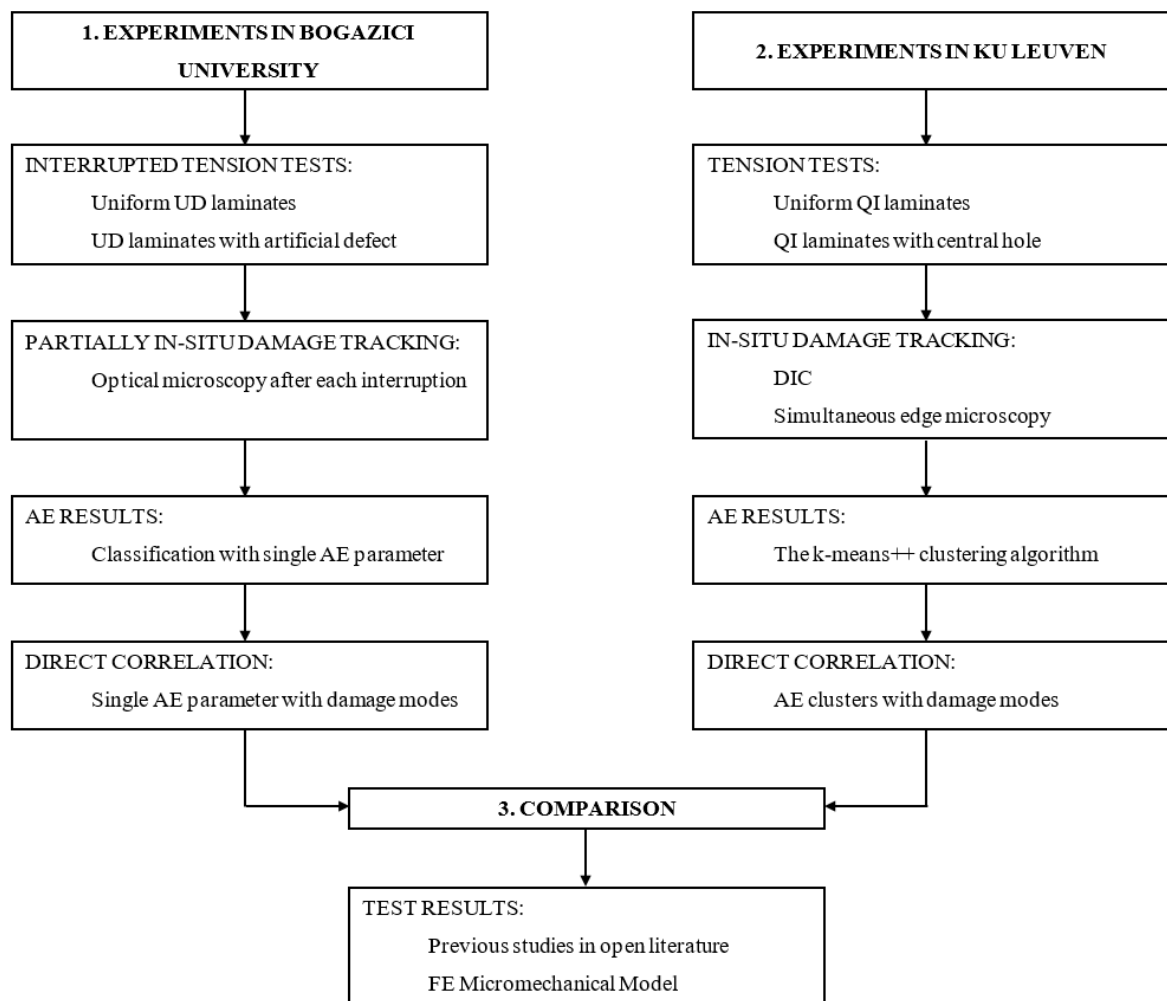


Figure 1.30. Outline of the thesis.

## 2. EXPERIMENTAL METHODS

### 2.1. Material and Manufacturing

Material used in this study is Hexcel AS4/8552. It is a prepreg system that consists of AS4 carbon fibres and 8552 resin with tradename HexPly® 8552. It is an amine cured, toughened and high-performance epoxy resin system supplied with unidirectional AS4 carbon fibres for use in primary aerospace structures [72]. Physical and mechanical properties of AS4/8552 prepreg system is given Table 2.1.

Table 2.1. Physical and mechanical properties of AS4/8552 [72–74].

		Data Sheet [72]	Shivakumar <i>et al.</i> [73]	FEMM [74]	
Fibre density	( $\rho_f$ )	1.79			g/cm <sup>3</sup>
Resin density	( $\rho_r$ )	1.30			
Laminate density	( $\rho_c$ )	1.58			
Ply thickness		0.184			mm
Fibre Volume Fraction		57.4			%
Longitudinal Elastic Modulus	( $E_1$ )	141000	141300	142840	MPa
Transverse Elastic Modulus	( $E_2$ )	10000	10000	10000	
In-Plane Shear Modulus	( $G_{12}$ )	-	4800	5571	
Out-of-Plane Shear Modulus	( $G_{23}$ )	-	-	3278	
Longitudinal Tensile Strength	( $\sigma_1^T$ )	2207	2206	2105	
Transverse Tensile Strength	( $\sigma_2^T$ )	81	-	51	
Longitudinal Compression Strength	( $\sigma_1^C$ )	1531	1531	-	
In-Plane Shear Strength	( $\tau_{12}^S$ )	-	114.5	-	
In-Plane Poisson's Ratio	( $\nu_{12}$ )	-	-	0.263	
Out-of Plane Poisson's Ratio	( $\nu_{23}$ )	-	-	0.525	-

Composite parts are manufactured by using the autoclave, shown in Figure 2.1, in Composites Laboratory of Boğaziçi University according to the Manufacturer's Recommended Cure Cycle [72]. It consists of five steps as shown in Figure 2.2. In the first step, the part is heated to 120 °C with a constant rate of 2°C/min. In the second step, it is held at 120 °C for 60 minutes. In the following step, it is heated to 180 °C at 2 °C/min. In this step, gelation of the resin begins and the part starts to sustain load. Then, the part is held at 180 °C for 120 minutes. Vitrification is completed at 45<sup>th</sup> minute of this step. Finally, the part is cooled down to room temperature. 0.1 MPa vacuum is applied to extract the air bubbles and 0.7 MPa pressure is applied to consolidate the part during the whole process.

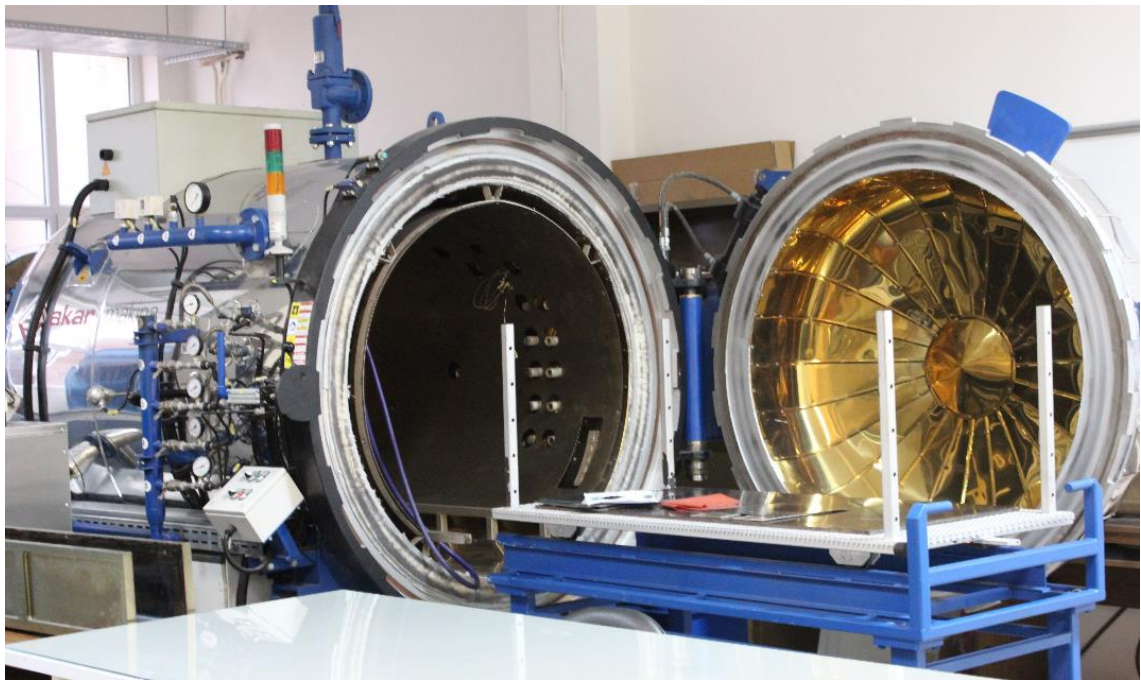


Figure 2.1. Autoclave at Boğaziçi University Composites Laboratory

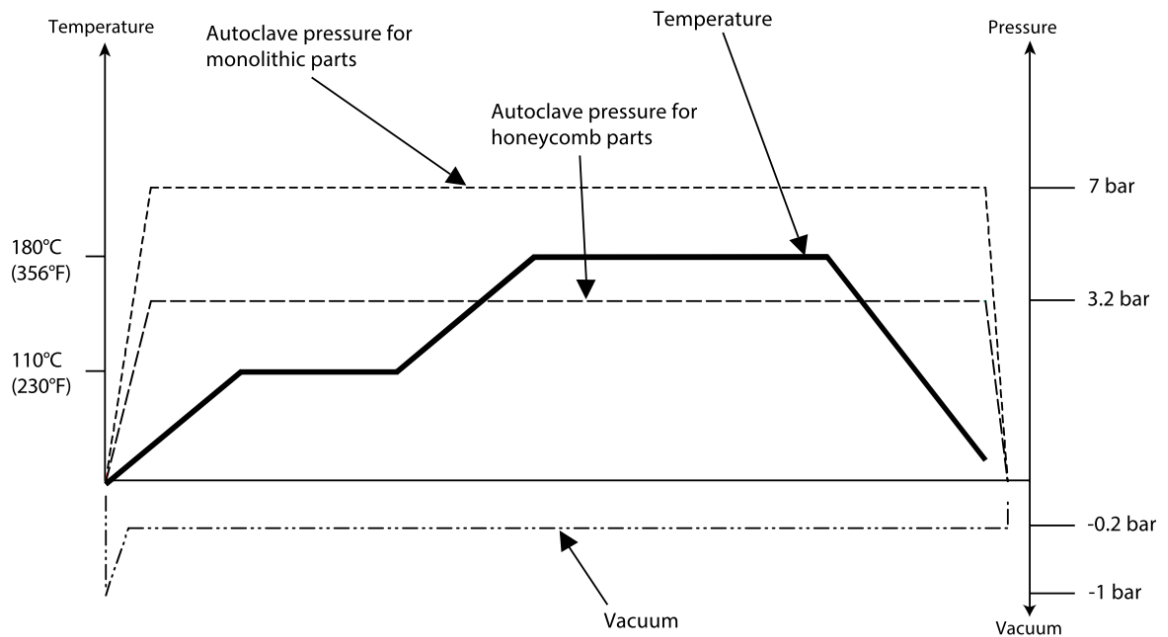


Figure 2.2. Manufacturer's recommended cure cycle for AS4/8552 [72].

## 2.2. Specimen Preparation

Regardless of the specimen size to be tested, large CFRP plates are manufactured in autoclave first. Then they are cut into smaller plates whose width is equal to the ten test specimens and lengths of the test specimens according to ASTM D-3039 [75] or ASTM D-5766 [76] test standards by using a water-cooled diamond disc. Schematic example of this is shown with layout in Figure 2.3. In order to obtain different QI specimens with dimensions of 15 mm width and 190 mm length, a large  $[+45_2/90_2/-45_2/0_2]_s$  plate in 455 x 455 mm dimensions is manufactured. Then smaller plates shown with 180 x 190 mm rectangles are cut with water cooled diamond disc. Numbers in these rectangles designate the laminate configurations. Afterwards, specimens are cut from these plates in the direction of arrows. In the end ten specimens from each QI variants are obtained.

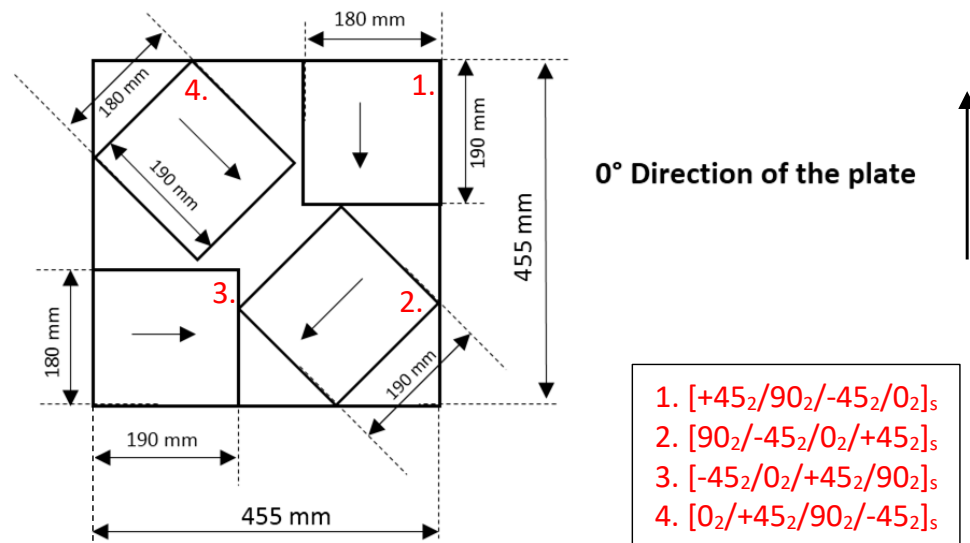


Figure 2.3. Layout for preparation of QI specimens.

### 2.2.1. Smooth Tension Specimens

Specimens can be crushed in gripping sections which can cause early failure during tension tests. End tabs should be used and they are very crucial especially for smooth tension specimens. QI GFRP plates with a length of 50 mm and thickness of 1.5 mm are bonded onto the upper and lower parts of the plates' front and back surfaces. These GFRP plates are end tabs used to prevent crushing in the grip sections. Before adhesively bonding the GFRP plates onto the CFRP plates of specimens, their gage section ends are tapered to  $20^\circ - 30^\circ$  by holding them in an inclined position on a grinding wheel. This tapered region enables to minimize stress concentrations at end tab-grip intersection and prevents failure from grip sections. Moreover, adhesive used between the plates and the end tabs should have high shear strength and should not cause a failure from these regions before sustaining the ultimate strength of the test specimen. *J-B Weld* is found to be the most cost-effective adhesive that can endure up to 80 kN load levels. It is used in this study due to its high strength and low cost.

Plates are cut into the test specimen sizes by using water-cooled diamond disc. Diamond disc has 2 mm thickness, which means 2 mm material is lost from one cut. Generally the recommended specimen size is given as 25 mm in ASTM D3039 [75] and 10 specimens are obtained from a plate which has the width of ten specimens.

### 2.2.2. Open-Hole Tension Specimens

In order to make open-hole tension (OHT) specimens with respect to the ASTM D5766 test standard [76]. According to this standard, the ratio between the hole diameter and the width of the specimen should be 6. Generally the specimen width and the hole diameter are recommended to be 36 mm and 6 mm respectively [76]. The specimen size is not strictly emphasized in the standard but the ratio between the hole diameter and the specimen width should be assured.

Circular central holes should be opened in the middle of the test specimens, after cutting the specimens in desired sizes as described in section 2.2.1. This can be done in various ways such as; using water jet, laser cut or drilling. The last technique is used during this work. It is the most cost-effective technique. Besides, since there are three drilling machines in the machine shop of Mechanical Engineering Department of Boğaziçi University, its accessibility is very easy. However, it is not the gentlest method among all. It can cause fibre breaks and delaminations.

Drilling quality can be affected with drill bit type, and its feed rate and rotational speed of the mandrel during drilling. There are various drill bits made from stainless steel to diamond. Their price can start from 20 TL up to 3000 €. *Sandvik CoroDrill 452 series* [77] are made from carbide and can provide the most optimum solution for composite drilling. Their price varies with respect to the diameter of the drill bit. Smallest one starts from 30 €. It can end up without any damage around hole region if it is used very carefully.

Drill bits from *Sandvik CoroDrill 452 series* [77] are used in this study. The specimen to be drilled is placed onto a wooden base to prevent damage as the drill bit after leaves the specimen. A steel plate containing a hole in the same size with the hole size of the test specimen is placed onto the specimen very carefully. A calliper is used to align the hole of the steel exactly in the middle of the specimen. These three materials are fixed by using C-clamp. Then they are fixed into the clamp table of the drilling machine to prevent vibration during drilling. Hence good quality holes are enhanced at the end of the drilling process. A view during drilling central hole is shown in Figure 2.4.

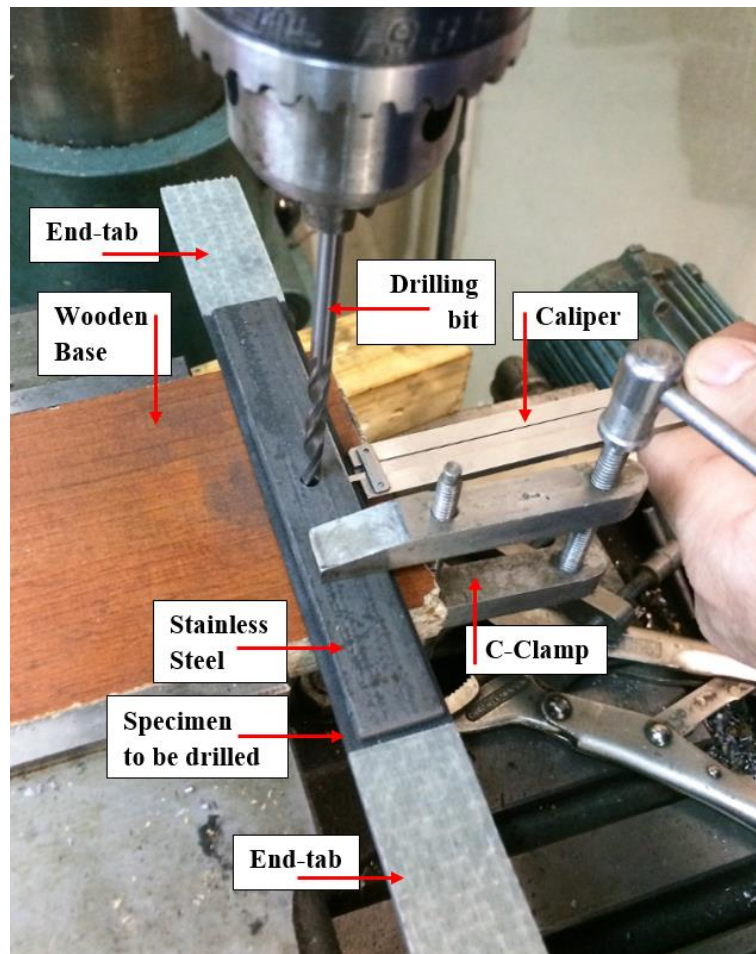


Figure 2.4. Drilling composite test specimens

### 2.2.3. Slit Specimens

In order to stimulate damage and obtain damage modes in desired sequence, some laminates are produced with artificial defects at inner plies. This is applied to UD  $[0]_5$  laminates. Slits are cut to the mid-ply (third ply) of these laminates before lay-up. Two different slit types are incorporated into the specimens in terms of geometry. First one is long slit that is a 5 mm cut. Second type is a short slit which is only 0.5 mm. The procedure given in section 2.2.1 is applied for manufacturing the test specimens. These slits are infused with resin during cure due to resin percolation. Edge micrographs of long and short slit cross-sections are shown with a schematic view in Figure 2.5.

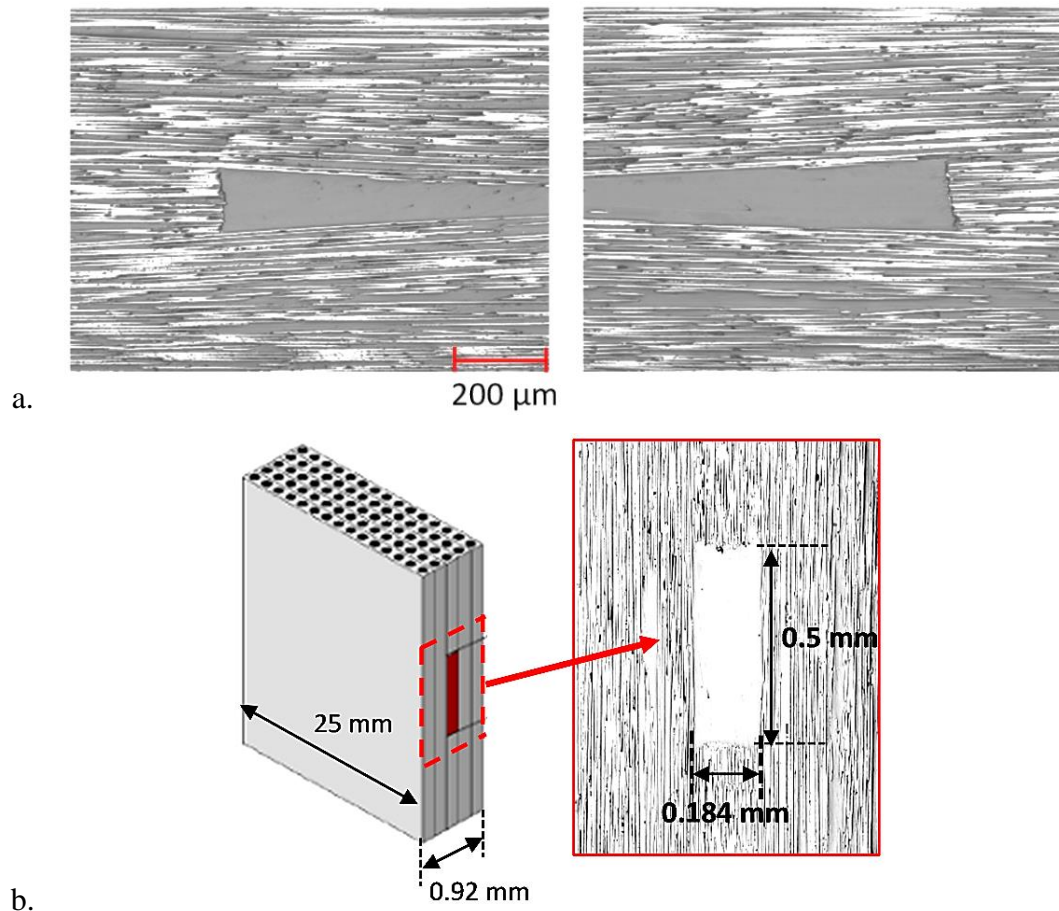


Figure 2.5. Schematic view and micrograph of (a) long-slit (b) short-slit

#### 2.2.4. Grinding and Polishing

In order to apply in-situ edge microscopy for damage tracking or microscopic observations after each tests without cutting a cross-section, the edges of the specimens should be grinded and polished very carefully. It is not easy to grind or polish the whole gauge length of the specimens of 200-250 mm length. Two different methods are applied to grind and polish the specimens. They are classified with respect to the grinding machines used in Boğaziçi University and KU Leuven.

First grinding and polishing operation takes place in metallography laboratory of Boğaziçi University in a METKON grinding machine in this lab. Its turntable has 250 mm

diameter and 10 mm width ring is used to fix the grinding paper and polishing cloth onto the turntable. So, at most, 220 mm long specimens can be grinded and polished with this machine. Only one specimen can be grinded at one time. Aluminum plates are put onto the specimens. They are all fixed with spring clamps. They are held constantly for 4 minutes against the rotating grinding paper and then holding direction is changed and held constantly for another 4 minutes again. This is repeated one more time and grinding of one side is completed. These three steps are repeated for the other edge of the specimen. Movement of the specimens are prevented by holding them carefully because it should not vibrate during grinding and polishing. Otherwise, edges of the specimens can be scratched. Grinding papers with 180 – 320 – 800 – 1200 – 2500 grits are used successively to grind specimens. Afterwards, suspension of 1  $\mu\text{m}$  alumina powder mixed with water is used to polish the specimens. Figure 2.6 shows a photo during grinding a specimen in Boğaziçi University.

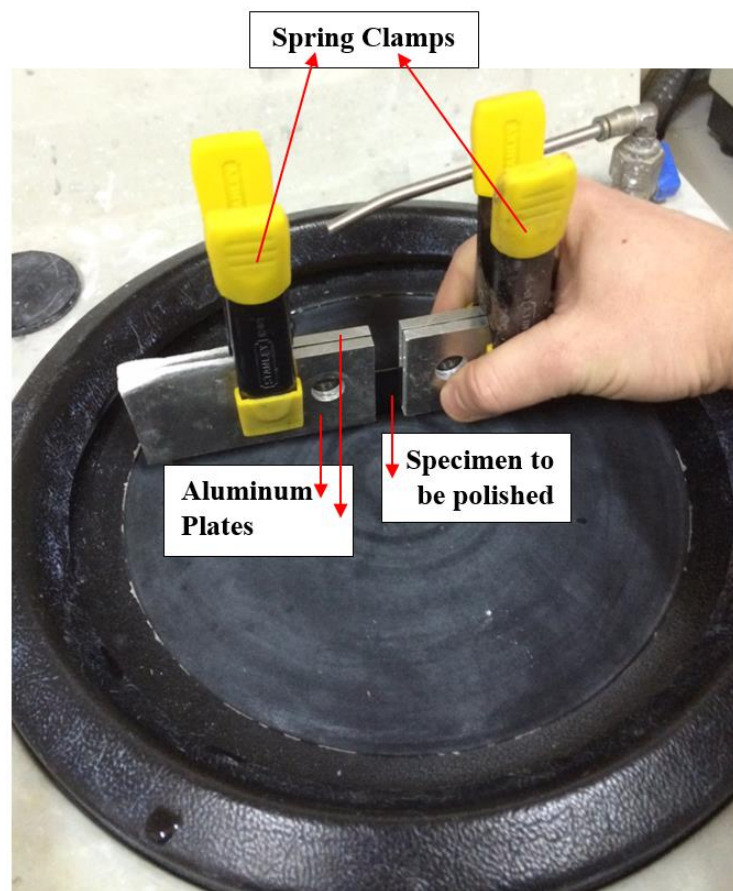


Figure 2.6. Grinding the specimens in Boğaziçi University.

Second grinding and polishing operation takes place in metallography laboratory of Materials Engineering Department in KU Leuven. Grinding and polishing are carried out by using PEDMAX-2 machine whose turntable has 350 mm diameter. Multiple specimens can be grinded and polished at one time by placing them in a metallic box shown in Figure 2.7.(a) They are fixed in the box by using the screws at the sides of the box. Turntable and metallic box rotates at the same time but with different speeds as shown in Figure 2.7.(b). As in previous procedure, grinding papers with 180 – 320 – 800 – 1200 – 2500 grits are used successively to grind specimens. Afterwards, suspension of 1  $\mu\text{m}$  alumina powder mixed with water is used to polish the specimen

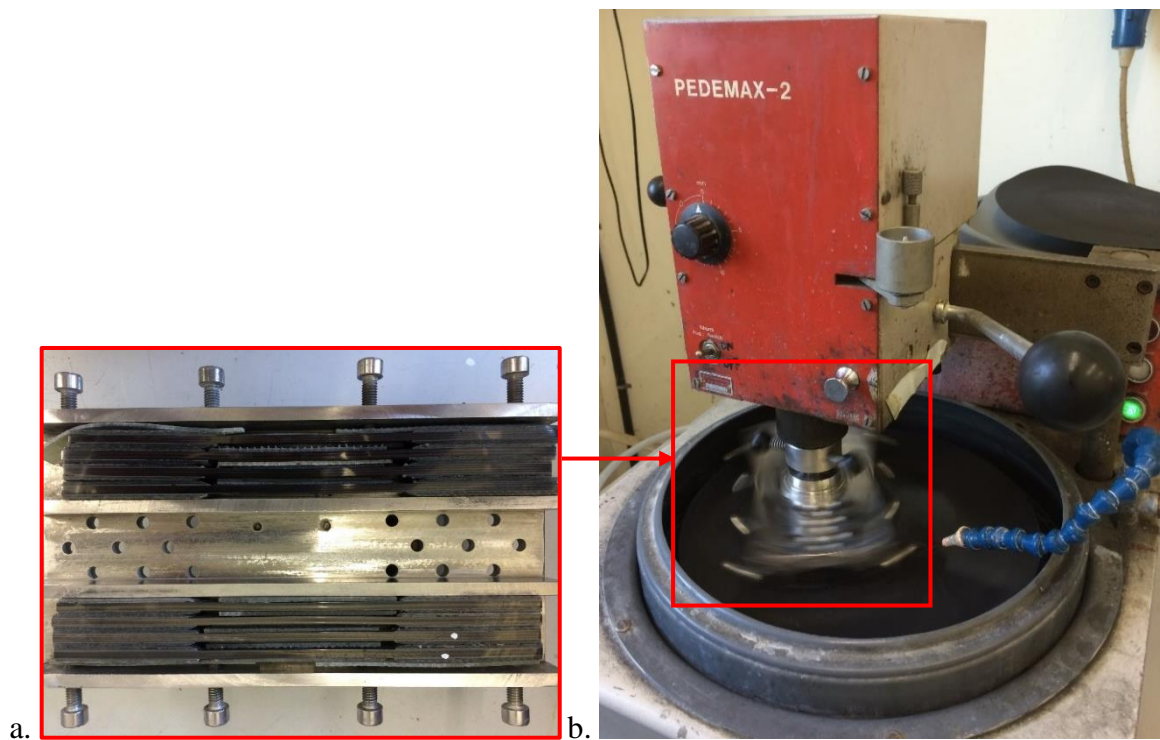


Figure 2.7. (a) Metallic box used to fix specimens constantly (b) Grinding machine in KU Leuven.

### 2.3. Tension Tests

Displacement controlled, uniaxial tension tests with online AE registration are performed. Tension tests of smooth and slit specimens are performed according to ASTM D3039 test standard [75]. OHT tests are performed according to ASTM D5766 test standard [76]. Test rate is selected as 1 mm/min for all tests.

UD specimen configurations are shown in Figure 2.8. Slit specimens are designed to stimulate damage and make damage progression in the order of; matrix cracking, fibre/matrix debonding, delamination and fibre breaks. Tension tests are performed in Mechanical Testing Laboratory of Boğaziçi University Mechanical Engineering Department, using a computer controlled servo-hydraulic Instron 8801 test machine with 100 kN load cell. Bluehill 3.0 software is used to control test parameters. Video extensometer is used to measure deformations in the axial and transverse directions. Five specimens are tested from each group. First two tests of each group end up with final failure. Important stress levels are determined by considering the cumulative AE energy plot together with stress-strain curves. Then interrupted tests are conducted up to predetermined stress levels, lower than the ultimate strength, to three specimens from each group. After each interrupted test, specimens are unloaded and free edges are examined with optical microscope to capture damage, then tested to the next interruption level and so on. This test procedure is actually a “cyclic loading” with “partially in-situ damage detection”. Because tests are stopped after unloading to observe induced damage modes at the end of each cycle. Besides, simultaneous AE recording and optical observations at the end of each cycle provides “partially in-situ damage detection”. Experimental setup can be seen in Figure 2.9. Red light on tension grips and specimens are led-lights of video extensometer. White dots on specimen gauge length are used to define the gauge length for axial and transverse strain calculations. Details of other instruments are given in next sub-sections.

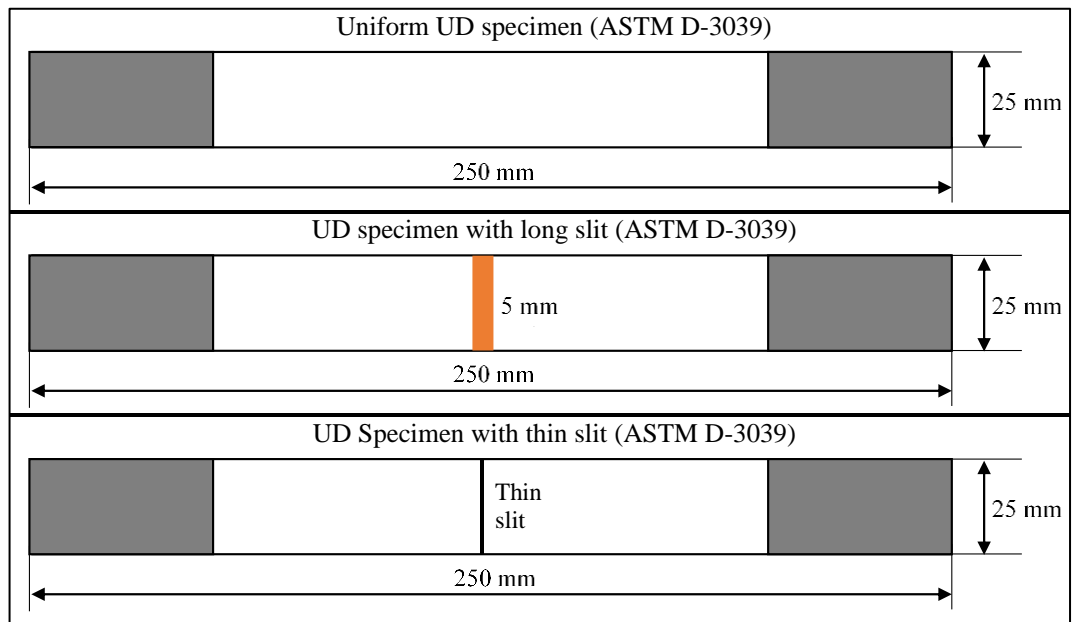


Figure 2.8. UD [0]<sub>5</sub> specimen configurations.

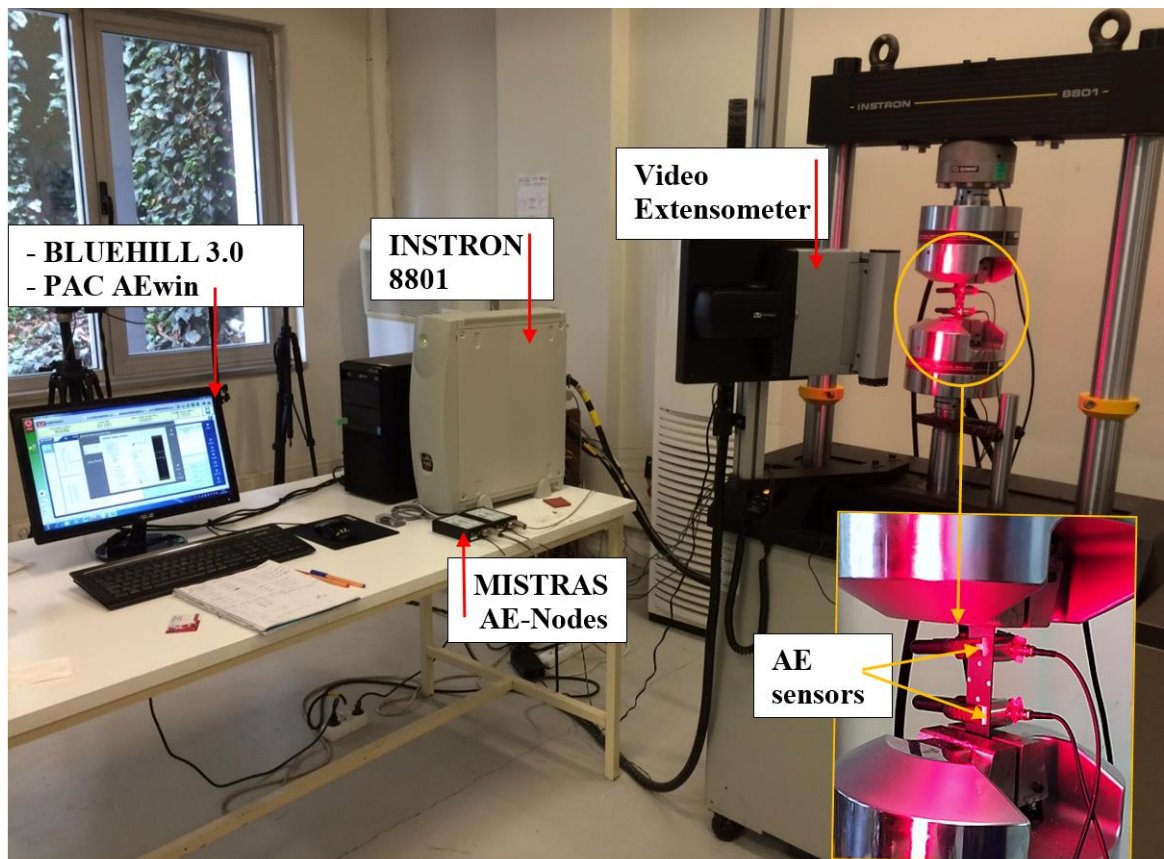


Figure 2.9. Test setup used in Boğaziçi University.

Specimen configurations of QI laminates used in this study are shown in Figure 2.10. Smooth specimens ( $d=0$ ) are designed according to ASTM D3039 [75] whereas specimens containing circular central hole are designed with according to ASTM D5766 [76]. Four different variants of QI laminates are tested as given in Table 2.2. They are thick plied laminates that consist of double inner plies which are named as ply-level scaled specimens [78]. Tension tests are performed at KU Leuven with electro-mechanical Instron 4505 test machine. Extensometry measurement is done optically with DIC technique by using VIC 2D software. Micro damage development on the specimen edges is observed with a second camera having high magnification lens. The experimental setup is shown in Figure 2.11. Details of each instrumentation technique are given in further subsections.

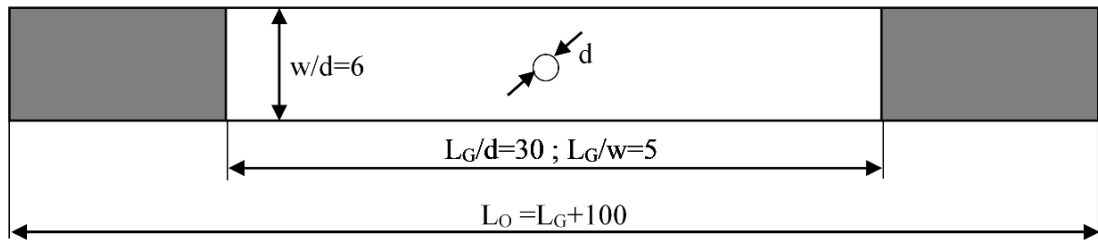


Figure 2.10. Specimen configurations of QI laminates.

Table 2.2. QI laminates

w/d=6 L <sub>G</sub> /d=30	Ply-Level Scaling		
		Hole Diameter, d (mm)	
t (mm)		0	2.5
3	[+45 <sub>2</sub> /90 <sub>2</sub> /-45 <sub>2</sub> /0 <sub>2</sub> ] <sub>s</sub> [90 <sub>2</sub> /-45 <sub>2</sub> /0 <sub>2</sub> /+45 <sub>2</sub> ] <sub>s</sub> [-45 <sub>2</sub> /0 <sub>2</sub> /+45 <sub>2</sub> /90 <sub>2</sub> ] <sub>s</sub> [0 <sub>2</sub> /+45 <sub>2</sub> /90 <sub>2</sub> /-45 <sub>2</sub> ] <sub>s</sub>	w/t=5 L <sub>G</sub> /t=25	w/t=5 L <sub>G</sub> /t=25 t/d=1.2

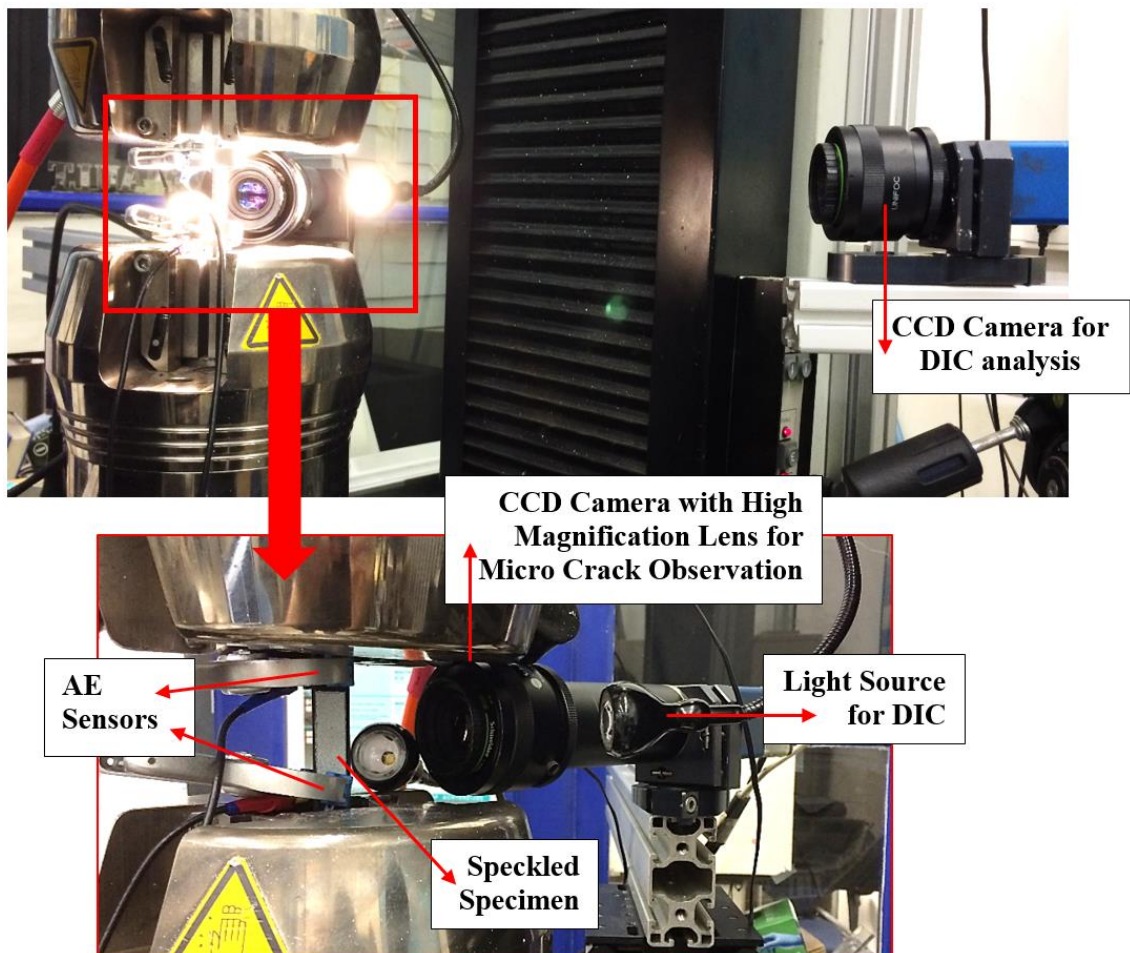


Figure 2.11. Test setup used in KU Leuven.

## 2.4. Acoustic Emission

Acoustic emission (AE) registration is a useful methodology, which allows “hearing” and identifying damage. An acoustic emission signal is an ultrasonic wave resulting from the sudden release of strain energy when damage happens. When critical stress values are exceeded in a material, it fails locally (on microscale) and the strain energy stored is suddenly released inducing mechanical stress waves. The energy released in this way can be detected with suitable sensors. The mechanical information picked up from the material is then converted into an electrical signal. Each of these signals contains time and frequency domain information that corresponds to characteristics of a micromechanical event. A schematic of AE technique for damage detection in composite materials and related

parameters are already given in Figure 1.7 and Table 1.2. Two different acoustic emission systems are used in this study. First one is MISTRAS AE node system in Boğaziçi University, and the second one is Vallen AE system in KU Leuven. Both have advantages and disadvantages over each other. MISTRAS AE system in Boğaziçi University consist of portable AE nodes but Vallen in KU Leuven is a very big system and larger space is required for it. On the other hand, location detecting capability of Vallen is much better than MISTRAS. Their specifications are given in this section.

#### **2.4.1. MISTRAS AE System**

During the tension tests of UD [0]<sub>5</sub> specimens, AE signals due to damage in the laminates are detected with a two-channel MISTRAS AE-Node system and PAC AEWIn software [79]. Two resonant type PK15I sensors having 20.6 mm diameter are used [80]. Their operating frequency range is between 100-450 kHz and resonant frequency is 150 kHz. They are highly sensitive for damage modes with low frequency characteristics, such as matrix cracks according to the literature given in Table 1.6. Contact surface of AE sensors are covered with ultrasound coupling gel and they are placed on test specimens with spring clamps as seen in Figure 2.9.

Noise or redundant signals in AE monitoring is one of the most important problem. In order to eliminate background noise from servo-hydraulic INSTRON 8801 test machine during a test, amplitude threshold level is adjusted to 55 dB. However, it is not easy to eliminate all noise signals totally. A second threshold is applied during post-processing of AE signals. This does not guarantee that all noise signals are eliminated, but it is seen that at least reliable signals for damage appears clearly. This post-processed threshold method is keeping only the signals which are recorded by both sensors. If the difference between the time of arrival to both sensors is less than or equal to 1 ms, then it is considered as a signal of a damage.

As shown in next sections, it is seen that damage development in each test is detected when the maximum stress level of previous interruption level is exceeded. AE technique manages to record small amount of damage during short intervals between maximum stresses of the previous cycle and current cycle, which are proved by optical observations after each cycle. Different damage modes initiate at different cycles and it is very easy to

correlate AE parameters with them. So, it can be said that simultaneous AE recording and optical observations at the end of each cycle provides “partially in-situ damage detection”. Single AE parameter classification can be used to group signals for this case. Because they can be easily correlated with observed damage modes.

Stress-strain responses of CFRP  $[0]_n$  specimens are upwardly concave due to two possible reasons; i) fibre waviness within the laminates, ii) non-Hookean behaviour of carbon fibres due to crystallite misorientations [81–83]. Catastrophic failure due to fibre breaks are assumed to be the only damage mode in  $[0]_n$  laminates. Presence of matrix damage, fibre/matrix splitting or delaminations during tension tests of  $[0]_n$  laminates is still a mystery. Even if they happen, it is not possible to detect from stress-strain curve since elastic modulus continues to increase up to final failure. AE registration can enable to make interpretations but optical observations can provide correlation between damage modes and AE characteristics. In this study, it is seen that application of both techniques to  $[0]_5$  laminates with artificial defect slit regions, enables to detect damage modes in pre-determined order and their AE correlations accurately for  $[0]_n$  specimens. That explains why both techniques (optical observations and AE registration) are used simultaneously for different  $[0]_5$  laminates in this study.

#### **2.4.2. VALLEN AE System**

During tension tests of QI laminates in Table 2.2, it is seen that larger AE sensors cannot be used for smaller specimens reliably. Too much noise signals are registered and it is not easy to remove these signals properly. Smaller sensors provide more reliable emissions of damage modes. Vallen AE system with Vallen AMSY-4 software, shown in Figure 2.12, is used to detect damage during tension tests of QI laminates. Two broadband Digital Wave B-1025 AE sensors, having 10 mm diameter, are used for detection. Frequency range of these sensors is 25-1600 kHz. Two filters are applied for AE registration. First one is amplitude threshold level. Since the test machine is not hydraulic, a lower amplitude level is sufficient to eliminate possible noise signals in electro-mechanical test machine. AE events having amplitude lower than 40 dB are filtered out. Second one is a location filter. AE sensors are placed 50 mm away from each other and only the events between and at least 5 mm away from each sensor are recorded.

One very important advantage of using Vallen AE system is its ability for localization of AE activity. Localisation of AE activity in one dimension is described in Figure 2.13. Wave speed of the elastic stress in the medium along longitudinal direction is represented with  $V$  in Equation 3. First sensor picks up the wave at time  $t_1$  and second sensor at  $t_2$ . Then the location of AE activity can be calculated by using Equation 5 in which  $\Delta t$  is the difference between  $t_2$  and  $t_1$ . In order to calibrate the real location of damage with AE detection, pencil lead break test is done before the tests. Mechanical pencil lead tip with dimension of 0.5 mm diameter and 3 mm length is broken at different locations on specimen surface. It is seen that pencil lead breaks have at least 80 db amplitude but there is about 1-2 mm discrepancy between the real location of the lead break and the corresponding AE event position.

AE signal classification is not done with respect to a single AE parameter for the results of this AE system since the damage mechanisms are very complex in QI laminates. In order to find similar AE signals and group them, an unsupervised pattern recognition technique is applied to the recorded AE signals. Its details are given in the next subsection.

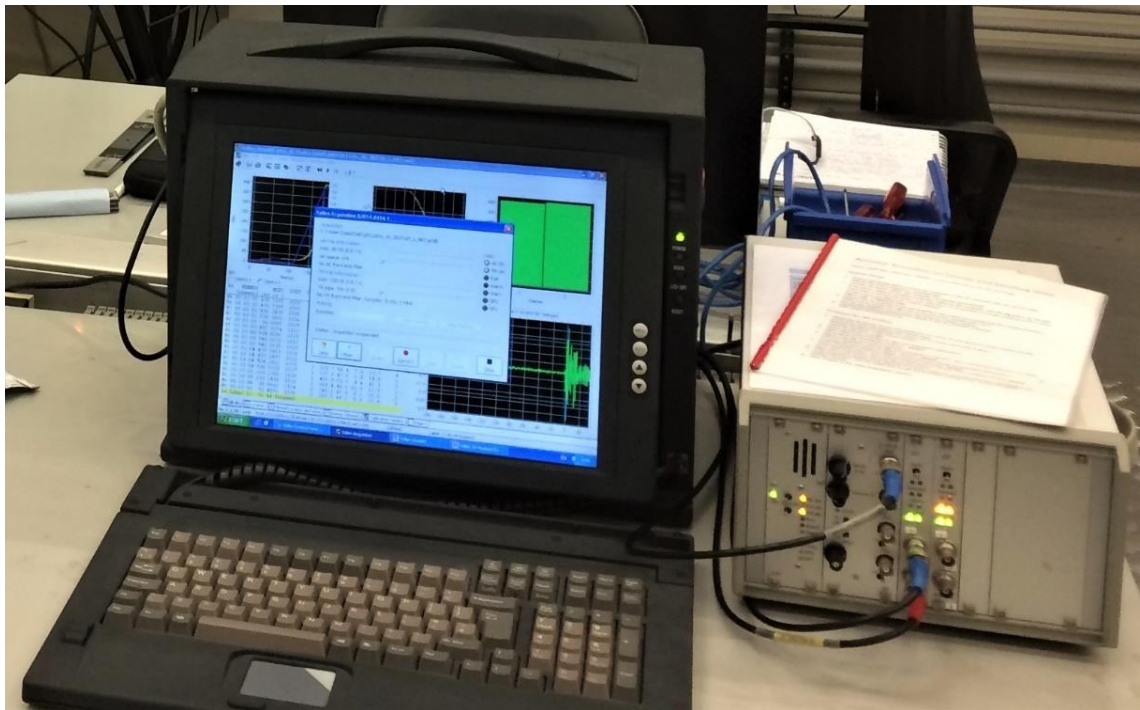


Figure 2.12. Vallen AE system

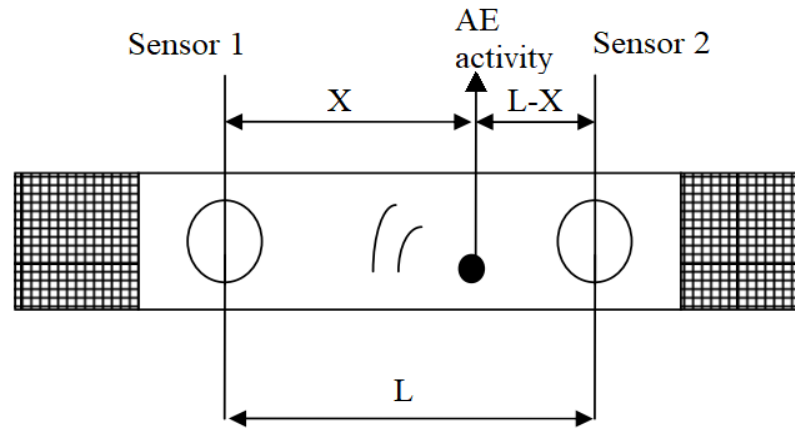


Figure 2.13. Localization of AE activity [84].

$$X = V \cdot t_1 \quad (3)$$

$$L - X = V \cdot t_2 \quad (4)$$

$$X = \frac{L - (V \cdot \Delta t)}{2} \quad (5)$$

#### 2.4.3. The k-means++ Clustering Algorithm.

In order to find similarities between the recorded AE signals and classify them properly to correlate with the damage modes, clustering algorithms are used. The k-means++ clustering algorithm is used in this study. It was developed by Li *et al.* and its efficient performance for transverse cracking was proven with woven GFRP and CFRP composites [57–59, 70]. It is turned out to be sufficient for effective cluster segregation in this work.

Nine features are identified for each AE event: Amplitude (A), Duration (D), Rise time (R), Energy (E), logarithmic value of Energy ( $\log E$ ), peak frequency (P-FRQ) and frequency centroid of gravity (FRQ-C), Rise Amplitude (RA) and Weighted Peak Frequency (WF). RA shows the reciprocal of gradient in AE signal waveform, its value is calculated by dividing rise time to amplitude. WF was first introduced by Sause *et al.* [52] to improve the representative characteristics of frequency associated with an acoustic emission signal combining the discriminative efficiency of the P-FRQ with the information on the average

frequency content of the signal expressed by the FRQ-C. Its value is geometric mean of P-FRQ and FRQ-C. Calculation of RA and WF are already shown with Equation 1 and Equation 2 in Section 1.1.

First step in this clustering algorithm is choosing the relevant features that are statistically representative. Laplacian score of the AE parameters are attained with a value between 0-1. A higher score means a more selective feature for clustering. Correlation coefficient is another parameter, evaluated with Laplacian score to choose relevant features. It shows the dependency of features on each other. If AE features have high Laplacian score and low dependency on other features, then they are selected for the clusters formed by Principal Component Analysis (PCA) and k-means++ algorithm. PCA is an orthogonal linear transformation that transforms multidimensional AE data into lower dimension set with a new coordinate system. The k-means++ is a modified way of choosing centres for the k-means algorithm [57]. It is based on an iterative algorithm where data samples are distributed to the closest centroids. The number of clusters is chosen with respect to two evaluation indices. First one is Silhouette Coefficient which has value between 0-1. Higher Silhouette Coefficient score means dense and well-separated clusters. Second one is Davies-Bouldin index which is based on a ratio within-cluster and between-clusters distances and it relates to the cluster centroids. Combination of higher Silhouette coefficient and lower Davies-Bouldin index means better cluster quality. In order to remind their definitions; Silhouette coefficient is used to measure the similarity of an object to its own cluster, whereas Davies-Bouldin index shows the measure of the validity of the number of clusters with k-means algorithm, whereas

In all the cases studied the clustering algorithm leads to the same configuration of three or four clusters, with the main parameters being the signal amplitude and one of the frequency-related parameters. Keeping in mind that the clusters are segregated in a full set of the AE event parameters, the clusters can be described in four “quadrants” in “amplitude – frequency” plane as “low/high amplitude – low/high frequency” clusters. This is explained Results and Discussion section.

#### 2.4.4. Digital Image Correlation

The main purpose of using Digital Image Correlation (DIC) is measuring local strains during tests. LIMESS DIC system is used for this purpose during the tension tests of QI laminates at KU Leuven. Speckle pattern is sprayed on one surface of the laminates to be used for DIC calculations. Two photos are captured per second by a CCD camera during testing. Acquisition is done with VIC snap software. Resolution of the photos is 1392 x 1040 pixels. VIC 2D software is used for DIC calculations. 27 x 14 mm region of the specimens is selected as Area of Interest (AoI) from a reference image taken at the beginning of the tests. Displacement of the speckles from the AoI is used to calculate deformation during testing by DIC. Subset and step sizes are set to 21 and 4 respectively. In this study, DIC analysis is performed with normalized square differences criterion, optimized 4-tap interpolation and Gaussian subset weights. Finally, Lagrangian strains are computed from the displacements of the speckles. At the end, deformation maps are investigated to identify surface cracks. An example of speckle pattern on specimen gauge length and strain map calculation is shown in Figure 2.14. C-clamps are used to fix AE sensors can be seen on the right side of Figure 2.14. Homogenously distributed speckles can be seen in Figure 2.14.(a). An AoI is selected from the speckled region and  $\epsilon_1$  strain map is shown in Figure 2.14.(b). Colours represent the amount of deformation with respect to the legend shown under Figure 2.14.(b). Moreover, DIC technique can be efficiently used to detect damage on surface plies. Surface cracks on +45° plies can be identified with high strain values (shown with green colour) in Figure 2.14.(b). Interestingly it is found in this study that, macro damage zones such as large delaminations within the laminates can also be determined from 2D full-field deformation maps for some laminate types.

#### 2.4.5. Edge Microscopy

Video extensometer is not sufficient to detect damage at inner plies of smooth and slit [0]<sub>5</sub> specimens. Because of this, damage progression is checked from the free edges of the specimens with optical microscopy at the end of each test. That is a “partially in-situ edge observation” method used to correlate corresponding AE signals with induced damage modes.

Surface DIC is not able capturing micro cracks in inner plies. For this aim, using a third damage detection technique is used and free edge of the specimen is observed directly during tension tests of QI laminates in KU Leuven. A CCD camera with high magnification lens is used to take photos simultaneously with DIC (2 photos per second). This technique enables to focus to a 5 x 3.2 mm frame of one edge of the specimens. The resolution of the image is 1392 x 1040 pixels. This allows capturing matrix cracks, fibre/matrix debonding and delaminations in the inner plies. Figure 2.15 shows a typical edge image with identification of the crack types.

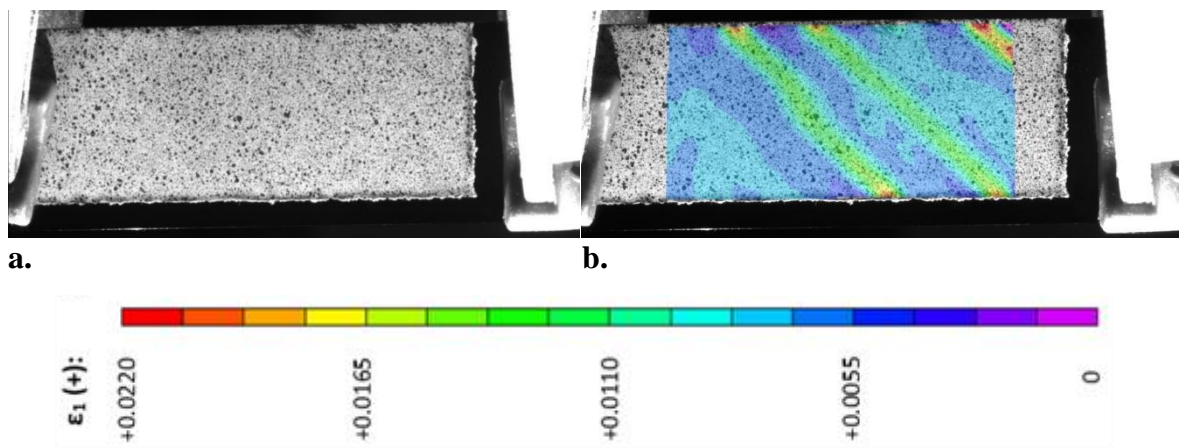


Figure 2.14. (a) Speckle pattern (b)  $\epsilon_1$  strain map calculation in AoI.

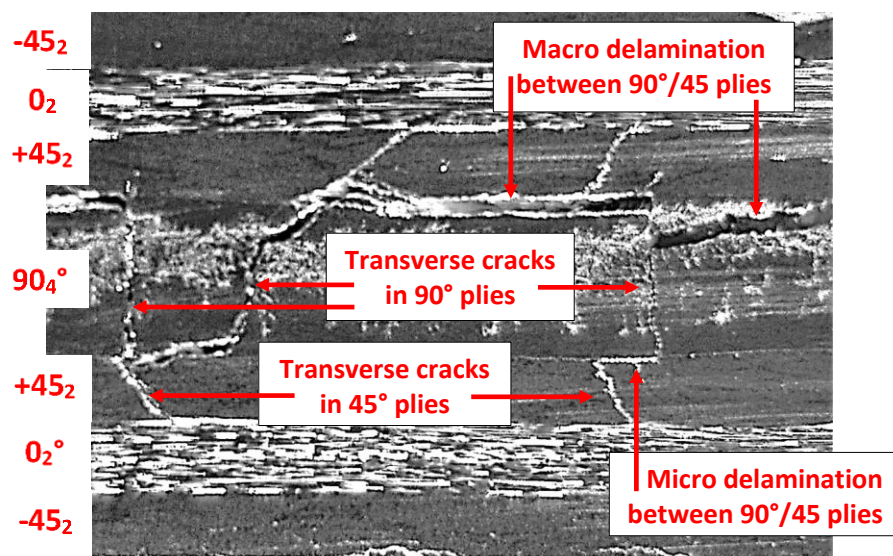


Figure 2.15. Typical edge image from  $[-45_2/0_2/+45_2/90_2]_s$  with certain damage modes.

### 3. RESULTS AND DISCUSSION

#### 3.1. Mechanical Test Results of Unidirectional [0]<sub>5</sub> Laminates

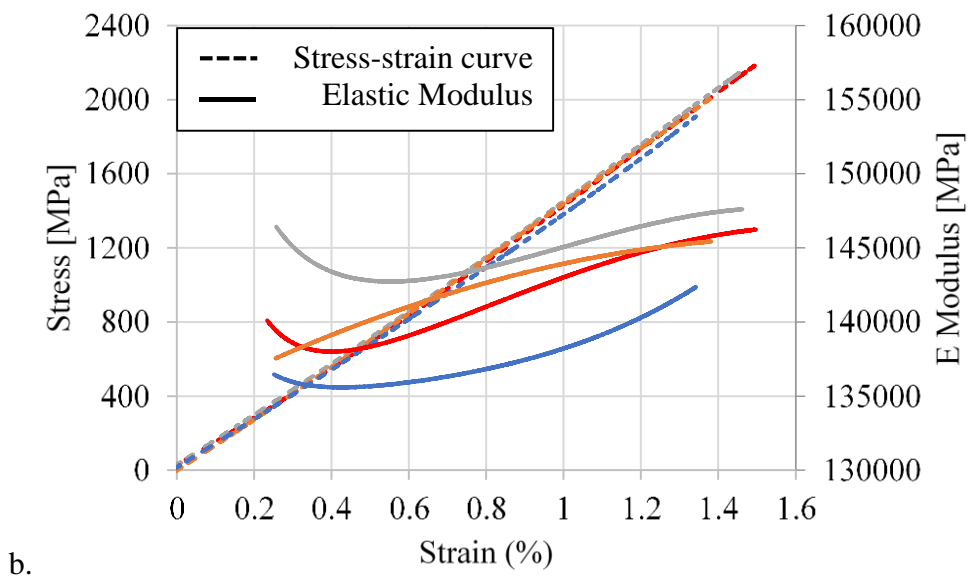
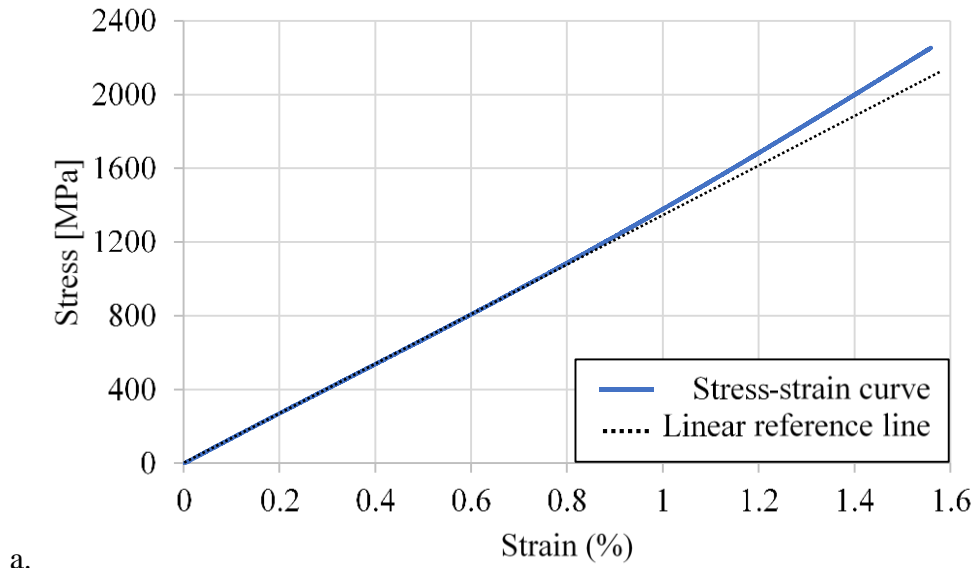
Mechanical test results of UD laminates can be seen in Table 3.1. Test results are compared to FEMM results. There is a very good agreement between elastic moduli and strength values. Total of twenty-four test results (eight interrupted tests for three specimen laminate types in each group) are taken into consideration for Elastic Modulus and Poisson's ratio values, whereas five test results are considered for strength values for each laminate type (two from non-interrupted tests and three from last interrupted tests). Previous loading history in interrupted tests do not cause a considerable change in mechanical properties of laminates. Difference between the strength values obtained from non-interrupted and interrupted tests is very small. Damage induced at the end of interrupted tests cause only a 4% decrease in strength of specimens. It should be mentioned that it is not easy to perform tension tests of [0]<sub>n</sub> laminates up to final failure. It is highly possible that early failures can occur from the grip regions, due to stress concentrations between the grips and gauge ends of end-tabs. Table 3.1 shows that this situation is not experienced in this study. Non-slit [0]<sub>5</sub> laminates are successfully loaded up to the cited strength value (2207 MPa in [72]) in literature as shown in Table 2.1. The effect of slit type on mechanical properties can be seen in Table 3.1. Short slit causes more decrease in elastic modulus and strength which is believed to be due to the higher stress concentration factor at the intersection of resin rich regions and the fibres in specimens.

Table 3.1. Mechanical Test Results for 5-ply UD specimens

Specimen Type	$E_1$ [MPa] (STD %)	$\nu_{12}$ (STD %)	$\sigma_1^T$ [MPa] (STD %)
No slit	144000 (1%)	0.32 (6 %)	2200 (4%)
Long Slit	139000 (2 %)	0.35 (6 %)	1795 (2 %)
Short Slit	137000 (2 %)	0.34 (6 %)	1650 (2 %)
FEMM	142840	0.26	2105

Figure 3.1.(a) shows that the stress-strain curve of non-slit, smooth  $[0]_5$  laminates are upward concave. It means that  $[0]_5$  laminates stiffens with increasing strain throughout the tests as shown in Figure 3.1.(b). Each colour represents a different interrupted test in Figure 3.1.(b). It shows that all of the tension tests are highly consistent with each other and previous loading history in interrupted tests do not cause a considerable change in elastic moduli of laminates. The elastic modulus varies between 135000-148000 MPa and the variation is less than 10 % which means that the results are reliable and consistent. Two reasons can cause such kind of stiffening behavior of UD laminates. First one is misalignment of fibres within the laminates. This does not seem to be the main reason in this study. Because the strength values in Table 3.1 shows that fibres are highly aligned in test direction so that the strength values, cited in data sheet, are obtained successfully. Second reason is non-Hookean behaviour of carbon fibres which consist of crystallites that can be misaligned initially and become aligned in test direction upon application of stress, and this causes the fibres and the laminate to be stiffened with increasing strain [81–83]. This situation is also observed in slit specimens. Figure 3.2 shows the upward concave stress-strain response of a thin-slit  $[0]_5$  specimen with non-Hookean behavior. It is also interesting that elastic moduli values measured from the first three interrupted tests up to 1100 MPa are higher than the subsequent tests. So, it can be said that high amount of damage occurs during the test that is interrupted at 1100 MPa causes elastic modulus to be lower during next tests.

It is not possible to determine the damage threshold levels during uniaxial tension tests of smooth UD laminates by checking the stress-strain curves in Figure 3.1 and Figure 3.2 only, because, there is no indication of any damage in the graphs. In order to find damage thresholds, slit-specimens are tested in which slits are incorporated to stimulate damage sequence to be in the order of; matrix cracking, fibre/matrix debonding, delamination and fibre breaks. However stress-strain curve only is not sufficient to determine damage levels in Figure 3.2. Only the presence of damage is obvious up to 1100 MPa which causes the elastic modulus to be lower during next tests. An in-situ NDT technique should be applied to identify possible damage modes during tension tests.



Stress-strain curves until:	Elastic Modulus until:
--- 1900 MPa	— 1900 MPa
--- 2000 MPa	— 2000 MPa
--- 2160 MPa	— 2160 MPa
--- 2210 MPa	— 2210 MPa

Figure 3.1. (a) Upward concave non-linear stress-strain curve (b) Stress-strain curves and stiffening elastic moduli developments in interrupted tests of smooth  $[0]_5$  laminates.

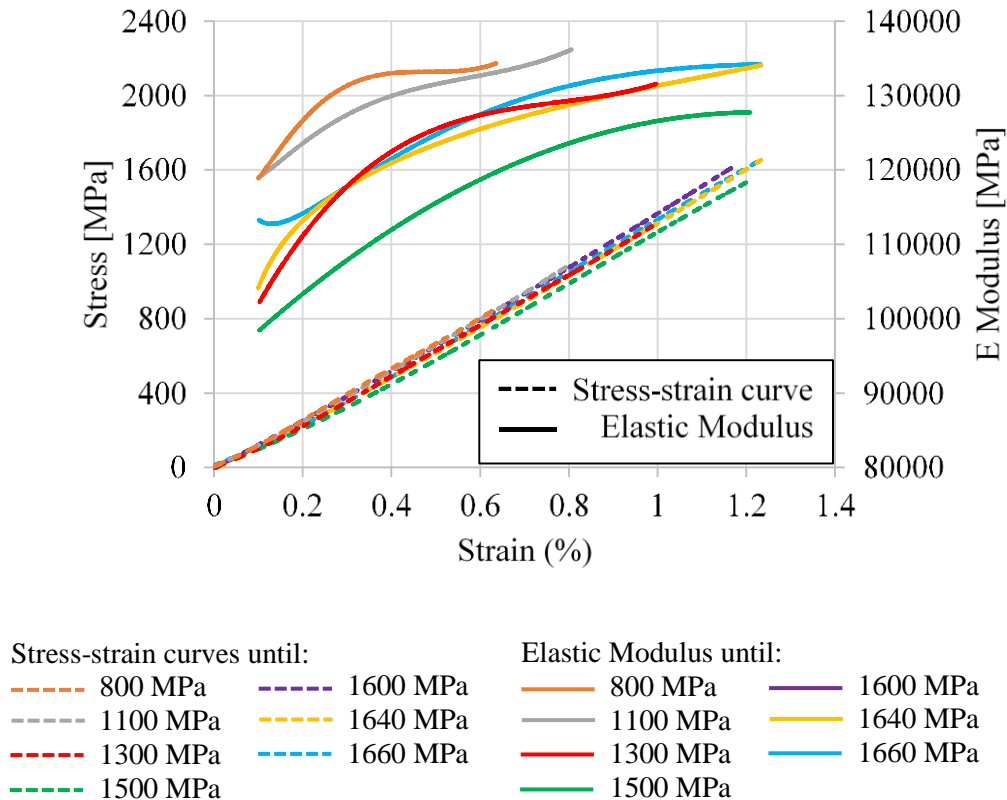


Figure 3.2. Stress-strain curves and stiffening elastic moduli developments in interrupted tests of thin-slit  $[0]_5$  laminates.

### 3.2. Damage Mode Identification in Unidirectional $[0]_5$ Laminates

#### 3.2.1. Long-Slit Specimens

First specimen in consideration is  $[0]_5$  laminates consisting long, 5 mm, resin pocket. In order to determine interruption stress levels, uninterrupted tests up to final failure are performed first. Stress-strain response with cumulative AE energy curve for a long-slit specimen can be seen in Figure 3.3. Interruption stress levels are marked on Figure 3.3. Most of the AE signals are recorded up to 1100 MPa during the test. Three specimens are used for interrupted tests. First interruption levels of three specimens are selected differently as; 600-1000-1400 MPa in order to check the consistency of AE registration and observe the effect of first induced damage on the overall behavior of specimens. It is seen that AE registration

is highly consistent and different interruption levels do not affect the mechanical behaviour of the specimens as explained in later parts of this section. Micrographs in Figure 3.4.(a) are taken from resin rich region of a long slit specimen failed in tension and show different damage modes present at the end of the test. Macro damage mode along the specimen gauge length can be seen in Figure 3.4.(b). It is seen that delaminations initiate from resin rich region, cause the specimen break from a location away from the slit region as shown in Figure 3.4.(b).

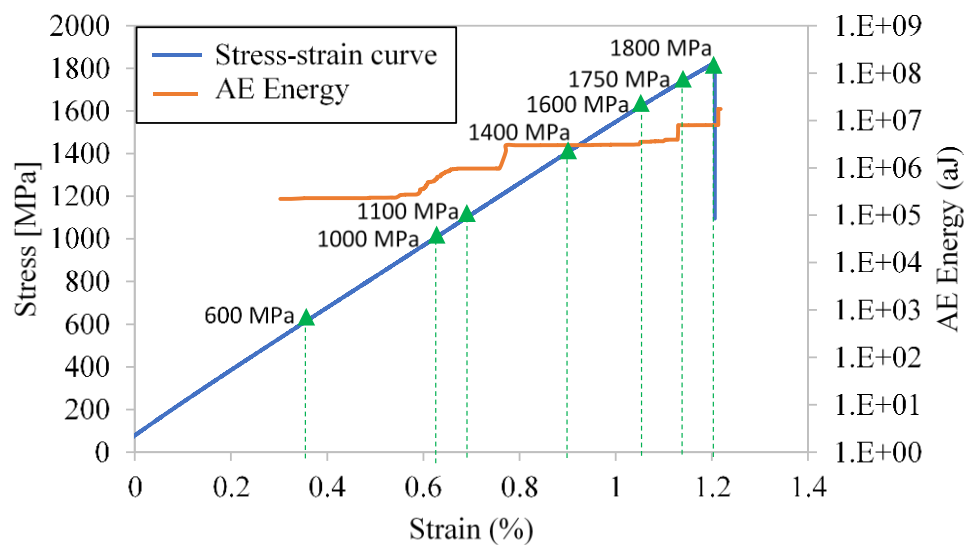


Figure 3.3. Stress-strain curve and cumulative AE energy up to final failure for a long-slit specimen. Interruption levels are indicated

In order to demonstrate the results of each test, stress-strain and AE parameters-strain plots are superimposed. Results of uninterrupted and interrupted tests with respect to different AE parameters (amplitude, duration and peak frequency) are shown in Figure 3.5 and Figure 3.6 respectively. Failure occurs at 1830 MPa during uninterrupted test in Figure 3.5. At the very end of each graph in Figure 3.5 and Figure 3.6, there are some signals shown with light pink colour that are not labelled in legend. As mentioned in subsection 2.4.1, only signals whose difference in time of arrival to each sensor is less than 1 ms is taken into consideration. However, it is seen that at very high stress levels, near to specimen fracture, difference in arrival time of signals to both sensors are mostly between 1 ms and 10 ms, a phenomenon not observed in low stress levels. So, an additional filter is applied to previous

filtering which is: choosing the signals whose difference in time of arrival to each sensor is between 1-10 ms and different from already selected signals. They only appear through the very end of tests when the final fracture is very close, as seen in Figure 3.5 and Figure 3.6. This situation is due to progression of delaminations, causing discontinuity in the specimen and increasing the path for acoustic waves in the specimen.

Each colour in Figure 3.6 represents AE events recorded in different interrupted tests, which are identified according to the interruption stress levels. Interrupted test results for both specimens are very similar to each other and to the uninterrupted test. This shows the consistency between the interrupted tests in Figure 3.6 and uninterrupted test in Figure 3.5. Final test after interruptions was planned to be performed up to 1830 MPa but failure occurred at 1790 MPa and 1765 MPa in Figure 3.6 for the two specimens respectively. Previous damages in interrupted tests caused only 4% decrease in strength which can be considered within experimental error margin. So, it can be said that the tests, done for  $[0]_5$  specimens with long slits, are repeatable and consistent.

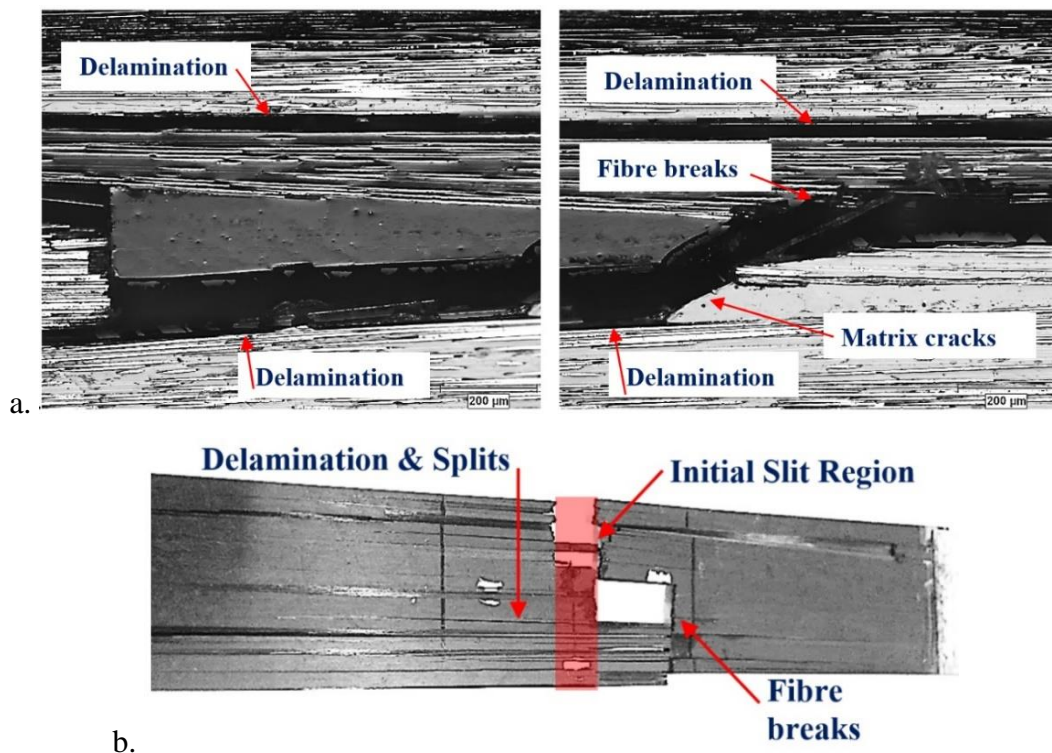


Figure 3.4. (a). Micro damage modes in long-slit specimen at the end of test (b). Macro damage mode on long-slit specimen at final failure.

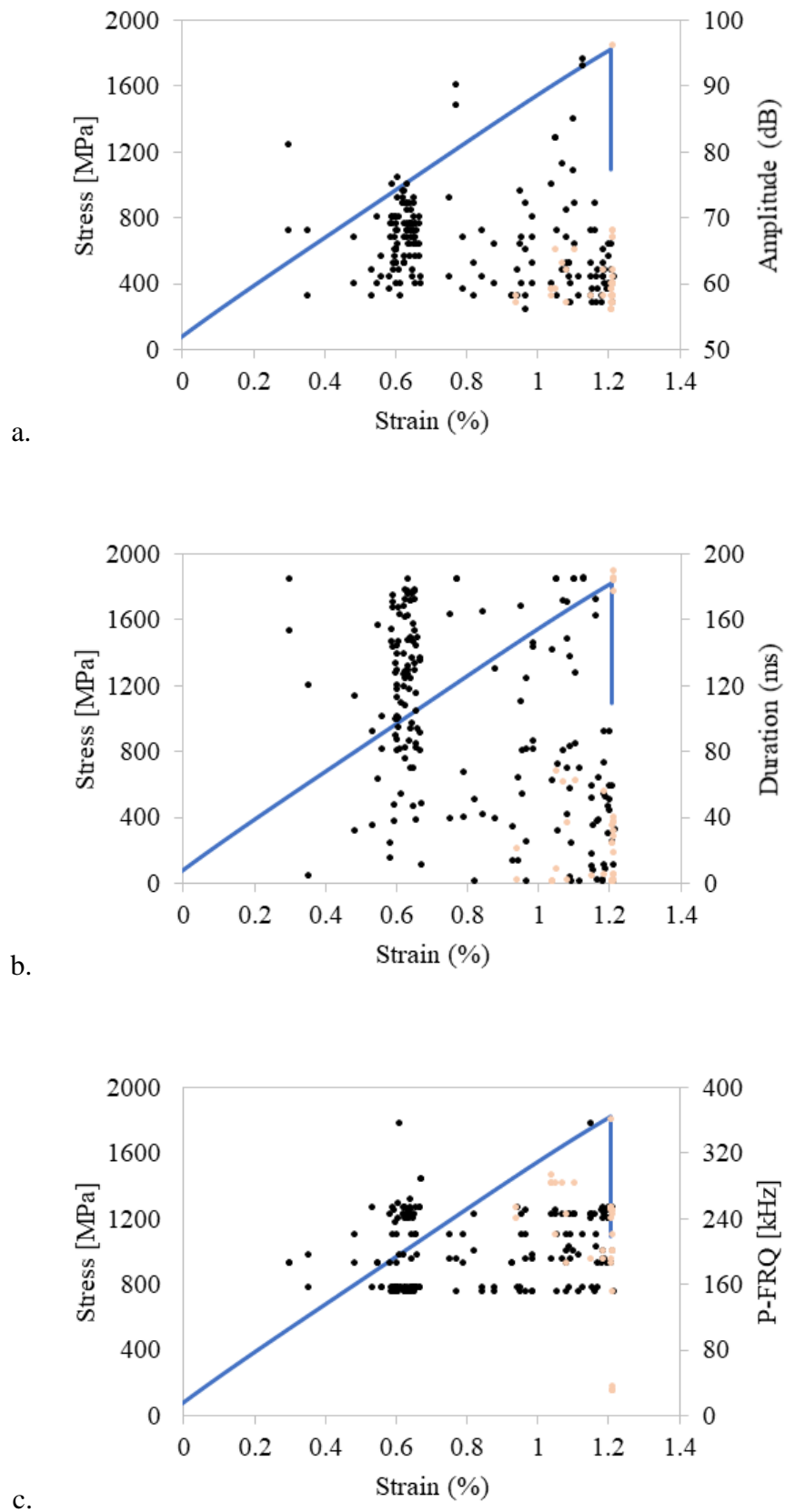


Figure 3.5. Stress-strain curve vs. different AE parameters for an uninterrupted test of a long-slit specimen.

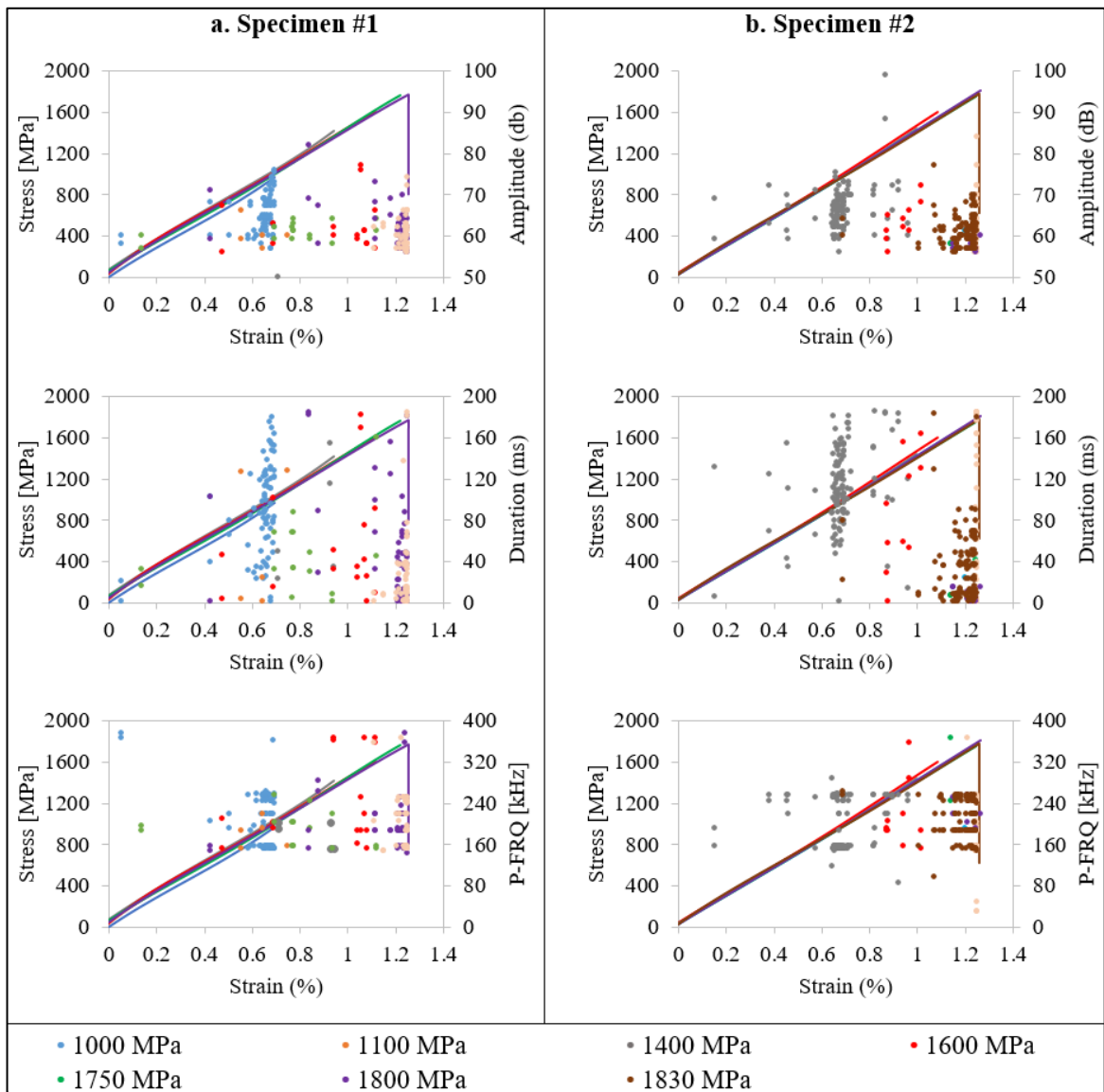


Figure 3.6. Interrupted test results for two different long slit specimens.

At the end of each interruption, specimen edges are observed under optical microscope. Since AE results in Figure 3.5 and Figure 3.6 are very similar, it means that damage evolution within these specimens are similar too. So, damage evolution only within Specimen #1 is presented in Figure 3.7. As mentioned before, the slit length is 5 mm and it is not easy to monitor the whole resin rich region with induced damage in one micrograph and frames of the resin pocket that correspond to three regions in the front and back edges are labelled as 1st, 2nd and 3rd region respectively in Figure 3.7.

The first interruption level is 600 MPa, however no damage was observed from the edges, and no AE signals were detected. Then the same specimen is loaded to 1000 MPa. The first damage modes observed from the edges are matrix crack in resin pocket and matrix cracking at fibre/resin pocket intersection as seen from the 1<sup>st</sup> and 2<sup>nd</sup> regions in Figure 3.7 respectively. This corresponds to signal clusters shown with blue colour for the Specimen #1 in Figure 3.6. Amplitude values for this damage mode is between 60-76 dB where duration is between 60-180 ms and peak frequency values for these signals correspond to four different bands which are around 150-185-210-250 kHz. It is obvious that amplitude and duration values are more selective than peak frequency.

When the specimen is loaded up to 1100 MPa, crack in resin pocket from 1<sup>st</sup> region extends and at the same time very few events are recorded with similar AE parameters in Figure 3.6. When the load is increased to 1400 MPa, matrix crack in 1<sup>st</sup> region reaches the top and bottom of fibres/resin pocket intersection. A new matrix crack can be seen from the 3<sup>rd</sup> region in Figure 3.7 at this stress level. This damage induces at inner portions and extends to the edge during the stress is increasing from 1100 MPa to 1400 MPa. Very few signals are registered for this progression during loading up to 1400 MPa. In previous test, the extension of the damage at fibre-matrix intersection is recorded with lower amplitude and duration. Therefore, it is believed that AE events with amplitude values around 70 dB and duration values greater than 100 ms at around 1390 MPa represent the crack in resin pocket in 3<sup>rd</sup> region in Figure 3.7.

More events are visible when the load is increased to 1600 MPa. After cracks in resin pocket reach to the corner of the resin pocket-fibre intersection, it causes delaminations from the corners of resin pocket. They are shown within box frames in Figure 3.7. These delaminations have low amplitude and duration values. However, there are few events with high amplitude around 75 dB and duration around 180 ms recorded at 1500 MPa. That is the matrix crack initiation from bottom corner section seen in 3<sup>rd</sup> region at 1600 MPa in Figure 3.7. At the end of the last interruption where the specimen is loaded up to 1750 MPa, it is seen that cracks in matrix coalesce and seen in 3<sup>rd</sup> region at 1750 MPa in Figure 3.7. Although, the specimen is loaded up to 1750 MPa, which is higher than previous interruption, evolution of matrix cracking from the bottom corner of fibre-matrix intersection occurs at around 1100 MPa. This is a new damage initiation. Its stress level is consistent

with the level of previously induced same damage mode. On the other hand, no damage can be observed on specimen surface by naked eye up to 1750 MPa.

Finally, the specimen is loaded up to final failure at 1800 MPa (Specimen #1 in Figure 3.6). Through the end of the test, generally AE events with low amplitude (56-67 dB) and low duration (1-80 ms) values are recorded. The number of recorded signals in this final test is higher than signals recorded between 1000-1600 MPa due to increasing number of delaminations through the end of test. These clusters, shown with purple colour in Figure 3.6, are registered due to delaminations within the specimen. They cause discontinuity in the specimen and increase the travel time of signals through the gauge length. Thus, difference between arrival times of the signals shown with pink colour is almost 10 times higher than all other signals in Figure 3.6. In this class, signals with low amplitude and duration are believed to belong to individual fibre breaks. It is not easy to detect them optically. They are most probably occurred at inner sections of test specimen. But the very last events have higher amplitude and duration values than other pink coloured signals. These signals (with amplitude and duration greater than 70 dB and 120 ms respectively) belong to final failure due to breaks of large number of fibres which causes separation of specimen as shown in Figure 3.5.(b). So, by analysing the results of interrupted tests for a long-slit specimen, one can positively say that amplitude and duration values are very high for matrix cracking where the values of these parameters are low for delamination and especially for fibre breaking.

A detailed correlation between the certain damage modes and their AE correspondence is obtained during tension tests of long-slit [0]<sub>5</sub> specimens. Sole application of AE registration would not provide a reliable correlation. However, it is seen that post edge-microscopy provide to detect certain damage modes and correlate them with registered AE signals up to the maximum stress levels of each interruptions. Findings are opposite to the general assumption of previous studies presented in Table 1.6. First of all, high amplitude AE signals are seen to represent matrix cracks and fibre/matrix debonding whereas these damage modes were believed to have low amplitude characteristics as seen in Table 1.6. Besides, it is not easy to distinguish them from each other in terms observation and AE characteristics. Secondly, delamination and fibre breaks are seen to have low amplitude characteristics which were believed to have high amplitude characteristics in literature.

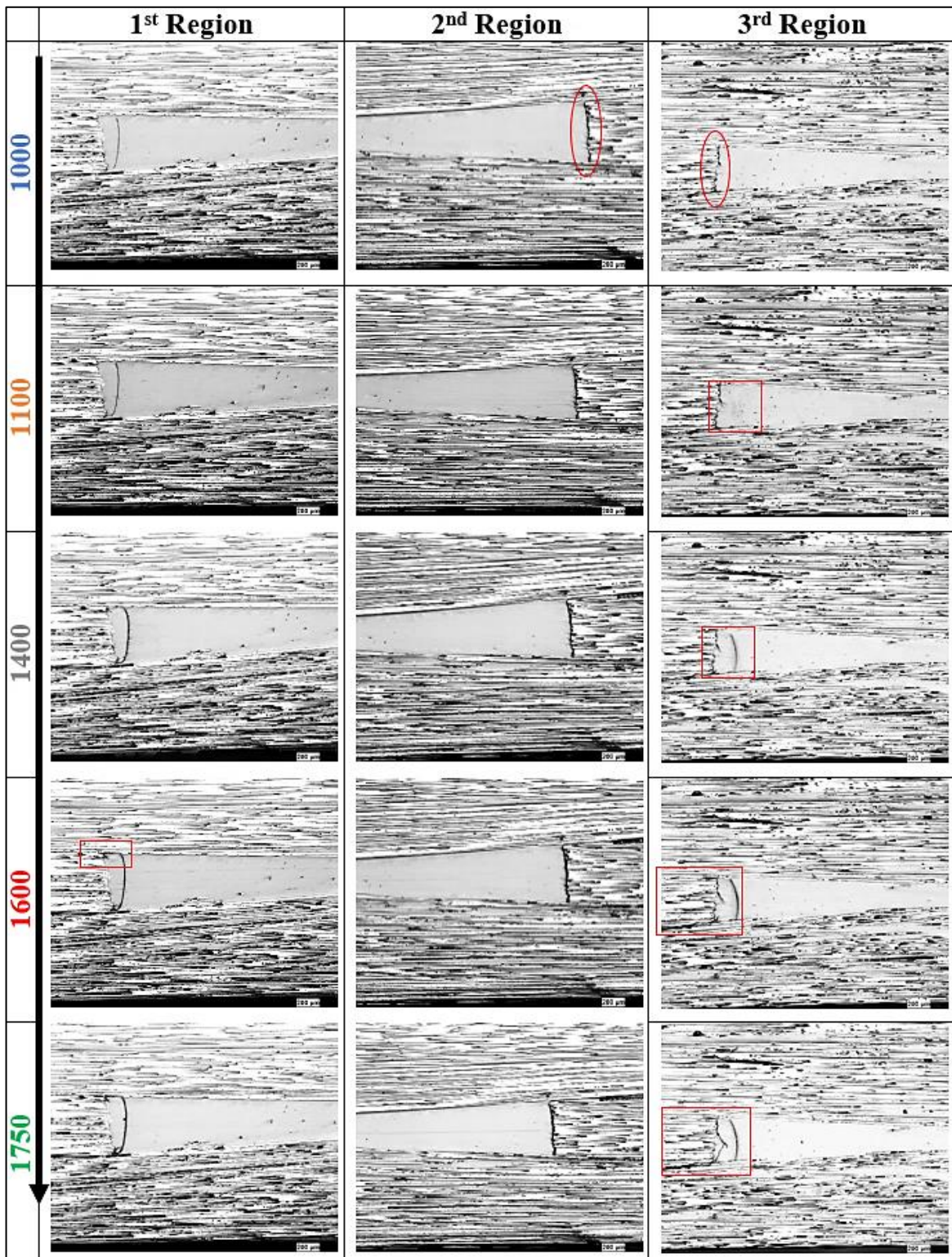


Figure 3.7. Damage progression within long-slit Specimen #1.

### 3.2.2. Short-Slit Specimens

Second specimen type in consideration is  $[0]_5$  laminates with short slit. Stress-strain curve of a short-slit specimen up to final failure is shown together with the cumulative AE energy in Figure 3.8. Interruption stress levels are labelled in Figure 3.8 on stress-strain curve.

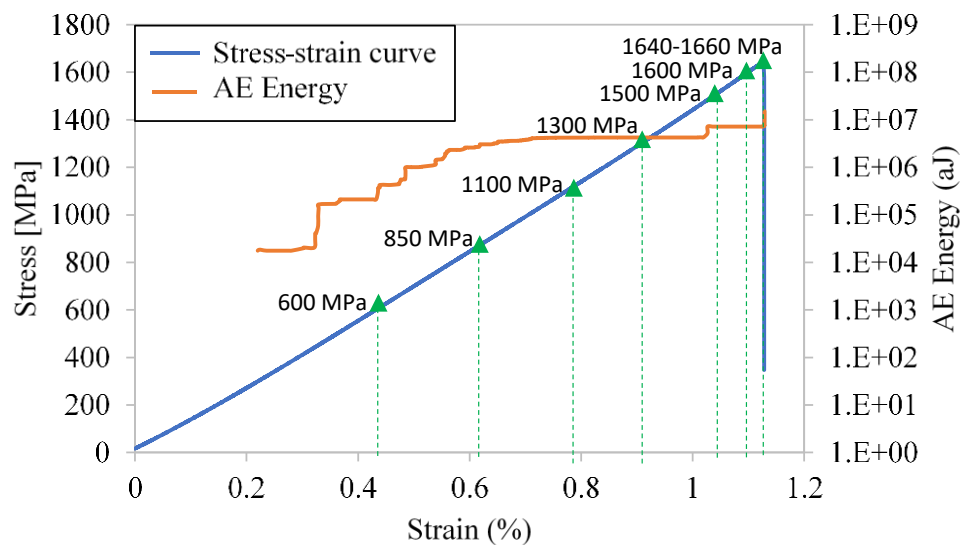


Figure 3.8. Stress-strain curve and cumulative AE energy up to final failure for a short-slit specimen. Interruption levels are indicated.

Test results for short slit specimens are very similar to long slit specimens and test results for only one specimen are presented in detail here. All interrupted tests are consistent with each other. This can be seen from the stress-strain response and elastic modulus diagrams in Figure 3.2. Figure 3.9 and Figure 3.10 show test results and micrographs of damage evolution through the test respectively. Since slit in these specimens is short, the whole resin pocket and induced damage can be clearly seen within a single frame. Micrographs of resin rich regions from opposite edges of the specimen are labelled as 1<sup>st</sup> region and 2<sup>nd</sup> region in Figure 3.10.

In Figure 3.9, a cluster of signals shown with grey colour appeared between 800-1000 MPa. It corresponds to matrix crack and fibre/matrix debonding at fibre/resin pocket intersections. This can be noticed by comparing the circled regions in “*INITIAL*” and “*1100*” rows in Figure 3.10. AE characteristics of this damage mode are similar to previous specimens. Amplitude range of recorded signals is between 60-80 dB, where the duration of signals is mostly between 60-190 ms. It is not possible to find a characteristic range for peak frequency values for this damage mode as those for long slit specimens. There are signals before 700 MPa but they are redundant signals and do not correspond to any damage. Reducing the width of the slit stimulates damage initiation and reduces the stress level of first damage from 900 MPa to around 750 MPa, possibly because of the increase in the constraints of the resin pocket which increases the triaxiality of the stresses as well as residual stresses at the resin pocket. Damage size increases at the end of the second interruption. Its signature in terms of AE features is the signals at 1200 MPa shown with red colour in Figure 3.9. Even though there are signals, shown with red colour at 700 MPa, they are noise signals and do not correspond to any damage. AE signals recorded due to damage are the ones after 1100 MPa in this test. At the end of the interruption at 1550 MPa, it is seen that AE signals having very low amplitude and duration values are started to be recorded. These signals, shown with green colour in Figure 3.9, are mostly due to delamination initiations as highlighted in Figure 3.10. At the end of the next interrupted test with a maximum stress of 1600 MPa, delaminations at the corners of resin rich regions propagate and become more visible in micrographs as pointed out in Figure 3.10. AE characteristics of these signals are low amplitude with low duration.

Final failure happens at 1650 MPa in last test. Many AE signals are recorded with low amplitude and duration characteristics. Delaminations cause a discontinuity as in long-slit specimens and travel time of the signal increases. AE signals recorded after this change are shown with pink colour in Figure 3.10. These AE signals having low amplitude and duration values correspond to individual fibre breaks. Signals with amplitude level greater than 70 dB and duration greater than 100 ms belong to final failure of specimen with separation of large numbers of fibres with resin. Final failure mode of the specimen can be seen in Figure 3.11. Micro matrix cracks cause micro delaminations which evolve and grow to visible size. Then macro delaminations occur and break the specimen from a region away from the slit-region as shown in Figure 3.11.

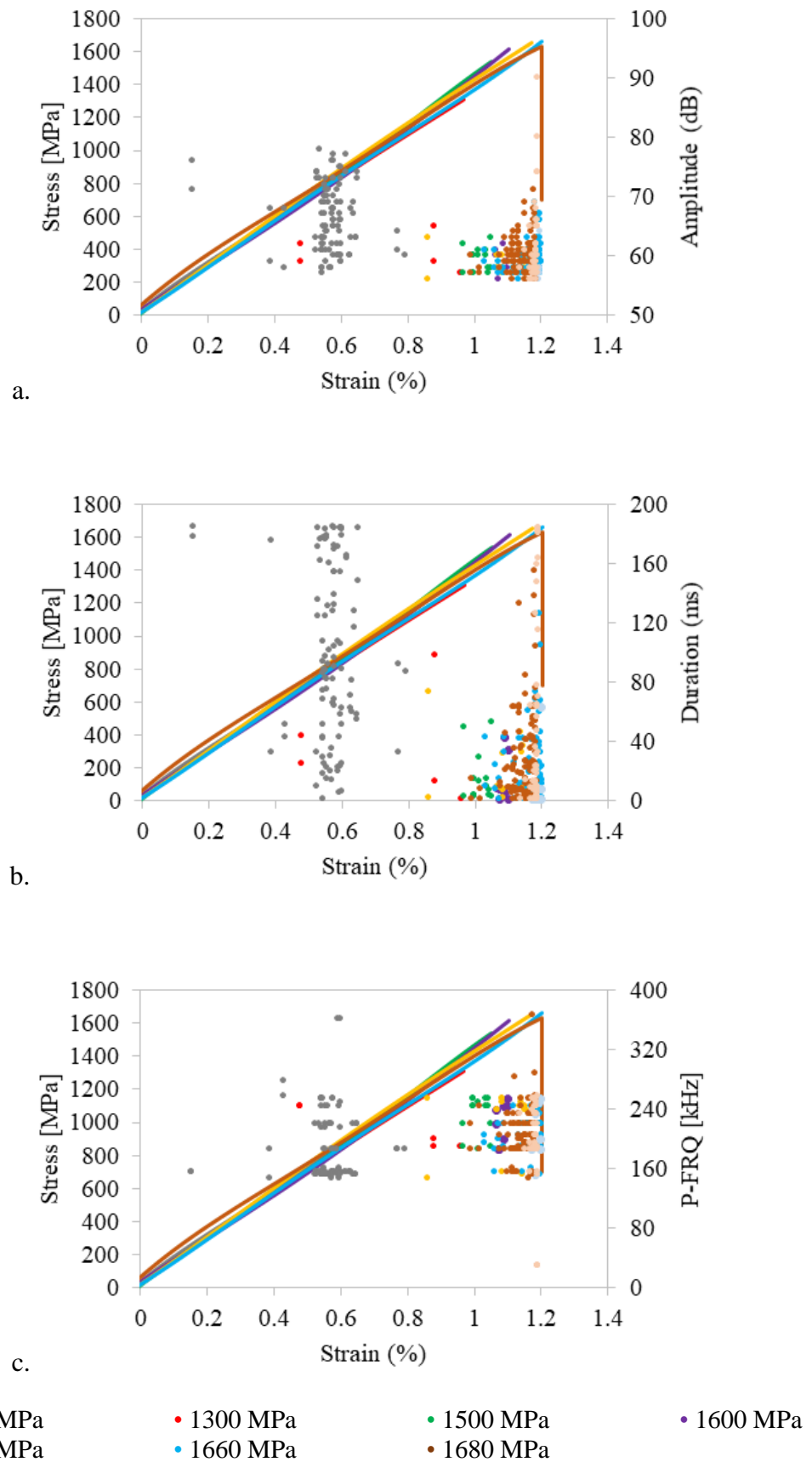


Figure 3.9. Interrupted test results for a short-slit specimen.

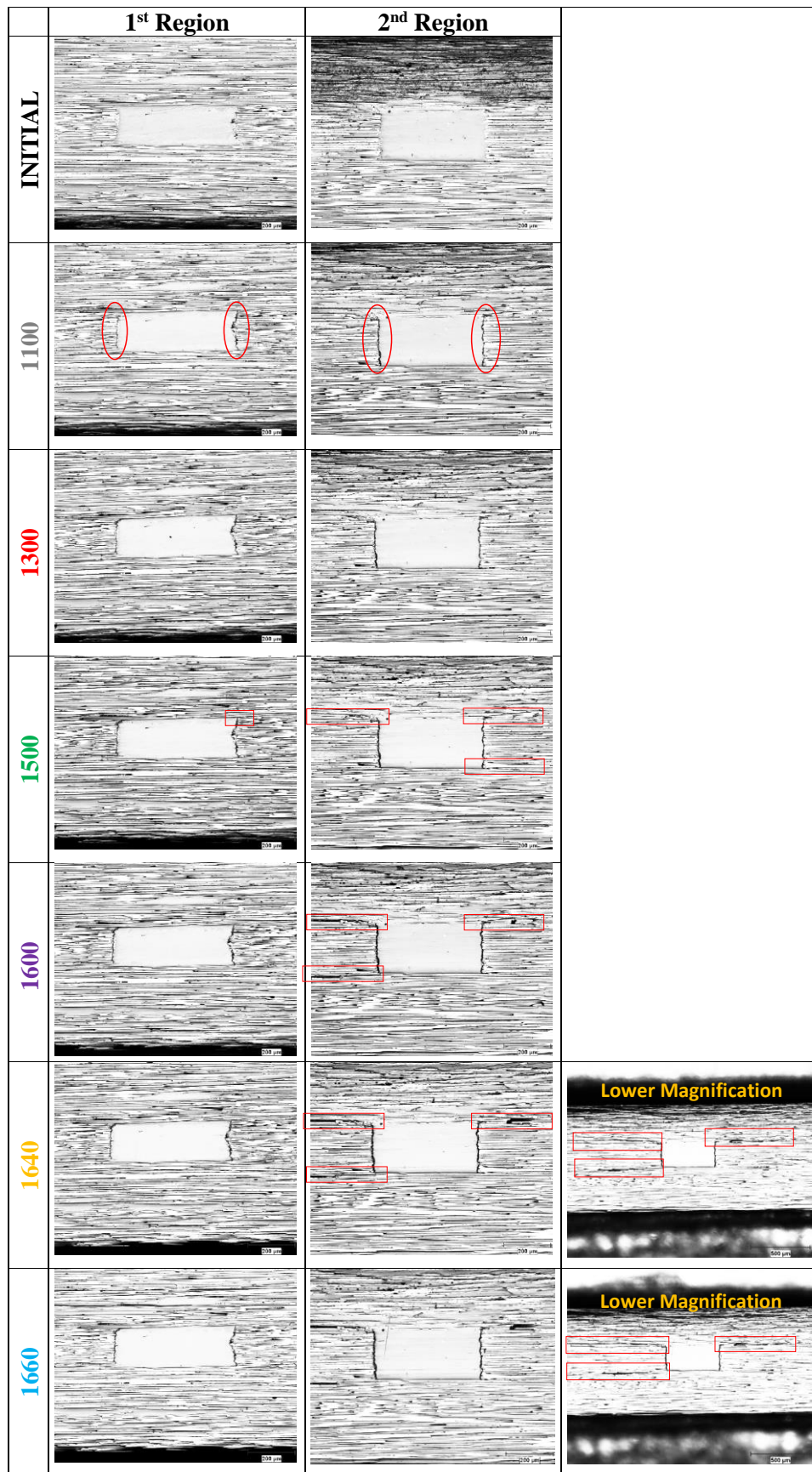


Figure 3.10. Damage progression in short-slit specimen.

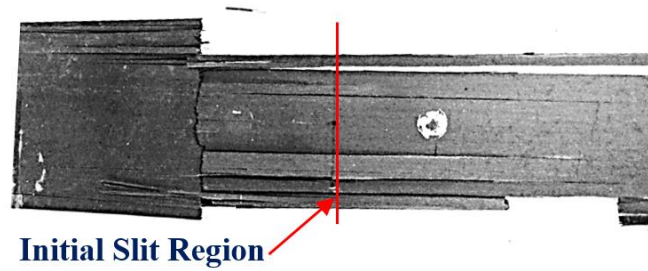


Figure 3.11. Macro damage mode on short-slit specimen at final failure.

### 3.2.3. Smooth Specimens

Third specimen type in consideration is non-slit, smooth  $[0]_5$  laminates. Stress-strain response of a non-slit  $[0]_5$  specimen up to final failure is shown with the cumulative AE energy curve in Figure 3.12. Interruption levels are marked on stress-strain curve.

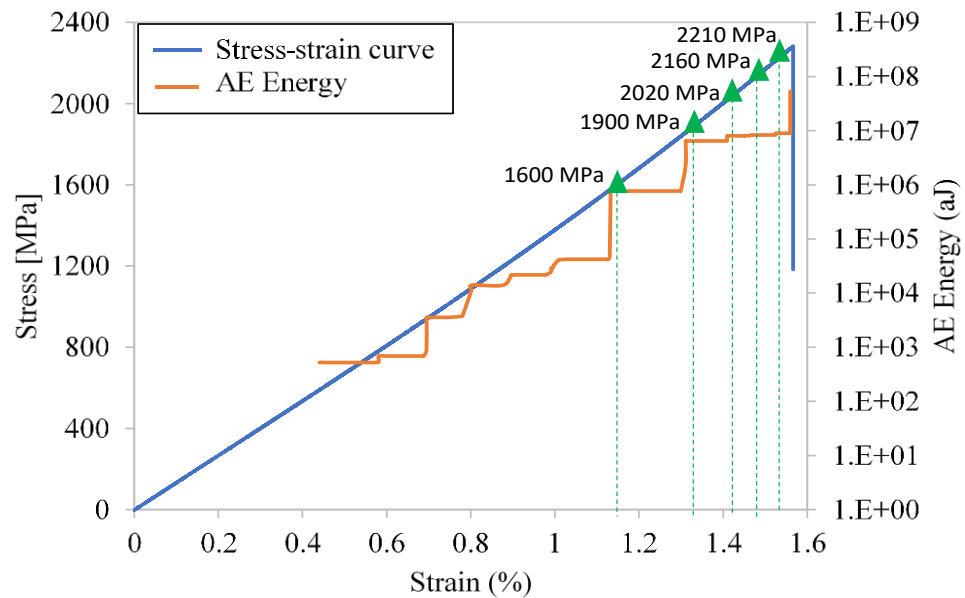


Figure 3.12. Stress-strain curve and cumulative AE energy up to final failure for a smooth  $[0]_5$  specimen. Interruption levels are indicated.

It is seen that matrix damage at fibre-matrix intersection in resin-rich region occurs in 750 MPa and 900 MPa for short and long-slit specimens respectively. AE characteristics of damage modes are found clearly and correlation between them is done by using micrographs. With respect to these results it is expected to see similar AE characteristics for certain damage modes if they exist in smooth UD specimens. Figure 3.13 shows the interrupted test results for two  $[0]_5$  specimens. Specimen #1 is not failed at the end of the tests but Specimen #2 is failed at 2210 MPa. It is not easy to detect a damage in  $[0]_5$  non-slit specimens since damage does not localize in specific positions and the whole edge of the specimen should be investigated under optical microscope. No damage was observed up to 1600 MPa. The expected initial damage mode was matrix cracking but it couldn't be detected easily as in slit-specimens. Damage is started to be detected after 1900 MPa. Some examples are presented in Figure 3.14. First matrix cracks and fibre/matrix debonding seen in Figure 3.14.(a) are detected at the end of 1900 MPa in Specimen #1. Then individual fibre breaks within Specimen #1 detected after 2000 MPa are shown in Figure 3.14.(b). Individual fibre breaks with breakage of clusters of fibres in Specimen #2 in the end are shown in Figure 3.14.(c). AE characteristics of these damage modes cannot be determined without difficulty as in slit-specimens since AE parameters are not well-distinguished. Low amplitude and low duration signals represent fibre breaks through the end of tests in slit-specimens. According to this finding, low amplitude – low duration signals recorded during loading to 2020 MPa and after this test in Figure 3.13 agree with the statement for fibre breaks in slit-specimens. In addition to this, high amplitude, high duration signals at the end of the last test of Specimen #2 (shown with pink color in Figure 3.13) represent the breakage of fibre clusters.

Although there are numerous individual fibre breaks induced at the same time as seen from the micrograph shown in Figure 3.14.(b) and Figure 3.14.(c), AE results in Figure 3.13, show that there are very few signals recorded through the end of the test where the specimen is loaded up to 2020 MPa or higher. So, it can be said that acoustic emission technique cannot be used to detect fibre breaks successively. Different techniques with higher sensitivity and resolution can be used to detect fibre breaks such as synchrotron X-ray tomography [85, 86].

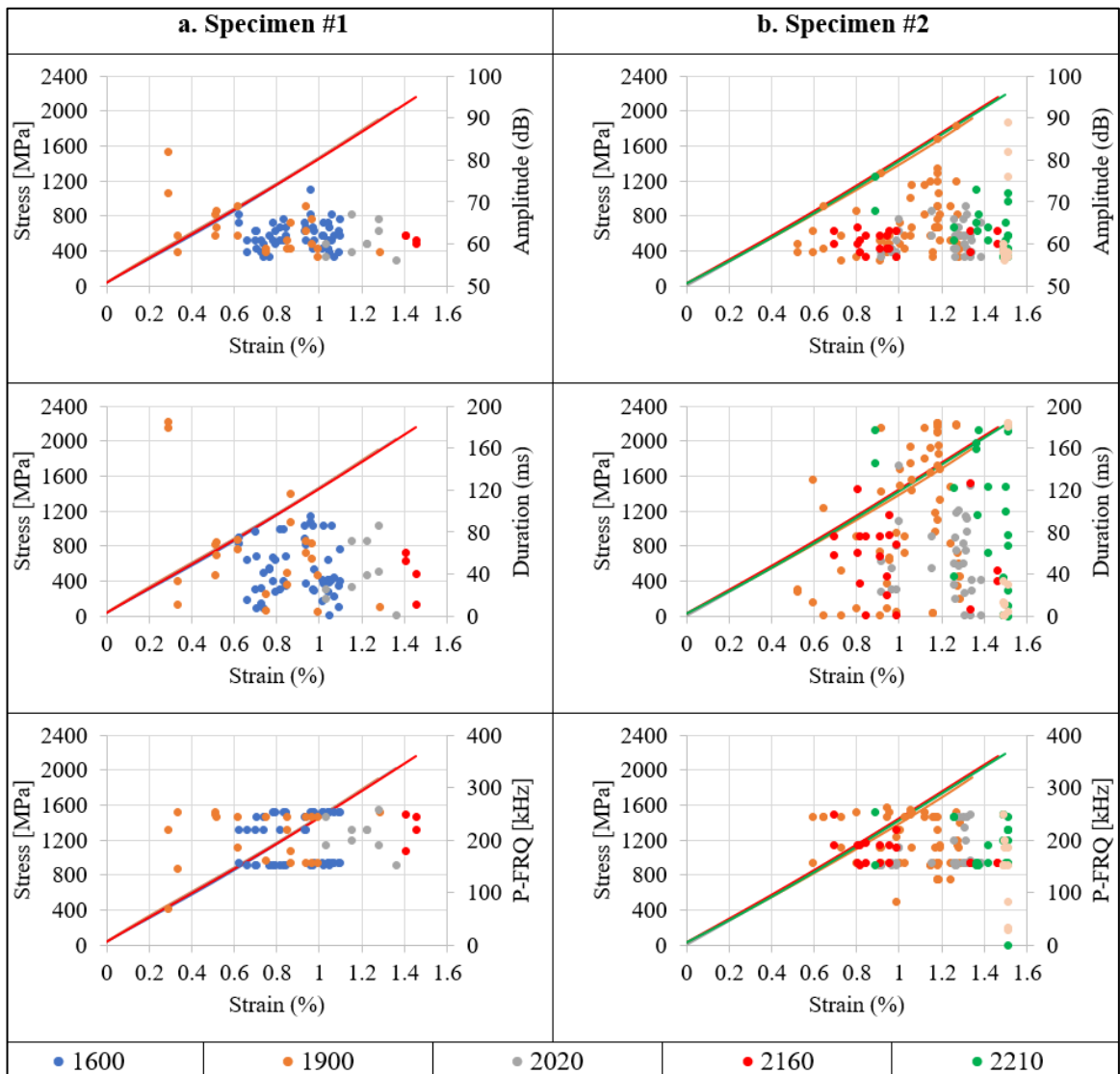


Figure 3.13. Interrupted test results for two different non-slit  $[0]_5$  specimens.

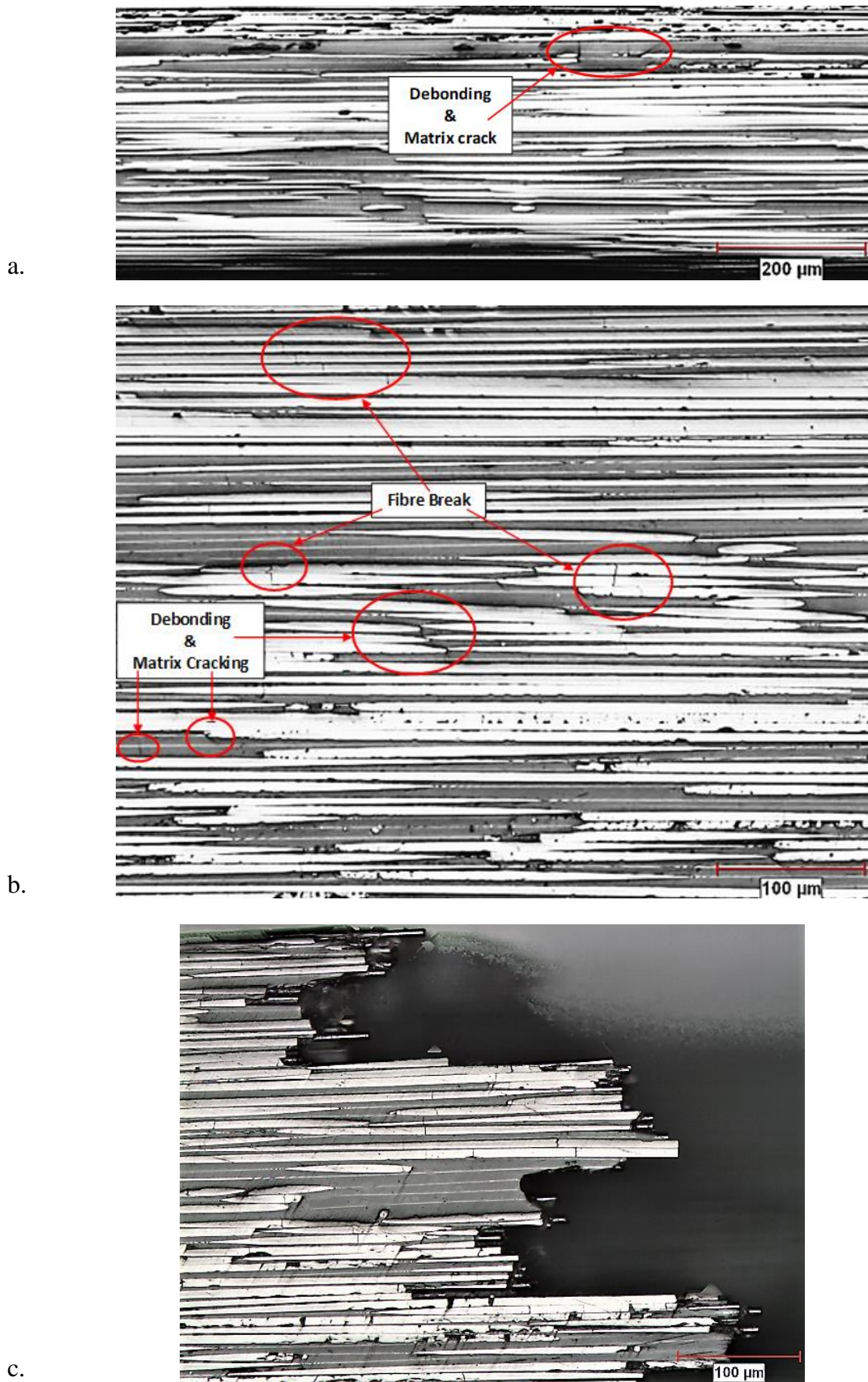


Figure 3.14. (a) Edge micrograph of damage after 1900 MPa (b) Damage modes observed after 2000 MPa, (c) Fibre breaks at the end of last test.

### 3.2.4. Kaiser and Felicity Effects

An important observation during the tests is the fact that if the specimen is unloaded at a specific stress level and reloaded again, no AE events are recorded up to previous stress level at which the specimen is unloaded. This phenomenon is called as “Kaiser effect” which was first observed by Joseph Kaiser and it states that if a material is unloaded from a stress level and reloaded again to a higher level, very few or no AE events are recorded up to the maximum stress level of previous loading [17]. Significant damage propagates after this level is passed over, that causes high number of events to be recorded. The whole results presented in this study clearly proves this phenomenon. That’s why no or few AE signals are registered before previous interruption levels in Figure 3.6, Figure 3.9 and Figure 3.13.

In order to show the Kaiser effect clearly, a short-slit specimen is taken into consideration. When the specimen edges are investigated under optical microscope after unloading from 600 MPa, no damage is detected as shown in Figure 3.15. Then, a small crack at fibres/resin pocket intersection is detected after unloading from 850 MPa as shown in Figure 3.15. Orange dots in Figure 3.15 are the AE signals registered due to this damage mode. When the specimen is unloaded from 850 MPa and reloaded again up to 1100 MPa, registration of grey coloured AE signals start from around 850 MPa in Figure 3.15. At the same time, extension of damage at fibres/resin pocket intersection with a new damage of the same mode can be seen from the micrographs in Figure 3.15. This is believed to be an accurate demonstration of Kaiser effect in composite materials. During loading specimens up to catastrophic failure in the final loading cycle, many events are recorded before previous interruption level, due to a phenomenon called Felicity effect in composite materials [22]. This situation can be seen clearly with brown dots for long slit “Specimen #2” in Figure 3.6 and short slit specimen in Figure 3.9 and in Figure 3.15. As mentioned before, interruptions cause 4% decrease in strength of laminates. Felicity effect phenomenon is observed when the specimens are reloaded after unloading from at least 95% of their ultimate strength. Figure 3.10 shows that, after loading up to 1640 MPa, delaminations propagate to long distances through gauge lengths as shown for short slit specimen. So, it can be said that long delaminations remove Kaiser effect whereas they activate Felicity effect in composite materials.

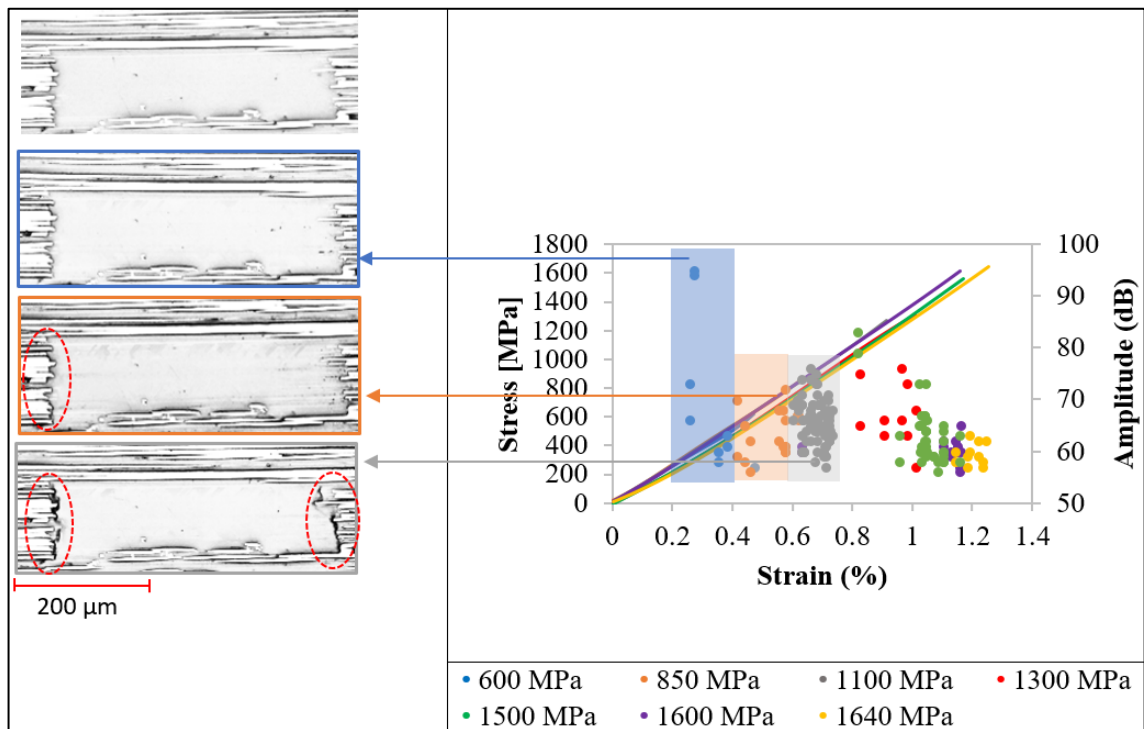


Figure 3.15. Comparison of test results with micrographs of short-slit specimens

### 3.2.5. Comparison with Finite Element Micromechanical Model

A Finite Element Micromechanical Model (FEMM model) was developed by the author of this thesis during his MSc. study in 2012 [74]. This FEMM model consists of uniform fibres and matrix with respect to hexagonal packed Representative Volume Element (RVE). It involves the effect of process-induced residual stresses and can predict the damage development in UD and XP composites under subsequent tension loading. Details of this model is not given here. Readers should refer to the thesis and subsequent conference papers published from this thesis [74, 87–89]. The last study compares the tension test results of UD  $[0]_5$  specimens with damage predictions of this FEMM [89]. It was a preliminary study to compare both techniques. According to the authors' knowledge, it was the first study that compares the FEMM predictions with damage detection with respect to AE results.

Figure 3.16 compares the tension test responses of different  $[0]_5$  specimens with FEMM results. Stress-strain curves almost overlap on each other in Figure 3.16. There is a

great consistency between the stress-strain curves of test results and the FEMM. Cumulative AE energy curves of long-slit and non-slit, smooth  $[0]_5$  specimens are plotted with dashed green and blue lines in Figure 3.16 respectively. AE energy values are scaled to the first y-axis to track the changes in their slopes easily. Important stress-strain levels, where abrupt changes happen in the cumulative AE energy curves are marked on Figure 3.16. At the same time, degradation in elastic modulus of the FEMM is shown with a dashed red line with respect to the values given in the second y-axis on the right side in Figure 3.16. It shows the damage threshold levels predictions with FEMM. There are three important stress-strain levels when degradation occurs in Elastic Modulus of FEMM. The first one is due to the initiation of matrix cracking and fibre/matrix debonding at 0.65 % strain (corresponds to 920 MPa). When damage progression in matrix is completed, second degradation occurs at 1.08 % strain level (corresponds to 1520 MPa). These are marked on Figure 3.16. Finally, stiffness of the model degrades to zero with fibre breaks at the end. Damage progression in the FEMM is presented in Figure 3.17.

FEMM predictions for damage mode progression are in very good agreement with the test results of various  $[0]_5$  laminates. Matrix cracking and fibre/matrix debonding stress levels are 920 MPa and 750 MPa in long-slit and short-slit specimens respectively. According to the cumulative AE energy curve of the long-slit specimen, FEMM predictions almost exactly match with the stress-strain level of the first increase of the slope of cumulative AE energy curve in Figure 3.16. In addition to this, initiation of delaminations are found to happen at around 1500-1600 MPa for slit-specimens. Second slope increase of cumulative AE energy curve of long-slit specimen happens at 1590 MPa in Figure 3.16. As presented in subsection 3.2.1. it was due to the delaminations. This is highly consistent with second stiffness drop of FEMM model. It occurs due to the matrix crack in RVE reaches to upper region of the model which means a delamination in the model. It is not possible to detect these damage modes in smooth  $[0]_5$  specimens as seen in Section 3.2.3. Finally, strength of the model was predicted to be 2105 MPa with FEMM, whereas it is measured 2210 MPa with non-slit  $[0]_5$  laminate.

In this section, it is seen that slit specimens can be successively used to investigate the damage development in UD laminates with in-situ AE registration and partially in-situ edge observation. It can provide a correlation between AE detection and FEMM predictions of various damage modes in AS4/8552 as found in this study.

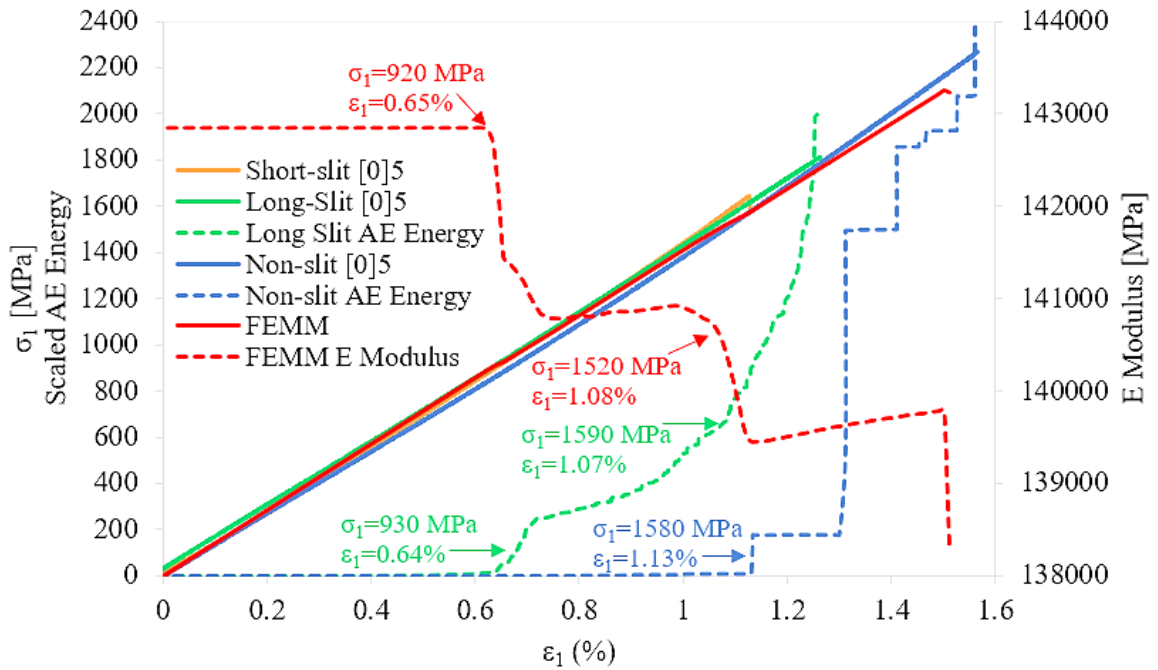


Figure 3.16. Comparison of [0]<sub>5</sub> test results with FEMM.

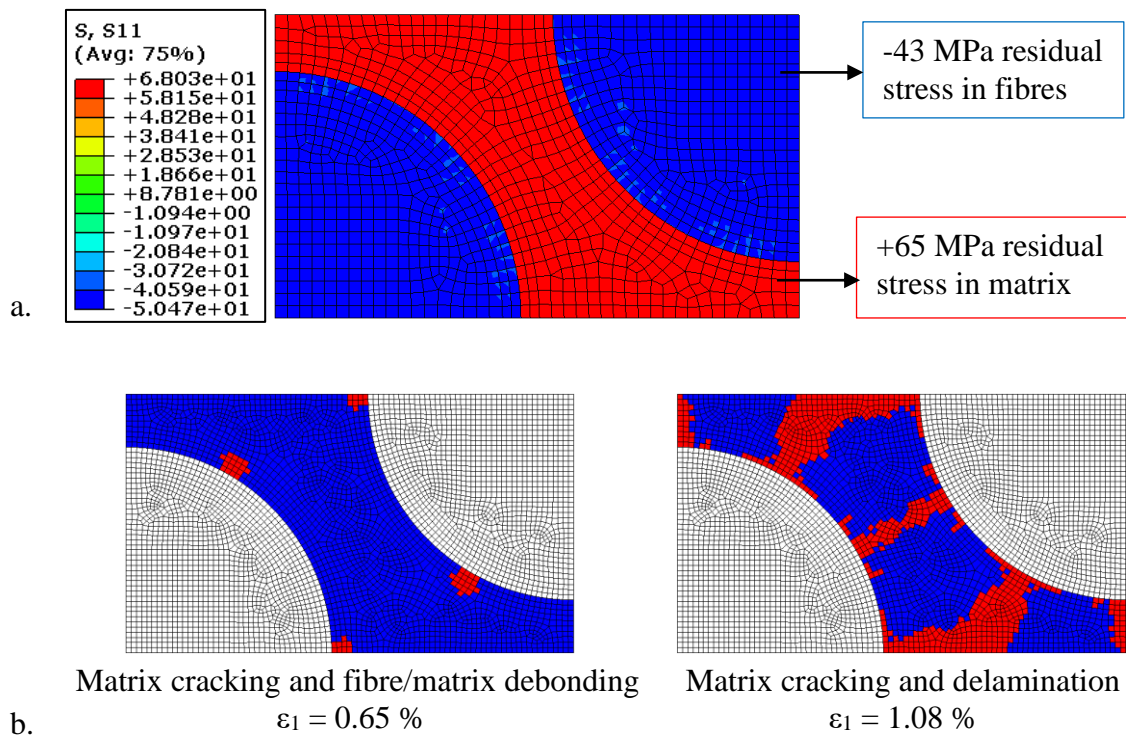


Figure 3.17. (a) Residual stress distribution at the end of cure cycle, (b) Damage progression during tension loading

### 3.3. Damage Mode Identification in Smooth Quasi-Isotropic Laminates

Five tension tests are performed for each laminate type with AE registration and DIC measurements. Direct edge observation is utilized during two of these tests. Figure 3.18 presents test results for all layups, combining in one graph stress-strain curve and AE parameters: Amplitude with cumulative AE energy and weighted frequency. Different colours of the symbols and lines represent a different test. Reason for choosing weighted frequency is explained in further sections. The specimens are not tested up to the final failure to prevent possible damage to the AE sensors, hence the maximum stress levels in Figure 3.18 correspond to the stress levels that particular tests are stopped. Figure 3.18 shows that the test results, and distribution of the AE events for each laminate type are consistent.

Stress-strain curves for the different layups are the same within the experimental scatter, which is of no surprise. AE patterns, both expressed as cumulative energy curves and as distribution of the amplitude and frequency of the events change considerably as lay-up orientation changes. When  $90^\circ$  plies are mid-ply or close to mid-section, high frequency events are registered massively, as in Figure 3.18.(a) and Figure 3.18.(c). Conversely, when  $90^\circ$  plies are on or close to surface of the laminate, AE events have low weighted frequency values between 100-400 kHz as in Figure 3.18.(b) and Figure 3.18.(d). Validity of the assumption in literature that states the correlation between fibre breaks and high frequency events and low frequency events with matrix cracks, as shown in Table 1.6, becomes contentious in the light of these measurements. High frequency events are registered from the very beginning of the AE activity in  $[-45_2/0_2/+45_2/90_2]_s$  and  $[0_2/+45_2/90_2/-45_2]_s$  laminates. These features are difficult to associate with fibre breakage, since the failure strain for the fibre break is stated as 0.018 strain for AS4 fibres in its data sheet [90]. In addition to this, a question can be asked: “Does the order of damage evolution change from one laminate to another and cause a different configuration of the AE event clusters?”

The AE patterns in QI laminates, presented in Figure 3.18, suggest that indeed the conventional identification of the high frequency events as fibre breakage is questionable and that the layup of a laminate can qualitatively modify the AE pattern. The subsequent sections present this general observation of the AE events in conjunction with DIC and the edge optical damage observations. Only the test results where all damage identification techniques are utilized are presented in subsequent sections.

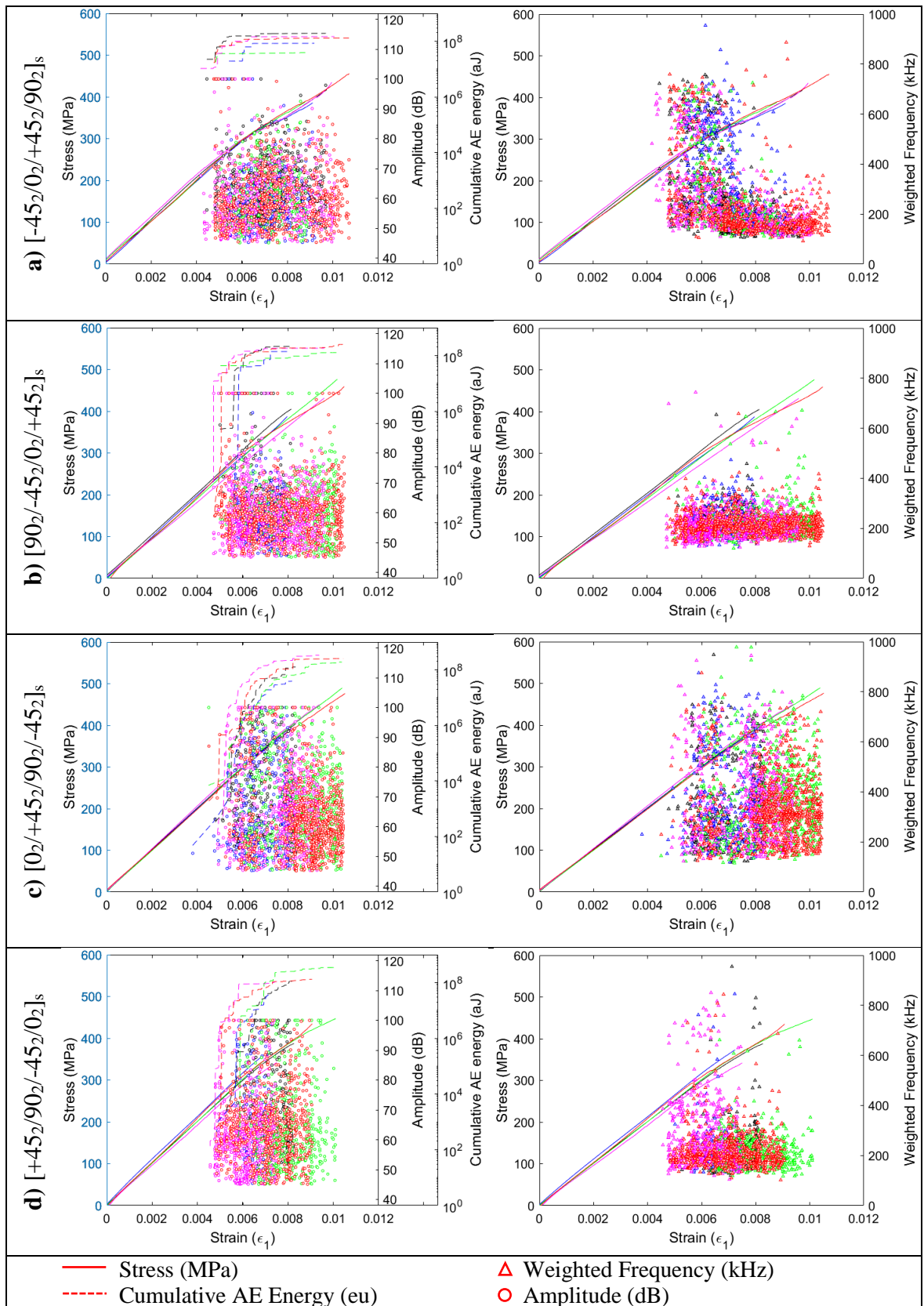


Figure 3.18. A summary of the stress-strain curves and AE registration for the tested laminates. Markers and lines of different colours correspond to different individual tests.

### 3.3.1. [-45<sub>2</sub>/0<sub>2</sub>/+45<sub>2</sub>/90<sub>2</sub>]<sub>s</sub> Laminates

First, QI laminate in consideration is [-45<sub>2</sub>/0<sub>2</sub>/+45<sub>2</sub>/90<sub>2</sub>]<sub>s</sub>. This lay-up orientation is very generic for investigation of damage progression. 90° in the middle and adjacent +45° plies causes transverse cracks easily. In addition to this, evident delaminations from the free edge expected due to adjacent stacking of aforementioned plies.

This lay-up is presented to confirm that the weighted frequency (WF) is the most selective frequency parameter. Because of this, from this section of this thesis, cluster boundaries are presented in terms of amplitude and weighted frequency. Table 3.2 shows the summary of cluster boundaries with respect to amplitude and weighted frequency. Comparison of clusters with respect to different frequency contents and amplitude can be seen in Figure 3.19. Selective characteristics of weighted frequency can be seen in Figure 3.19.(c) when compared with different frequency parameters vs. amplitude for this laminate. It is seen that the clusters are well-separated with respect to weighted frequency vs. amplitude, and clusters are interpenetrating to each other for peak frequency and frequency centroid.

Table 3.2. Summary of cluster groups of AE results for [-45<sub>2</sub>/0<sub>2</sub>/+45<sub>2</sub>/90<sub>2</sub>]<sub>s</sub> laminate

Summary of cluster boundaries			
		A (dB)	WF [kHz]
CL1	◇	≥66	≤260
CL2	△	<66	≤260
CL3	▽	<66	260<WF≤480
CL4	▷	<66	>480

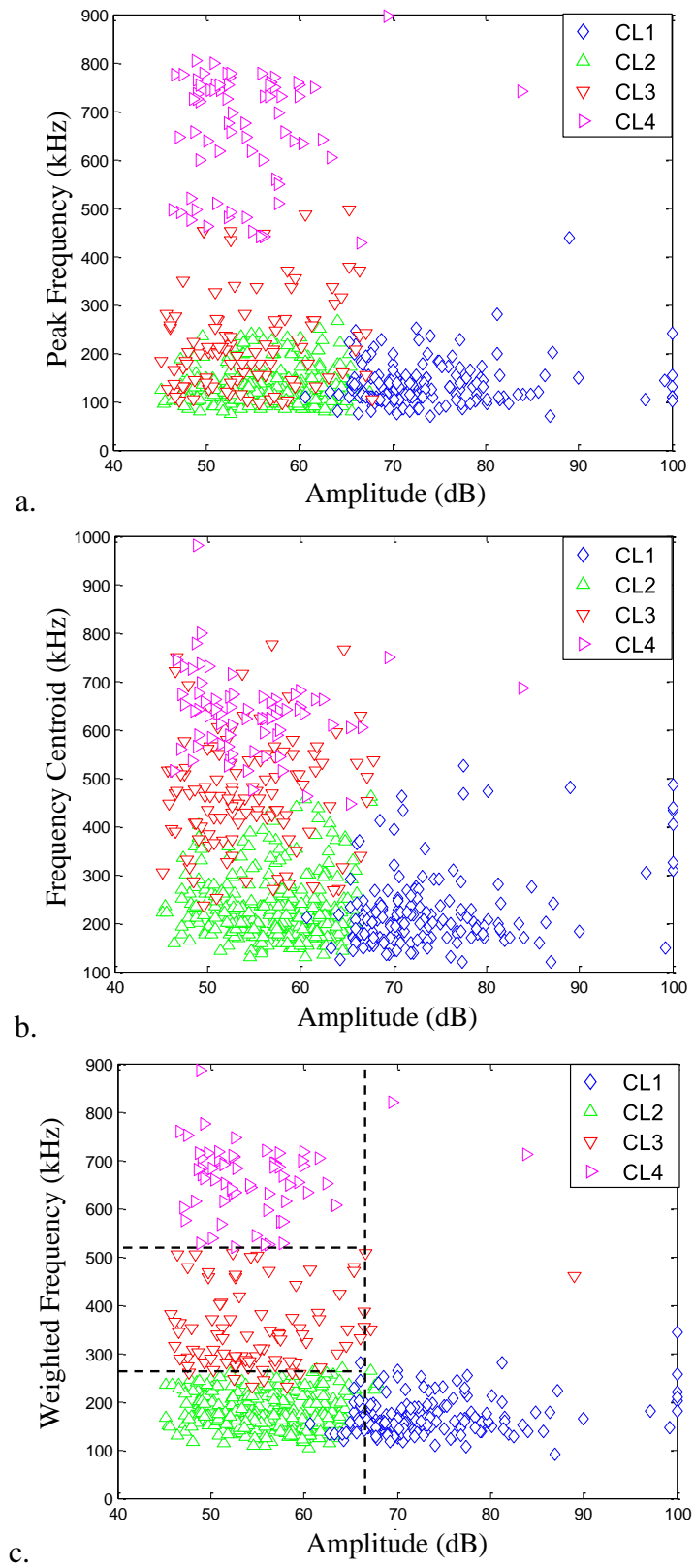


Figure 3.19. Cluster groups for of  $[-45_2/0_2/+45_2/90_2]_s$  laminate.

Figure 3.20.(a) shows the accumulation of clusters with respect to the two most selective parameters for the gauge region between the AE sensors. High frequency - low amplitude events (CL3-CL4) are mostly recorded during early AE registration whereas high amplitude - low frequency features (CL1-CL2) are seen after around 0.0067 strain. Figure 3.20.(b) presents the same for the edge observation region only. It shows that the events pattern for this region is representative for the whole specimen.

Damage evolution throughout the test can be seen in Figure 3.21. The very left column in Figure 3.21 shows strain levels in test direction. These strains are the average  $\epsilon_1$  values (direction 1 designates the loading direction, direction 2 is the transverse direction), calculated from the AoI used for the strain mapping. “Edge observation region” is marked on Figure 3.21. The distance of this region to the first AE sensor (which is considered as the origin) is 18 mm; the region covers the location range 18-23 mm. Due to discrepancy between AE detection and real location, the region between 18-24 mm is taken into consideration. Snapshots of micro damage evolution within this 5 mm region can be seen on second column of the Figure 3.21. Next two columns present full field  $\epsilon_1$  and  $\epsilon_2$  strain maps respectively.

First micro damage mode is a transverse matrix crack in mid-90° plies; it is seen at 0.0058 strain in Figure 3.21. The moment that this image is taken is about 0.0010 strain after the first signals passing the damage threshold are registered (Figure 3.20.b). Then the damage propagates to adjacent lower 45° plies at 0.0060 strain with micro delamination at 90°/45° interface. A similar damage, consisting of transverse matrix cracks in mid 90° plies, off-axis cracks in adjacent lower 45° plies and micro delamination between them are seen at around 3 mm away from the first damage at 0.0070 strain. Then, the first transverse crack propagates to upper 45° plies at 0.0076 strain. Similar damage propagation occurs with the second transverse cracks at 0.0080 strain. Afterwards, 90° plies and adjacent 45° plies separate from each other at 0.0087 strain, as seen in Figure 3.21. Large separation of 90° layers from 45° layers is called “macro delamination” in this study. This test is stopped at 0.011 strain and 455 MPa stress level.

As shown in Figure 3.20.(a-3), the origins of the AE events, belonging to different clusters, are quite evenly distributed over the length of the specimen. This suggests that the sequence of the damage events seen in the 5 mm length of the edge observation region also

happens in other parts of the specimen. Hence we can discuss the damage evolution using overall AE registration and DIC images of the full AoI.

Figure 3.20 shows that the number of events in high frequency clusters, (CL3-CL4) are more than in low frequency clusters (CL1-CL2) up to around 0.0067 strain, after which number of events in the low frequency - high amplitude cluster (CL1) increases. At the same time, there is very high contraction (green-blue zone, corresponding to the high absolute values of  $\varepsilon_2$ ) on one side of the specimen, seen from the DIC strain map of  $\varepsilon_2$  at 0.0070 strain in Figure 3.21. This contraction is due to the delamination between 90° and 45° plies which initiates at 0.0061 strain and completely propagates through the gauge length at around 0.0070 strain. Before delamination, the surface plies could not develop Poisson contraction because they are constrained by the 90° ply. After delamination the constraint is removed, and  $\varepsilon_2$  increases in the delamination area. Delamination of 90° and 45° layers from each other in the edge observation region occurs at 0.0087 strain level as shown in Figure 3.21. It can be assumed that the increase in the number of CL1 events is due to this delamination between 90° and 45° plies. Similar damage mode initiates from the polished side of the specimen, marked within a box inside  $\varepsilon_2$  plot at 0.0080 strain level.

Correlation between damage modes and AE clusters can be done using the in-situ optical observations. Figure 3.21 shows that only micro cracks occur at inner plies before 0.0070 strain, and most of the recorded signals before 0.0070 strain are high frequency - low amplitude clusters (CL3-CL4) as seen in Figure 3.20. Macro delamination initiates near one side of the specimen at 0.0061 strain and propagates through the gauge length at 0.0070 strain as shown in Figure 3.21 whereas, Figure 3.20.a shows that the number of events in the high amplitude-low frequency cluster, CL1, increases considerably in gauge length during the same strain interval. Figure 3.20.(a-3) shows that high number of CL1 starts to be recorded from 0.0061 strain at 8-9 mm away from the sensor, then it propagates to 10-12 mm away at around 0.0067 strain level, afterwards it is distributed to further regions. CL1 appears after around 0.0065 strain in the edge observation region as shown in Figure 3.20.b.

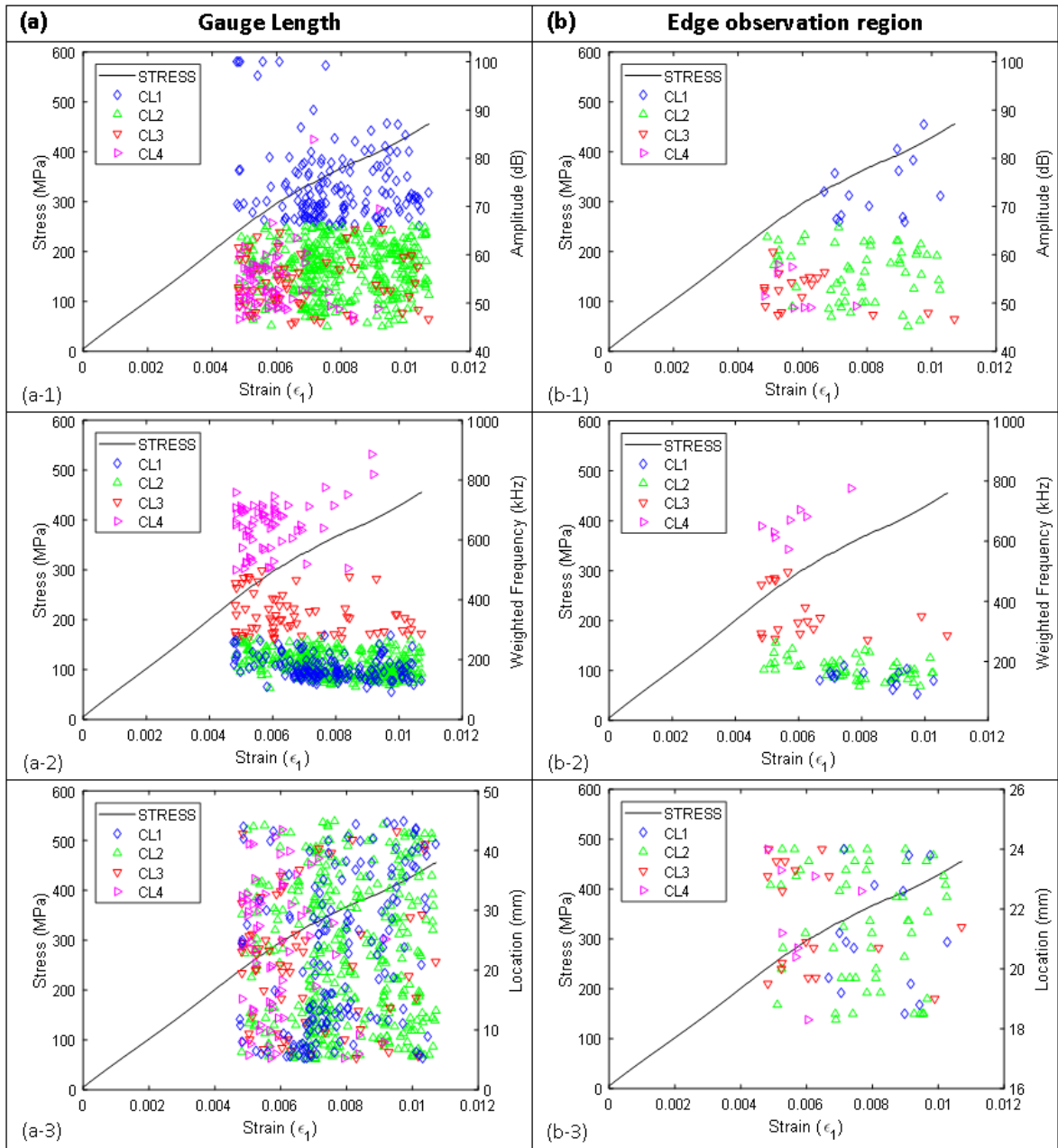


Figure 3.20. Accumulation of AE clusters throughout a test in  $[-45_2/0_2/+45_2/90_2]_s$  laminate:

(a) full gauge length; (b) edge observation region only; (1) events amplitude; (2) events weighted frequency; (3) events location.

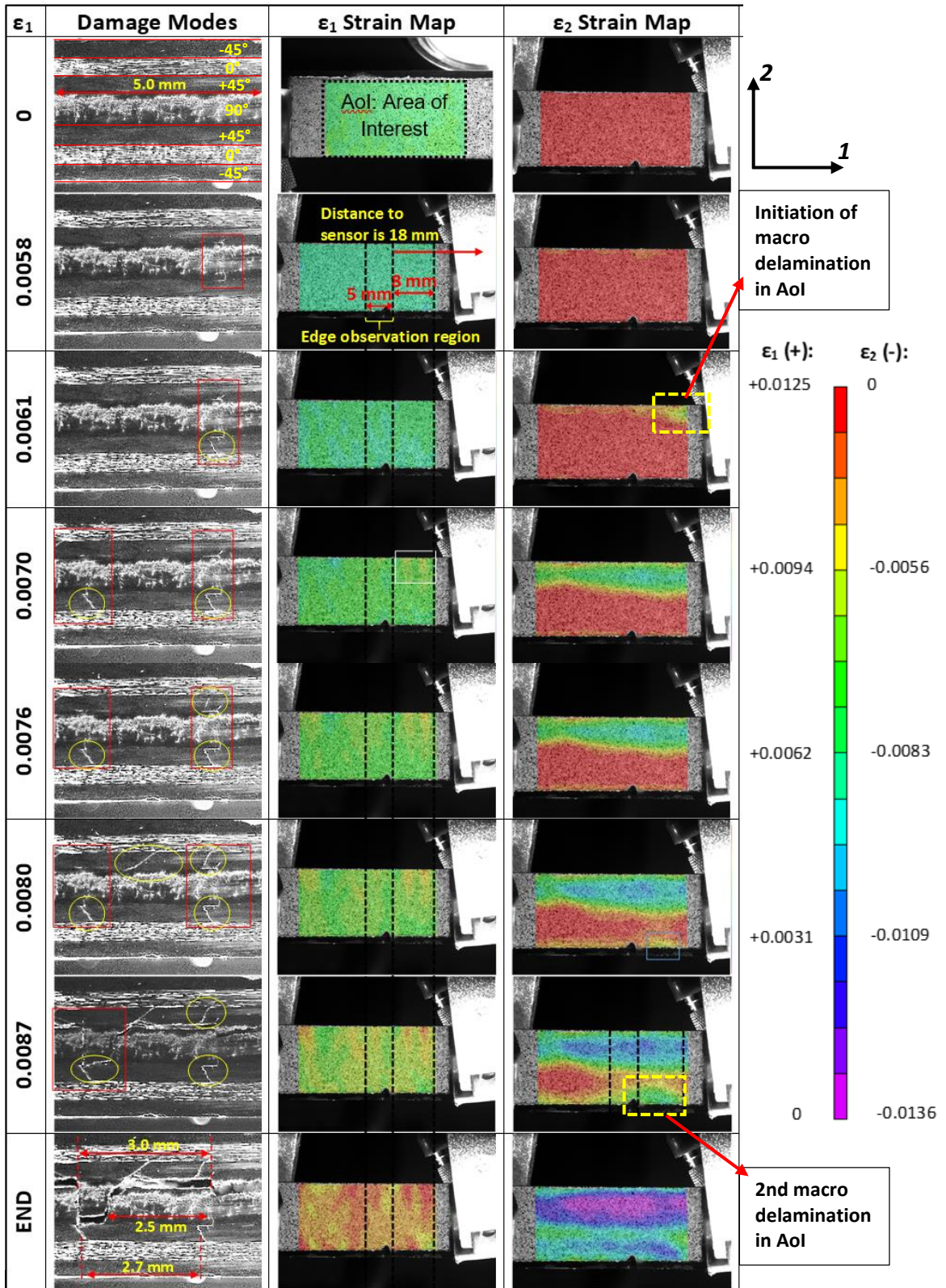


Figure 3.21. Damage progression in  $[-45_2/0_2/+45_2/90_2]_s$ .

Hence a correlation between the clusters and observed damage modes in order of appearance can be done as follows:

- CL3-CL4 (high frequency – low amplitude) represent transverse matrix cracks in 90° and 45° plies.
- CL2 (low amplitude – low frequency) represents micro delaminations already present from first damage initiation stress level up to the end of the test.
- CL1 (low frequency – high amplitude) represent macro delaminations – separation of 90° and 45° plies.

Although fibre breaks are not present in this classification, one can correlate all the clusters with certain damage types. Evidently, it is found out that high frequency events represent matrix cracks at inner 90° and +45° plies. Doubts in Refs. [36, 37] are supported: high frequency events do not necessarily represent fibre breaks. However the question of where the fibre breaks are still remains unanswered. One possibility is that there are no fibre breaks occurring. Another possibility is that even if they occur, they may cause low amplitude AE signals which are filtered away by the threshold of 40 dB. Lowering this threshold is not possible because of the level of the noise in the sensors and the testing and acquisition system used.

Additional evidence supporting the proposed correlation between the AE events clusters and the damage modes is given by the analysis of the crack spacing. Figure 3.22 presents distribution of location of the AE events in different clusters for a region of 10 - 25 mm away from one AE sensor; the region of the edge microscopic observation is marked on these graphs. Note that the error in the event location is about 1 mm.

Figure 3.22.a presents the agreement between macro delamination and its AE detection. It is seen that the number of CL1 events, suggested to represent macro delaminations, is the highest in the region 10 - 14 mm in Figure 3.22.a. DIC strain map shows that macro delaminations initiate around this region of the laminate. Also, there are larger delaminations in 10-14 mm region of the gauge length, (please refer to  $\varepsilon_2$  legend in Figure 3.21). Figure 3.20.(a-3) shows that high number of CL1 starts to be recorded from 0.0061 strain at 8-9 mm away from the sensor, then it propagates to 10-12 mm away at

around 0.0067 strain level, afterwards it is distributed to further regions. At the end of the test, a large delamination can be seen between 45° layers and 90° layers in the edge observation region in Figure 3.21. Its correspondence in Figure 3.22.a shows that there is a gap at 20 mm and 22.5 mm distances. This can be due to discrepancy between AE detection and real location. However, it can also be due to a physical reason: In Figure 3.21, distance of the second transverse crack in edge observation region, the one on left, is around 21-22.5 mm away from the AE sensor at 0.0080 strain. There are micro delaminations and transverse cracks already present at this strain level. Final failure modes are separation of 45° plies from 90° plies and separation within mid-90° plies from the pre-induced transverse cracks in these mid-ply. Prior damage mode, separation of 90° layers from 45° layers, is delamination and that is consistent with occurrence of CL1 but the latter is not really delamination. That's why the AE properties of this separation might not be recorded within CL1 at around 22.5mm distance in Figure 3.22.a. This is a very important finding of this thesis.

CL2 is suggested to represent micro delaminations that occur everywhere in the specimens. That's why it has the highest number of events, evenly distributed in Figure 3.22.b. CL3 and CL4 are the clusters representing the matrix cracks in 90° and 45° plies. Distance between these cracks is 2.5 – 3 mm as seen in Figure 3.22.c and Figure 3.22.d. The distance between these events are approximately constant at 3 mm for CL3 and 2– 3 mm for CL4, which seem to correlate with the optical observations.

Two different in-situ observation techniques provides to obtain very important findings from the  $[-45_2/0_2/+45_2/90_2]_s$  laminate configuration. Especially for the transverse matrix cracks which happen easily. It would not be possible to distinguish the difference of AE characteristics for transverse cracks in 90° and +45° plies. In fact, it was not even mentioned in literature before. In addition to this, AE correspondence of transverse cracks in 90° and +45° plies were always believed to have low amplitude and frequency characteristics. Thanks to in-situ optical observation techniques, it is found that this is not always true. Low amplitude and high frequency events are seen to be registered due to the transverse cracks in 90° and +45° plies. Next sections present the effect of stacking sequence to the AE characteristics of damage modes.

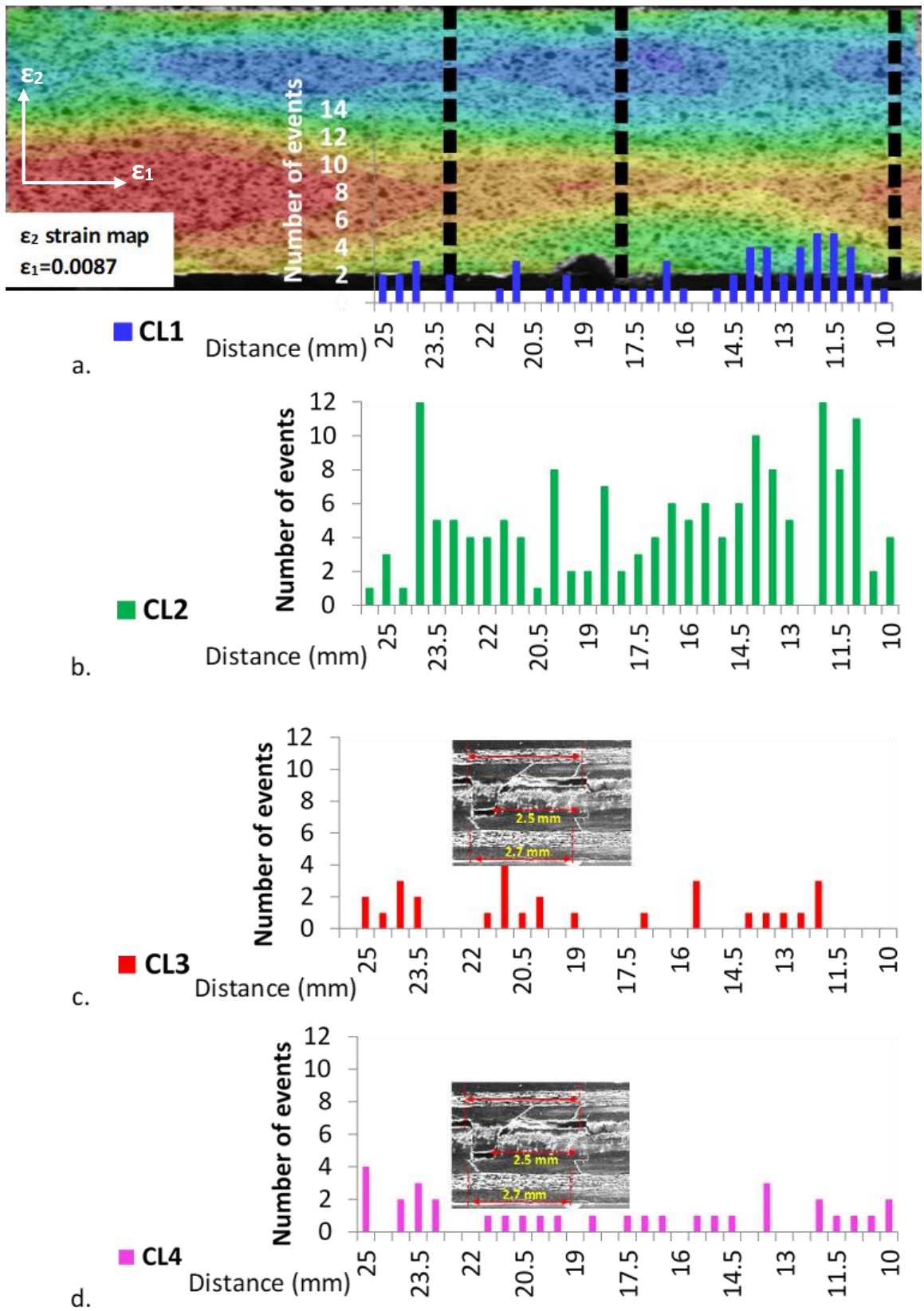


Figure 3.22. Distance of clusters to AE sensor on  $[-45_2/0_2/+45_2/90_2]_s$  laminate.

### 3.3.2. $[90_2/-45_2/0_2/+45_2]_s$ Laminates

Second laminate in consideration is  $[90_2/-45_2/0_2/+45_2]_s$ . Figure 3.18.b shows that weighted frequency values of AE events for this lay-up lie below 400 kHz, whereas amplitude values are distributed widely. Frequency content is not statistically representative for  $[90_2/-45_2/0_2/+45_2]_s$  but amplitude is a selective feature. Optimal cluster number is found to be three. Clusters are not separated so distinctly by amplitude as in previous laminate type. Only the boundary for high amplitude cluster (CL1) is consistent for all tests: it is around 75 dB. Accumulation of clusters throughout the test with respect to amplitude values can be seen in Figure 3.23 and damage progression is shown in Figure 3.24. Edge observation region in Figure 3.24 is between 20–25 mm, but due to the 1 mm error between real damage location and AE detection, a region between 19–26 mm is taken into consideration in Figure 3.23.b. For this laminate type,  $\varepsilon_2$  strain map does not provide useful information for damage mode identification. So, surface cracks are shown instead of  $\varepsilon_2$  strain map in Figure 3.24.

Figure 3.23.a shows that first AE events are recorded around 0.0048 strain level in the gauge length. However, it is seen in Figure 3.24 that the first damage is detected at 0.0044 strain level with DIC but was most probably filtered out from the AE registration, as the damage site is too close to the sensors (less than 5 mm distance). Surface cracks can be clearly identified with DIC in Figure 3.24. These cracks cause damage in adjacent  $-45^\circ$  plies immediately with delamination between  $90^\circ$  and  $-45^\circ$  plies as seen at 0.0065 strain in Figure 3.24. Damage initiates in surface  $90^\circ$  plies, reaching adjacent  $-45^\circ$  plies evolve through  $0^\circ$  plies as in 0.0072 strain in Figure 3.24. A correlation between DIC deformation maps and edge observation can be done at 0.0076 strain for the top  $90^\circ$  surface layer. The measured distance of the crack indicated to AE sensor is 21.5 mm. Surface damage events at 0.0065 and 0.0076 strain are registered with highest amplitude. Levels of the corresponding events in CL1 has the highest value (100 dB, which is the maximum set by the AE system) (see Figure 3.23.(b-1), 0.0065 and 0.0076 strain). CL1 most probably represents surface cracks. Also, their distances to the AE sensor are 24.5 and 21.4 mm with respect to AE detection (see Figure 3.23.(b-2), 0.0065 and 0.0076 strain) which is highly consistent with measurement. Meanwhile, there are multiple AE events recorded with lower amplitude levels, belonging to other clusters, CL2 and CL3. Source of these events is not fully clear.

Most probably, they are caused by damage in adjacent  $-45^\circ$  plies and delamination between  $90^\circ/-45^\circ$  interfaces.

A correlation between surface damage and CL1 is presented in Figure 3.25. When an event from CL1 is recorded, corresponding damage is captured with one of optical observation techniques as shown in Figure 3.25.(a). Some AE events do not correspond to an optical identification. That is probably because they occur at the opposite surface of the laminate which is not monitored by DIC. Figure 3.25.(b) presents a correlation between the damage present at the end of the test with AE location detections. Overall, there is good agreement between position of the events in the high amplitude cluster, CL1, and optical detections.

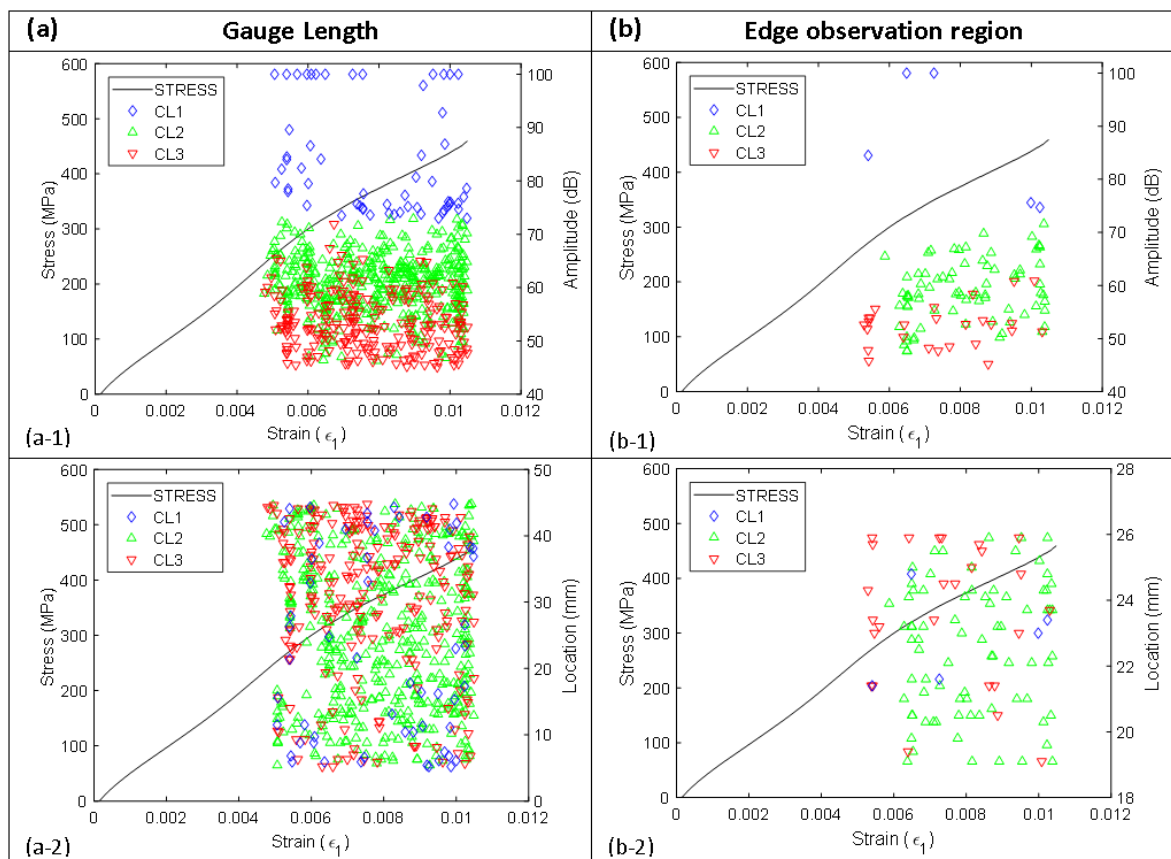


Figure 3.23. Accumulation of AE clusters throughout the test in  $[90_2/-45_2/0_2/+45_2]_s$  laminate: (a) full gauge length; (b) edge observation region only; (1) events amplitude; (2) events location.

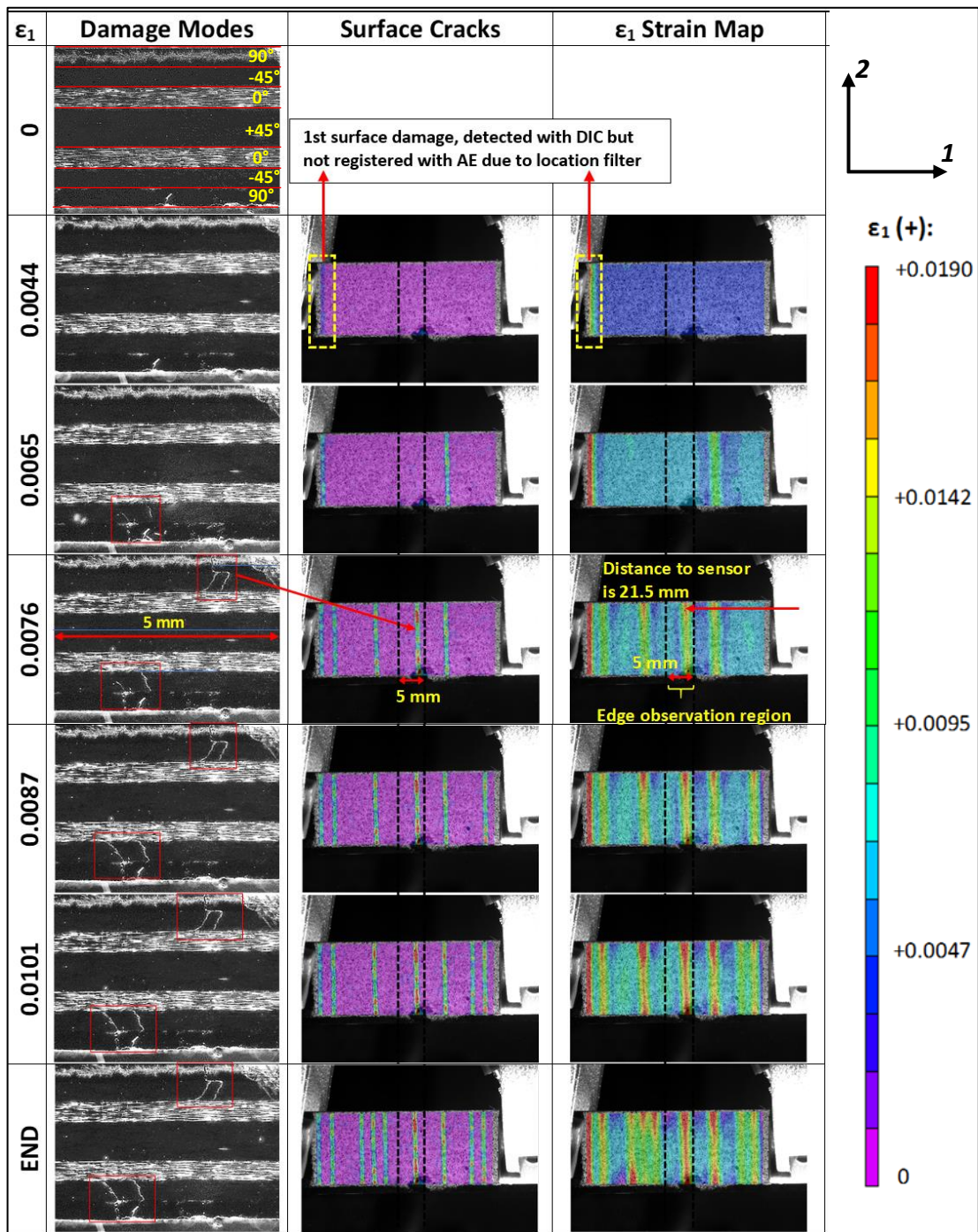


Figure 3.24. Damage progression in  $[90_2/-45_2/0_2/+45_2]_s$ .

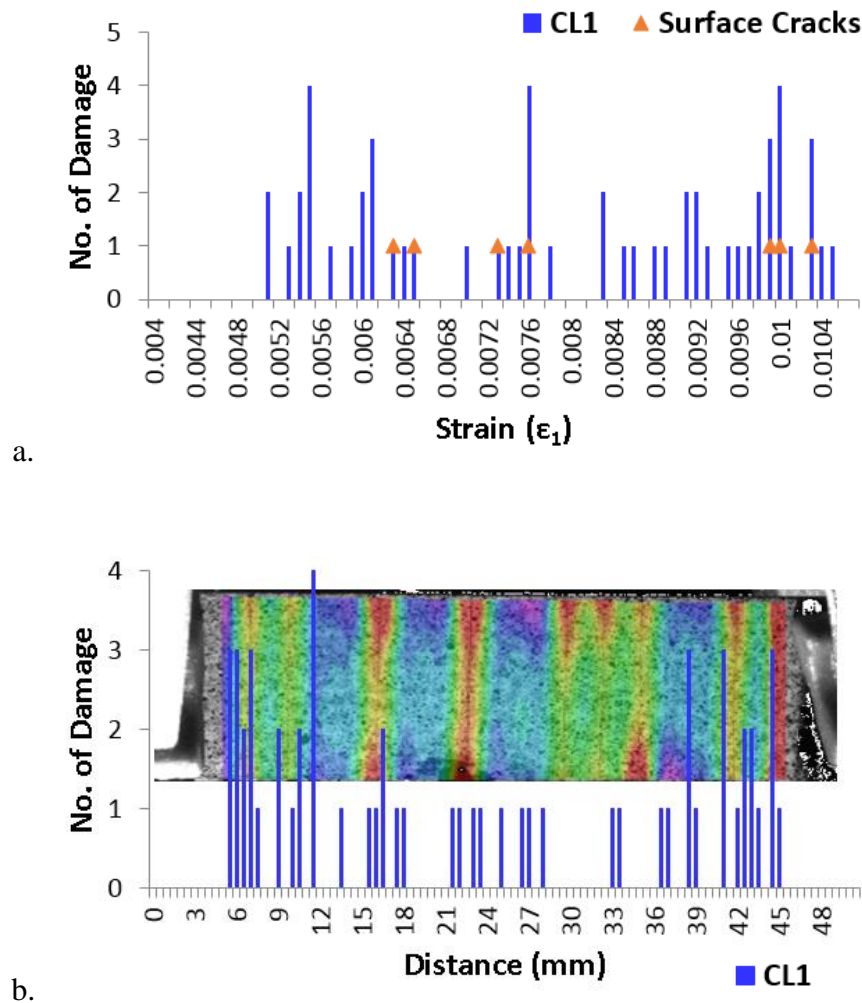


Figure 3.25. (a) Comparison of CL1 with optical detection (b) Surface cracks through the specimen gauge length at the end of the test and its comparison with AE detections throughout all the test in  $[90_2/-45_2/0_2/+45_2]_s$ .

### 3.3.3. $[0_2/+45_2/90_2/-45_2]_s$ Laminates

Figure 3.18 shows that the number of high frequency events is very high in  $[0_2/+45_2/90_2/-45_2]_s$  laminate. The number of AE events with high weighted frequency values are very high for this laminate and this parameter is statistically representative. Separation of clusters from a representative test and the average values for cluster boundaries from five tests and are shown in Figure 3.26.(a) and Figure 3.26.(b) respectively. Very consistent and well-separated clusters are obtained.

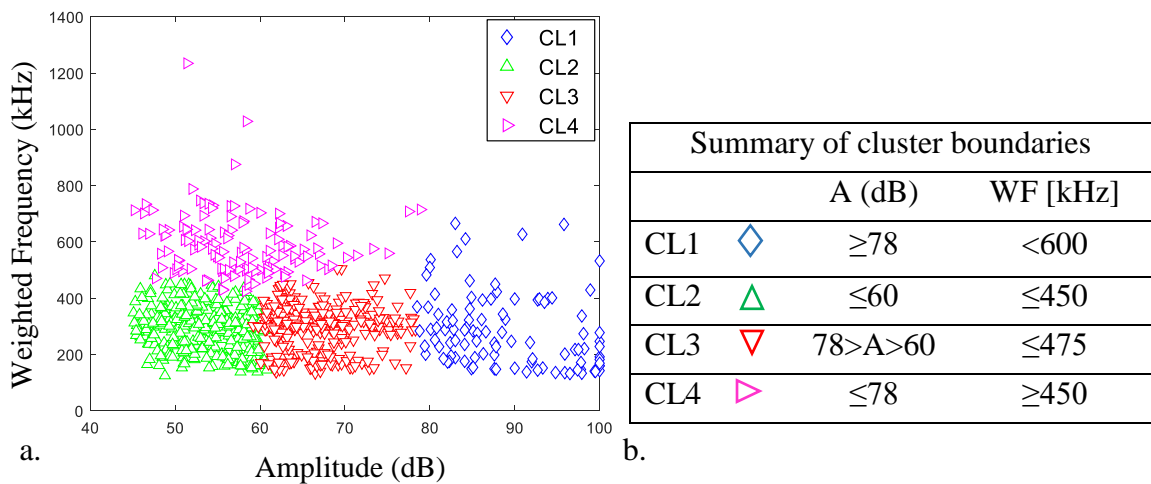


Figure 3.26. (a) Distribution of AE clusters in a representative test (b) Summary of cluster boundaries from five tests for  $[0_2/+45_2/90_2/-45_2]_s$ .

DIC strain maps do not provide a helpful information for any surface damage, since surface plies are laid in  $0^\circ$  direction and no cracks appear in these plies. It means that only micro damage modes at inner plies are present in  $[0_2/+45_2/90_2/-45_2]_s$  laminate up to 90 % of ultimate strength.

Accumulation of AE clusters in the whole gauge length and the edge observation region are shown in Figure 3.27. Location distribution of clusters in Figure 3.27.(a-3) shows that clusters are well dispersed to the whole gauge length of the specimens. It means that damage modes induced at edge observation region are representative. The 5 mm edge observation region occupies position 20–25 mm from the AE sensor. A transverse crack in upper  $90^\circ$  ply almost goes out of view of the edge observation region through the end of the test as it is shown in Figure 3.28. Therefore, edge observation region is considered as 20–26 mm distance from AE sensor in Figure 3.27.(b-3). The number of AE events in CL1 is higher than in other clusters through the gauge length as shown in Figure 3.27.(a). When the edge observation region is taken into consideration only, it is seen that the first events registered mostly belong to CL1 in Figure 3.27.(b) as well. Then CL1 almost disappears in the edge observation region after 0.0080 strain. Meanwhile, the number of events from other clusters increase as seen in Figure 3.27.(b).

Figure 3.28 shows damage progression in  $[0_2/+45_2/90_2/-45_2]_s$  laminate. When transverse cracks in  $90^\circ$  plies (shown in red rectangles) occur, it causes micro delaminations at  $90^\circ/-45^\circ$  and  $90^\circ/+45^\circ$  interfaces at the same time. First transverse crack appears at 0.0063 strain in upper  $90^\circ$  plies and the second one occurs at 0.0064 strain in Figure 3.28. Only transverse cracks in  $90^\circ$  and plies –are seen up to 0.0083 strain level. Transverse cracks in adjacent  $\pm 45^\circ$  plies appear later. First damage in lower  $+45^\circ$  plies initiates at 0.0083 strain level but it becomes more visible at 0.0084 strain, shown within yellow circles in Figure 3.28. At the same time two more transverse cracks occur in  $90^\circ$  plies. Off-axis crack in  $+45^\circ$  plies reaches to adjacent  $0^\circ$  plies and another off-axis crack in mid  $-45^\circ$  plies occurs at 0.0090 strain. Test ends at 0.0105 strain and more off-axis cracks occur in lower and upper  $+45^\circ$  plies as shown in Figure 3.28.

There is a good agreement between the accumulation of high number of CL1 events in Figure 3.27.(b) and accumulation of transverse cracks in  $90^\circ$  plies in Figure 3.28 up to 0.0080 strain. This is supported by Figure 3.29.a where each transverse crack in  $90^\circ$  plies corresponds to an event from CL1 up to 0.0076 strain but subsequent cracks do not necessarily match with CL1 events. High frequency clusters correspond to transverse cracks at inner  $90^\circ$  and  $+45^\circ$  plies in  $[-45_2/0_2/+45_2/90_2]_s$ . By taking this into consideration, correlation between CL4 and transverse cracks are compared for  $[0_2/+45_2/90_2/-45_2]_s$  laminate in Figure 3.29.b. Interestingly it is seen that transverse cracks in  $90^\circ$  plies after 0.0079 strain are highly consistent with CL4.

Number of CL3 events, which has intermediate amplitude level, increases after 0.0080 strain in Figure 3.27. Meanwhile, off-axis cracks in  $\pm 45^\circ$  plies initiate at 0.0083 strain as seen from the edge observation in Figure 3.28. It is highly possible that this damage initiates near or at opposite unpolished edge of the specimen, then propagates to polished edge observation region in Figure 3.28. This correspondence shows that events in CL3 represent off-axis cracks in  $\pm 45^\circ$  plies. Initiation of damage in  $\pm 45^\circ$  plies at around this level possibly causes a change in wave propagation properties of signals corresponding to certain damage modes in  $[0_2/+45_2/90_2/-45_2]_s$  laminate. So, it can be said that transverse cracks in  $90^\circ$  plies correspond to high amplitude AE events (CL1) before the initiation of damage in  $\pm 45^\circ$  plies whereas it shifts to high frequency AE events (CL4) after the initiation of damage in  $\pm 45^\circ$  plies. Finally, CL1 events correspond to micro delaminations between  $90^\circ/\pm 45^\circ$  which is distributed to overall specimen gauge length.

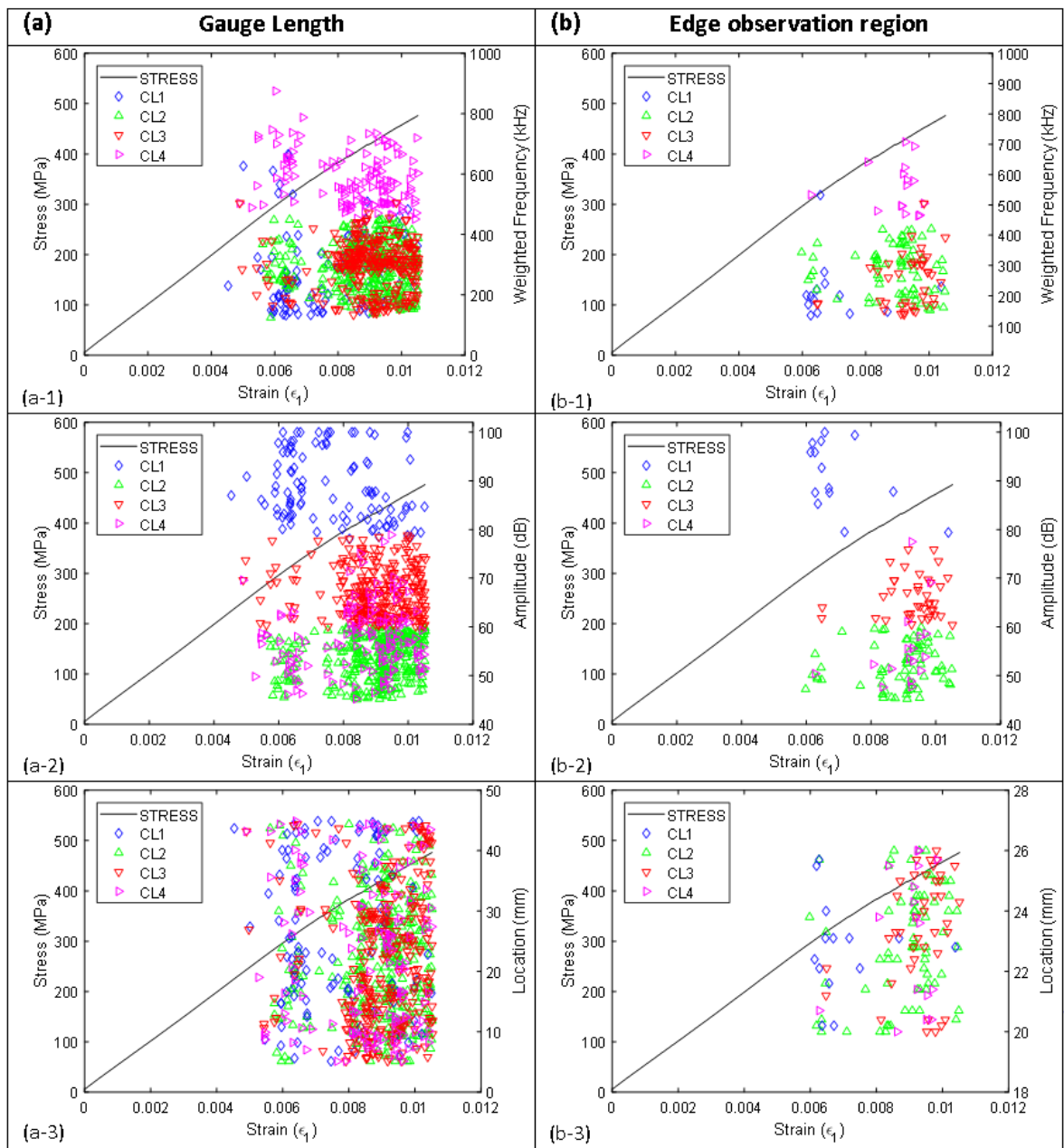


Figure 3.27. Accumulation of AE clusters throughout a test in  $[0_2/+45_2/90_2/-45_2]_s$  laminate:

- (a) full gage length; (b) edge observation region only; (1) events amplitude; (2) events weighted frequency; (3) events location

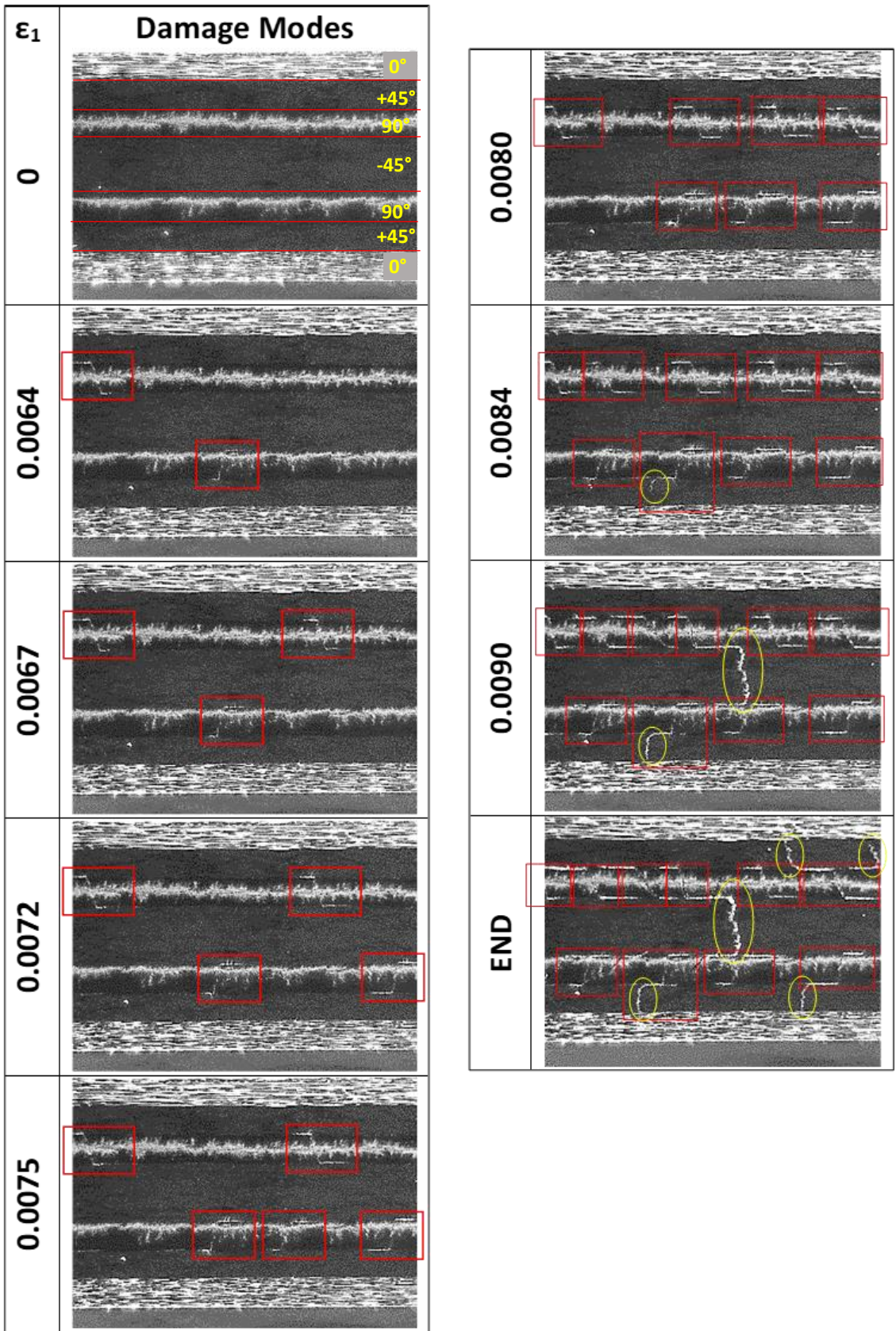


Figure 3.28. Damage progression in  $[0_2/+45_2/90_2/-45_2]_s$ .

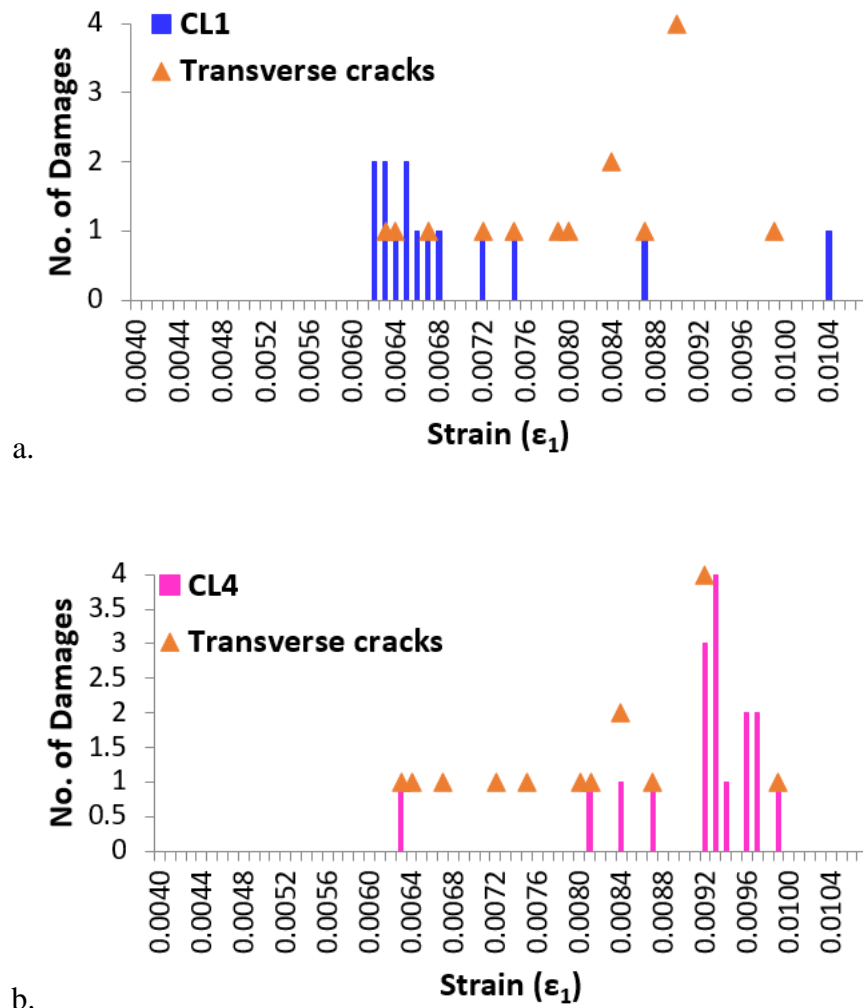


Figure 3.29. Comparison of transverse cracks in 90° plies a. with CL1, b. with CL4.

### 3.3.4. $[+45_2/90_2/-45_2/0_2]_s$ Laminates

Last laminate in consideration is  $[+45_2/90_2/-45_2/0_2]_s$ . Figure 3.18.d shows that general characteristics of AE events are high amplitude with low frequency values. As 90° plies approach the surface, frequency values of registered events become lower. Three meaningful clusters are obtained for this laminate type, as  $[90_2/-45_2/0_2/+45_2]_s$ . Since any frequency parameter is not distinctive, clusters can be separated well with respect to amplitude as shown in Figure 3.30. Amplitude boundaries are similar to  $[0_2/+45_2/90_2/-45_2]_s$ .

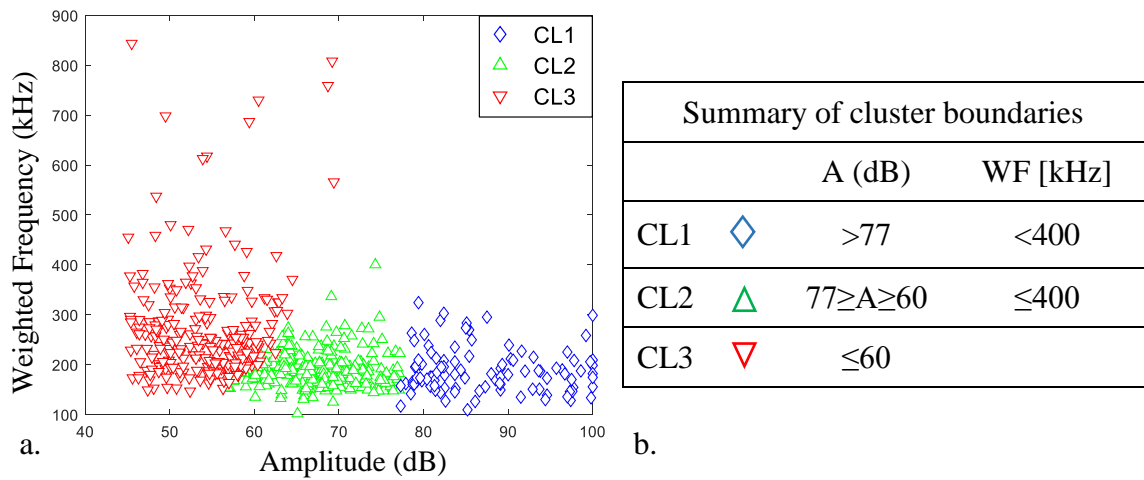


Figure 3.30. (a) Distribution of AE clusters in a representative test (b) Summary of cluster boundaries from five tests of [+45<sub>2</sub>/90<sub>2</sub>/-45<sub>2</sub>/0<sub>2</sub>]<sub>s</sub>.

Accumulation of clusters throughout the test with respect to amplitude is presented in Figure 3.31 (frequency parameters are not selective). First events are registered at 0.0048 strain as shown in Figure 3.31.a. These events are mostly registered at distances higher than 30 mm and lower than 20 mm as seen in Figure 3.31.(a-2), whereas the distance of edge observation region is between 21-26 mm. Registration of first events in this region starts around 0.0060 strain level as shown in Figure 3.31.(b-2). Events in all clusters initiated at the same time.

The first damage, seen in the edge observation region, is a transverse crack in upper 90° plies at 0.0065 strain (Figure 3.32). It corresponds to 330 MPa. As in previous laminate types, transverse cracks in 90° plies occur with delaminations between adjacent ±45° plies. Then, first crack in surface +45° layer is seen at 0.0069 strain Figure 3.32. Immediately after, this surface crack reaches the opposite edge at 0.0070 strain and two transverse cracks occur in lower 90° plies at the same time as seen in Figure 3.32. These strain levels correspond to 340-350 MPa stress levels. Second surface crack occurs at 0.0072 strain and crosses through the edge observation region as seen from DIC strain maps in Figure 3.32. 0.0073 is the strain level when damage in -45° plies become visible from the edge micrographs. AE events in the edge observation region start earlier, at 0.0062 strain. This may be caused by cracking on the opposite side of the specimen. Then another transverse crack in lower 90° plies occurs

at 0.0077 strain. Two more surface cracks occur at the same time at 0.0083 strain level in Figure 3.32. Delaminations propagating from the left side of the  $90^\circ/-45^\circ$  interface becomes highly visible at 0.0086 strain and causes another crack in lower  $-45^\circ$  plies. Damage distribution seen from the edge observation region and DIC strain map at the end of the test are identical at 0.0086 strain.

According to the results of  $[90_2/-45_2/0_2/+45_2]_s$ , AE events from surface cracks are registered with high amplitude values during tests. It can be said that CL1 events in Figure 3.32 represent damage in surface  $+45^\circ$  layers. Early registered events in Figure 3.31.(a-2) do not contain much CL1 events up to around 0.0070 strain. There are no surface cracks seen up to this strain level in Figure 3.32. In addition to this, successive events are recorded around 0.0072 strain and shown within a dashed box in Figure 3.31.(b-1) represent the passage of the second surface crack through the edge observation region in Figure 3.32. It is also seen in Figure 3.31.(b-2) that CL1 events recorded around 0.0072 strain are distributed through the edge observation region from 21 mm to 26 mm. It is consistent with surface crack passing across the width of the edge observation region in DIC strain map in Figure 3.32. Early CL2 events are recorded at 24 mm distance from the sensor up to around 0.0072 strain as shown in Figure 3.31.(b-2). First three transverse cracks in  $90^\circ$  plies are seen to occur near the end of the edge observation region up to 0.0072 strain in Figure 3.32. Its distance to AE sensor is around 25-26 mm. Then a new transverse crack occurs near the closer side of the edge observation region at around 0.0073 strain. It is highly possible that CL2 events between 22-23 mm away from the sensor, recorded after 0.0071 strain in Figure 3.31.(b-2) represent the evolution of transverse crack from the unpolished edge of the specimen through the edge observation side of the specimen. Thus, CL2 represents transverse cracks in  $90^\circ$  plies. CL3 events with low amplitude and relatively high frequency properties are believed to represent delaminations at  $90^\circ/-45^\circ$  interface and damage in inner  $-45^\circ$  plies. They are mostly registered as CL2 in edge observation region in Figure 3.31.(b-2). Moreover, damage in  $-45^\circ$  plies initiate from the delaminations at  $90^\circ/-45^\circ$  interface. However, strong evidences cannot be presented neither for its correlation nor damage in  $-45^\circ$  plies. Because, wave propagation properties in this laminate does not enable to distinguish AE correspondence of damage at inner  $-45^\circ$  plies as in  $[0_2/+45_2/90_2/-45_2]_s$  lay-up configuration.

In-situ optical observation enabled to make a comparison with a previous study. IM7/8552 laminates with same lay-up configuration and very similar dimensions were tested by Wisnom *et al.* [91]. First damage mode was stated as matrix cracks on surface  $+45^\circ$  plies between 343-396 MPa. It was relied on naked eye observations. That is consistent with the stress levels of the same damage mode (between 340-350 MPa), identified by DIC in this thesis. However, in-situ edge microscopy proved that is not the first damage mode within this laminate. First damage mode in  $[+45_2/90_2/-45_2/0_2]_s$  laminates is transverse cracks in  $90^\circ$  plies that initiate at around 320-330 MPa with micro delaminations between  $\pm 45/90$  interfaces. Delamination stress levels were estimated due to the load drops in stress-strain curves, whereas damage at the inner  $-45^\circ$  plies and their stress-strain levels were not even mentioned [91]. Thanks to the multi-instrumental in-situ damage detection techniques, all damage modes, their propagation and stress-strain levels are detected precisely in this thesis.

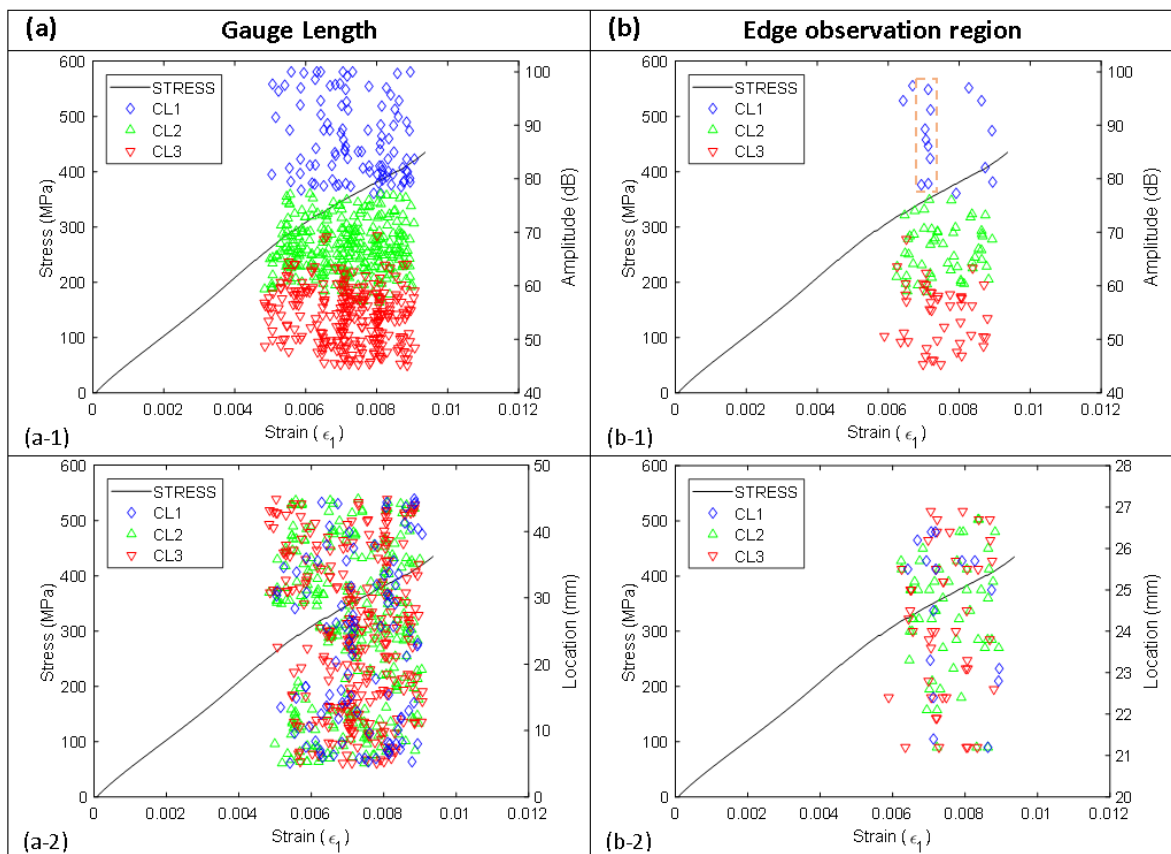


Figure 3.31. Accumulation of AE clusters throughout a test in  $[+45_2/90_2/-45_2/0_2]_s$  laminate:

- (a) full gauge length; (b) edge observation region only; (1) events amplitude; (2) events location.

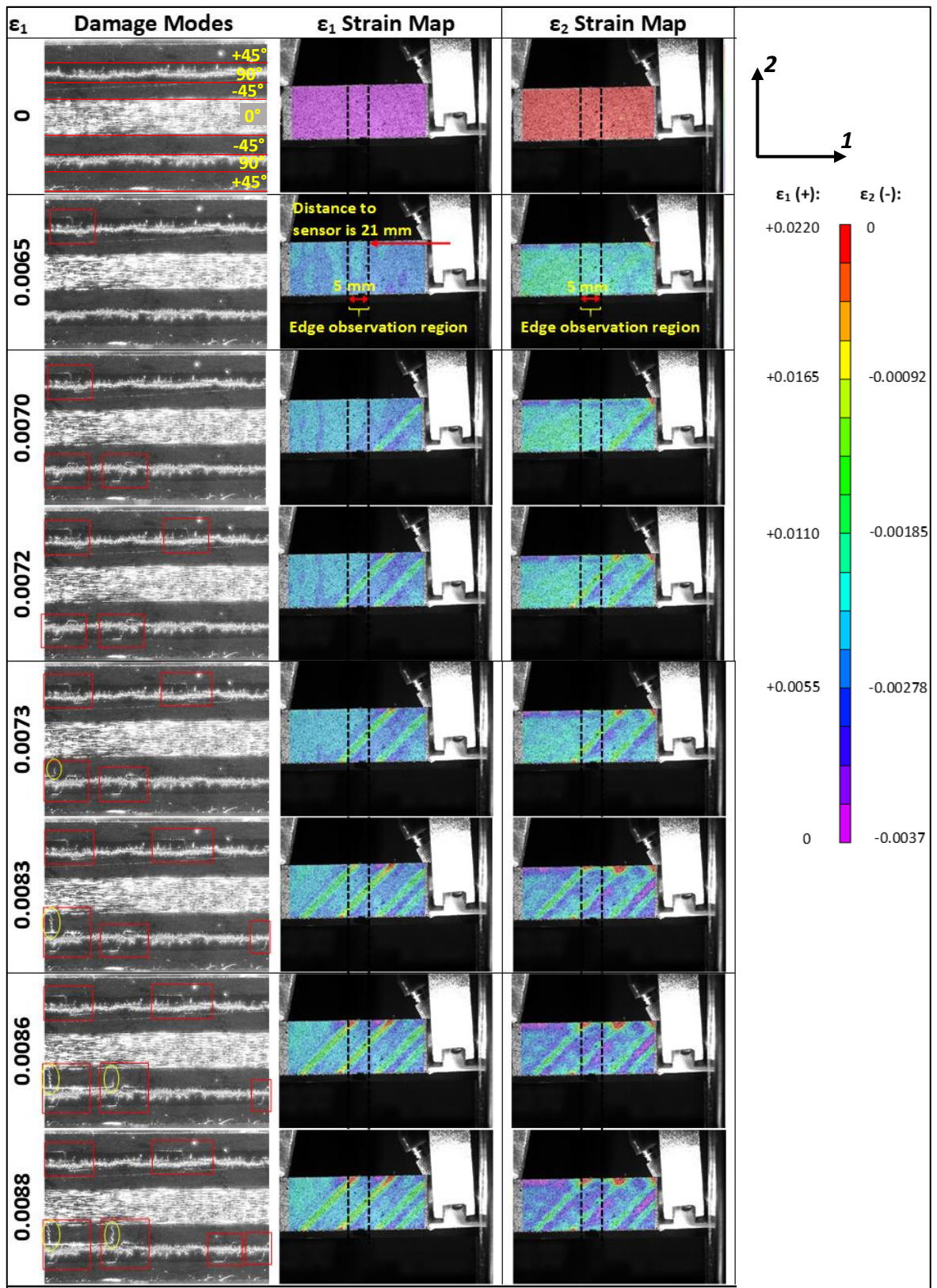


Figure 3.32. Damage progression in  $[+45_2/90_2/-45_2/0_2]_s$ .

### 3.3.5. Summary of the Damage Sequence in Smooth QI Laminates

In sections 3.3.1-3.3.4 sequence of the damage development and corresponding characteristics of the AE events for four QI laminate types were established and discussed. Table 3.3 summarizes this data with ultimate strength and strain levels of the laminates.

Five different damage modes are observed in this study that are highlighted with different colours in Table 3.3. However, no “fibre breaks” were monitored, since this failure mode probably causes lower amplitude than 40 dB or it occurs at higher strain ranges than the specimens are loaded in this experimental study. These results indicate that high frequency AE events do not necessarily represent fibre breaks.

First of all, transverse cracks occur in  $90^\circ$  plies which is followed by micro delaminations at  $90/\pm 45$  interfaces and then, transverse cracks propagate to  $\pm 45^\circ$  plies. This damage sequence is same in each laminate type. In fact they are the only damage modes observed in  $[90_2/-45_2/0_2/+45_2]_s$ ,  $[0_2/+45_2/90_2/-45_2]_s$  and  $[+45_2/90_2/-45_2/0_2]_s$  laminates. Damage in surface  $+45^\circ$  plies can be considered as transverse cracking at  $45^\circ$  plies but it is shown with a different colour in Table 3.3 due to their different AE characteristics from damage at inner  $\pm 45^\circ$  plies. Its AE characteristics are similar to surface cracks of  $[90_2/-45_2/0_2/+45_2]_s$ . Aside from these three laminates, damage progresses with macro delaminations from the free edge of  $[-45_2/0_2/+45_2/90_2]_s$  laminate after transverse cracks at inner plies.

AE detection strain levels are considered for strain ranges in Table 3.3. Transverse cracks in  $90^\circ$  plies initiate at 0.0048 strain in  $[-45_2/0_2/+45_2/90_2]_s$  laminate and micro delaminations at  $90/\pm 45$  interface occurs immediately after 0.0049 strain. Then damage propagates to  $+45^\circ$  plies at 0.0050 strain, followed by macro delamination between  $90^\circ$  and  $+45^\circ$  plies which initiates at 0.0061 strain. Similarly, transverse cracks in  $90^\circ$  plies initiate in  $[90_2/-45_2/0_2/+45_2]_s$  laminate at 0.0048 strain as surface cracks. Micro delamination at  $90/-45$  interface and transverse cracking at  $-45^\circ$  plies occur at the same time with  $90^\circ$  plies. Damage initiation level is delayed in  $[0_2/+45_2/90_2/-45_2]_s$  laminate. Initiation of transverse cracks in  $90^\circ$  plies are seen to occur together with micro delaminations at 0.0060 and 0.0061 strain levels respectively. Then, propagation of transverse cracks in  $\pm 45^\circ$  plies is detected at 0.0080 strain levels. AE records for  $[+45_2/90_2/-45_2/0_2]_s$  laminate indicates that all damage

types are seen at the same threshold level of 0.0048 strain but observations provide a clear sequence. Therefore, damage sequence is considered with respect to observations. Transverse cracks in  $90^\circ$  plies are observed at 0.0065 strain level. Then damage propagates to  $+45^\circ$  plies and damage initiation in these plies occur as surface cracks at 0.0069 strain level. Finally, damage in inner  $-45^\circ$  plies are seen to be started at 0.0073 strain.

Not only damage threshold levels but also the AE characteristics of damage modes are different in each laminate type. It is seen that, regardless of laminate type, micro delaminations are registered with low amplitude-low frequency events. It is found that if  $90^\circ$  or  $45^\circ$  plies are inner plies, transverse cracks in these plies have high frequency-low amplitude characteristics and large separation of these plies are registered with highest amplitude events in  $[-45_2/0_2/+45_2/90_2]_s$ . When  $90^\circ$  or  $45^\circ$  plies are on surface, damage in these plies are registered with high amplitude events as in  $[90_2/-45_2/0_2/+45_2]_s$  and  $[+45_2/90_2/-45_2/0_2]_s$ . Interesting situation is observed for  $[0_2/+45_2/90_2/-45_2]_s$  in which transverse cracks in  $90^\circ$  plies are registered with high amplitude-low frequency events and then with high frequency-low amplitude events after the initiation of damage in  $\pm 45^\circ$  plies, which have mid-level amplitude - low frequency AE characteristics. That is probably due to the initiation of damage at the inner  $\pm 45^\circ$  plies causes discontinuity of the material and changes its wave propagation properties. However, finding the reason of this situation is out of the scope of this thesis. Detailed analysis of this situation is left as a future work. Boundaries of the clusters can be seen with details in Table 3.3.

Damage sequence and their AE characteristics for these smooth QI laminates, presented in Table 3.3, are opposite to the literature, presented in Table 1.6. However, strong optical evidences in this thesis of the results in Table 3.3 prove the reliability of the results in Table 3.3. The effect of the AE sensors can be seen when the results of Section 3.2 is compared with results of this section. It is seen that, AE events with very high frequency values are registered with broadband Digital Wave B-1025 AE sensors in this section, however only AE events having frequency values between 0-300 kHz are registered with resonant type MISTRAS PK 15I sensors in Section 3.2. Moreover, the effect of lay-up sequence or stacking sequence on AE characteristics of damage modes is evident for different QI laminates as described above.

Table 3.3. Damage sequence and their AE characteristics in smooth QI laminates.

Laminates (Failure Levels)	Damage sequence	AE Characteristics		Strain Ranges
		A (dB)	WF [kHz]	
[-45 <sub>2</sub> /0 <sub>2</sub> /+45 <sub>2</sub> /90 <sub>2</sub> ] <sub>s</sub> $\left( \begin{array}{l} \sigma_u^T=540 \text{ MPa} \\ \varepsilon_u^T=0.0125 \end{array} \right)$	1. Transverse cracking in 90° plies	<66	>480	0.0048-0.0063
	2. Micro delamination at 90/+45 interface	<66	≤260	0.0049-0.0102
	3. Transverse cracking in +45° plies	<66	260...480	0.0050-0.0080
	4. Macro delamination	≥66	≤260	0.0061-0.0107
[90 <sub>2</sub> /-45 <sub>2</sub> /0 <sub>2</sub> /+45 <sub>2</sub> ] <sub>s</sub> $\left( \begin{array}{l} \sigma_u^T=520 \text{ MPa} \\ \varepsilon_u^T=0.0125 \end{array} \right)$	1. Transverse cracking in surface 90° plies	>75		0.0048-0.0105
	1. Micro delamination between 90/-45 interface			
[0 <sub>2</sub> /+45 <sub>2</sub> /90 <sub>2</sub> /-45 <sub>2</sub> ] <sub>s</sub> $\left( \begin{array}{l} \sigma_u^T=540 \text{ MPa} \\ \varepsilon_u^T=0.0123 \end{array} \right)$	1. Transverse cracking in 90° plies	≥78	<600	0.0060-0.0080
		≤78*	≥450*	0.0080-0.0100
	2. Micro delamination at 90/+45 interface	≤60	≥450	0.0061-0.0101
	3. Transverse cracking in ±45° plies	60...78	≤475	0.0080-0.0101
*: AE characteristics change from the above to these values with initiation of Transverse cracking in ±45° plies				
[+45 <sub>2</sub> /90 <sub>2</sub> /-45 <sub>2</sub> /0 <sub>2</sub> ] <sub>s</sub> $\left( \begin{array}{l} \sigma_u^T=460 \text{ MPa} \\ \varepsilon_u^T=0.0110 \end{array} \right)$	1. Transverse cracking in 90° plies	60...77	≤400	0.0048-0.0088
	2. Micro delaminations at 90/±45 interface	≤60		0.0048-0.0088
	3. Damage in surface +45° plies	>77	<400	0.0069-0.0083
	4. Transverse cracking in -45° plies	≤60		0.0073-0.0088

### 3.4. Damage Mode Identification in Open-Hole Quasi-Isotropic Laminates

Tension test results of quasi-isotropic laminates with a central hole are presented in this section. The presence of a 2.5 mm hole causes considerable changes in damage progression and AE characteristics of these damage modes in OHT specimens. Figure 3.33 presents test results for all layups of OHT specimens, combining in one graph stress-strain curve and parameters of the AE events: Amplitude with cumulative AE energy and weighted frequency. Different colours of the symbols and lines represent a different test. The specimens are not tested up to the final failure as in smooth specimens. Figure 3.33 shows that the measurements for different specimens with the same layup present small scatter. Stress-strain curves for the different layups are the same within the experimental scatter, which is of no surprise. AE patterns, both expressed as cumulative energy curves and as distribution of the amplitude and frequency of the events change considerable as lay-up orientation changes.

First registered AE events generally have low amplitude characteristics. The average amplitude values of registered events increase through the end of the test. On the other hand, laminates in which  $90^\circ$  plies are positioned near the mid-ply have large number of high frequency events (see  $[-45_2/0_2/+45_2/90_2]_s$  and  $[0_2/+45_2/90_2/-45_2]_s$  in Figure 3.33.(a) and Figure 3.33.(c) respectively). Weighted frequency values of registered events range between 100-400 kHz for the laminates in which  $90^\circ$  plies are positioned at or adjacent to surface plies (see  $[90_2/-45_2/0_2/+45_2]_s$  and  $[+45_2/90_2/-45_2/0_2]_s$  in Figure 3.33.(b) and Figure 3.33.(d) respectively). These overall characteristics of AE results are similar to smooth QI specimen results in Figure 3.18. However, detailed analysis of test results in further subsections show that damage modes and their progression throughout the tests change due to the presence of a central hole and the lay-up configuration within the QI laminates.

In-situ multi instrumental damage detection techniques applied in this thesis enables to make comparison with the results of previous studies regarding OH tests of QI CFRP laminates where less or no in-situ damage detection techniques were applied [66–68, 78, 92–97].



### 3.4.1. [-45<sub>2</sub>/0<sub>2</sub>/+45<sub>2</sub>/90<sub>2</sub>]<sub>s</sub> OHT Laminates

First laminate type in consideration is [-45<sub>2</sub>/90<sub>2</sub>/+45<sub>2</sub>/0<sub>2</sub>]<sub>s</sub>. Consistency between mechanical test and AE results for five tests can be seen in Figure 3.33.(a). Ultimate strength of this laminate is 392 MPa, however the highest stress and strain values in Figure 3.33 are the levels where the tests are stopped. Figure 3.33.(a) shows that amplitude and energy levels of AE events increase with increasing strain throughout the tests. At the same time, high weighted frequency events are registered at low strain levels whereas, low weighted frequency values are registered at higher strain levels.

Optimal cluster number is found to be four and their groups are presented in terms of weighted frequency vs. amplitude since the clusters are well-separated with respect to these parameters. Distribution of cluster groups from a representative test and the average values of the boundaries, calculated from the five tests are shown in Figure 3.34.(a) and Figure 3.34.(b) respectively. Accumulation of AE events with respect to these clusters throughout the test is shown in Figure 3.35.(a). Central hole is placed between 21.5 to 24 mm distance to AE sensor. Edge observation region is around 21 to 26 mm, but due to discrepancy between AE detection and real locations, 20 to 26 mm distance to AE sensor is considered in Figure 3.35.(b). Considerable number of events are started to be recorded at 0.0025 strain level which means that damage initiation strain level is 0.0025 for the five tests. Presence of a central hole decreases damage initiation level to almost its half from smooth laminate type (see Table 3.3). On the other hand, accumulation of AE events is similar to smooth specimens; first low-amplitude/high frequency events (CL3-CL4) are registered, then the number of high-amplitude/low-frequency events (CL1) increase considerably through the end of the test in Figure 3.35.

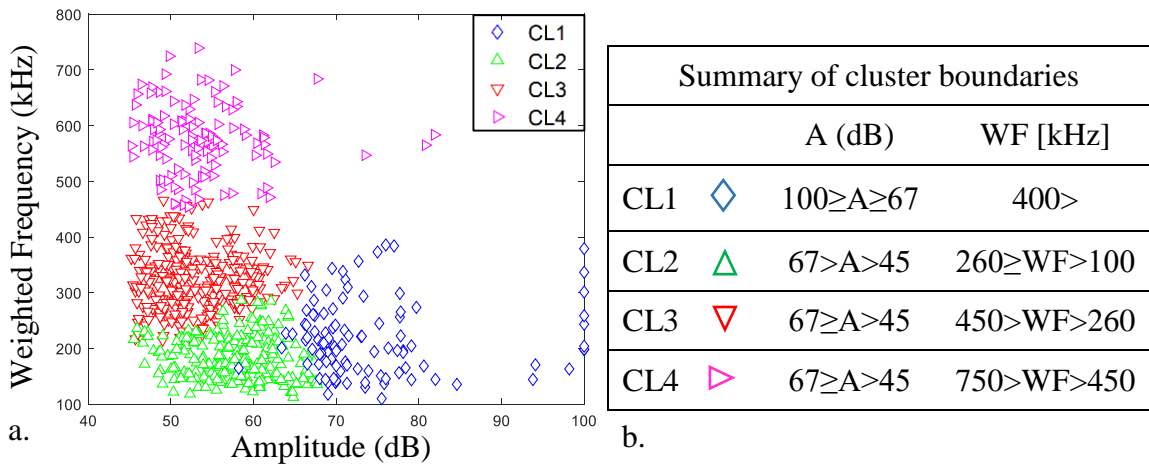


Figure 3.34. (a) Distribution of AE clusters in a representative test, (b) Summary of cluster boundaries from five tests for  $[-45_2/0_2/+45_2/90_2]_s$ .

A correlation between AE events in Figure 3.35 and damage progression in Figure 3.36 can be done. Although first AE event is registered at 0.0025 strain, the first damage observed at the edge is a transverse crack in mid- $90^\circ$  plies at 0.0035 strain. This is probably due to the fact that the transverse cracks initiate at the notch root at lower strain levels and progress to the edge observed at higher strain levels. Micro delamination at  $+45/90$  interface is seen at 0.0067 strain level. Low-amplitude/high-frequency events (CL4) and low-amplitude/mid-frequency (CL3) events are recorded mostly up to 0.0067 strain level of the test in Figure 3.35. Then, macro delamination at  $+45/90$  interface initiates from the free edge of the specimen and near the upper grip (very close to the AE sensor clamp on the right side in Figure 3.36 at this strain level. Large contraction in transverse direction ( $\epsilon_2$ ), due to separation of  $+45^\circ/90^\circ$  plies, is shown in white rectangles Figure 3.36 (green-blue region at 00067 – 0.0076 strains, and blue-purple regions at higher strain levels in Figure 3.36). Initiation of macro delamination at 0.0067 strain level and its propagation in Figure 3.36 is highly consistent with registration and accumulation of high-amplitude/low-frequency AE events (CL1) in Figure 3.35. The location of delamination initiation region of the specimen is concentrated at 5 mm distance to AE sensor as seen in Figure 3.35.(a-3). This proves the aforementioned location of delamination initiation and shows its propagation throughout the test. 5 mm distance is very close to the AE sensor and it is out of AoI for DIC. That is why delamination propagation cannot be seen at 0.0067 strain level in Figure 3.36. Also, some

CL1 events can be seen at 0.0042 strain level in Figure 3.35.(b). It is highly possible that these events represent delamination initiation around hole region since their locations are between 22 – 24 mm. Second transverse crack in mid-90° plies occurs with transverse cracks in adjacent +45° plies and micro delaminations at their interface at 0.0076 strain level in Figure 3.36. Meanwhile, large contraction in transverse direction at  $\varepsilon_2$  strain map can be seen clearly now. Number of CL1 events increase rapidly while the registration of CL3-CL4 events almost stops after this strain level of the test, as clearly seen in Figure 3.35. Progression of macro delamination through the gauge length can be noticed by tracking the CL1 events from 0.0062 strain through the end of the test in Figure 3.35.(a-3). They climb up to the further regions through the gauge length in Figure 3.35.(a-3). Damage progression and AE registration up to this strain level shows that low-amplitude/high-frequency events (CL4) with low-amplitude/mid-frequency events (CL3) represent damage at inner 90° and +45° plies respectively, while high-amplitude/low-frequency events (CL1) represent macro delamination at +45/90 interface. Difference between transverse cracks in 90° and +45° plies can be determined by following the propagation of CL3 in Figure 3.35.(b-3). These events propagate from the hole region toward the AE sensor. It is highly possible that these events are transverse cracks in +45° plies whose propagation direction is aligned 45° from the test direction. Propagation of this damage mode can be identified with propagation of yellow-red coloured regions near the hole in  $\varepsilon_1$  strain map of Figure 3.36 until 0.0082 strain level. After this strain level, macro delaminations at +45/90 interface becomes dominant and its CL1 events dominate other AE events. Thus, it can be said that CL3 events represent damage at the inner +45° plies, while CL4 events are transverse cracks in 90° plies. Finally, CL2 represents micro delaminations at 90/+45 interface. They initiate at 0.0050 strain level and continue up to the end in Figure 3.35. This correlation is the same as the smooth [-45<sub>2</sub>/0<sub>2</sub>/+45<sub>2</sub>/90<sub>2</sub>]<sub>s</sub> laminate in Section 3.3.1.

It is seen that macro delaminations at +45/90 interface are identified with DIC technique in smooth [-45<sub>2</sub>/0<sub>2</sub>/+45<sub>2</sub>/90<sub>2</sub>]<sub>s</sub> laminate in section 3.3. Open-hole type of this laminate provides to identify transverse cracks at inner +45° plies with  $\varepsilon_1$  strain map, in addition to macro delamination with DIC technique. This was not mentioned in literature before. Its validity is verified with in-situ AE and edge microscopy techniques. This is a very important finding for the use of DIC in terms of damage detection.

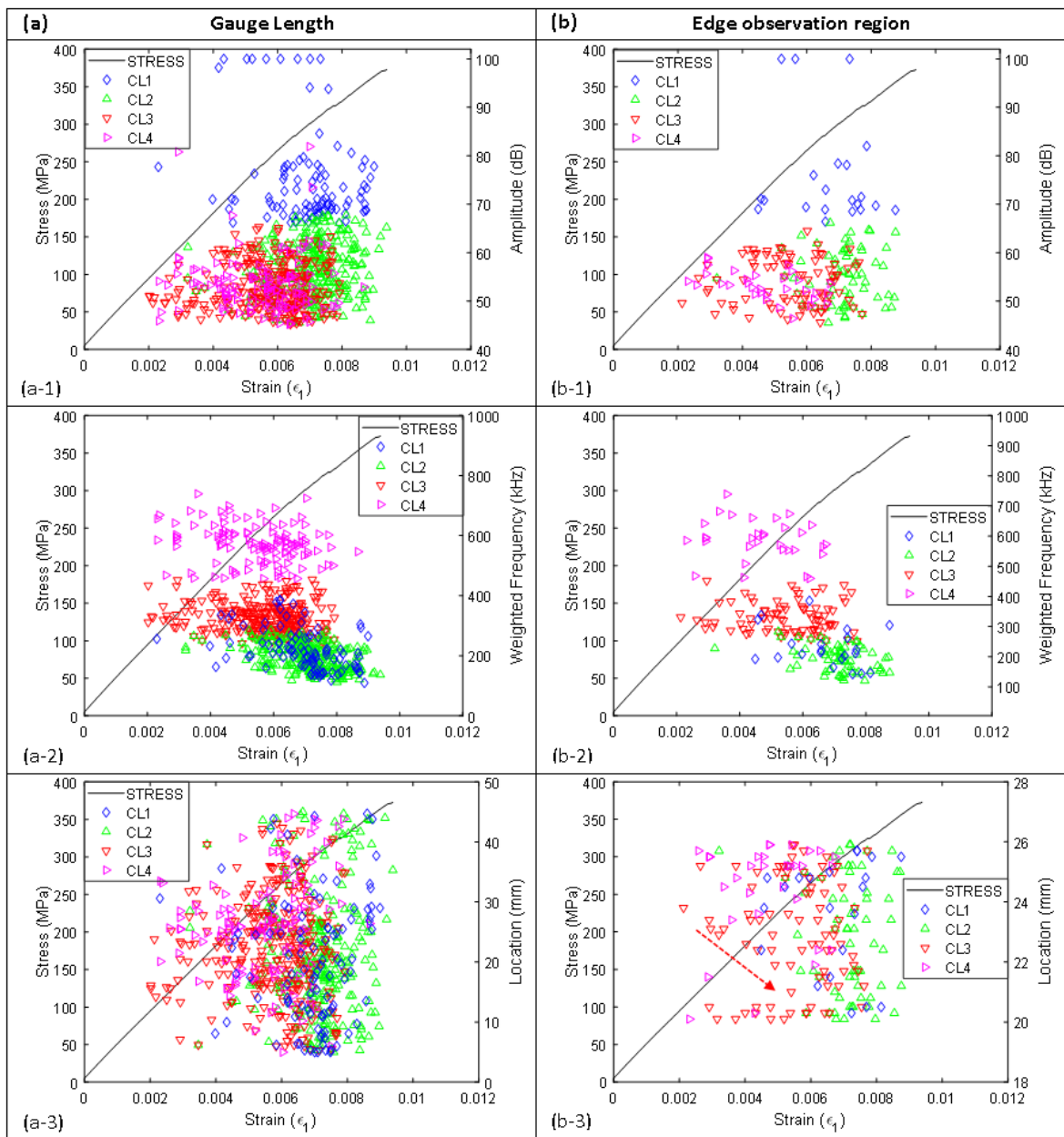


Figure 3.35. Accumulation of AE clusters throughout a test in  $[-45_2/0_2/+45_2/90_2]_s$  laminate:  
 (a) full gage length; (b) edge observation region only; (1) events amplitude; (2) events  
 weighted frequency; (3) events location.

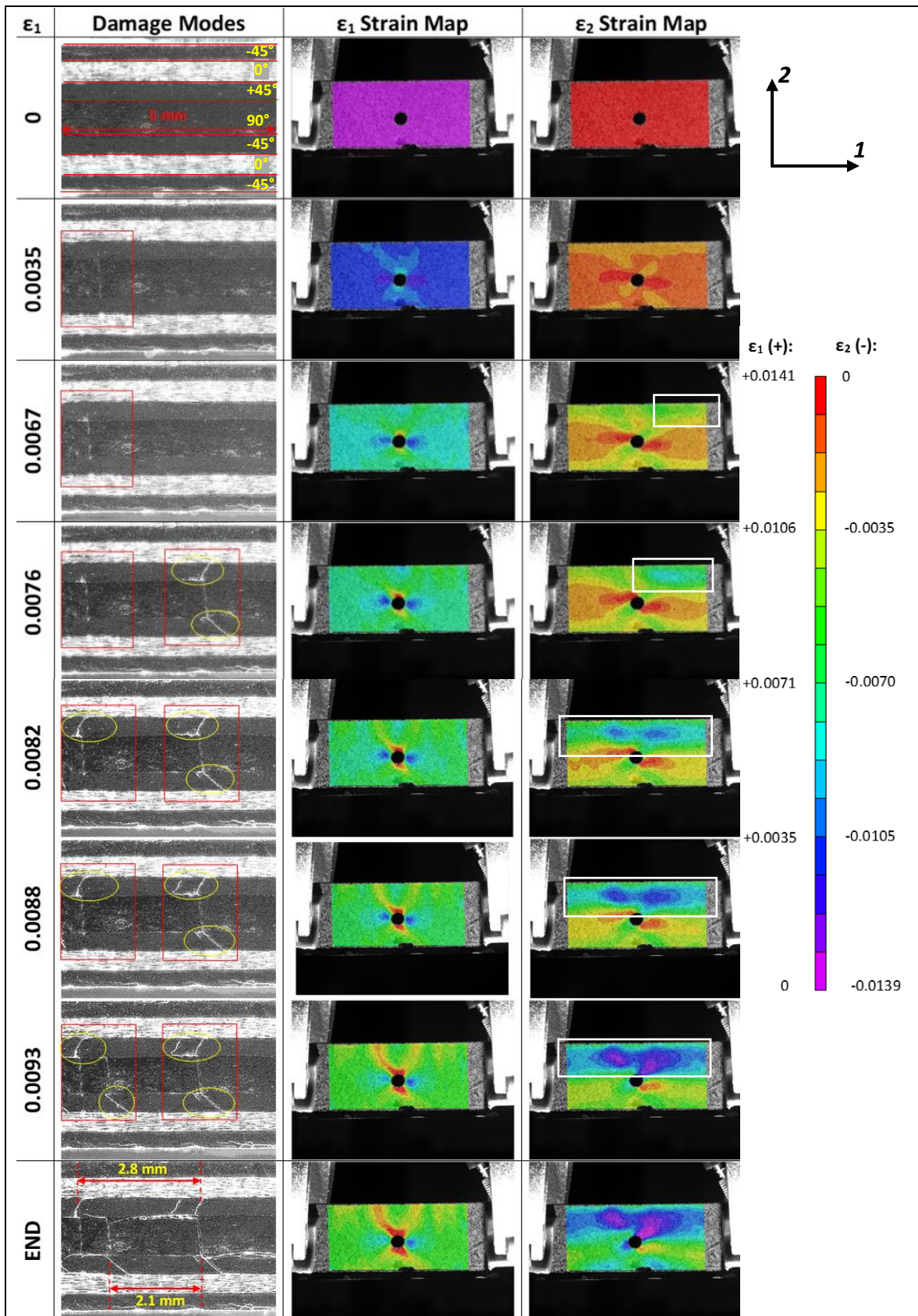


Figure 3.36. Damage progression in  $[-45_2/0_2/+45_2/90_2]_s$  laminate.

### 3.4.2. $[90_2/-45_2/0_2/+45_2]_s$ OHT Laminates

Second laminate in consideration is  $[90_2/-45_2/0_2/+45_2]_s$ . Laminates consisting  $90^\circ$  plies on surface are favourable specimens for DIC measurements. Because the highest number of transverse cracks occur in  $90^\circ$  plies, the surface cracks in the  $90^\circ$  plies can be easily detected with DIC [66].

Consistency of test results for  $[90_2/-45_2/0_2/+45_2]_s$  laminates can be seen in Figure 3.33.(b). Representation of clusters with respect to the weighted frequency and amplitude is shown in Figure 3.37. It is similar to the cluster groups in Figure 3.34 but some cluster groups in Figure 3.37 (CL2-CL3) overlap each other and not well separated as in Figure 3.34. That is due to most of the high frequency contents are limited between 100 – 400 kHz and it reduces the selective characteristics of frequency contents and cannot separate clusters distinctly. Hence causes overlapping during clustering. However, this does not prevent to obtain AE classification for damage modes.

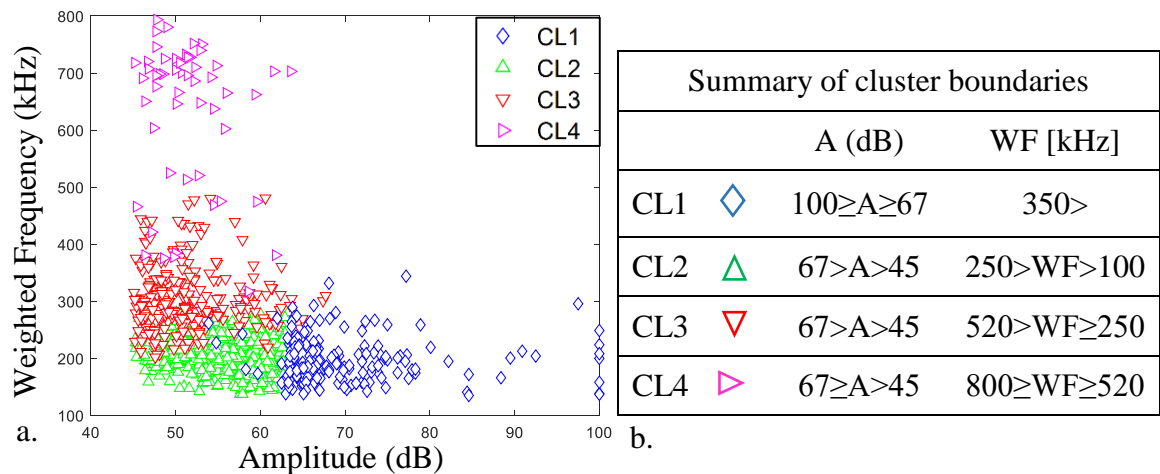


Figure 3.37. (a) Distribution of AE clusters in a representative test (b) Summary of cluster boundaries from five tests for  $[90_2/-45_2/0_2/+45_2]_s$ .

Damage initiation strain level is 0.0029 in the whole gauge length whereas, the first damage occurs at 0.0032 strain level in Figure 3.38.(a). Initially, the density of low-amplitude/low-frequency events (CL2) and low-amplitude/mid-frequency events (CL3) are higher than the other two clusters. Then, the density of the CL3 and low-amplitude/high frequency events (CL4) increases after 0.0059 strain level. Increasing number of events from these clusters are more prominent in the edge observation region as shown in Figure 3.38.(b). Finally, large number of high amplitude events (CL1) are started to be registered after 0.0062 and 0.0078 strain levels in the gauge length and edge observation region in Figure 3.38.(a) and Figure 3.38.(b) respectively.

First transverse crack is detected in bottom 90° plies in Figure 3.39 at 0.0037 strain, much later than the first AE registration at 0.0029 strain. Then, a transverse crack initiates at opposite side of hole on surface plies at 0.0045 strain level. This damage propagates and becomes visible from edge observation region at 0.0047 strain level in Figure 3.39. At the same time, delamination around the hole region initiates at this strain level in Figure 3.39. Micro delamination at 90°/-45 interface of top plies are becoming visible at the edge observation region at 0.0067 strain level. Quickly after, surface crack at the hole region becomes more detectable on the DIC strain map at 0.0068 strain level. At the same time, large delaminations become visible around the hole region (purple coloured regions in the  $\epsilon_2$  strain map in Figure 3.39). After this strain level, multiple surface cracks occur in surface 90° plies and delaminations around the hole propagate up to the end of the test. Meanwhile, two transverse cracks occur in -45° plies. One occurs in the upper -45° plies is at 0.0075 strain level, which is shown by using the edge micrograph at 0.0078 strain level in Figure 3.39 and the other one occurs at 0.0090 strain level which is the end of the test in Figure 3.39.

Correlation between damage modes and the corresponding AE events can be done by comparing Figure 3.38 and Figure 3.39. First registered AE events at 0.0032 strain level in the edge observation region belong to low-amplitude/low-frequency (CL2) and low-amplitude/mid-frequency events (CL3) mostly with the initiation of first transverse cracks in 90° plies. Then, low amplitude/high-frequency events (CL4) are registered in the edge observation region in Figure 3.38.(b) after 0.0064 strain level. Damage initiations at upper and lower -45° plies can be noticed in edge observation region at 0.0068 strain in Figure 3.39. A transverse crack through the thickness of the upper -45° plies occurs at 0.0075 strain

level. This damage mode is shown at 0.0078 strain level in Figure 3.39. The progression of damage in  $-45^\circ$  plies is highly consistent with accumulation of CL4 events which proves that AE events from this group represent transverse cracks at  $-45^\circ$  plies. However, due to large amount of surface cracks after 0.0078 strain, the continuity in the material decreases and the signal path becomes more tortuous, hence damage in lower  $-45^\circ$  plies at the end (0.0090 strain level) is detected at 28 mm distance from AE sensor, not its exact position of between 26-27 mm. It is not easy to distinguish the AE characteristics of surface cracks and delaminations around the hole region, because their propagation and accumulation of CL1-CL2 and CL3 all happen at the same time as seen from Figure 3.38.(b) and Figure 3.39. It was found that AE characteristics of surface cracks were registered with high amplitude events in unnotched  $[90_2/-45_2/0_2/+45_2]_s$  laminate. This statement is valid for the central-holed version of the same laminate in this study. Figure 3.38.(a) shows that, CL1 events propagate to the further regions through the end of the test, whereas CL3 events are mostly clustered around the hole region (between 20-32 mm). Multiple surface cracks occur in different regions on the specimen surface in Figure 3.39 that is consistent with accumulation of CL1 events. Delaminations around hole region are localized between 20-30 mm. After 0.0078 strain level, delaminations (shown with purple colour in  $\epsilon_2$  strain map in Figure 3.39) start propagation in longitudinal direction (through the gauge length). This is consistent with accumulation of CL3 events after 0.0078 strain level in Figure 3.38. It can be concluded that; high-amplitude events (CL1) represent surface cracks, low-amplitude/mid-frequency events (CL3) events represent delaminations around hole region, and low-amplitude/high-frequency events (CL4) represent damage at inner  $\pm 45^\circ$  plies, but mostly in  $-45^\circ$  plies as evidenced in Figure 3.39. Finally, low-amplitude/low-frequency events (CL2) represent micro delaminations at  $-45/90$  interface due to the transverse cracks in  $90^\circ$  plies.

Transverse cracks in  $90^\circ$  plies (or surface cracks) in smooth  $[90_2/-45_2/0_2/+45_2]_s$  laminates are seen to happen with transverse cracks at adjacent  $-45^\circ$  plies. However, presence of a central hole causes the latter to occur after the first one. In addition to this, while a damage on surface propagates to the entire width of the smooth  $[90_2/-45_2/0_2/+45_2]_s$  laminate, this occurs gradually around the hole of the OHT type. This is due to the damage is concentrated around the hole, and causes delaminations. Then, it propagates to width. On the other hand, only surface cracks are correlated with AE correspondence in smooth type, whereas, different damage modes are correlated with their AE correspondence for OHT type.

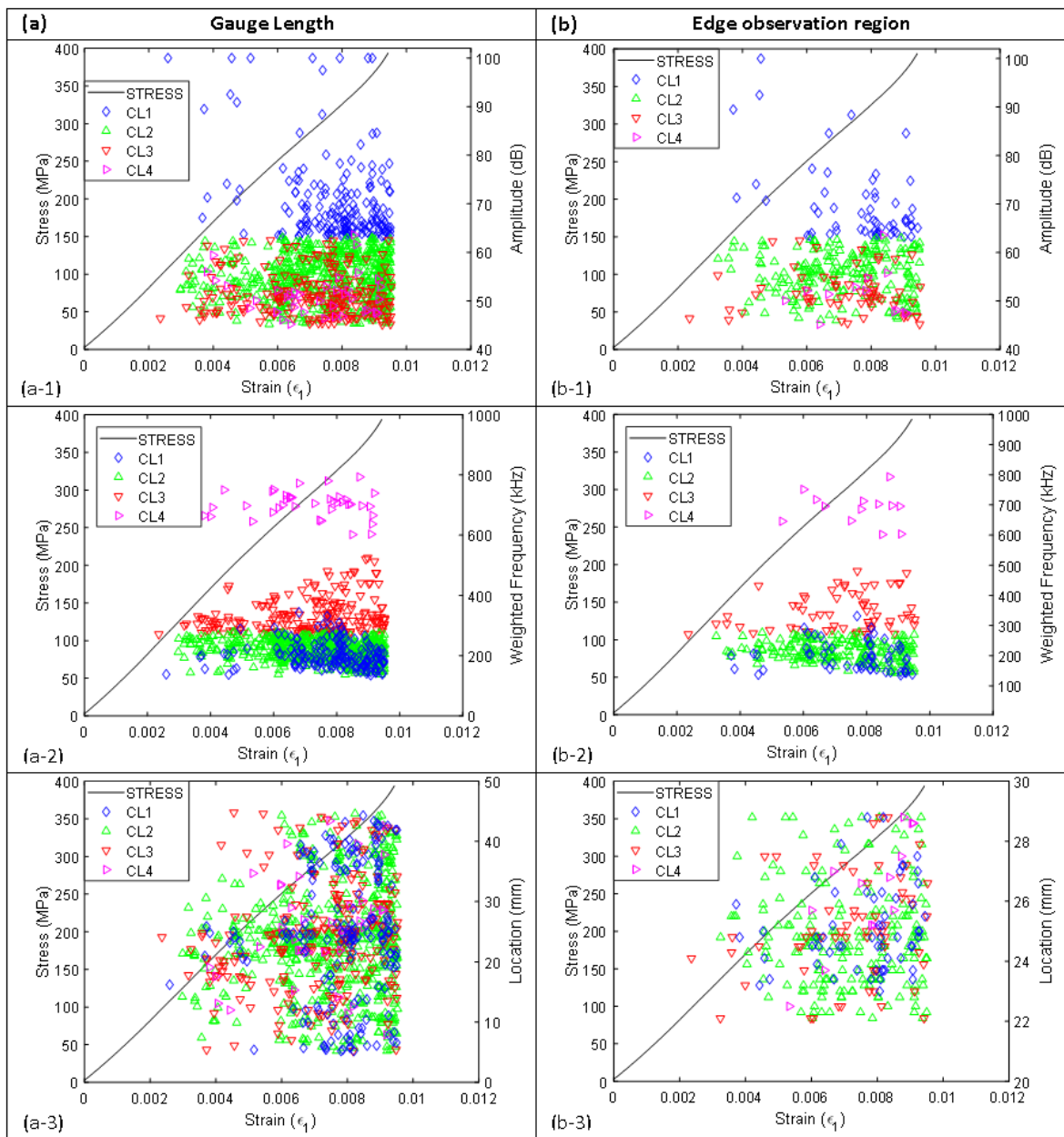


Figure 3.38. Accumulation of AE clusters throughout a test in  $[90_2/-45_2/0_2/+45_2]_s$  laminate:  
 (a) full gage length; (b) edge observation region only; (1) events amplitude; (2) events weighted frequency; (3) events location

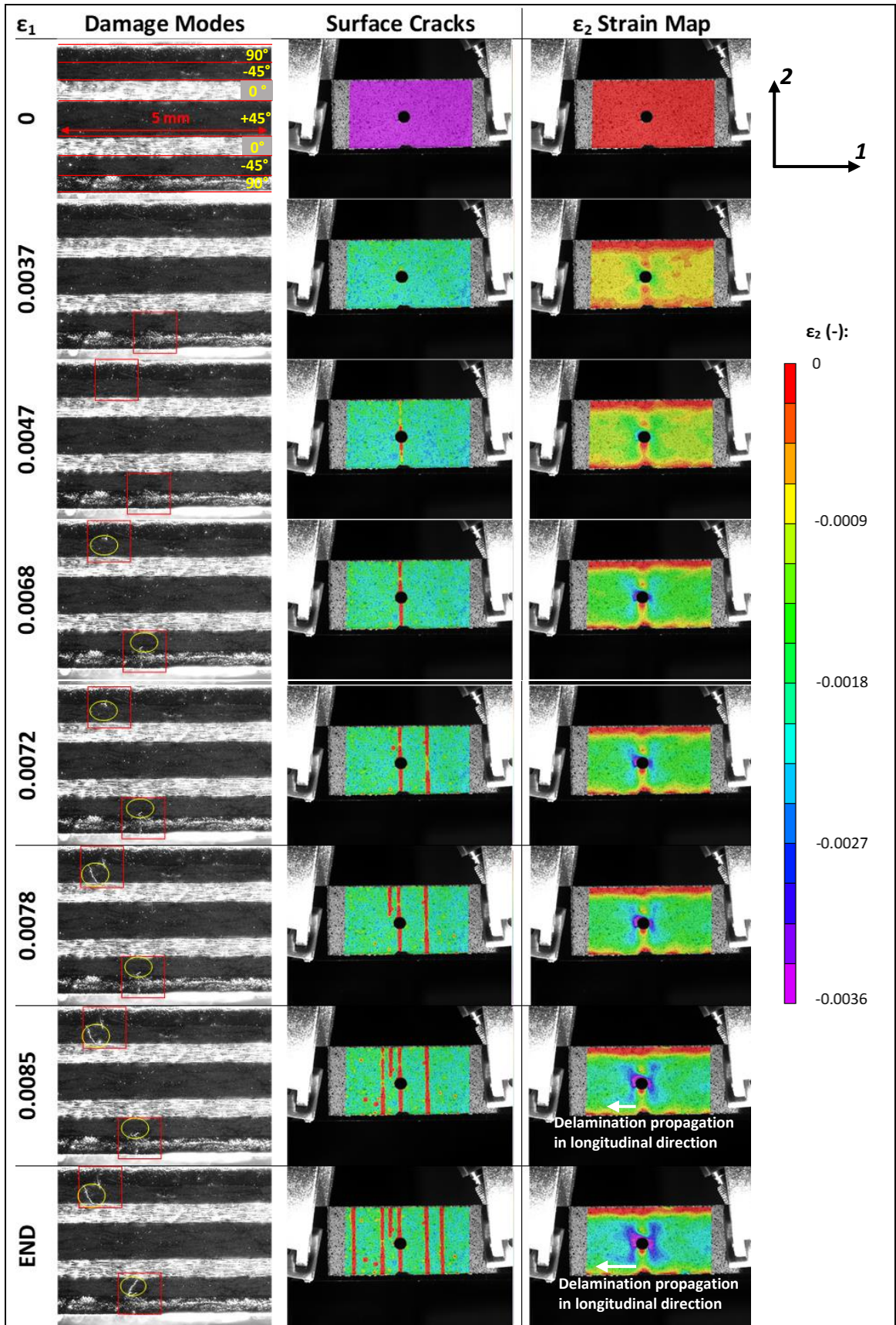


Figure 3.39. Damage progression in  $[90_2/-45_2/0_2/+45_2]_s$  laminate.

### 3.4.3. $[0_2/+45_2/90_2/-45_2]_s$ OHT Laminates

Thirdly,  $[0_2/-45_2/90_2/+45_2]_s$  laminates are tested. Stress-strain responses of five tests with cumulative AE energy-amplitude and weighted frequency parameters are presented in Figure 3.33.(c) Number of high amplitude events ( $A > 65$  dB) in Figure 3.33.(a) is more than in previous laminate types. High frequency events are mostly registered between 0.0042-0.0060 strain levels in Figure 3.33.(c). Figure 3.40 shows the cluster distributions and the average boundary values of these clusters. The trend is similar to previous laminate types. However, there is one distinction. Five damage modes are observed during tension tests of this laminate as stated below. It is seen that CL1 in Figure 3.40 represents two damage modes. 80 dB amplitude level is the boundary that separates AE characteristics of each damage mode. CL1 events with amplitude level greater than 80 dB are named as CL1-2.

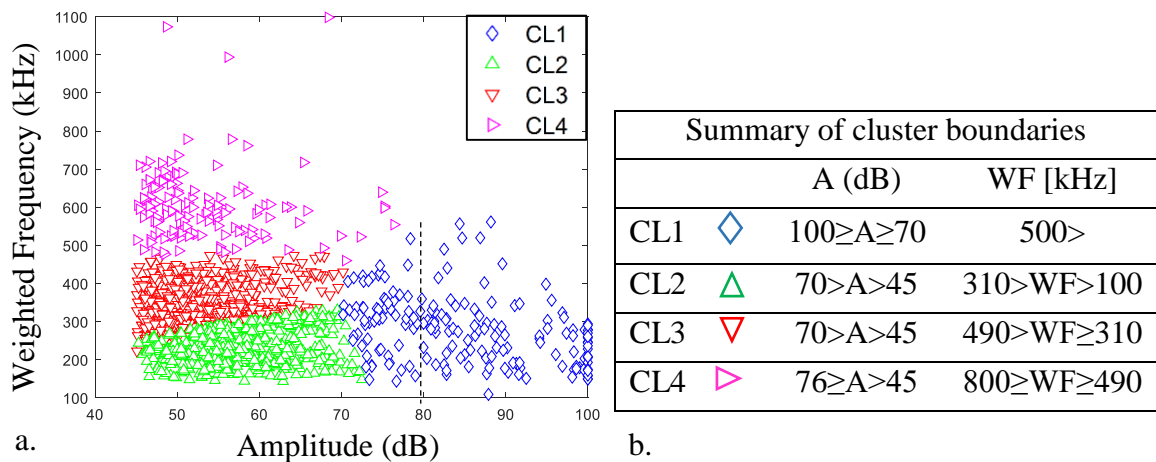


Figure 3.40. (a) Distribution of AE clusters in a representative test (b) Summary of cluster boundaries from five tests for  $[0_2/+45_2/90_2/-45_2]_s$ .

Average strain level for damage initiation is 0.0044. Accumulation of cluster throughout the test is presented in Figure 3.41. Density of low amplitude/high frequency AE events (CL4) is very high between 0.0042 – 0.0060 strain levels. This is more prominent for the edge observation region, where almost no events from this group are registered after 0.0073 strain level in Figure 3.41.(b). Conversely, the number of high-amplitude/low-frequency events (CL1 and CL1-2) increase after 0.0067 strain level. Low amplitude/low

frequency events (CL2) are registered evenly through the tests. Low amplitude/mid-frequency events (CL3) goes evenly up to 0.0088 strain level and then decreases.

Figure 3.42 presents damage progression in  $[0_2/+45_2/90_2/-45_2]_s$  laminate. Although the first AE events occur as early as 0.0042 strain, first transverse crack in  $90^\circ$  plies are seen to happen at 0.0058 strain level in the edge observation region. The delay can be attributed to the fact that the damage initiates around the hole and then reaches to the edge later during the test. Three transverse cracks initiate up to 0.0066 strain level. This is the strain level when the initiation of transverse crack at the upper  $+45^\circ$  plies is seen from the edge observation region in Figure 3.42. Moreover, splitting in surface  $0^\circ$  plies start at this strain level. That is due to the fibre/matrix debonding. Debonding propagates quickly until 0.0074 strain level. Red coloured regions in the  $\varepsilon_2$  strain map in Figure 3.42 represents fibre/matrix debonding. Considerable number of transverse crack at the mid  $-45^\circ$  plies occur at 0.0089 strain level. At the same time, large delaminations around the hole region and near the free edge occur at this strain level too. That is identified with the contraction in the transverse direction in  $\varepsilon_2$  strain map in Figure 3.42. After this strain level, number of cracks, seen from the edge observation region, saturates. Only debonding and macro delaminations around the hole and near the free edge propagates slowly until the end of the test.

Comparison of Figure 3.41 and Figure 3.42 can enable to make correlations between damage modes and AE events. High density of CL4 events up to 0.0060 strain level in Figure 3.41.(b) correspond to the transverse cracks at the  $90^\circ$  plies. They initiate around the hole and propagate through the edge. A transverse crack is seen from the edge observation region at 0.0058 strain level, and the number of CL4 events decreases after 0.0066 strain level. Damage initiates at the notch tip at 0.0058 strain level. This is noticed from the  $\varepsilon_1$  strain map in Figure 3.42. It blunts the notch until 0.0067 strain level and then causes splitting in surface  $0^\circ$  plies. It propagates quickly until 0.0074 strain level. Splitting can be noticed with red coloured region through the specimen length in  $\varepsilon_2$  strain map in Figure 3.42. Registration of high number of CL3 events up to 0.0088 strain level is seen in Figure 3.41.(b), and their density decreases after this strain level. Multiple number of transverse cracks in  $\pm 45^\circ$ , containing the damage in mid  $-45^\circ$  plies, occur at 0.0089 strain level in Figure 3.42. They do not propagate and remain stagnant up to the end of the test. Accumulation of CL3 events and propagation of transverse cracks in  $\pm 45^\circ$  plies stop at the same strain level in Figure 3.41 and Figure 3.42 respectively. It is highly possible that low-amplitude/mid-frequency events

(CL3) correspond to transverse cracks in  $\pm 45^\circ$  plies. Density of high amplitude events (CL1 and CL1-2) increase after 0.0066 strain level in Figure 3.41. Their accumulation is consistent with splitting in surface  $0^\circ$  plies and increasing amount of macro delaminations around the hole region and near the free edge in Figure 3.42. In order to correlate each high amplitude clusters with these damage modes, locations of each CL1 and CL1-2 events are plotted in Figure 3.43. It should be noted that the location detecting AE sensor is placed on the right side in Figure 3.42. AE events from the both cluster groups are mostly registered between 20-30 mm distance to the AE sensor. CL1-2 events ( $A > 80$  dB) are registered from further distances to the sensor after 0.0068 strain level in Figure 3.43. This is consistent with propagation of macro delaminations from the free edge of the specimen in Figure 3.42. Meanwhile, CL1 events are registered between 20-30 mm after 0.0066 strain level and that is highly consistent with propagation of splitting in surface  $0^\circ$  plies. Hence, highest amplitude events ( $A > 80$  dB) represent macro delaminations at  $\pm 45/90$  interface, whereas CL1 events ( $80 > A > 70$  dB) represent fibre/matrix splitting in surface  $0^\circ$  plies. Finally, the highest number of registered events have low-amplitude/low-frequency characteristics. They are CL2 events which are accumulated from the damage initiation level up to the end of the test in Figure 3.41. These events represent micro delaminations at the  $\pm 45/90$  interfaces which always happen simultaneously with a transverse crack in  $90^\circ$  plies.

DIC strain map of smooth  $[0_2/+45_2/90_2/-45_2]_s$  laminate do not enable to detect any fibre/matrix splitting on the specimen surface. However, this damage mode is seen to happen in OHT type due to the presence of a hole. AE characteristics of transverse cracks in  $90^\circ$  plies of smooth type shift from high amplitude to high frequency cluster. This situation is not observed for the OHT type. Probably, due to the high amplitude characteristics of large delaminations around the hole and fibre/matrix splitting on surface  $0^\circ$  plies reduces the sensitivity for AE registration and this prevents to observe such a detailed consequence of change in wave propagation property of the laminate. Not only for  $[0_2/+45_2/90_2/-45_2]_s$  laminate but also for the other OHT specimens, high amplitude AE events due to macro delaminations around the hole region prevent to register corresponding AE signals of micro damage modes sensitively.

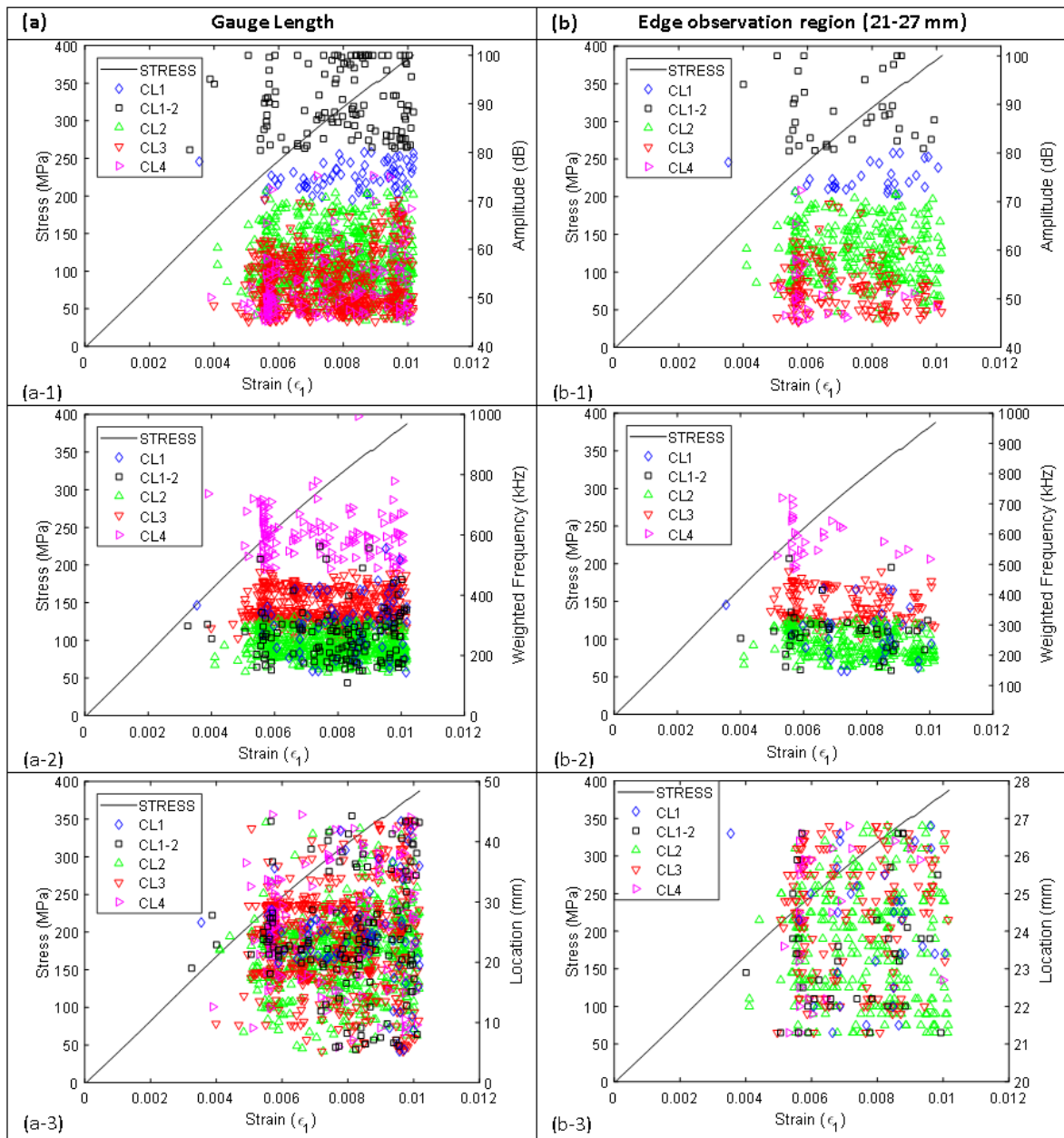


Figure 3.41. Accumulation of AE clusters throughout a test in for  $[0_2/+45_2/90_2/-45_2]_s$  laminate: (a) full gage length; (b) edge observation region only; (1) events amplitude; (2) events weighted frequency; (3) location.

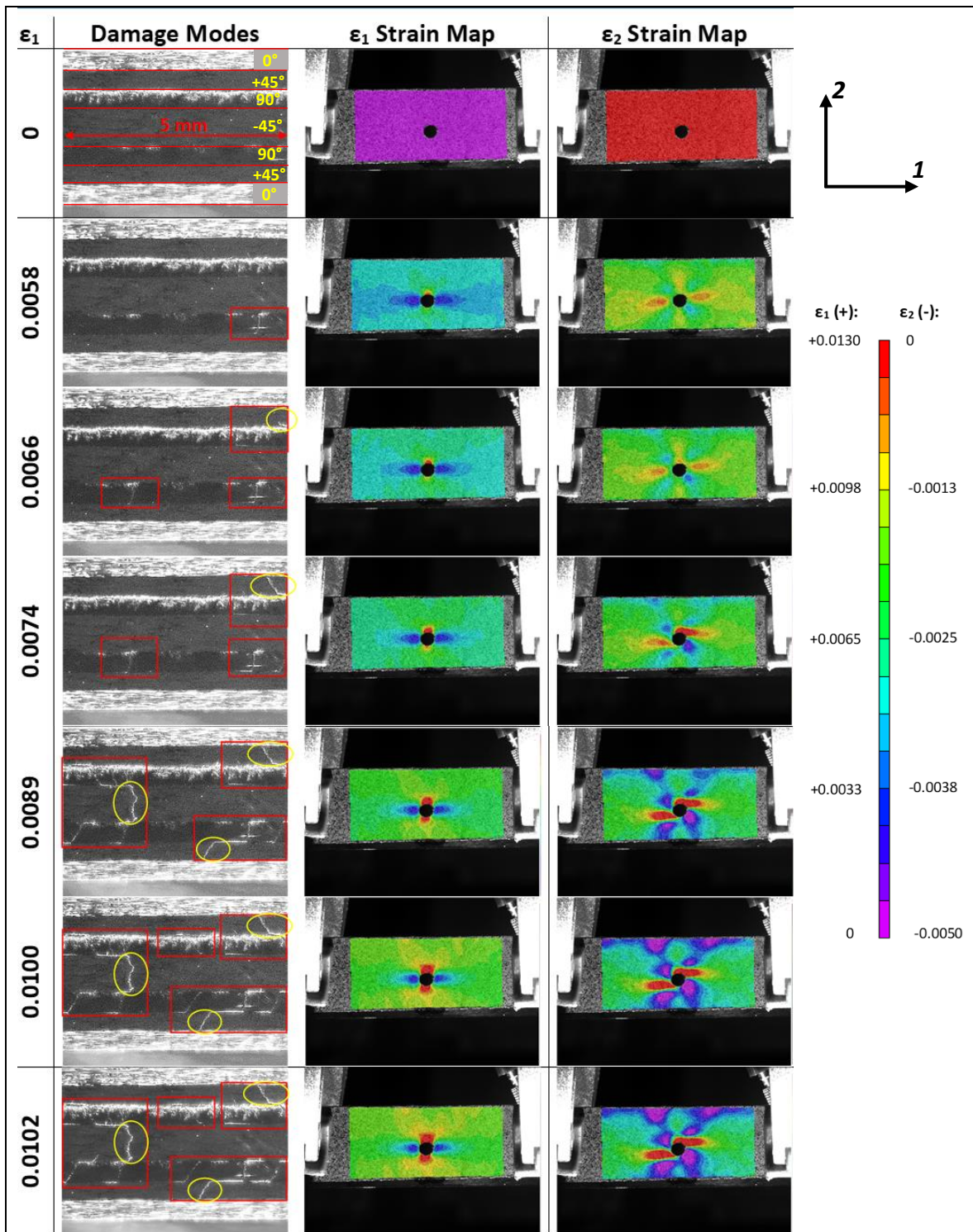


Figure 3.42. Damage progression in  $[0_2/+45_2/90_2/-45_2]_s$  laminate.

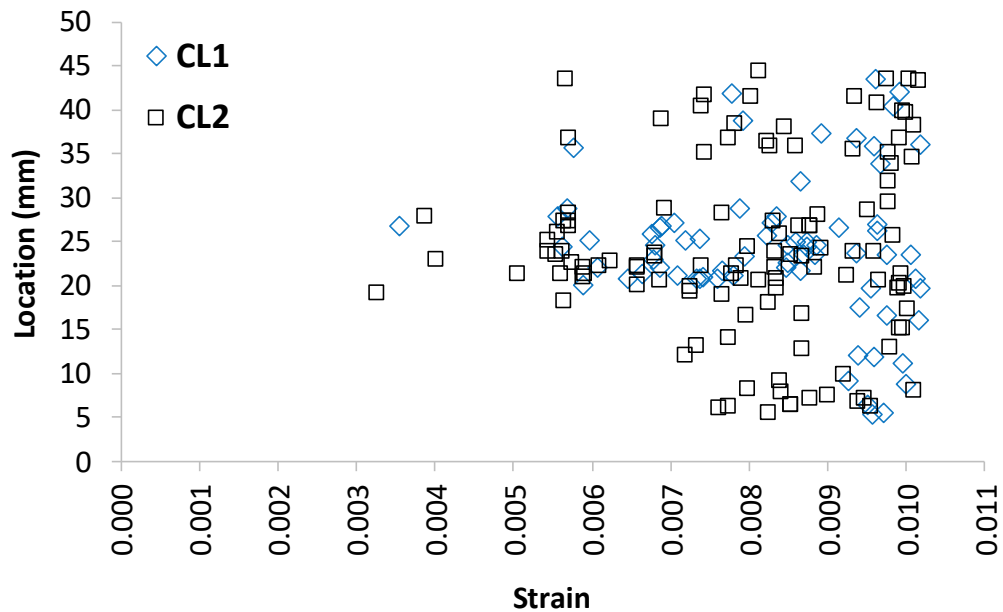


Figure 3.43. Location of high amplitude events.

#### 3.4.4. $[+45_2/90_2/-45_2/0_2]_s$ OHT Laminates

Last laminate type in consideration is  $[+45_2/90_2/-45_2/0_2]_s$ . Large delaminations can be noticed from the stress-strain curves presented in Figure 3.33.d. Average strain level for damage initiation is calculated to be 0.0044 strain from the test results in Figure 3.33.d. It is seen that the number of registered signals reduce considerably after large load drops due to the macro delaminations at around 0.0075 and 0.0081 strain levels. Load drops were stated to occur due to large delaminations at  $-45/0$  interfaces by Wisnom and Hallett *et al.* [78, 92–95]. At the same time, Figure 3.33.d shows that the weighted frequency values of registered AE events after macro delaminations decrease considerably with the macro delaminations as observed in  $[-45_2/0_2/+45_2/90_2]_s$  laminate. Cluster groups from a representative test and the average boundary values, calculated from the five tests, are presented in Figure 3.44. Cluster groups overlap on each other (CL2 and CL3) in Figure 3.44 as in  $[90_2/-45_2/0_2/+45_2]_s$  laminate.

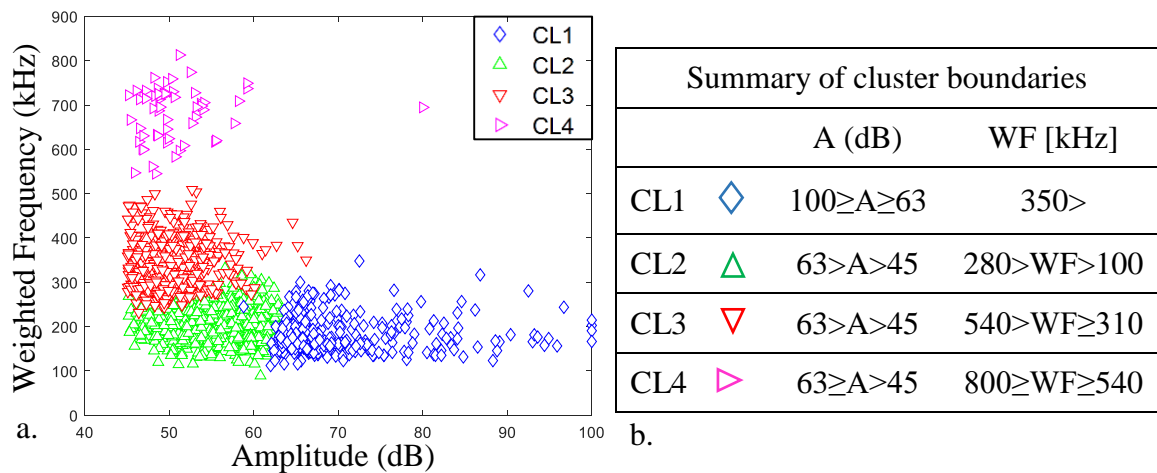


Figure 3.44. Summary of cluster groups for  $[+45_2/90_2/-45_2/0_2]_s$  (a) Clusters from a representative test (b) Cluster boundaries, averaged from five test results.

Figure 3.45 shows that damage initiation begins at 0.0046 strain level. Four cluster groups are registered at the same time with damage initiation in Figure 3.45.(a). High number of AE events with low-amplitude/high-frequency characteristics (CL3) are registered mostly after 0.0047 strain level in Figure 3.45. They are initially localized between 15 – 21 mm in Figure 16.(a-3). They propagate to the hole region after 0.0051 strain level. Then to the further regions (through 30 mm away from the AE sensor) after 0.0070 strain level. Registration of these events decrease with the load drop at 0.0076 strain level and then they disappear with the second load drop at 0.0081 strain level. High-amplitude events (CL1) are localized around the hole region since their first registration at 0.0047 strain level. Their propagation to the outer regions start after 0.0070 strain level and then to further regions after 0.0076 strain level with the load drops due to the macro delamination. It should be noted that, the distance of the central hole to the AE sensor is between 23-25.5 mm. However, location graph for edge observation region is plotted for between 21-29 mm in Figure 3.45.(a-3). Because long delaminations, propagating quickly, are seen in the edge observation region. In addition to this, delaminations around the hole region and surface cracks at  $+45^\circ$  plies propagates quickly to larger regions as will be discussed in the next paragraph. Because of this, location plot is considered for a longer region than other laminates in Figure 3.45.(a-3).

First surface crack next to the hole initiates at 0.0048 strain level and it is detected with DIC in Figure 3.46. At the same time, a free edge delamination is detected and shown within white rectangle in the  $\epsilon_2$  strain map in Figure 3.46. It is highly possible that, this free edge delamination occurs due to the transverse cracks at the inner  $90^\circ$  plies. Unfortunately, they are not detected with optical instruments before this strain level. However, during the second test of this laminate where all optical instruments are used for damage detection, it is seen that a transverse crack in  $90^\circ$  plies occurs 0.5 second before surface crack. This observation justifies the assertion. Surface crack propagates to the unobserved edge of the specimen at 0.0053 strain level. Meanwhile, the delamination grows at this strain level, approaches to the hole as shown within the white rectangle in Figure 3.46. Progression of the surface crack and delamination up to this strain level is consistent with the accumulation of CL1 and CL3 events, clearly seen in Figure 3.45.(a). Early CL3 events are registered between 15-21 mm at 0.0047-0.0052 strain levels in Figure 3.45.(a-3). Then they propagate to the hole region (22-27 mm) after 0.0052 strain level. That is consistent with the propagation of the free edge delamination, shown within white rectangle, in the  $\epsilon_2$  strain map in Figure 3.46. Then they accumulate to further regions after 0.0070 strain level in Figure 3.45.(a-3) where delamination regions can be observed on the other side of the hole region at this strain level in Figure 3.46. So, it is highly possible that CL3 events represent macro delaminations at the  $-45/90$  interface. Meanwhile CL1 events are registered due to the cracks on surface  $+45^\circ$  plies. A surface crack initiated next to the hole at 0.0048 strain level then propagated to the further regions at 0.0053 strain level in Figure 3.46. This propagation is consistent with the accumulation of CL1 events in Figure 3.45.(a-3). They were localized at the hole region (between 22-27 mm) and then a quick propagation happens at 0.0053 strain level in Figure 3.45.(a-3). Their propagation through the observed edge of the specimen between 0.0071 – 0.0076 strain levels in Figure 3.46 can be traced by following the CL1 events between the same interval in Figure 3.45.(a-3). With the load drop at 0.0077 strain, very few or no CL1 events are registered between 22-28 mm anymore as seen in Figure 3.45.(b-3) because this surface is already separated near the hole region and it continues to separate near the free edges that is less than 22 mm (at the observed edge) and greater than 28 mm (at the unobserved edge) far from the AE detecting sensor. Thus, it is said that CL1 events represent cracks at the surface  $+45^\circ$  plies. First transverse crack in  $90^\circ$  plies is detected at 0.0070 strain level in Figure 3.46. However, free edge delamination at 0.0048 strain level is believed to initiate due to the transverse crack at  $90^\circ$  plies. Unfortunately, this

is not detected with optical instruments in Figure 3.46. Tip of a delamination at  $-45/90$  interface is observed in the edge at 0.0071 strain level, immediately after first detection of transverse crack in  $90^\circ$  plies. Its propagation until 0.0076 strain level can be seen in Figure 3.46. Then it causes transverse cracks at the inner  $-45^\circ$  plies at this strain level. Also, the surface crack propagates through the observed edge of the specimen between 0.0071 – 0.0076 strain levels in Figure 3.46. Then, macro delamination separates the upper  $-45/90$  interface in the edge observation region at 0.0077 strain level. Moreover, transverse cracks in  $-45^\circ$  plies causes delaminations at  $-45/0$  interfaces at 0.0077 strain level. Very few CL3 events are registered after this load drop and at further regions as shown in Figure 3.45.(a-3) since the macro delamination is already propagated to the further region. High-frequency (CL4) events decrease and almost disappear after this load drop too. They are believed to represent transverse cracks at the inner  $90^\circ$  and  $-45^\circ$  plies. Their propagation in Figure 3.45.(b) is consistent with their optical detection in Figure 3.46. Three CL4 events are registered at around 0.0044 strain level in the edge observation region in Figure 3.45.(b). They represent transverse cracks at the inner  $90^\circ$  plies that cause free edge delamination, detected within  $\varepsilon_2$  strain map at 0.0048 strain level in Figure 3.46. Then CL4 events are registered after 0.0062 strain level in Figure 3.45.(b) and detected from the edge observation region at 0.0070 strain level in Figure 3.46. Another load drop occurs due to delamination at lower plies at 0.0081 strain level. Consequently, the CL1 events disappear with this load drop because surface layer is completely separated as seen in Figure 3.46.

It is not easy to distinguish damage at inner  $90^\circ$  and  $-45^\circ$  plies. There are two dominant damage modes present in this laminate type. Damage at surface  $+45^\circ$  plies (CL1 events) and macro delamination (CL3 events). Since these damage modes are considerably large, their presence reduces the sensitivity of AE registration of micro damage modes. It is highly possible that low-amplitude/high-frequency events (CL4) consist of transverse cracks both at the inner  $90^\circ$  and  $-45^\circ$  plies. Finally, low-amplitude/low-frequency AE events (CL2) are believed to represent micro delaminations at  $\pm 45/90$  interfaces as in previous laminate types, because they are registered from the whole gauge length and during the whole test.

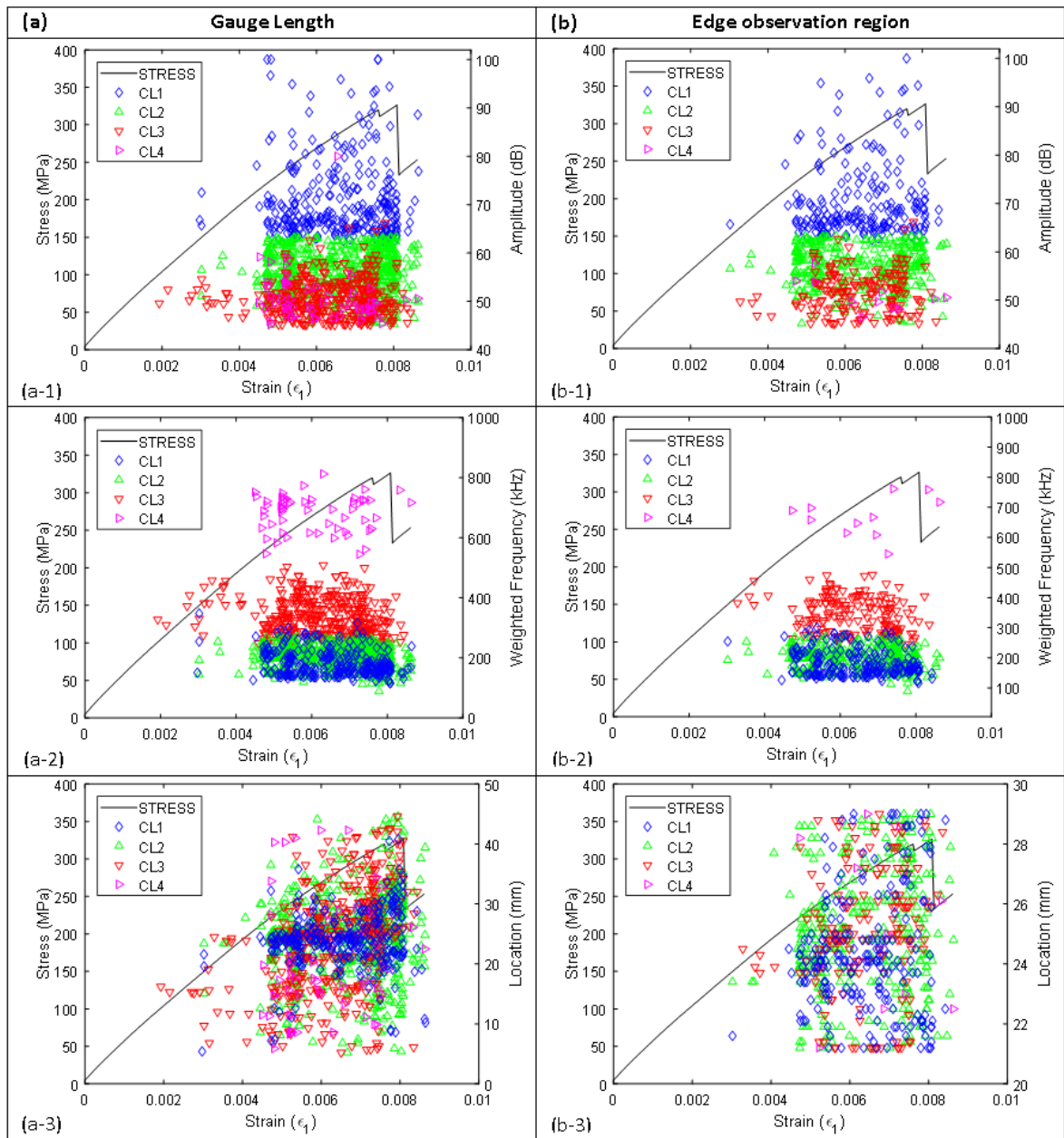


Figure 3.45. Accumulation of AE clusters throughout a test in for  $[+45_2/90_2/-45_2/0_2]_s$  laminate: (a) full gage length; (b) edge observation region only; (1) events amplitude; (2) events weighted frequency; (3) events location.

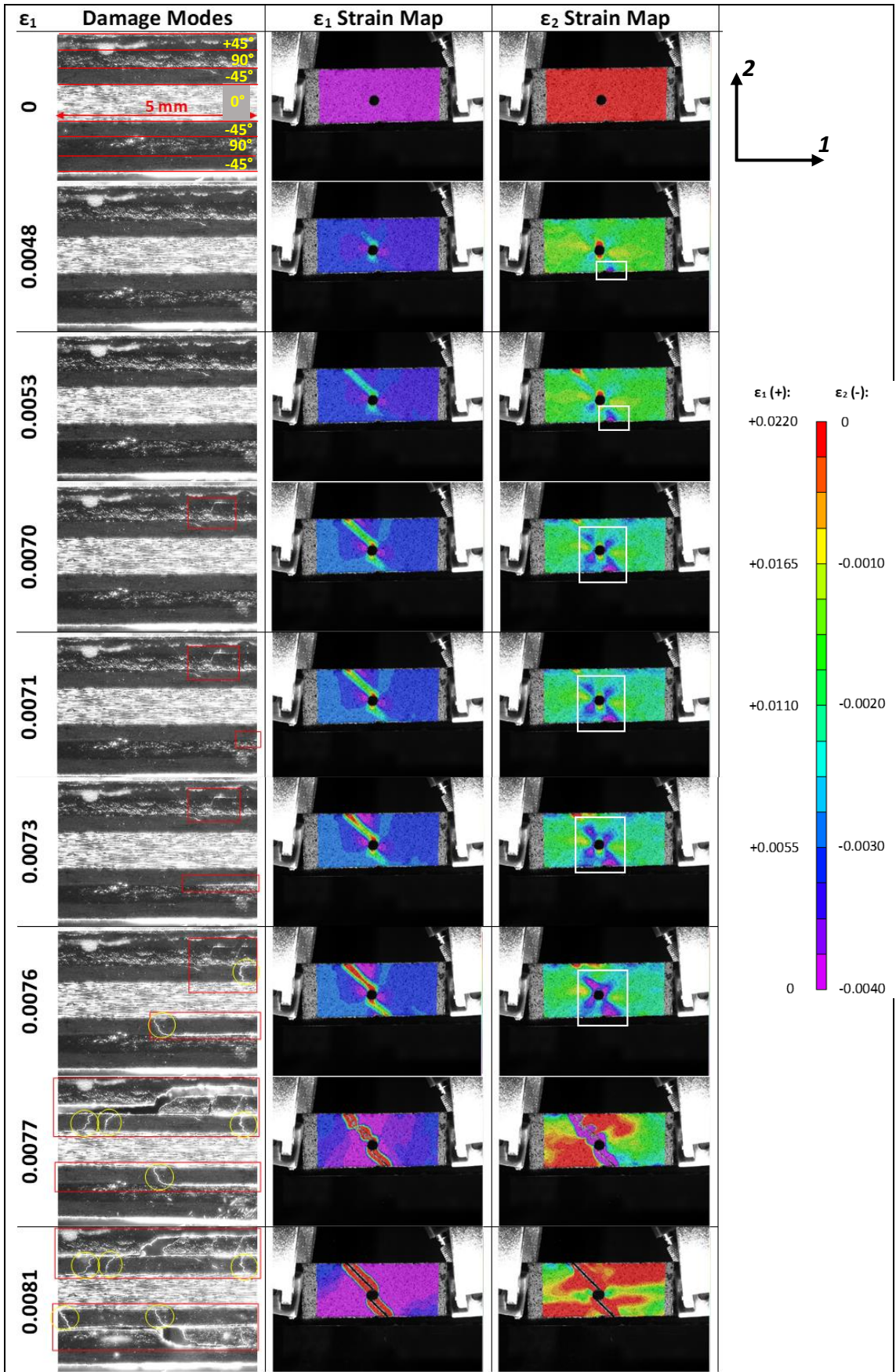


Figure 3.46. Damage progression in  $[+45_2/90_2/-45_2/0_2]_s$  laminate.

Wisnom and Hallet *et al.* [78, 92–95] performed extensive experimental programme to investigate the strength and failure mechanisms in  $[+45_m/90_m/-45_m/0_m]_{ns}$  laminates with different scaling, geometrical properties and hole sizes. Laminates were made from IM7/8552 prepregs. Ply-level scaled laminates (as defined in their studies) where  $m=2$  and  $m=4$  with a central hole size of 3.175 mm showed similar damage progression under tension loading [78, 92–95]. Online damage detection techniques were not used in these studies. AE was said to have low resolution and does not unambiguously identify the damage mode [94, 95]. Moreover, optical or electron microscopy and DIC were said to be unsuccessful to provide a 3D damage map of the laminates [94, 95]. Because of this assertion, Nixon-Pearson and Hallett performed post-mortem X-Ray micro-CT analysis to investigate induced damage modes after quasi-static tension and tension-tension fatigue tests [94, 95]. X-Ray micro-CT images at the end of interrupted tests at 60% and 80% the ultimate strength are shown in Figure 3.47.(a) and Figure 3.47.(b) [94]. X-Ray micro CT images provided very detailed damage map within the tested specimens. Damage sequence during loading was concluded with respect to micro-CT images in Figure 3.47 as follow [94]; Damage initiated with matrix splitting in surface  $+45^\circ$  plies from the hole edge. It was followed by isolated matrix splits in the  $90^\circ$  and  $-45^\circ$  plies, near the delamination regions of surface plies where the matrix splits were often accompanied by small local delaminations at adjacent  $\pm 45/90$  interfaces. Matrix cracks propagated across the width from the hole. This caused delaminations at  $90/-45$  interface. Splitting of the  $0^\circ$  plies in the middle section of the specimens occurred in this step. Major delamination occurred at  $-45/0$  interface, causing load drop. Final failure modes observed from the free edge of a  $[+45_4/90_4/-45_4/0_4]_s$  laminate is compared with the final failure of  $[+45_2/90_2/-45_2/0_2]_s$  laminate in this thesis in Figure 3.48. Dye-penetrant was used to highlight the damage modes from the free edge of the specimen in Figure 3.48.(a) [78].

Damage progression and final failure modes in previous studies [78, 92–95] are very similar to the identified damage modes and their propagation in this thesis. This can be clearly seen by comparing Figure 3.46, Figure 3.47 and Figure 3.48. Multi-instrumental damage detection approach, used in this thesis, provides easier and cheaper methodology for damage mode identification in QI laminates than previous studies [78, 92–95]. X-Ray micro CT is a very precise technique for damage mode identification in composite materials. However, it is a post-processing method and the specimens should be cut into very small

sizes to get better resolution of the induced damage modes. More importantly it is a very long process to get the damage maps in Figure 3.47. This thesis proved that simultaneous application of AE and DIC can provide strong evidences for damage modes and their propagation throughout the tests as opposed to Nixon-pearson *et al.* [94, 95]. Identification of AE characteristics of damage modes can require an easier experimental methodology for the subsequent tests such as the fatigue tests [94, 95]. This is a very important achievement and it can contribute to Nixon-pearson *et al.*'s [94, 95] study by identifying the induced damage modes with online AE technique. There are two very important finding from the results of  $[+45_2/90_2/-45_2/0_2]_s$  laminates in this thesis. First of all, the first damage mode induces in the laminate is transverse cracks in  $90^\circ$  plies which causes surface cracks at  $+45^\circ$  plies and free edge delaminations. Secondly, not only  $-45/0$  delaminations cause load drops but also delaminations at the  $\pm 45/90$  interfaces cause considerable load drops in stress-strain curves as presented in Figure 3.46.

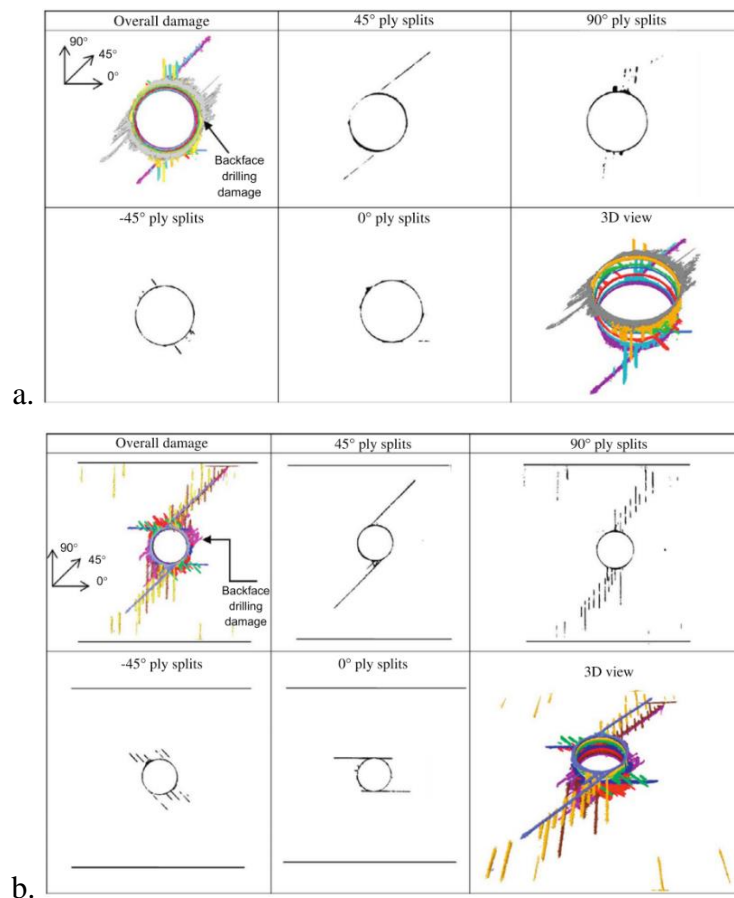


Figure 3.47. X-Ray micro CT images of  $[+45_2/90_2/-45_2/0_2]_s$  laminates at the end of; (a) 60% of ultimate strength, (b) 80% of ultimate strength [94].

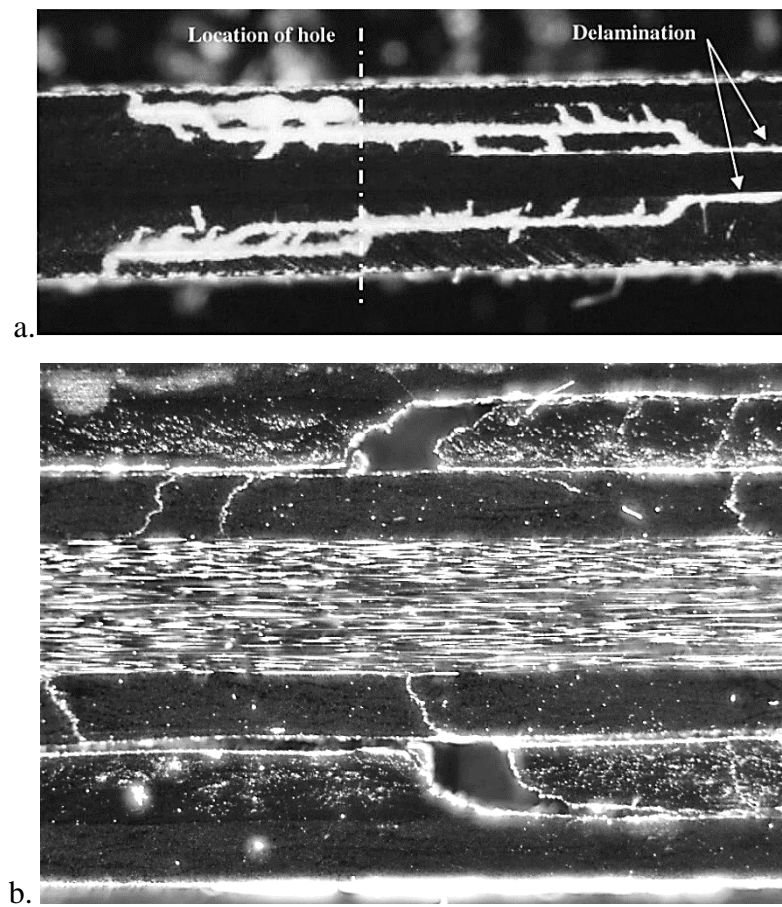


Figure 3.48. Final failure modes in (a)  $[+45_4/90_4/-45_4/0_4]_s$  laminates [78] (b)  $[+45_2/90_2/-45_2/0_2]_s$  in this thesis.

### 3.4.5. Summary of the Damage Sequence in OHT QI Laminates

Sections 3.4.1. – 3.4.4 present reliable correlations between damage modes and AE characteristics in details. Table 3.4 presents the damage sequences with AE characteristics according to these correlations. In addition to this, ultimate strength and strain levels of the laminates are presented in Table 3.4. Damage sequence in notched  $[-45_2/0_2/+45_2/90_2]_s$  laminate can be traced from Figure 3.35.(a) as follow: Transverse cracks at  $90^\circ$  plies initiate at 0.0025 strain level which are represented with CL4 events. Then CL3 events start at 0.0029 strain level due to the transverse cracks at  $+45^\circ$  plies. Large delaminations around hole region initiates at 0.0042 strain, represented by CL1 events. Micro delaminations at  $+45/90$  interface start at 0.0050 strain level and it is registered with CL2 events. Finally,

large number of CL1 events started due to the initiation of macro delaminations at 0.0062 strain level near the free edge of the specimen.

Damage sequence and AE correspondences are different in  $[90_2/-45_2/0_2/+45_2]_s$  laminate. Figure 3.38.(a) shows that first a damage initiates at 0.0032 strain level. Secondly transverse cracks at  $90^\circ$  plies occur through the width of the specimen at 0.0037 strain level and they are registered with CL1 events. Finally, macro delamination begins around the hole region at 0.0047 strain and that is detected due to the increasing number of CL3 events in Figure 3.38.(a) and Figure 3.38.(b).

Figure 3.41.(a) shows the damage sequence in notched  $[0_2/+45_2/90_2/-45_2]_s$  laminate as follow: First transverse cracks in  $90^\circ$  plies initiate at 0.0051 strain level, that are registered with CL4 events. Their initiations cause micro delaminations at the  $\pm 45/90$  interfaces at the same time which are registered with CL2 events. Then, large number of CL3 events start at 0.0054 strain level due to the transverse cracks in  $\pm 45^\circ$  plies. Then, damage initiation at the hole tip is detected with DIC at 0.0058 strain. It blunts the notch until 0.0066 strain level and causes propagation of fibre/matrix splitting through the gauge length of the specimen. This is represented with CL1 events. Finally, macro delaminations around the hole region and near the free edge becomes visible in  $\varepsilon_2$  strain map in Figure 3.42 at 0.0066 strain level. They are represented with CL1-2 events.

Finally, Figure 3.45.(a) shows the damage progression in  $[+45_2/90_2/-45_2/0_2]_s$ . First transverse cracks at the inner  $90^\circ$  and  $-45^\circ$  plies initiate at 0.0044 strain level that are registered with CL4 events. They cause micro delaminations at the  $\pm 45/90$  interfaces at the same time which are registered with CL2 events. Then, surface cracks at the  $+45^\circ$  plies start at 0.0047 strain level that are registered with CL1 events and immediately causes macro delaminations between  $+45/90$  interface at 0.0048 strain that can be traced by CL3 events in Figure 3.45.(a).

Table 3.4. Damage sequence and their AE characteristics in each OHT laminates.

Laminates (Failure Levels)	Damage sequence	AE Characteristics		Damage initiation Strain Level
		A (dB)	WF [kHz]	
$[-45_2/0_2/+45_2/90_2]_s$ $\left( \begin{array}{l} \sigma_u^T=390 \text{ MPa} \\ \varepsilon_u^T=0.0110 \end{array} \right)$	1. Transverse cracking in 90° plies	45...82	450...750	0.0025
	2. Transverse cracking in +45° plies	45...67	260...450	0.0029
	3. Micro delamination at 90/+45 interface	45...67	100...260	0.0050
	4. Macro delamination	67...100	100...400	0.0062
$[90_2/-45_2/0_2/+45_2]_s$ $\left( \begin{array}{l} \sigma_u^T=410 \text{ MPa} \\ \varepsilon_u^T=0.0110 \end{array} \right)$	1. Transverse cracking in surface 90° plies	67...100	100...350	0.0037
	2. Micro delamination at 90/+45 interface	45...67	100...250	0.0037
	3. Transverse cracking in -45° plies	45...67	520...800	0.0040
	4. Macro delamination	45...67	250...520	0.0048
$[0_2/+45_2/90_2/-45_2]_s$ $\left( \begin{array}{l} \sigma_u^T=460 \text{ MPa} \\ \varepsilon_u^T=0.0140 \end{array} \right)$	1. Transverse cracking in 90° plies	45...76	490...800	0.0051
	2. Micro delaminations at 90/±45 interface	45...70	100...310	0.0051
	3. Transverse cracking in ±45° plies	45...70	310...490	0.0054
	4. Fibre/matrix splitting in surface 0° plies	80...100	100...500	0.0058
	5. Macro delamination	70...80	100...500	0.0066
$[+45_2/90_2/-45_2/0_2]_s$ $\left( \begin{array}{l} \sigma_u^T=330 \text{ MPa} \\ \varepsilon_u^T=0.0116 \end{array} \right)$	1. Transverse cracking in 90° plies	45...63	540...800	0.0044
	2. Transverse cracking in -45° plies	45...63	100...280	0.0045
	3. Micro delaminations at 90/±45 interface	63...100	100...350	0.0047
	4. Surface cracks at +45° plies	45...63	280...540	0.0048
	5. Macro delamination	45...63	280...540	0.0048

## 4. CONCLUSION

Available literature shows that AE registration technique alone is not sufficient for damage mode identification in CFRP composites. In this thesis, two different CFRP laminate types are taken into consideration for damage mode identification under tension tests. First laminate type is UD [0]<sub>5</sub> specimens. Three different variants of this laminate type are tested. Specimens containing two different slit types (long-slit, short-slit specimens), and smooth (non-slit) are tested with real time AE registration. These slits are filled with resin during cure cycle and act as artificial defects to stimulate damage and provide damage modes to occur in desired order; matrix cracking, fibre/matrix debonding, delamination and fibre breaks.

A non-stopped tension test is completed up to final failure with AE registration. Then, interruption stress levels are determined by considering abrupt changes in cumulative AE energy curves. Next tests are performed to new specimens up to the determined interruption levels. At the end of each test, specimen edges are investigated under optical microscope to identify the induced damage modes and correlate with registered AE signals. It was seen that, AE registrations in non-stopped test are highly consistent with the results of interrupted tests.

Matrix cracking with fibre/matrix debonding from the boundaries of the fibres and resin pocket are happened first. AE characteristics of this damage is very selective. They have high amplitude and duration characteristics. Then this damage extends through the corners of boundaries in transverse to test direction and followed by delaminations which initiate from the corners of resin pockets. They are registered with lower amplitude and duration signals. It is seen that, discontinuities between plies, caused by delaminations, change the path of wave propagation within the material and increase the travel time of emitted waves. While the difference between the arrival time of signals for matrix cracks and delaminations are lower than 1 ms, it increases to 1-10 ms after delaminations. Next, individual fibre breaks are detected with AE signals having lowest amplitude and duration values. Their signals are seen to have higher travel time than previous damage modes. Finally, the specimens are separated due to breaks of large number of fibres at the end with highest amplitude and duration values.

Kaiser effect and Felicity effect in composite materials are reproduced. It is observed that very few or no AE signals are recorded up to the previous interruption levels up to 95% of ultimate strength due to Kaiser effect in composite materials. When the specimens are unloaded from 95% of their ultimate strength and loaded again, it is seen that large number of AE signals are recorded before reaching the last interruption level because of Felicity effect. Clear demonstrations are presented for these phenomena in this study. AE characteristics of possible damage modes in UD [0]<sub>n</sub> specimens are clearly identified. Moreover, in-situ AE registration and observation techniques applied to UD [0]<sub>5</sub> specimens enables to verify FEMM model for UD specimens.

Second laminate types are different variants of quasi-isotropic laminates consisting thick inner plies. Different in-situ observation techniques are applied simultaneously with AE registration. Additionally, pattern recognition technique is applied with the k-means++ clustering algorithm to AE results to group similar AE signals. Even though k-means++ clustering algorithm can recognise well-separated and dense clusters, it is found that those clusters cannot be unambiguously used to identify the type of the damage which caused the event. This study presents the necessity of multi-instrument optical observations for damage-mode identification and correlation with AE registrations.

Four different variants of QI laminates are tested. Application of AE registration, optical edge observations and surface strain mapping by DIC method simultaneously during tension tests provides invaluable insight for identifying the damage modes in progressive damage induced in the laminates during testing. Observations of QI laminates prove that high frequency signals are related to transverse matrix cracks at inner 90° plies and not fibre breaks as conventionally believed. Three to four cluster groups are found for classification of recorded AE events. However, their structures differ for each laminate. It is seen that low amplitude-high frequency events represent transverse cracks at inner 90° and ±45° plies whereas high amplitude-low frequency events represent damage at surface plies. Cluster groups are correlated to four different damage mode.

Damage initiation occurs with transverse cracks in 90° plies which is followed by micro delaminations at 90/±45 interfaces and propagation of transverse cracks to ±45° plies afterwards. This damage sequence is same in each laminate type but damage progression continues with macro delamination of 90°/±45° plies in [-45<sub>2</sub>/0<sub>2</sub>/+45<sub>2</sub>/90<sub>2</sub>]<sub>s</sub> laminate.

Furthermore, delaminations inside the laminate can be observed as disturbances in the surface strain maps, which is a novel observation, and as for the authors' knowledge not mentioned before in the open literature.

Finally Open-Hole Tension (OHT) tests of thick plied QI laminates are tested. These laminates contain 2.5 mm central hole in the middle. It is seen that, presence of a central hole causes the characteristics of clusters to be similar with each other. Because, damage modes are concentrated around the hole and causes different damage modes to occur around this region. In addition to this, due to the damage on surface and large delaminations are registered with high amplitude AE events, especially through the end of the tests. This situation prevents to register different micro damage modes sensitively.

In OHT specimens, AE characteristics of damage modes are highly affected with the position of the plies as in smooth specimens. It is proved that high frequency events are registered due to transverse cracks at the inner  $\pm 45^\circ$  or  $90^\circ$  plies, but not fibre breaks as stated in literature, for all laminates tested  $[-45_2/0_2/+45_2/90_2]_s$ ,  $[90_2/-45_2/0_2/+45_2]_s$ ,  $[0_2/+45_2/90_2/-45_2]_s$  and  $[+45_2/90_2/-45_2/0_2]_s$ . High amplitude events are registered due to delaminations between  $\pm 45/90$  plies around hole region of  $[-45_2/0_2/+45_2/90_2]_s$  and  $[0_2/+45_2/90_2/-45_2]_s$  laminates. However, the AE trend for damage modes change for the  $[90_2/-45_2/0_2/+45_2]_s$  and  $[+45_2/90_2/-45_2/0_2]_s$  laminates. It is seen that, cracks at surface plies (regardless of fibre orientation) are registered with high amplitude events and delaminations are registered with low-amplitude/mid-frequency events.

It would not have been possible to identify all damage modes and determine the AE characteristics of them if optical observation techniques had not been applied simultaneously in this study. Robust correlations between damage modes and their corresponding AE characteristics are achieved with the multi-instrumental damage detection approaches during tension tests of various AS4/8552 laminates in this study. Fibre breaks are not observed in this study and mostly matrix dominated damage modes were identified. Their AE characteristics are identified during the tension tests of UD laminates but left as interpretations and direct observation proofs are not provide clear evidence as matrix dominated damage modes. It can be concluded that fibre breaks need more detailed analysis, probably with instruments having higher resolution such as in-situ micro-CT device [85, 86].

## 5. FUTURE WORK

The first work in future consist the identification of AE characteristics of fibre breaks and determining their damage levels. Matrix dominated damage modes are identified clearly with UD  $[0]_5$  slit-specimens. Fibre breaks are also identified but they are not accurately validated. In order to validate the characteristics of fibre breaks; different UD laminates are designed and manufactured. These new UD laminates consist resin rich regions, as the one in this thesis, and an additional fibre tow on mid-ply through the length of the laminates., aforementioned damage sequence will happen as in this thesis, then additional fibre tows will sustain the load after these damage modes and those fibres will start breaking through the end of the test and hence fibre breaks and their AE characteristics will be identified with AE technique.

Secondly, the effect of different number of inner plies, symmetric plies on the damage progression and their AE characteristics will be investigated. Table 5.1 presents the variations for the lay-up and geometrical properties of the specimens. Results of the shaded specimens are presented in this thesis. The other specimens are already tested with the experimental setup shown in Figure 2.11. However, the analysis of their test results with AE, DIC and edge microscopy observations are not finalized yet. Previously, Wisnom and Hallet *et al.* [78, 92–95] performed an extensive test programme for the bold laminates in Table 5.1. As presented in Section 3.4.5, in-situ observations provided very important information about damage progression in  $[+45_2/90_2/-45_2/0_2]_s$  laminates than their results. Invaluable optical evidences and AE characteristics of damage mode and their progression in different types of quasi-isotropic composite will be obtained for AS4/8552 at the end of this study.

Thirdly, it is seen that AE properties of transverse cracks in  $90^\circ$  plies shift from high amplitude to high frequency characteristics in  $[0_2/+45_2/90_2/-45_2]_s$  laminates after the damage initiation at the inner  $\pm 45^\circ$  plies. However, the physical reason causing this shift is a mystery in this thesis. Finding the reasons is left as a future work.

Furthermore, a Finite Element Model is being developed for these laminates by Sina Ahmadvashagbash currently. The predictions of the model will be presented in his MSc thesis.

Table 5.1. Test specimens and their lay-up and geometrical properties.

t (mm)	Scaling		Hole Diameter (mm)		Scaling		Hole Diameter (mm)	
	Sub-Laminate	0	2.5	Ply-Level	0	2.5		
1.5	[+45/90/-45/0] <sub>s</sub> [90/-45/0/+45] <sub>s</sub> [-45/0/+45/90] <sub>s</sub> [0/+45/90/-45] <sub>s</sub>	w/t=10 L <sub>G</sub> /t=50	w/t=10 L <sub>G</sub> /t=50 t/d=0.6	[+45/90/-45/0] <sub>s</sub> [90/-45/0/+45] <sub>s</sub> [-45/0/+45/90] <sub>s</sub> [0/+45/90/-45] <sub>s</sub>	w/t=10 L <sub>G</sub> /t=50	w/t=10 L <sub>G</sub> /t=50 t/d=0.6		
3	[+45/90/-45/0] <sub>2s</sub> [90/-45/0/+45] <sub>2s</sub> [-45/0/+45/90] <sub>2s</sub> [0/+45/90/-45] <sub>2s</sub>	w/t=5 L <sub>G</sub> /t=25	w/t=5 L <sub>G</sub> /t=25 t/d=1.2	[+45 <sub>2</sub> /90 <sub>2</sub> /-45 <sub>2</sub> /0 <sub>2</sub> ] <sub>s</sub> [90 <sub>2</sub> /-45 <sub>2</sub> /0 <sub>2</sub> /+45 <sub>2</sub> ] <sub>s</sub> [-45 <sub>2</sub> /0 <sub>2</sub> /+45 <sub>2</sub> /90 <sub>2</sub> ] <sub>s</sub> [0 <sub>2</sub> /+45 <sub>2</sub> /90 <sub>2</sub> /-45 <sub>2</sub> ] <sub>s</sub>	w/t=5 L <sub>G</sub> /t=25	w/t=5 L <sub>G</sub> /t=25 t/d=1.2		

## 6. REFERENCES

1. Callister, W. D., *Materials science and engineering: An introduction*. John Wiley & Sons Inc., New York, 1987.
2. Ashby, M., “Material and process charts”, *The CES EduPack Resource Booklet 2*, p. 42, 2010.
3. Vectorply, “Reinforcement Fibers - Vectorply.” <http://vectorply.com/reinforcement-fibers/>, accessed at September 2017 .
4. The Japan Carbon Fiber Manufacturers Association (JCFA), “Aircraft and Aerospace Fields.” <http://www.carbonfiber.gr.jp/english/field/craft.html>, accessed at September 2017 .
5. Taslim Badeghar, “Market Trends: Lightning Up with Carbon Fiber-Reinforced Plastics | 2016-01-04 | Adhesives Magazine.” <https://www.adhesivesmag.com/articles/94350-market-trends-lightening-up-with-carbon-fiber-reinforced-plastics>, accessed at September 2017 .
6. Aran, A., *Non-Destructive Testing*. ITU School of Mechanical Engineering, 2006.
7. Schreier, H., J.-J. Orteu, and M. A. Sutton, *Image Correlation for Shape, Motion and Deformation Measurements*. Springer US, 2009.
8. Elsevier, “Scopus, the largest database of peer-reviewed literature.” [www.scopus.com](http://www.scopus.com), accessed at September 2017 .
9. Barré, S. and M. L. Benzeggagh, “On the use of acoustic emission to investigate damage mechanisms in glass-fibre-reinforced polypropylene”, *Composites Science and Technology*, Vol. 52, No. 3 pp. 369–376, 1994.

10. de Groot, P. J., P. A. M. Wijnen, and R. B. F. Janssen, “Real-time frequency determination of acoustic emission for different fracture mechanisms in carbon/epoxy composites”, *Composites Science and Technology*, Vol. 55, No. 4 pp. 405–412, 1995.
11. Suzuki, M., S. Kida, M. Shimbo, and Y. Miyani, “Effects of fiber content on fracture mechanisms of short fiber reinforced PET composites,” *Tsai S.W., Springer G.S. (Eds.), Proceedings of the 8th International Conference on Composite Materials*, 1988.
12. Suzuki, M., H. Nakanishi, M. Iwamoto, and E. Jinen, “Application of static fracture mechanisms to fatigue fracture behavior of class A-SMC composite,” *Proceedings of the 4th Japan-US Conference on Composite Materials*, 1988.
13. Komai, K., K. Minoshima, and T. Shibutani, “Investigations of the Fracture Mechanism of Carbon/Epoxy Composites by AE Signal Analyses”, *Bioscienci Biotechnology Biochemistry*, Vol. 34, No. 4 pp. 381–388, 1991.
14. Russell, S. S. and E. G. Henneke, *Signature analysis of acoustic emission from graphite/epoxy composites. Interim report*, 1977.
15. Ceysson, O., M. Salvia, and L. Vincent, “Damage mechanisms characterisation of carbon fibre/epoxy composite laminates by both electrical resistance measurements and acoustic emission analysis”, *Scripta Materialia*, Vol. 34, No. 8 pp. 1273–1280, April 1996.
16. Kim, S.-T. and Y.-T. Lee, “Characteristics of damage and fracture process of carbon fiber reinforced plastic under loading-unloading test by using AE method”, *Materials Science and Engineering: A*, Vol. 234, pp. 322–326, 1997.
17. Tensi, H. M., “Kaiser effect and its background”, *Journal of Acoustic Emission*, Vol. 22, pp. s1–s16, 2004.

18. Kotsikos, G., J. T. Evans, A. G. Gibson, and J. Hale, "Use of acoustic emission to characterize corrosion fatigue damage accumulation in glass fiber reinforced polyester laminates", *Polymer Composites*, Vol. 20, No. 5 pp. 689–696, October 1999.
19. Bohse, J., "Acoustic emission characteristics of micro-failure processes in polymer blends and composites", *Composites Science and Technology*, Vol. 60, pp. 1213–1226, 2000.
20. Quispitupa, A., B. Shafiq, F. Just, and D. Serrano, "Acoustic emission based tensile characteristics of sandwich composites", *Composites Part B: Engineering*, Vol. 35, No. 6–8 pp. 563–571, 2004.
21. Ramirez-Jimenez, C. R., N. Papadakis, N. Reynolds, T. H. Gan, P. Purnell, and M. Pharaoh, "Identification of failure modes in glass/polypropylene composites by means of the primary frequency content of the acoustic emission event", *Composites Science and Technology*, Vol. 64, No. 12 pp. 1819–1827, 2004.
22. Loutas, T. H., V. Kostopoulos, C. Ramirez-Jimenez, and M. Pharaoh, "Damage evolution in center-holed glass/polyester composites under quasi-static loading using time/frequency analysis of acoustic emission monitored waveforms", *Composites Science and Technology*, Vol. 66, No. 10 pp. 1366–1375, 2006.
23. Jong, H.-J., "Transverse Cracking in a Cross-ply Composite Laminate - Detection in Acoustic Emission and Source Characterization", *Journal of Composite Materials*, Vol. 40, No. 1 pp. 37–69, 2006.
24. Bussiba, A., M. Kupiec, and S. Ifergane, "Damage evolution and fracture events sequence in various composites by acoustic emission technique", *Composites Science and Technology*, Vol. 68, No. 5 pp. 1144–1155, 2008.

25. Bourchak, M., I. R. Farrow, I. P. Bond, C. W. Rowland, and F. Menan, “Acoustic emission energy as a fatigue damage parameter for CFRP composites”, *International Journal of Fatigue*, Vol. 29, No. 3 pp. 457–470, 2007.
26. Gutkin, R., C. J. Green, S. Vangrattanachai, S. T. Pinho, P. Robinson, and P. T. Curtis, “On acoustic emission for failure investigation in CFRP: Pattern recognition and peak frequency analyses”, *Mechanical Systems and Signal Processing*, Vol. 25, No. 4 pp. 1393–1407, 2011.
27. Naderi, M., A. Kahirdeh, and M. M. Khonsari, “Dissipated thermal energy and damage evolution of Glass/Epoxy using infrared thermography and acoustic emission”, *Composites Part B: Engineering*, Vol. 43, No. 3 pp. 1613–1620, 2012.
28. Cuadra, J., P. A. Vanniamparambil, K. Hazeli, I. Bartoli, and A. Kontsos, “Damage quantification in polymer composites using a hybrid NDT approach”, *Composites Science and Technology*, Vol. 83, pp. 11–21, 2013.
29. Liu, P. F., J. K. Chu, Y. L. Liu, and J. Y. Zheng, “A study on the failure mechanisms of carbon fiber/epoxy composite laminates using acoustic emission”, *Materials & Design*, Vol. 37, pp. 228–235, 2012.
30. Truong, T. C., M. Vettori, S. Lomov, and I. Verpoest, “Carbon composites based on multi-axial multi-ply stitched preforms. Part 4. Mechanical properties of composites and damage observation”, *Composites Part A: Applied Science and Manufacturing*, Vol. 36, No. 9 pp. 1207–1221, 2005.
31. Lomov, S. V., D. S. Ivanov, T. C. Truong, I. Verpoest, F. Baudry, K. Vanden Bosche, and H. Xie, “Experimental methodology of study of damage initiation and development in textile composites in uniaxial tensile test”, *Composites Science and Technology*, Vol. 68, No. 12 pp. 2340–2349, 2008.

32. Lomov, S. V., A. E. Bogdanovich, D. S. Ivanov, D. Mungalov, M. Karahan, and I. Verpoest, “A comparative study of tensile properties of non-crimp 3D orthogonal weave and multi-layer plain weave E-glass composites. Part 1: Materials, methods and principal results”, *Composites Part A: Applied Science and Manufacturing*, Vol. 40, No. 8 pp. 1134–1143, August 2009.
33. Ivanov, D. S., S. V. Lomov, A. E. Bogdanovich, M. Karahan, and I. Verpoest, “A comparative study of tensile properties of non-crimp 3D orthogonal weave and multi-layer plain weave E-glass composites. Part 2: Comprehensive experimental results”, *Composites Part A: Applied Science and Manufacturing*, Vol. 40, No. 8 pp. 1144–1157, 2009.
34. Bogdanovich, A. E., M. Karahan, S. V Lomov, and I. Verpoest, “Quasi-static tensile behavior and damage of carbon / epoxy composite reinforced with 3D non-crimp orthogonal woven fabric”, *Mechanics of Materials*, Vol. 62, pp. 14–31, 2013.
35. Lomov, S., M. Karahan, A. Bogdanovich, and I. Verpoest, “Monitoring of acoustic emission damage during tensile loading of 3D woven carbon/epoxy composites”, *Textile Research Journal*, Vol. 84, No. 13 pp. 1373–1384, 2014.
36. Baker, C., G. N. Morscher, V. V. Pujar, and J. R. Lemanski, “Transverse cracking in carbon fiber reinforced polymer composites: Modal acoustic emission and peak frequency analysis”, *Composites Science and Technology*, Vol. 116, pp. 26–32, 2015.
37. Maillet, E., C. Baker, G. N. Morscher, V. V. Pujar, and J. R. Lemanski, “Feasibility and limitations of damage identification in composite materials using acoustic emission”, *Composites Part A: Applied Science and Manufacturing*, Vol. 75, pp. 77–83, 2015.

38. Fotouhi, M., P. Suwarta, M. Jalalvand, G. Czel, and M. R. Wisnom, “Detection of fibre fracture and ply fragmentation in thin-ply UD carbon/glass hybrid laminates using acoustic emission”, *Composites Part A: Applied Science and Manufacturing*, Vol. 86, pp. 66–76, 2016.
39. Mohammadi, R., M. A. Najafabadi, M. Saeedifar, J. Yousefi, and G. Minak, “Correlation of acoustic emission with finite element predicted damages in open-hole tensile laminated composites”, *Composites Part B: Engineering*, Vol. 108, pp. 427–435, 2017.
40. Bakhtiary Davijani, A. A., M. Hajikhani, and M. Ahmadi, “Acoustic Emission based on sentry function to monitor the initiation of delamination in composite materials”, *Materials and Design*, Vol. 32, No. 5 pp. 3059–3065, 2011.
41. Fotouhi, M. and M. Ahmadi Najafabadi, “Investigation of the mixed-mode delamination in polymer-matrix composites using acoustic emission technique”, *Journal of Reinforced Plastics and Composites*, Vol. 33, No. 19 pp. 1767–1782, 2014.
42. Mohammadi, R., M. Saeedifar, H. H. Toudeshky, M. A. Najafabadi, and M. Fotouhi, “Prediction of delamination growth in carbon/epoxy composites using a novel acoustic emission-based approach”, *Journal of Reinforced Plastics and Composites*, Vol. 34, No. 11 pp. 868–878, 2015.
43. Fotouhi, M., M. Saeedifar, S. Sadeghi, M. Ahmadi Najafabadi, and G. Minak, “Investigation of the damage mechanisms for mode I delamination growth in foam core sandwich composites using acoustic emission”, *Structural Health Monitoring*, Vol. 14, No. 3 pp. 265–280, 2015.
44. Fotouhi, M. and M. A. Najafabadi, “Acoustic emission-based study to characterize the initiation of delamination in composite materials”, *Journal of Thermoplastic Composite Materials*, Vol. 29, No. 4 pp. 519–537, 2016.

45. Saeedifar, M., M. Fotouhi, M. Ahmadi Najafabadi, H. Hosseini Toudeshky, and G. Minak, "Prediction of quasi-static delamination onset and growth in laminated composites by acoustic emission", *Composites Part B: Engineering*, Vol. 85, pp. 113–122, 2016.
46. Nazmdar Shahri, M., J. Yousefi, M. Fotouhi, and M. Ahmadi Najfabadi, "Damage evaluation of composite materials using acoustic emission features and Hilbert transform", *Journal of Composite Materials*, Vol. 50, No. 14 pp. 1897–1907, 2016.
47. Huguet, S., N. Godin, R. Gaertner, L. Salmon, and D. Villard, "Use of acoustic emission to identify damage modes in glass fibre reinforced polyester", *Composites Science and Technology*, Vol. 62, No. 10–11 pp. 1433–1444, 2002.
48. Mao, J. and A. K. Jain, "Artificial neural networks for feature extraction and multivariate data projection", *IEEE Transactions on Neural Networks*, 1995.
49. Godin, N., S. Huguet, R. Gaertner, and L. Salmon, "Clustering of acoustic emission signals collected during tensile tests on unidirectional glass/polyester composite using supervised and unsupervised classifiers", *NDT and E International*, Vol. 37, No. 4 pp. 253–264, 2004.
50. Godin, N., S. Huguet, and R. Gaertner, "Integration of the Kohonen's self-organising map and k-means algorithm for the segmentation of the AE data collected during tensile tests on cross-ply composites", *NDT and E International*, Vol. 38, No. 4 pp. 299–309, 2005.
51. Godin, N., S. Huguet, and R. Gaertner, "Influence of hydrolytic ageing on the acoustic emission signatures of damage mechanisms occurring during tensile tests on a polyester composite: Application of a Kohonen's map", *Composite Structures*, Vol. 72, No. 1 pp. 79–85, 2006.

52. Sause, M. G. R., A. Gribov, A. R. Unwin, and S. Horn, "Pattern recognition approach to identify natural clusters of acoustic emission signals", *Pattern Recognition Letters*, Vol. 33, No. 1 pp. 17–23, 2012.
53. Sause, M. G. R. and S. Horn, "Simulation of acoustic emission in planar carbon fiber reinforced plastic specimens", *Journal of Nondestructive Evaluation*, 2010.
54. Sause, M. G. R., T. Muller, A. Horoschenkoff, and S. Horn, "Quantification of failure mechanisms in mode-I loading of fiber reinforced plastics utilizing acoustic emission analysis", *Composites Science and Technology*, Vol. 72, No. 2 pp. 167–174, 2012.
55. Kempf, M., O. Skrabala, and V. Altstädt, "Reprint of: Acoustic emission analysis for characterisation of damage mechanisms in fibre reinforced thermosetting polyurethane and epoxy", *Composites Part B: Engineering*, Vol. 65, pp. 117–123, 2014.
56. Refahi Oskouei, A., H. Heidary, M. Ahmadi, and M. Farajpur, "Unsupervised acoustic emission data clustering for the analysis of damage mechanisms in glass/polyester composites", *Materials and Design*, Vol. 37, pp. 416–422, 2012.
57. Li, L., S. V. Lomov, X. Yan, and V. Carvelli, "Cluster analysis of acoustic emission signals for 2D and 3D woven glass/epoxy composites", *Composite Structures*, Vol. 116, No. 1 pp. 286–299, 2014.
58. Li, L., S. V. Lomov, and X. Yan, "Correlation of acoustic emission with optically observed damage in a glass/epoxy woven laminate under tensile loading", *Composite Structures*, Vol. 123, pp. 45–53, 2015.
59. Li, L., Y. Swolfs, I. Straumit, X. Yan, and S. V. Lomov, "Cluster analysis of acoustic emission signals for 2D and 3D woven carbon fiber/epoxy composites", *Journal of Composite Materials*, Vol. 50, No. 14 pp. 1921–1935, 2016.

60. Grédiac, M., “The use of full-field measurement methods in composite material characterization: interest and limitations”, *Composites Part A: Applied Science and Manufacturing*, Vol. 35, No. 7–8 pp. 751–761, July 2004.
61. Pierron, F., B. Green, and M. R. Wisnom, “Full-field assessment of the damage process of laminated composite open-hole tensile specimens. Part I: Methodology”, *Composites Part A: Applied Science and Manufacturing*, Vol. 38, No. 11 pp. 2307–2320, 2007.
62. Pierron, F., B. Green, M. R. Wisnom, and S. R. Hallett, “Full-field assessment of the damage process of laminated composite open-hole tensile specimens. Part II: Experimental results”, *Composites Part A: Applied Science and Manufacturing*, Vol. 38, No. 11 pp. 2321–2332, 2007.
63. Lomov, S. V., D. S. Ivanov, I. Verpoest, M. Zako, T. Kurashiki, H. Nakai, J. Molimard, and A. Vautrin, “Full-field strain measurements for validation of meso-FE analysis of textile composites”, *Composites Part A: Applied Science and Manufacturing*, Vol. 39, No. 8 pp. 1218–1231, 2008.
64. Feissel, P., J. Schneider, Z. Aboura, and P. Villon, “Use of diffuse approximation on DIC for early damage detection in 3D carbon/epoxy composites”, *Composites Science and Technology*, Vol. 88, pp. 16–25, 2013.
65. Goidescu, C., H. Weleman, C. Garnier, M. Fazzini, R. Brault, E. Péronnet, and S. Mistou, “Damage investigation in CFRP composites using full-field measurement techniques: Combination of digital image stereo-correlation, infrared thermography and X-ray tomography”, *Composites Part B: Engineering*, Vol. 48, pp. 95–105, May 2013.
66. Erçin, G. H., P. P. Camanho, J. Xavier, G. Catalanotti, S. Mahdi, and P. Linde, “Size effects on the tensile and compressive failure of notched composite laminates”, *Composite Structures*, Vol. 96, pp. 736–744, February 2013.

67. Caminero, M. A., M. Lopez-Pedrosa, C. Pinna, and C. Soutis, “Damage Assessment of Composite Structures Using Digital Image Correlation”, *Applied Composite Materials*, Vol. 21, No. 1 pp. 91–106, 2014.
68. Furtado, C., A. Arteiro, G. Catalanotti, J. Xavier, and P. P. Camanho, “Selective ply-level hybridisation for improved notched response of composite laminates”, *Composite Structures*, Vol. 145, pp. 1–14, 2016.
69. Sawan, H. A., M. E. Walter, and B. Marquette, “Unsupervised learning for classification of acoustic emission events from tensile and bending experiments with open-hole carbon fiber composite samples”, *Composites Science and Technology*, Vol. 107, pp. 89–97, 2015.
70. Carvelli, V., A. D’Ettorre, and S. V Lomov, “Acoustic emission and damage mode correlation in textile reinforced PPS composites”, *Composite Structures*, Vol. 163, pp. 399–409, March 2017.
71. Andrew, J. J., V. Arumugam, D. J. Bull, and H. N. Dhakal, “Residual strength and damage characterization of repaired glass/epoxy composite laminates using A.E. and D.I.C”, *Composite Structures*, Vol. 152, pp. 124–139, 2016.
72. Hexcel, “HexPly ® 8552 - Product Data Sheet - EU Version”pp. 1–6, 2016.
73. Shivakumar, K. N., R. Panduranga, J. Skujins, and S. Miller, “Assessment of mode-II fracture tests for unidirectional fiber reinforced composite laminates”, *Journal of Reinforced Plastics and Composites*, Vol. 34, No. 23 pp. 1905–1925, 2015.
74. Oz, F. E., *Micromechanical Progressive Damage Model for Predicting Resin Dominated Strength Values of Fibre Reinforced Composites Under Various Types of Loading*, M.S. Thesis, Boğaziçi University, 2012.

75. ASTM, “D3039/D3039M: Standard Test Method for Tensile Properties of Polymer Matrix Composite Materials”, *Annual Book of ASTM Standards*, Vol. 14, pp. 1–13, 2014.
76. ASTM, “D5766/5766M: Standard Test Method for Open-Hole Tensile Strength of Polymer Matrix Composite”, *Annual Book of ASTM Standards*, Vol. 13, pp. 1–7, 2013.
77. Sandvik, “Composite Product Solutions”, *Sandvik Coromat*, pp. 34–55, 2011.
78. Green, B. G., M. R. Wisnom, and S. R. Hallett, “An experimental investigation into the tensile strength scaling of notched composites”, *Composites Part A: Applied Science and Manufacturing*, Vol. 38, No. 3 pp. 867–878, 2007.
79. MISTRAS, “Application of USB AE Node to Fatigue and Tension / Compression Tests”, *MISTRAS USB AE Node*, 2013.
80. MISTRAS, “PK15I Sensor Product Data Sheet”, *MISTRAS Products*, 2011.
81. Takaku, A. and M. Shioya, “X-ray measurements and the structure of polyacrylonitrile- and pitch-based carbon fibres”, *Journal of Materials Science*, Vol. 25, No. 11 pp. 4873–4879, 1990.
82. Shioya, M., E. Hayakawa, and a. Takaku, “Non-hookean stress-strain response and changes in crystallite orientation of carbon fibres”, *Journal of Materials Science*, Vol. 31, No. 17 pp. 4521–4532, 1996.
83. Djordjevic, I. M., D. R. Sekulic, M. N. Mitric, and M. M. Stevanovic, “Non-Hookean Elastic Behavior and Crystallite Orientation in Carbon Fibers”, *Journal of Composite Materials*, Vol. 44, No. 14 pp. 1717–1727, 2010.

84. Bourchak, M., *The use of acoustic emission for damage assessment of composite materials and life prediction under spectrum fatigue loading*, Ph.D. Thesis, University of Bristol, 2007.
85. Scott, A. E., M. Mavrogordato, P. Wright, I. Sinclair, and S. M. Spearing, “In situ fibre fracture measurement in carbon-epoxy laminates using high resolution computed tomography”, *Composites Science and Technology*, Vol. 71, No. 12 pp. 1471–1477, 2011.
86. Swolfs, Y., H. Morton, A. E. Scott, L. Gorbatikh, P. A. S. Reed, I. Sinclair, S. M. Spearing, and I. Verpoest, “Synchrotron radiation computed tomography for experimental validation of a tensile strength model for unidirectional fibre-reinforced composites”, *Composites Part A: Applied Science and Manufacturing*, Vol. 77, pp. 106–113, October 2015.
87. Oz, F. E., K. Cinar, and N. Ersoy, “Micromechanical progressive damage model for predicting resin dominated strength values of fibre reinforced composites under various types of loading,” *ECCM 2012 - Proceedings of the 15th European Conference on Composite Materials*, 2012.
88. Ersoy, N. and F. E. Oz, “Micromechanical Investigation of Residual Stresses and Strength of Cross-Ply Laminates,” *ICCM 19 - Proceedings of the 19th International Conference on Composite Materials*, 2013.
89. Oz, F. E. and N. Ersoy, “Acoustic Emission Analysis for Validation of Micro Mechanical Models,” *ICCM 2015 - Proceedings of the 20th International Conference on Composite Materials*, 2015.
90. Hexcel, “HexTow ® AS4”, *Material Datasheet*, Vol. 0, p. 2, 2015.

91. Wisnom, M. R., B. Khan, and S. R. Hallett, “Size effects in unnotched tensile strength of unidirectional and quasi-isotropic carbon/epoxy composites”, *Composite Structures*, Vol. 84, No. 1 pp. 21–28, 2008.
92. Wisnom, M. R., S. R. Hallett, and C. Soutis, “Scaling Effects in Notched Composites”, *Journal of Composite Materials*, Vol. 44, No. 2 pp. 195–210, 2010.
93. Wisnom, M. R. and S. R. Hallett, “The role of delamination in strength, failure mechanism and hole size effect in open hole tensile tests on quasi-isotropic laminates”, *Composites Part A: Applied Science and Manufacturing*, Vol. 40, No. 4 pp. 335–342, 2009.
94. Nixon-pearson, O. J., S. R. Hallett, P. J. Withers, and J. Rouse, “Damage development in open-hole composite specimens in fatigue . Part 1 : Experimental investigation”, *Composite Structures*, Vol. 106, pp. 882–889, 2013.
95. Nixon-Pearson, O. J. and S. R. Hallett, “An investigation into the damage development and residual strengths of open-hole specimens in fatigue”, *Composites Part A: Applied Science and Manufacturing*, Vol. 69, pp. 266–278, 2015.
96. Aidi, B. and S. W. Case, “Experimental and Numerical Analysis of Notched Composites Under Tension Loading”, *Applied Composite Materials*, Vol. 22, No. 6 pp. 837–855, 2015.
97. Amacher, R., J. Cugnoni, J. Botsis, L. Sorensen, W. Smith, and C. Dransfeld, “Thin ply composites: Experimental characterization and modeling of size-effects”, *Composites Science and Technology*, Vol. 101, pp. 121–132, 2014.